

# **Oxidation Kinetics of Molten Copper Sulphide**

By

Abdelmonem Hussein Alyaser

B.Sc. (Metallurgical Engineering), Laurentian University, 1990

A THESIS SUBMITTED IN PARTIAL FULFILLMENT OF  
THE REQUIREMENTS FOR THE DEGREE OF  
MASTER OF APPLIED SCIENCE

in

THE FACULTY OF GRADUATE STUDIES  
(Department of Metals and Materials Engineering)

We accept this thesis as conforming  
to the required standard

---

THE UNIVERSITY OF BRITISH COLUMBIA

July 1993

© Abdelmonem Hussein Alyaser, 1993

In presenting this thesis in partial fulfilment of the requirements for an advanced degree at the University of British Columbia, I agree that the Library shall make it freely available for reference and study. I further agree that permission for extensive copying of this thesis for scholarly purposes may be granted by the head of my department or by his or her representatives. It is understood that copying or publication of this thesis for financial gain shall not be allowed without my written permission.

(Signature)

Department of Metals and Materials Engineering

The University of British Columbia  
Vancouver, Canada

Date July 12 1993

## ABSTRACT

The oxidation kinetics of molten copper sulphide were investigated by quantitative measurements and qualitative observations. Off-gas analyses for  $\text{SO}_2$  and  $\text{O}_2$  were conducted to determine the oxidation rates of approximately 200-gram samples, of molten 99.5%  $\text{Cu}_2\text{S}$ . The molten sulphide was held in alumina crucibles (approximately 44 mm diameter and 75 mm height), and top-lanced with Ar- $\text{O}_2$  gas mixtures in the hot zone of a vertical tube furnace. During the oxidation reaction, gravimetric measurements of the copper sulphide baths were also conducted to further support the results of the gas analysis measurements. A series of laboratory tests, involving reaction gas ranging in composition from 20-78%  $\text{O}_2$ , was conducted to determine the effect of oxygen concentration on the kinetics of the oxidation reaction. To determine the influence of volumetric gas flow rate on the kinetics of the oxidation reaction and to study the gas phase mass transfer, a series of laboratory tests was carried out utilizing a gas flow rate range of 1-4 liters/min. The effects of other operating conditions, on the oxidation rates, such as bath mixing, and reaction temperature (1200-1300 °C), were also determined.

The effect of surface-tension driven flow (the Marangoni effect) on the reaction kinetics was also investigated via surface observation and photography. The overall surface behavior was monitored for spontaneous motion, and the eruption of gas bubbles from the melt.

The quantitative analysis of reaction rates was also aided by the micro-examination of quenched bath samples via optical microscopy. Approximately 4-gram samples were extracted at specific reaction times, using U-shaped quartz tubes. The samples were examined microscopically to determine the reaction progress based on the characteristics of gas bubbles, copper droplets and the phases present.

The oxidation reaction of molten copper sulphide was found to take place in two distinct kinetic stages. During the primary stage, simultaneous partial desulphurization and oxygen saturation of the melt, via liquid-gas reaction at the melt surface, takes place. Upon saturation of the melt with oxygen, the secondary stage immediately commences. Throughout the secondary stage, the sulphide phase remains at a constant composition (approximately 80.83 wt% Cu, 17.7 wt% S and 1.47 wt% O at 1200 °C and 1 atm), due to simultaneous surface and melt reactions, until the overall reaction is complete. Three simultaneous melt reactions occur within the sulphide phase which are responsible for the formation of the metal phase (approximately 98.89 wt% Cu, 0.95 wt% S and 0.16 wt% O at 1200 °C and 1 atm). As a result of settling oxygen- and sulphur-saturated copper droplets, the metal phase accumulates at the bottom of the bath.

The experimental results revealed that the rate of reaction is controlled by the gas phase mass transfer of oxygen to the melt surface; the liquid phase mass transfer resistance and chemical reaction resistance are negligible. The bath was found to be vigorously mixed, primarily due to the effect of the Marangoni effect although the degree of mixing is slightly enhanced during the secondary stage as a result of rising SO<sub>2</sub> gas bubbles and falling copper droplets.

Based on the electrochemical behavior of the sulphide melt and the experimental revelations, a mathematical model was constructed to carry out a fundamental study of the problem and provide an overall analysis extending beyond the experimental conditions. The model predictions were found to be in good agreement with the observed results.

The practical implications of this work are: the copper-making reaction in copper converting is limited by gas phase mass transfer; in the Peirce-Smith converter, one of the factors for the high degree of mass transfer in the bath is the effect of surface-tension

driven flows. It is also suggested that the ionic nature of the sulphide bath is another factor for the low liquid phase mass transfer resistance.

## Table of Contents

ABSTRACT .....	ii
Table of Contents.....	v
List of Figures .....	viii
List of Tables .....	xv
List of Symbols .....	xix
Acknowledgments .....	xxiii
1. Introduction.....	1
2. Literature Review .....	4
2.1. Copper Converting.....	4
2.1.1. History of the Copper Converter.....	4
2.1.2. Metallurgy of Copper Converting.....	5
2.1.2.1. The Slag-Forming Stage: .....	7
2.1.2.2. The Copper-Making Stage:.....	7
2.2. Thermodynamics of Copper Sulphide Oxidation .....	8
2.2.1. Cu-S System .....	9
2.2.2. Cu-S-O System .....	10
2.3. Gas-Liquid Interactions .....	13
2.3.1. Superficial Gas-Liquid Contact .....	16
2.3.2. Convective Gas-Liquid Contact.....	17
2.3.2.1. Gas Jets Impinging on Liquid Surfaces .....	17
2.3.2.1.1. High Momentum Jetting Systems.....	19
2.3.2.1.2. Low Momentum Jetting Systems .....	21
2.4. Oxidation Kinetic Studies.....	23
2.5. Interfacial Phenomena .....	26
2.5.1. Generation of Spontaneous Interfacial Motion.....	27
2.5.1.1. Driving Force.....	27
2.5.1.2. Mechanism.....	29
3. Objectives and Scope.....	32
3.1. Experimental Objectives.....	34
3.2. Theoretical Objectives .....	35
4. Experimental.....	36
4.1. Experimental Apparatus .....	36
4.1.1. Reactor.....	36
4.1.2. Gas Drying And Control System .....	41
4.1.3. Gas Analysis System.....	41
4.1.3.1. SO <sub>2</sub> Absorber .....	42
4.1.3.2. Final Off-Gas Flow Rate Measurement.....	48
4.1.4. Gravimetric Measurement System.....	49
4.1.5. Optical Photography System.....	52
4.2. Material.....	54
4.2.1. Copper Sulphide .....	54
4.2.1.1. Supplied Copper Sulphide .....	54
4.2.1.2. Prepared Copper Sulphide .....	54

4.2.2.	Gases.....	55
4.2.3.	Hydrogen Peroxide Solution.....	56
4.2.4.	Titration Reagents.....	57
4.3.	Experimental Procedure.....	58
4.3.1.	Oxidation Rate Measurement .....	58
4.3.1.1.	Gas Analysis .....	60
4.3.1.2.	Gravimetric Measurement .....	61
4.3.2.	Microscopic-Examination of Frozen Melt Samples .....	61
4.3.3.	Surface Observation.....	61
5.	Experimental Results and Discussion.....	62
5.1.	Oxidation Rate Results .....	62
5.1.1.	Gas Analysis Data.....	62
5.1.1.1.	Sulphur and Sulphur Dioxide Analyses.....	62
5.1.1.2.	Oxygen Analysis.....	65
5.1.1.3.	Overall Reaction Rate .....	68
5.1.2.	Gravimetric Measurement Data.....	70
5.1.3.	Summary Of The Oxidation Rate Results .....	71
5.1.3.1.	Oxidation Rates .....	71
5.1.3.1.1.	Effect of Admitted Gas Flow Rate .....	72
5.1.3.1.2.	Effect of Gas Composition .....	75
5.1.3.1.3.	Effect of Temperature .....	78
5.1.3.1.4.	Effect of Bath Mixing.....	81
5.1.3.2.	Reaction Transition Characteristics .....	82
5.2.	Micro-Examination Of The Melt Samples .....	85
5.3.	Observations of the Bath Surface .....	95
6.	Gas Phase Mass Transfer.....	103
6.1.	Mathematical Analysis for Mass-Transfer Coefficient.....	103
6.1.1.	Material Balance .....	103
6.1.2.	Flux Equation: .....	103
6.1.3.	Equilibrium At Phase Boundaries: .....	103
6.1.4.	Stoichiometry:.....	104
6.1.5.	Solution:.....	104
6.2.	Experimental Gas Phase Mass-Transfer Coefficient.....	105
6.3.	Gas Phase Mass-Transfer Correlation .....	109
6.4.	Sensitivity Analysis of the Effect of the Interfacial Area on Gas Phase Mass-Transfer Coefficient.....	113
6.5.	Sensitivity Analysis of the Effect of Temperature on Gas Phase Mass-Transfer Coefficient .....	116
7.	Mathematical Modeling and Theoretical Predictions.....	122
7.1.	Mathematical Model .....	122
7.1.1.	Assumptions .....	122
7.1.2.	Reaction Mechanism and Flux Equations .....	124
7.1.2.1.	Primary Stage.....	124
7.1.2.2.	Secondary Stage.....	125
7.1.3.	Equilibrium at Phase boundaries .....	128

7.1.4. Stoichiometry .....	130
7.1.4.1. Primary Stage.....	130
7.1.4.2. Secondary Stage.....	131
7.1.5. Material Balance .....	132
7.1.5.1. Primary Stage.....	132
7.1.5.1.1. Sulphur Balance.....	132
7.1.5.1.2. Oxygen Balance .....	133
7.1.5.2. Secondary Stage.....	133
7.1.5.2.1. Sulphide Phase.....	133
7.1.5.2.1.1. Sulphur Ion Balance.....	133
7.1.5.2.1.2. Oxygen Ion Balance.....	134
7.1.5.2.1.3. Copper Ion Balance.....	135
7.1.5.2.2. Metal Phase.....	135
7.1.5.2.2.1. Sulphur Balance.....	135
7.1.5.2.2.2. Oxygen Balance .....	136
7.1.5.2.2.3. Copper Balance.....	136
7.1.6. Mathematical Solution.....	137
7.1.6.1. Primary Stage.....	137
7.1.6.2. Secondary Stage.....	140
7.2. Model Validation .....	147
7.3. Model Sensitivity .....	150
7.3.1. Temperature .....	150
7.3.2. Pressure.....	151
7.3.3. Reaction Gas Flow Rate .....	153
7.3.4. Reaction Gas composition .....	154
7.3.5. Reaction Interfacial Area .....	155
7.4. Theoretical Predictions .....	156
7.4.1. Oxidation Path .....	156
7.4.2. Oxidation Rates .....	160
7.4.2.1. Oxidation Rate as a Function of Gas Flow Rate.....	160
7.4.2.2. Oxidation Rate as a Function of Gas Composition .....	164
7.4.2.3. Oxidation Rate as a Function of Temperature .....	170
7.4.3. Oxygen Utilization.....	173
8. Summary and Conclusions .....	175
References.....	178
Appendix A Experimental .....	187
1. Reactor Insulating Materials .....	187
2. Reactor Power Supply .....	189
3. Load Cell Components .....	190
Appendix B Gas Analysis Raw Data.....	191
Appendix C Reaction gas Transport Properties.....	210
1. Viscosity .....	210
2. Diffusion Coefficient .....	212
3. Density .....	214
Appendix D Temperature Measurements .....	215



## List of Figures

Figure 2.1. (a) Cutaway of a horizontal side-blown Pierce-Smith converter, (b). Positions of the Pierce-Smith converter for charging, blowing, and skimming (slag or blister copper).....	6
Figure 2.2. The Cu-S system; high temperature portion only, not to scale (after Kellogg [15]). .....	10
Figure 2.3. The 1300 °C isotherm of the Cu-O-S system, at 1 atm, (after Elliott [20]) .....	11
Figure 2.4. Schematic diagram of a hypothetical case of oxygen dissolution in a liquid metal bath, $R_g$ and $R_l$ are the gas phase resistance and the liquid phase resistance respectively .....	14
Figure 2.5. Comparative geometry of flow modes in top-blown systems .....	18
Figure 2.6. Model of impinging gas jet used by Wakelin (after Themelis and Szekely [52]).....	19
Figure 2.7. (a) Mass-transfer coefficient in gas phase at room temperature, (b) Mass-transfer coefficient in gas phase at elevated temperatures, (after Kikuchi et al [48]) .....	22
Figure 2.8. Type of adsorption at liquid-metal interfaces: (a), positive adsorption; (b) negative adsorption; (c), electrocapillary behaviour (after Brimacombe [83]) .....	27
Figure 2.9. Effect of oxygen on the surface tension of liquid copper, (after Monma [87]) .....	28
Figure 2.10. Effect of sulphur on the surface tension of liquid copper, (after Monma [87]).....	29
Figure 2.11. Interfacial motion generated on micro-scale due to eddy penetration (after Brimacombe [83]) .....	30
Figure 2.12 Interfacial motion generated on macro-scale by presence of partially immersed piece of $Cu_2S$ in molten copper.....	30
Figure 2.13. Mechanism of copper oxide patch spreading on the liquid copper surface.....	31
Figure 4.1. Cross-sectional view of the reactor .....	37
Figure 4.2. Sectional view of the bottom of the reaction tube, including the crucible supporting system .....	38
Figure 4.3. Schematic diagram of the top of the reaction tube .....	40
Figure 4.4. Schematic diagram of the gas train .....	41
Figure 4.5. Schematic diagram of the off-gas analysis system, not including the soap bubble-meter.....	42

Figure 4.6. Schematic diagram of the absorber rubber stopper .....	43
Figure 4.7. Plot of the amount of SO <sub>2</sub> absorbed as a function of time for a test of 2 l/min of 13 % SO <sub>2</sub> and 87% Ar at 23 °C.....	45
Figure 4.8. Photograph of the SO <sub>2</sub> absorber with a gas flow rate of 2 l/min, 13 % SO <sub>2</sub> and 87 % Ar.....	46
Figure 4.9. Photograph of the SO <sub>2</sub> absorber with a gas flow rate of 260 ml/min pure SO <sub>2</sub> .....	47
Figure 4.10. Schematic diagram of the soap bubble-meter .....	48
Figure 4.11. Schematic diagram of the load cell .....	49
Figure 4.12. Load cell calibration plot obtained with standard weights.....	51
Figure 4.13. Schematic diagram of the optical system used in the photography of the melt surface.....	53
Figure 5.1. Gas flows in the oxidation experiments .....	62
Figure 5.2. The reaction gas and off-gas as function of time, for the experimental conditions of: 200 grams of Cu <sub>2</sub> S, 2 l/min of 35% O <sub>2</sub> and 65% Ar, at 1200 °C.....	63
Figure 5.3. The final volumetric off-gas flow rate as a function of time for the experimental conditions of : 200-grams of Cu <sub>2</sub> S, 2 l/min of 35% O <sub>2</sub> and 65% Ar, at 1200 °C .....	64
Figure 5.4. The molar sulphur and oxygen contents in the bath as a function of time, for the experimental conditions of: 200-grams of Cu <sub>2</sub> S, 2 l/min of 35% O <sub>2</sub> and 65% Ar, at 1200 °C.....	68
Figure 5.5. Change of bath weight with time for the experimental conditions of: 200-grams of Cu <sub>2</sub> S, 2 l/min of 35% O <sub>2</sub> and 65% Ar, at 1200 °C.....	69
Figure 5.6. A gravimetric plot for the experimental conditions of : 200-grams of Cu <sub>2</sub> S, 2 l/min of 22% O <sub>2</sub> and 78% Ar, at 1200 °C.....	71
Figure 5.7. Oxygen reaction rate as a function of reaction gas volumetric flow rate; for the experimental conditions of 200-gram samples, 1200 °C, average pressure of 1.08 atm and 23 % O <sub>2</sub> .....	72
Figure 5.8. Sulphur removal rate as a function of reaction gas volumetric flow rate; for the experimental conditions of 200-gram samples, 1200 °C, average pressure of 1.08 atm and 23 % O <sub>2</sub> .....	73
Figure 5.9. Sulphur removal rate as a function of reaction gas volumetric flow rate; for the experimental conditions of 200-gram samples, 1200 °C, average pressure of 1.08 atm and 23 % O <sub>2</sub> .....	74
Figure 5.10. Oxygen reaction rate as a function of oxygen pressure for the experimental conditions of: 1200 °C and 2000 ml/min.....	75

Figure 5.11. Sulphur removal rate as a function of oxygen pressure for the experimental conditions of: 1200 °C and 2000 ml/min.....	76
Figure 5.12. Rate of weight loss as a function of oxygen pressure for the experimental conditions of: 1200 °C and 2000 ml/min.....	77
Figure 5.13. Oxygen reaction rate as a function of temperature for the experimental conditions of: 2000 ml/min of 20-23% O <sub>2</sub> and average pressure of 1.08 atm .....	79
Figure 5.14. Sulphur removal rate as a function of temperature for the experimental conditions of: 2000 ml/min of 20-23% O <sub>2</sub> and average pressure of 1.08 atm .....	80
Figure 5.15. Bath weight as a function of time for the experimental conditions of: 1200 C, average pressure of 1.08 atm and 22 % O <sub>2</sub> .....	81
Figure 5.17. Photomicrograph of polished section of frozen melt sample, at 7 min of reaction time (during the primary stage) .....	86
Figure 5.17. Photomicrograph of polished section of frozen melt sample, at 7 min of reaction time (during the primary stage) .....	87
Figure 5.18. Photomicrograph of polished section of frozen melt sample, at 15 min of reaction time (1 min after the copper droplets and SO <sub>2</sub> gas bubbles start to form in the melt) .....	87
Figure 5.19. Photomicrograph of polished section of frozen melt sample, at 25 min of reaction time.....	88
Figure 5.20. Photomicrograph of polished section of frozen melt sample, at 25 min of reaction time.....	89
Figure 5.21. Photomicrograph of polished section of frozen melt sample, at 35 min of reaction time.....	89
Figure 5.22. Photomicrograph of polished section of frozen melt sample, at 40 min of reaction time.....	90
Figure 5.23. Photomicrograph of polished section of frozen melt sample, at 50 min of reaction time.....	90
Figure 5.24. Photomicrograph of polished section of frozen melt sample, at 60 min reaction time (final reaction time is 70 min) .....	92
Figure 5.25. Photomicrograph of polished section of frozen melt sample, at 60 min reaction time (final reaction time is 70 min) .....	94
Figure 5.26. Photomicrograph of polished section of a 99.99% Cu standard sample .....	94
Figure 5.27. Bath surface, at 1200 °C with top-lancing at 2 l/min of Ar.....	95
Figure 5.28. Photograph of the bath surface at the same time of the admittance of the reaction gas .....	96

Figure 5.29. Photograph of the surface of the bath at approximately 60 s, after the initiation of the reaction.....	97
Figure 5.30. Photograph of the surface at approximately 3.5 min.....	97
Figure 5.31. Photograph of the surface of the bath at approximately 5 min.....	98
Figure 5.32. Photograph of the surface of the melt at approximately 21 min .....	99
Figure 5.33. Photograph of the surface of the melt at approximately 20 min for the experimental conditions of 200 grams of $\text{Cu}_2\text{S}$ , at 1200 °C, and under the top-lancing of 2 l/min of 22% $\text{O}_2$ and 78% Ar .....	99
Figure 5.34. Photograph of the surface of the melt at approximately 10 min after the end of reaction.....	100
Figure 5.35. Photograph of the surface of the melt at approximately 14.5 min, under the top-lancing of 2 l/min of 80% $\text{O}_2$ and 20% Ar.....	101
Figure 5.36. Photograph of the surface of the melt at approximately 14.5 min, under the top-lancing of 2 l/min of 80% $\text{O}_2$ and 20% Ar.....	101
Figure 6.1. The gas phase mass-transfer coefficient as a function of gas flow rate for the experimental conditions of 200 grams of $\text{Cu}_2\text{S}$ at 1200 °C, 1.084 atm, 3 mm inside diameter lance and 44 mm diameter of the interfacial reaction area .....	106
Figure 6.2. The gas phase mass-transfer coefficient vs. the partial pressure of oxygen.....	107
Figure 6.3. The gas phase mass-transfer coefficient vs. the inverse of temperature for the experimental conditions of: 2000 ml/min of 20-23% $\text{O}_2$ and average pressure of 1.08.....	108
Figure 6.4. The Sherwood number as a function of the Reynolds number for the top-blown conditions of 200 grams of $\text{Cu}_2\text{S}$ at 1200 °C, 1.084 atm, 3 mm inside diameter lance and 44 mm diameter of the interfacial reaction area .....	110
Figure 6.5. $Sh(r_s/d)^{1.5} Sc^{-0.5}$ plotted against the Reynolds number for top-blown conditions of $\text{O}_2\text{-Ar/N}_2$ onto molten $\text{Cu}_2\text{S}$ bath, at 1200-1300 °C, 1.084 atm, $0.5 \leq Sc \leq 0.63$ , $7 \leq r_s/d \leq 11$ , 2-3 mm inside diameter lance and 44 mm diameter of the interfacial reaction .....	111
Figure 6.6. Computed streamline patterns and concentration profiles at $u = 200$ m/sec (laminar flow) (after Taniguchi et al [48]) .....	114
Figure 6.7. The sensitivity of the gas phase mass-transfer coefficient to the reaction interfacial area, for the experimental conditions of 200-grams of $\text{Cu}_2\text{S}$ at 1200 °C, 3 mm inside diameter lance and 44 mm diameter of the interfacial reaction area.....	115
Figure 6.8. The temperature change, due to the heat of reaction, as a function of the reaction gas flow rate.....	117

Figure 6.9. The temperature change, due to the heat of reaction, as a function of the reaction gas oxygen content .....	118
Figure 6.10. The sensitivity of the gas phase mass-transfer coefficient to temperature, for the experimental conditions of 200-grams of $\text{Cu}_2\text{S}$ at 1200 °C, 20-26% $\text{O}_2$ , 3 mm inside diameter lance and 44 mm diameter of the interfacial reaction area .....	120
Figure 6.11. The effect of reaction gas composition on the gas phase mass-transfer coefficient, for the experimental conditions of 200 grams of $\text{Cu}_2\text{S}$ , average system pressure of 1.09 atm, 3 mm inside diameter lance and 44 mm diameter of interfacial reaction area.....	121
Figure 7.1. Schematic diagram of the primary stage reaction system.....	125
Figure 7.2. Schematic diagram of the secondary stage reaction system .....	127
Figure 7.3. Secondary stage reaction rates.....	127
Figure 7.4. Comparison of model predictions to measurements of the sulphur and oxygen contents in the bath as a function of time at a constant reaction gas composition and for the range of reaction gas flow rate of 1480-4055 ml/min .....	148
Figure 7.5. Comparison of model predictions to measurements of sulphur and oxygen contents in the bath as a function of time at a constant reaction gas flow rate and for the range of reaction gas composition of 22-78% $\text{O}_2$ .....	149
Figure 7.6. Model-predicted sensitivity of transient bath weight to bath temperature .....	151
Figure 7.7. Model-predicted sensitivity of transient bath weight to total pressure.....	152
Figure 7.8. Model-predicted sensitivity of transient bath weight to flow rate of admitted gas .....	153
Figure 7.9. Model-predicted sensitivity of transient bath weight to composition of admitted gas .....	154
Figure 7.10. Model-predicted sensitivity of transient bath weight to bath surface area.....	155
Figure 7.11. The sulphur content as a function of the oxygen content in the bath, showing the oxidation path of molten copper sulphide .....	157
Figure 7.12. Selected portions of the Cu-S-O isothermal section, showing the oxidation path of molten $\text{Cu}_2\text{S}$ at 1200 °C and 1 atm.....	158
Figure 7.13. Oxygen reaction rate as a function of reaction gas volumetric flow rate for the experimental conditions of: 200-gram samples, 1200 °C, 23 % $\text{O}_2$ and average pressure of 1.08 atm .....	161
Figure 7.14. Sulphur removal rate as a function of reaction gas volumetric flow rate for the experimental conditions of: 200-gram samples, 1200 °C, 23 % $\text{O}_2$ and average pressure of 1.08 atm .....	162

Figure 7.15. Rate of weight loss as a function of reaction gas volumetric flow rate for the experimental conditions of: 200-gram samples, 1200 °C, 23 % O <sub>2</sub> and average pressure of 1.08 atm .....	163
Figure 7.16. Oxygen reaction rate as a function of oxygen pressure for the experimental conditions of: 1200 °C and 2000 ml/min.....	164
Figure 7.17. Percent increase in gas phase mass transfer as a function of oxygen pressure for the experimental conditions of: 1200 °C and 2000 ml/min.....	165
Figure 7.18. Sulphur removal rate as a function of oxygen pressure for the experimental conditions of: 1200 °C and 2000 ml/min.....	167
Figure 7.19. Oxygen reaction rate as a function of oxygen pressure for the experimental conditions of: 1500 grams of Cu <sub>2</sub> S under the top-lancing of high velocity jets of O <sub>2</sub> -N <sub>2</sub> gas mixtures at 1250 °C, nozzle pressure of 5.4105 N/m <sup>2</sup> , nozzle diameter of 1 mm, .....	168
Figure 7.20. Oxygen reaction rate as a function of temperature for the experimental conditions of: 2000 ml/min of 20-23 % O <sub>2</sub> and average pressure of 1.08 atm .....	171
Figure 7.21. Sulphur removal rate ( $dN_S/dt$ ) as a function of temperature for the experimental conditions of: 2000 ml/min of 20-23 % O <sub>2</sub> and average pressure of 1.08 atm .....	172
Figure 7.22. Oxygen utilization as a function of reaction gas volumetric flow rate; for the top-blown conditions of 200 grams of Cu <sub>2</sub> S at 1200 °C, 1.08 atm, 23% O <sub>2</sub> , reaction interfacial diameter of 44 mm and lance nozzle diameter of 3 mm.....	173
Figure A.1. Electrical circuit for the furnace power supply.....	189
Figure A.2. Circuit design of the load cell.....	190
Figure C.1. The viscosity of Ar-O <sub>2</sub> gas mixtures as a function of temperature, at 1 atm .....	211
Figure C.2. The diffusion coefficients of some selected binary gas mixtures as a function of temperature, at 1 atm.....	213
Figure C.3. The density of Ar-O <sub>2</sub> gas mixtures as a function of temperature.....	214
Figure D.1. The manual temperature measurement of the center of the melt; 200-grams Cu <sub>2</sub> S, at 1200 °C.....	215
Figure D.2. The manual temperature measurement of the gas at the same height of the lance nozzle; 200-grams Cu <sub>2</sub> S, at 1200 °C .....	216
Figure D.3. The gas temperature measurement at the same height of the lance nozzle for Run No. 27, the experimental conditions of 200-grams Cu <sub>2</sub> S, at 1200 °C, 1998 ml/min of 27% O <sub>2</sub> and 73% Ar.....	217

Figure D.4. The temperature measurement at the center of the melt for Run No. 29, the experimental conditions of 200 grams $\text{Cu}_2\text{S}$ , at 1275 °C, 1994 ml/min of 23% $\text{O}_2$ and 77% Ar.....	217
Figure D.5. The gas temperature measurement at the same height of the lance nozzle for Run No. 30, the experimental conditions of 200 grams $\text{Cu}_2\text{S}$ , at 1300 °C, 2000 ml/min of 22% $\text{O}_2$ and 78% Ar.....	218
Figure D.6. The gas temperature measurement at the same height of the lance nozzle for Run No. 33, the experimental conditions of 200 grams $\text{Cu}_2\text{S}$ , at 1200 °C, 3500 ml/min of 29% $\text{O}_2$ and 71% Ar.....	218
Figure D.7. The gas temperature measurement at the same height of the lance nozzle for Run No. 34, the experimental conditions of 200 grams $\text{Cu}_2\text{S}$ , at 1200 °C, 2000 ml/min of 79% $\text{O}_2$ and 21% Ar.....	219
Figure D.8. The gas temperature measurement at the same height of the lance nozzle for Run No. 37, for the experimental conditions of 200 grams of $\text{Cu}_2\text{S}$ at 1200 °C, 2000 ml/min of 21% $\text{O}_2$ and 79% $\text{N}_2$ .....	219
Figure D.9. The gas temperature measurement at the same height of the lance nozzle for Run No. 41, for the experimental conditions of 200 grams of $\text{Cu}_2\text{S}$ at 1200 °C, 3500 ml/min of 24% $\text{O}_2$ and 76% Ar.....	220

## List of Tables

Table 1.1. Copper and copper-nickel smelters in Canada, 1991 .....	3
Table 4.1. Trace analysis (wt%) of supplied copper sulphide .....	54
Table 4.2. Impurity specification of gases in ppm.....	56
Table 4.3. Maximum limits of impurities for the 29.0-32.0 % hydrogen peroxide solution (supplied by BDH).....	56
Table 4.4. Maximum limits of impurities for the 98.0 % sodium hydroxide pellets (supplied by BDH).....	57
Table A.1. Physical properties of the insulating alumina brick.....	187
Table A.2. Chemical analysis of the insulating alumina brick .....	187
Table A.3. Thermal conductivity as a function of mean temperature for refractory fibrous material.....	188
Table A.4. Approximate chemical analysis ( wt %-binder removed) for refractory fibrous material.....	188
Table A.5. Strain gauges manufacturer (HBM ELEKRISCHES MESSEN MECHANISCHER GRÖSSEN) specifications .....	190
Table B.1. Run No. 4, the data for the experimental conditions of: 922 ml/min of 26% O <sub>2</sub> and 74% Ar, at 1200 °C, 1.05 atm pressure, ambient temperature of 23 °C and average final gas temperature of 23 °C.....	191
Table B.2. Run No. 5, the data for the experimental conditions of: 922 ml/min of 26% O <sub>2</sub> and 74% Ar, at 1200 °C, 1.05 atm pressure, ambient temperature of 23 °C and average final gas temperature of 23 °C.....	191
Table B.3. Run No. 6, the data for the experimental conditions of: 922 ml/min of 26% O <sub>2</sub> and 74% Ar, at 1200 °C, 1.05 atm pressure, ambient temperature of 23 °C and average final gas temperature of 25 °C.....	192
Table B.4. Run No. 7, the data for the experimental conditions of: 922 ml/min of 26% O <sub>2</sub> and 74% Ar, at 1200 °C, 1.05 atm pressure, ambient temperature of 23 °C and average final gas temperature of 25 °C.....	192
Table B.5. Run No. 8, the data for the experimental conditions of: 1010 ml/min of 24% O <sub>2</sub> and 76% Ar, at 1200 °C, 1.05 atm pressure, ambient temperature of 23 °C and average final gas temperature of 24 °C.....	193
Table B.6. Run No. 9, the data for the experimental conditions of: 1480 ml/min of 22% O <sub>2</sub> and 79% Ar, at 1200 °C, 1.07 atm pressure, ambient temperature of 23 °C and average final gas temperature of 23 °C.....	193
Table B.7. Run No. 10, the data for the experimental conditions of: 2078 ml/min of 20% O <sub>2</sub> and 80% Ar, at 1200 °C, 1.07 atm pressure, ambient temperature of 23 °C and average final gas temperature of 24 °C.....	194



Table B.8. Run No. 11, the data for the experimental conditions of: 1987 ml/min of 20% O <sub>2</sub> and 80% Ar, at 1200 °C, 1.05 atm pressure, ambient temperature of 23 °C and average final gas temperature of 25 °C.....	194
Table B.9. Run No 12, the data for the experimental conditions of: 1580 ml/min of 22% O <sub>2</sub> and 78% Ar, at 1200 °C, 1.06 atm pressure, ambient temperature of 25 °C and average final gas temperature of 25 °C.....	195
Table B.10. Run No. 13, the data for the experimental conditions of: 1521 ml/min of 20% O <sub>2</sub> and 80% Ar, at 1200 °C, 1.08 atm pressure, ambient temperature of 27 °C and average final gas temperature of 26 °C.....	195
Table B.11. Run No. 14, the data for the experimental conditions of: 1530 ml/min of 21% O <sub>2</sub> and 79% Ar, at 1200 °C, 1.07 atm pressure, ambient temperature of 22 °C and average final gas temperature of 22 °C.....	196
Table B.12. Run No. 15, the data for the experimental conditions of: 2006 ml/min of 22% O <sub>2</sub> and 78% Ar, at 1200 °C, 1.07 atm pressure, ambient temperature of 26 °C and average final gas temperature of 27 °C.....	196
Table B.13. Run No. 16, the data for the experimental conditions of: 2510 ml/min of 23% O <sub>2</sub> and 77% Ar, at 1200 °C, 1.08 atm pressure, ambient temperature of 25 °C and average final gas temperature of 25 °C.....	197
Table B.14. Run No. 17, the data for the experimental conditions of: 1755 ml/min of 22% O <sub>2</sub> and 78% Ar, at 1200 °C, 1.07 atm pressure, ambient temperature of 22 °C and average final gas temperature of 24 °C.....	197
Table B.15. Run No. 18, the data for the experimental conditions of: 2230 ml/min of 23% O <sub>2</sub> and 77% Ar, at 1200 °C, 1.08 atm pressure, ambient temperature of 23 °C and average final gas temperature of 23 °C.....	198
Table B.16. Run No. 19, the data for the experimental conditions of: 3015 ml/min of 22% O <sub>2</sub> and 78% Ar, at 1200 °C, 1.07 atm pressure, ambient temperature of 26 °C and average final gas temperature of 27 °C.....	198
Table B.17. Run No. 21, the data for the experimental conditions of: 4055 ml/min of 22% O <sub>2</sub> and 78% Ar, at 1200 °C, 1.13 atm pressure, ambient temperature of 26 °C and average final gas temperature of 26 °C.....	199
Table B.18. Run No. 22, the data for the experimental conditions of: 2006 ml/min of 27% O <sub>2</sub> and 73% Ar, at 1200 °C, 1.10 atm pressure, ambient temperature of 26 °C and average final gas temperature of 26 °C.....	199
Table B.19. Run No. 23, the data for the experimental conditions of: 2009 ml/min of 35% O <sub>2</sub> and 65% Ar, at 1200 °C, 1.10 atm pressure, ambient temperature of 21 °C and average final gas temperature of 21 °C.....	200
Table B.20. Run No. 24, the data for the experimental conditions of: 1997 ml/min of 46% O <sub>2</sub> and 54% Ar, at 1200 °C, 1.10 atm pressure, ambient temperature of 24 °C and average final gas temperature of 24 °C.....	200

Table B.21. Run No. 25, the data for the experimental conditions of: 1997 ml/min of 64% O <sub>2</sub> and 36% Ar, at 1200 °C, 1.10 atm pressure, ambient temperature of 22 °C and average final gas temperature of 22 °C.....	201
Table B.22. Run No. 27, the data for the experimental conditions of: 1998 ml/min of 23% O <sub>2</sub> and 77% Ar, at 1250 °C, 1.13 atm pressure, ambient temperature of 23 °C and average final gas temperature of 23 °C.....	201
Table B.23. Run No. 28, the data for the experimental conditions of: 1999 ml/min of 23% O <sub>2</sub> and 77% Ar, at 1300 °C, 1.08 atm pressure, ambient temperature of 22 °C and average final gas temperature of 22 °C.....	202
Table B.24. Run No. 29, the data for the experimental conditions of: 1994 ml/min of 21% O <sub>2</sub> and 79% Ar, at 1275 °C, 1.08 atm pressure, ambient temperature of 24 °C and average final gas temperature of 24 °C.....	202
Table B.25. Run No. 30, the data for the experimental conditions of: 2006 ml/min of 22% O <sub>2</sub> and 78% Ar, at 1325 °C, 1.08 atm pressure, ambient temperature of 25 °C and average final gas temperature of 24 °C.....	203
Table B.26. Run No. 31, the data for the experimental conditions of: 2006 ml/min of 22% O <sub>2</sub> and 78% Ar, at 1275 °C, 1.08 atm pressure, ambient temperature of 23 °C and average final gas temperature of 21 °C.....	203
Table B.27. Run No. 33, the data for the experimental conditions of: 3490 ml/min of 27% O <sub>2</sub> and 73% Ar, at 1200 °C, 1.11 atm pressure, ambient temperature of 24 °C and average final gas temperature of 22 °C.....	204
Table B.28. Run No. 34, the data for the experimental conditions of: 1996 ml/min of 78% O <sub>2</sub> and 22% Ar, at 1200 °C, 1.11 atm pressure, ambient temperature of 23 °C and average final gas temperature of 22 °C.....	204
Table B.29. Run No. 36, the data for the experimental conditions of: 2032 ml/min of 22% O <sub>2</sub> and 78% Ar, at 1200 °C, 1.08 atm pressure, ambient temperature of 23 °C and average final gas temperature of 22 °C.....	205
Table B.30. Run No. 37, the data for the experimental conditions of: 2000 ml/min of 21% O <sub>2</sub> and 79% N <sub>2</sub> , at 1200 °C, 1.08 atm pressure, ambient temperature of 21 °C and average final gas temperature of 22 °C.....	205
Table B.31. Run No. 41, the data for the experimental conditions of: 3516 ml/min of 24% O <sub>2</sub> and 76% Ar, at 1200 °C, 1.10 atm pressure, ambient temperature of 24 °C and average final gas temperature of 24 °C.....	206
Table B.32. The effect of volumetric flow rate of reaction gas on the reaction rates; sample weight of 200-grams of Cu <sub>2</sub> S; at 1200 °C and 1.08 atm; 22% O <sub>2</sub> and 78% Ar; lance inside diameter of 3 mm .....	207
Table B.33. The effect of volumetric flow rate of reaction gas on the reaction rates; sample weight of 200-grams of Cu <sub>2</sub> S; at 1200 °C and 1.08 atm; 24% O <sub>2</sub> and 76% Ar; lance inside diameter of 3 mm .....	207

Table B.34. The effect of reaction gas composition on the reaction rates; sample weight of 200-grams of $\text{Cu}_2\text{S}$ ; at 1200 °C and 1.10 atm, 2000 ml/min; lance inside diameter of 3 mm .....	208
Table B.35. The effect of temperature on the reaction rates; sample weight of 200-grams of $\text{Cu}_2\text{S}$ ; at 1200 °C and 1.09 atm, 2000 ml/min of 22% $\text{O}_2$ and 78% Ar; lance inside diameter of 3 mm.....	208
Table B.36. The effect of temperature on the reaction rates; sample weight of 200 grams of $\text{Cu}_2\text{S}$ ; at 1.09 atm, 2000 ml/min of 23% $\text{O}_2$ and 77% Ar; lance inside diameter of 3 mm.....	209
Table B.37. The effect of bath mixing on the reaction rates; sample weight of 200-grams of $\text{Cu}_2\text{S}$ ; at 1200 °C and 1.09 atm, 2000 ml/min of 22% $\text{O}_2$ and 78% Ar; lance inside diameter of 3 mm (approximately 77 ml/min Ar was used to invoke artificial mixing) .....	209
Table B.38. The effect of carrier gas type on the reaction rates; sample weight of 200-grams of $\text{Cu}_2\text{S}$ ; at 1200 °C and 1.09 atm, 2000 ml/min of 21% $\text{O}_2$ and 79% Ar .....	209
Table C.1. The critical properties of some selected gases .....	212

### List of Symbols

$A$	cross-sectional area ( $m^2$ )
$a$	constant
$b$	constant
$C_s$	concentration of reactants (moles/ $m^3$ )
$D_{A-B}$	diffusion coefficient of species A in B ( $m^2/s$ )
$d$	diameter (m)
$d_c$	diameter of cavity (m)
$d_o$	diameter of orifice (m)
$d_s$	degree of desulphurization of the melt (%) (percent sulphur removed)
$Fr'$	modified Froude number
$G^\circ$	standard Gibbs free energy (kJ/mole)
$g$	acceleration due to gravity ( $9.81 m/s^2$ )
$H$	distance from the lance nozzle to the reaction interfacial area (m)
$H_c$	depth of cavity (m)
$H_{Cu_2S}^i$	initial height of the sulphide melt (m)
$K_{j,u}$	jet constant for momentum transfer
$K'$	equilibrium constant
$k$	mass transfer-coefficient (m/s)
$M_A$	molecular weight of species A (kg/kg mole)
$M_j$	jet momentum (kg.m/s <sup>2</sup> ), ( $1 g/cm.s^2 = 1 \text{ dyne} = 1 \times 10^{-5} \text{ kg.m/s}^2$ (Newton))
$m$	constant in the gas phase mass transfer correlation
$N_A$	molar quantity of substance A
$\dot{N}_A$	molar transfer rate of specie A (moles/s)
$n_{Re}$	exponent of the Reynolds number
$n_{Sc}$	exponent of the Schmidt number
$n_s$	exponent of ( $d/r_s$ )
$\dot{n}_A$	molar flux of species A (moles/ $m^2.s$ )
$P_A$	pressure of species A (Pa), ( $1 \text{ atm} = 101325 \text{ Pa}$ )

$P_s$	system pressure (Pa)
$P_{st}$	pressure due to static head (Pa)
$Q_A$	volumetric flow rate of substance A ( $m^3/s$ )
$Q_{off}$	off-gas volumetric flow rate ( $m^3/s$ )
$Q_r$	reaction gas volumetric flow rate (the same as $Q$ ) ( $m^3/s$ )
$R$	universal gas constant (8.3144 J/°K.mole), (82.06 $cm^3$ .atm/°K.mole)
$Re$	Reynolds number
$R_g$	gas phase mass transfer resistance (s/m)
$R_l$	liquid phase mass transfer resistance (s/m)
$R_s$	load cell response
$r_j$	radius of impacted surface (m)
$r_o$	radius of orifice (m)
$r_s$	radius of reaction surface (m)
$Sc$	Schmidt number
$Sh$	Sherwood number
$T$	temperature (°K)
$T_g$	final off-gas temperature (°K), measured at the entrance to the bubble meter
$T_{gas}$	gas temperature inside the reaction chamber (°K)
$T_{melt}$	melt temperature inside the reaction chamber (°K)
$t$	time (s)
$u$	mean velocity inside nozzle of the lance (m/s)
$u_c$	jet velocity at axis (m/s)
$u_o$	jet velocity at orifice (m/s)
$V$	volume of the bath ( $m^3$ )
$V_a$	volume of absorbing solution ( $m^3$ )
$V_{NaOH}$	volume of NaOH titrated ( $m^3$ )
$V_s$	volume of the sample obtained from the absorber ( $m^3$ )
$W$	sample weight (kg)
$W_{ga}$	sample weight obtained from gas analysis (kg)
$Wt\% A$	weight percent of specie s A
$W_w$	sample weight obtained from gravimetric measurement (kg)

$\dot{W}$	rate of weight change (kg/s)
$X_A$	mole fraction of species A
$y$	distance from orifice (m)

### Greek Symbols

$\alpha$	the molar ratio of reacted oxygen to removed sulphur
$\Gamma_s$	surface excess of solute s (mole/m <sup>2</sup> )
$\gamma_A$	activity coefficient of species A
$\Delta x$	finite change in variable $x$
$\delta x$	variation in variable $x$
$\zeta$	percent increase in mass transfer (likely due to the Marangoni effect)
$\epsilon_B^A$	interaction parameter of A on B
$\mu_g$	gas viscosity (kg/m.s), (1 g/cm.s = 1 poise = 0.1 kg/m.s)
$\rho_{Cu}, \rho_{Cu_2S}$	the density of the metal phase and the sulphide phase (kg/m <sup>3</sup> )
$\rho_g$	gas density (mole/m <sup>3</sup> )
$\rho_l$	liquid density (mole/m <sup>3</sup> )
$\sigma$	interfacial tension (Newton/m), (1 dyne/cm = 1×10 <sup>-7</sup> Newton/m)
$\sigma_b$	interfacial tension at the interface
$\sigma_i$	bulk interfacial tension
$\sigma_m$	interfacial tension at maximum of zero charge

### Other Symbols

[A]	concentration of species A (moles/m <sup>3</sup> )
[%A] <sub>B</sub>	weight percent of species A in B
$\langle \rangle$	solid substance
$(( ))$	liquid substance
$( )$	gaseous substance

[ ] in liquid or ionic solution

### Superscripts

- a admitted (for the total admitted substance such as oxygen or argon)
- b bulk (property of the material in the bulk)
- f final (designation for the variables at the end of the secondary stage)
- i interfacial (property of the material at the interface) or initial (designation for the variables at the beginning of reaction ,  $t = 0$ )
- p primary (primary stage variables)
- r reacted (for the total reacted substance such as oxygen)
- s secondary (secondary stage variables)
- u unreacted (for the total unreacted substance such as oxygen)
- \* transition (designation for the variables at transition from the primary stage to the secondary stage)

## Acknowledgments

For his patience, understanding and guidance, I would like to express my utmost gratitude to my supervisor, Professor J. Keith. Brimacombe.


For their valuable discussions with me on the thermodynamics of copper sulphide melts, I would like to thank Professor E. Peters and Dr. G. G. Richards. My gratitude is also extended to Dr. S. Taniguchi, of Tohoku University, Sendai, Japan, for the helpful discussions I have had with him in the area of gas phase mass transfer during the early period of this research project, and for the translations of some of the relevant issues of his Japanese written papers that were used in the literature review.

I am indebted to Mr. P. R. Musil for his voluntary assistance in machining some parts of the experimental apparatus and with the setup of the optical system used in the surface photography. I would also like to thank Mr. S. Milaire, of the departmental electronic shop, for his assistance in the setup of the electrical systems of the experimental apparatus. The assistance of Mr. R. McLeod, of the departmental machine shop, is also appreciated. I am also glad to acknowledge the assistance of Mrs. J. Kitchen, Mrs. M. Jansepar, Mr. R. Bennett, Mr. E. R. Armstrong and Mr. B. N. Walker, of the Metals and Materials Engineering Department staff.

I am greatly indebted to the Natural Sciences and Engineering Research Council of Canada for financial support in the form of a research assistantship.



## 1. Introduction

Since ancient times copper has been the back-bone of human civilization. The word copper originates from the Greek word "*Kyprios*" - the island of Cyprus, where much of copper of ancient Mediterranean was found. The Romans called copper *aes Cyprium* - "metal of Cyprus". Gradually the Roman name was changed to *Cuprum*. In the English language, the word became "Copper". Today the chemical symbol for this valuable metal is Cu, the first two letters of the Roman word. Because it occurs in the native state, much like gold, copper was known to early man as far ago as 8000 B.C. It was about 4000 B.C. that man learned to produce copper and bronze by the smelting of copper and tin ores in a charcoal fire. History of the ancient civilizations indicates that copper played an important role in shaping the past as well as the present of our world. Due to its nobility, the ancient Egyptians gave copper their symbol for everlasting life - a circle above a cross . For the modern world, copper is still as important as ever. It was the development of the electrical industry in the late nineteenth and early twentieth centuries that caused a dramatic increase in the demand for copper.

Although it is a classic of extractive metallurgy, the extraction of copper from its ores remains a subject that has to be further unravelled. Because approximately 90% of the world's primary copper originates in sulphide ores, most of the copper today is produced by pyrometallurgical techniques. In general, the extraction of copper is carried out as follows: concentration by froth flotation; roasting (an optional step); matte smelting (in blast, reverberatory, electric or flash furnaces); and converting to blister copper. One of the relatively recent advances in the extractive metallurgy of copper is the continuous production of blister copper by combining the smelting, roasting and converting operations in a single unit process, such as in the Worcra, Noranda, Mitsubishi and Isasmelt processes. Most of the copper producing companies convert copper mattes, in

which blister copper is the ultimate product. In Canada, for example, there are a variety of copper extraction processes employed by several companies, most of which involve the copper converting process, as shown in Table 1.1.

In copper converting, blister copper is produced by several cycles of matte oxidation in which the metallurgical phenomena are complex, such as heat transfer and accretion growth at the tuyeres. These have been studied in depth but many other important aspects of copper converting are not fully comprehended. Perhaps some of the most important fundamental aspects of copper converting to be further understood are the thermodynamics and kinetics of the copper-making reactions. In such fundamental studies, the methods of studying the problem, as well as the solution to the problem itself, are of relevance to the process of knowledge accumulation.

Aiming to explain the kinetics of the oxidation of molten copper sulphide and to explore some fundamental principles of gas-liquid reactions, this work was launched. Mass transfer and the effect of interfacial phenomena on the gas-liquid reactions are important examples of these fundamental principles.

Table 1.1. Copper and copper-nickel smelters in Canada, 1991 (rated annual capacity is in tonnes of concentrates); Taken from the Canadian Minerals Yearbook.

Company and Location	Product	Rated Annual Capacity	Remarks
Falconbridge Limited, Falconbridge, Ontario	Copper-nickel matte	600,000	Fluid bed roasters and electric furnaces; 1800 t/d sulphuric acid plant treats roaster gases. Matte from the smelter is refined in Norway.
Inco Limited, Sudbury, Ontario	Molten "blister" copper, nickel sulphide and nickel sinter for the company's refineries; nickel oxide sinter for market, soluble nickel oxide for market	500,000	Oxygen flash-smelting of copper concentrate; converters for production of blister copper. Roasters, reverberatory furnaces for smelting of nickel-copper concentrate, converters for production of nickel-copper Bessemer matte. Production of matte followed by matte treatment, flotation, separation of copper and nickel sulphides, then by sintering to make sintered nickel products for copper sulphide and conversion to blister copper
Falconbridge Limited, Timmins, Ontario	Molten "blister" copper	440,000	Mitsubishi-type smelting, separation and converting furnaces, acid plant and oxygen plant to treat continuous copper concentrate feed stream to yield molten 99% pure copper.
Noranda Inc. Horne smelter, Noranda, Quebec	Copper anodes	770,000 <sup>a</sup>	One continuous Noranda process reactor and five converters. Acid plant became operational at end of 1989. Treats concentrates from Noranda's mining operations in Quebec and Ontario as well as custom concentrates and scrap.
Noranda Inc. Gaspé smelter, Murdochville, Quebec	Copper anodes	221,500 <sup>a</sup>	Green charge reverberatory furnace, two converters, rotary anode furnace and on acid plant. Treats Gaspé and custom concentrates.
Hudson Bay Mining and Smelting Co., Limited (HBMS), Flin Flon, Manitoba	Copper anodes	320,000	Five roasting furnaces, one reverberatory furnace and three converters. Company treats its own copper concentrate as well as custom copper concentrates: zinc plant residues and stockpiled zinc-plant residues fed to reverberatory furnace. Project under way to replace concentrate roasting and calcine smelting with Noranda continuous converter technology.

Source: Data provided by each company. <sup>a</sup> Concentrate and copper scrap.

## **2. Literature Review**

### **2.1. Copper Converting**

#### **2.1.1. History of the Copper Converter**

As is the case with most metallurgical processes, implementation of new ideas for the production of copper initially produced disappointing results. Rittinger conducted the first experiments on the converting of copper matte in 1867, in Hungary, at the Schmollnitz works. Others such as Kupelweisse in 1868, and Jossa and Lalitin in 1871, used a Bessemer steel converter. The early experiments were halted as a result of tuyere blockage due to freezing of copper as it formed. It was the success of the Bessemer converter in steel-making that kept the work on bessmerizing the copper matte going. In 1880, Pierre Manhés and Paul David conducted their first experiments of copper converting, in Vaucluse, France. They encountered their first success when they adopted horizontal tuyeres instead of bottom blown tuyeres that caused the copper to freeze among other difficulties[1]. The cylindrical shape of the converter was adopted after realizing that in order to be able to treat different matte grades, the relative position of the tuyeres had to be varied with respect to the bottom of the bath. The need for tuyere punching was soon realized to be a condition for the success of the operation, when the copper converter was put to work at the Parrot Smelter (USA). The other major problem was the refractory lining which was consumed by the slagging process that required silica flux for the removal of iron from the matte phase. The use of neutral refractory lining was implemented by Peirce and Smith in 1909, in Baltimore.

The other significant developments in the Peirce-Smith converter, after 1909, were the increase of its capacity, the improvement of its refractory lining life time and the addition of automatic tuyere punching. Further understanding of the metallurgy of copper converting has been gained as a result of several fundamental studies [6,8,41,45,58-67].

Despite the many new developments in the production of copper, such as chalcocite flash converting and the Isasmelt process, "the case of the Peirce-Smith converter is particularly outstanding" [61].

### **2.1.2. Metallurgy of Copper Converting**

Due to its energy efficiency, the definition of copper converting is simply the autogenous process of iron and sulphur transfer from the matte to the slag and gas phases respectively.

Depending on the matte grade, the feed to the copper converter might contain up to 40% Fe, 25% S and 3% dissolved O [2]. The matte also contains minor amounts of impurity metals (e.g. As, Bi, Ni, Pb, Sb, Zn and precious metals). The whole purpose of the converting process is the production of blister copper, that is about 98.5-99.5% Cu.

The commonly used Peirce-Smith converter is shown in Figure 2.1<sup>1</sup>. Iron is removed from matte as liquid fayalite ( $2\text{FeO}\cdot\text{SiO}_2$ ) slag as a result of silica fluxing during the slag formation stage. The slag and blister copper are formed at different stages of the converting process and they are poured separately from the converter mouth by rotating the converter about its axis, as shown in Figure 2.1(b). The sulphur is removed as  $\text{SO}_2$  which normally is recovered and processed to by-products such as  $\text{H}_2\text{SO}_4$ , liquid  $\text{SO}_2$  and elemental sulphur.

---

<sup>1</sup>An industrial Peirce-Smith converter is typically 4 m in diameter and 9 m long (inside shell). It is constructed of a steel shell 40-50 mm thick, lined with 250-750 cm of burned magnesite or chrome-magnesite brick. There are forty to fifty tuyeres, which consist of steel pipes imbedded in the refractory and they are connected to a bustle pipe running along the vessel. The matte is charged to the converter through a large opening (mouth), which is covered with a loose-fitting hood during the blow to collect the resulting off-gas [2-5].

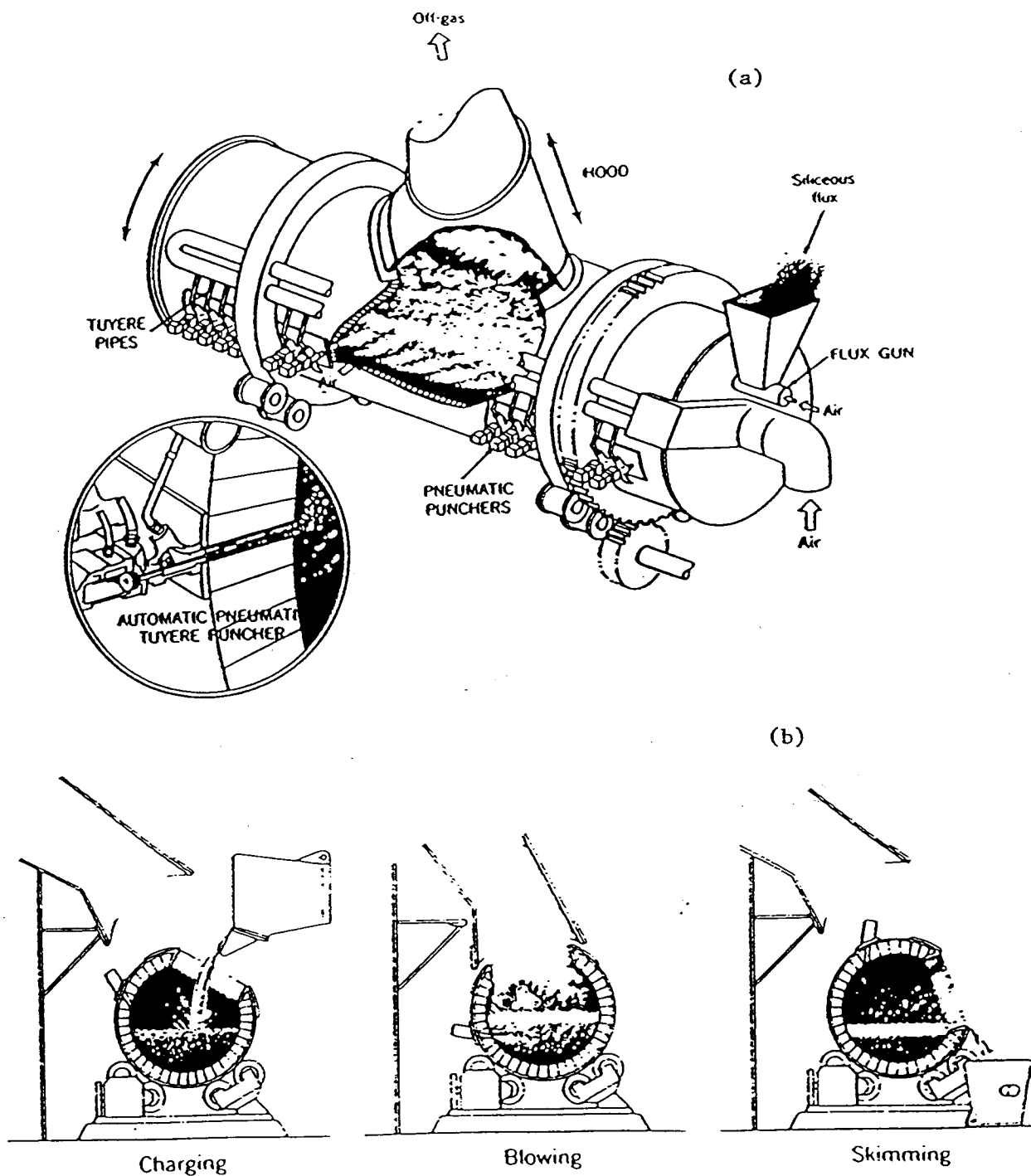
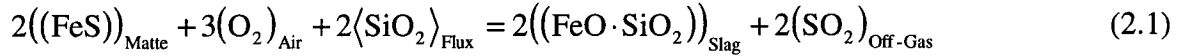


Figure 2.1. (a) Cutaway of a horizontal side-blown Peirce-Smith converter (Boldt and Queneau, 1967), (b). Positions of the Peirce-Smith converter for charging, blowing, and skimming (slag or blister copper) (Boldt and Queneau, 1967).

### 2.1.2.1. The Slag-Forming Stage:

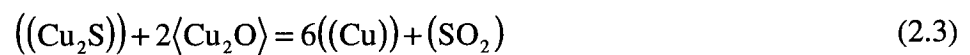
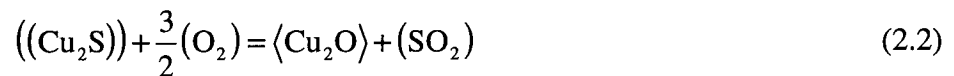
In the slag-forming stage, FeS is oxidized mainly to FeO and some Fe<sub>3</sub>O<sub>4</sub> according to Reaction (2.1).



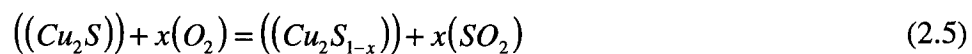
The silica flux is added by means of a flux gun to combine with the FeO and some of the Fe<sub>3</sub>O<sub>4</sub> as liquid slag (Figure 2.1 (a)). The slag forming-stage ends when the FeS matte content is reduced to about 1wt%. Due to its relatively large volume, and for the purpose of matte addition, the slag is skimmed at various times during the slag - forming stage.

### 2.1.2.2. The Copper-Making Stage:

The copper-making stage is characterized by the removal of sulfur and remaining iron, resulting in the formation of blister copper. The literature was found to be unclear in explaining the metallurgy of this stage. Biswas and Davenport [2] presented different and inconsistent explanations of the metallurgical chemistry of the copper-making stage and failed to support or reject either of the claims of King et al., 1973 [9] and Peretti, 1948 [10]. King et al. suggested that the copper formation takes place by a combination of Reactions (2.2) and (2.3) according to the overall Reaction (2.4).



However, Peretti indicated that the copper making-stage proceeds in two steps. The melt is partially desulphurized until the sulphur content is lowered to about 19.4%, according to Reaction (2.5).



During the second step, the sulphur deficient (white metal) phase is oxidized to form the metal phase (blister copper) according to Reaction (2.4).

Rosenquist [11] indicated that the copper-making step proceeds in one distinct stage according to Reaction (2.4). Habashi [12] suggested that the copper-making stage proceeds according to Reactions (2.2) and (2.3) with the overall reaction being (2.4).

In view of the disagreement in the literature about the actual chemistry of the copper-making stage, further investigation of this process is warranted.

## 2.2. Thermodynamics of Copper Sulphide Oxidation

Thermodynamic knowledge of the Cu-S-O system is paramount to the understanding of the metallurgy of copper converting and of vital importance to any related kinetic studies. Since the birth of extractive metallurgy, the practical and fundamental aspects of the Cu-Fe-S-O have always been of tremendous interest to the pyrometallurgist. The literature is apparently rich in thermodynamic studies of the Cu-Fe-S-O system [13-26,116].

However, most of the knowledge accumulated fails to deal with the ionic nature of such a system. The paucity of knowledge in this field is attributed to the complexity of molten salt thermodynamics and the lack of pure fundamental research in this area.

As just stated, most thermodynamic studies on mattes, have failed to address mattes as ionic substances and rather have dealt with them as neutral compounds that can only be characterized as hypothetical species having no real physical existence. Very few studies have attempted to tackle this problem in depth [24-25,116]. The literature survey on this topic yielded no important data. For example, there has never been a high temperature spectroscopic identification of the ionic species of molten Cu-S-O mixtures or measurements of their ionic activities.



### 2.2.1. Cu-S System

The high temperature portion of the Cu-S binary, in which the composition limits are purposely distorted to show the phase relations more clearly, is shown in Figure 2.2. The liquid state region of this phase diagram clearly indicates the existence of only two distinct phases with a wide miscibility gap. Liquid I (metal phase) has a finite but limited solubility for sulphur of 0.95-1.0 wt% at the monotectic temperature of 1105°C (1378°K). Liquid II (sulphide phase) is often called liquid Cu<sub>2</sub>S, but its composition can deviate from exact stoichiometry. Copper sulphide melts of 20-22.19 wt% S are within the range of single phase Cu<sub>2</sub>S. The gas phase over the Cu-S system contains (Cu), (S<sub>2</sub>) and (S). Species such as (CuS) and (Cu<sub>2</sub>S) are negligible. The partial pressure of (Cu) is very small over the sulphide phase and is maximum over the metal phase ( $1.2 \times 10^{-6}$  atm at 1127°C). The partial pressures of (S<sub>2</sub>) and (S) are also very small for the Cu<sub>2</sub>S exact stoichiometry and slightly richer in copper. It is important to note that, based on this discussion, the partial pressures of all of these species over the melt under study were assumed to be negligible, for simplicity, in the kinetic analysis applied in the present study.

Lumsden [24] reported one of the very few studies on the electrochemical thermodynamics of the Fe-Cu-S-O system. He suggested that in melts on the sulphur-rich side of Cu<sub>2</sub>S, it can be assumed that Cu<sup>+</sup>, Cu<sup>2+</sup> and Cu<sup>0</sup> are present together with S<sup>2-</sup> anions. The calculated standard free energy of Reaction (2.6) is given by Equation (2.7).



$$\Delta G^\circ = 87.7 + 0.012T \quad (2.7)$$

Based on the Flood model [24], the free energy of the dissociation reaction of ((Cu<sub>2</sub>S)) to Cu<sup>+</sup> and S<sup>2-</sup> has been also calculated as given by Equation (2.8).

$$\Delta G^\circ = 1.8 - 0.0015T$$

(2.8)

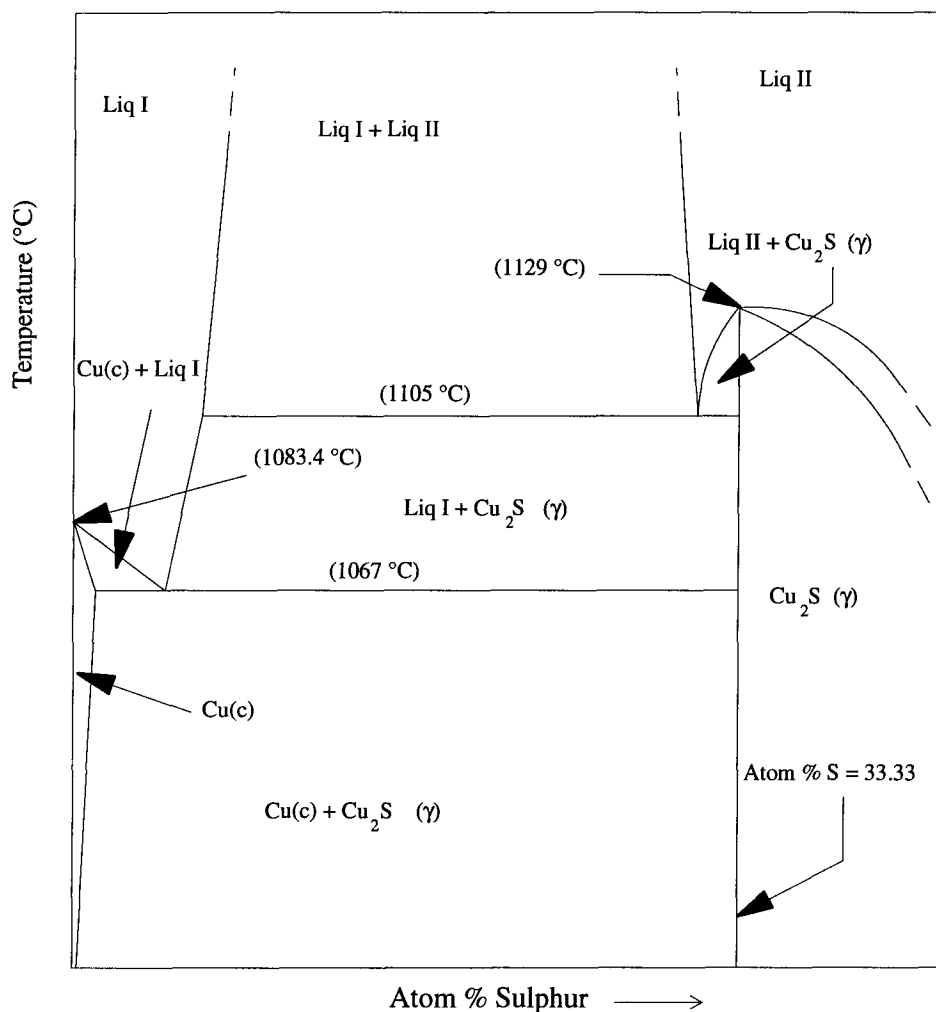


Figure 2.2. The Cu-S system; high temperature portion only, not to scale (after Kellogg [15]).

### 2.2.2. Cu-S-O System

The Cu-S-O ternary system is of great importance to the current investigation of the oxidation kinetics of molten copper sulphide. An isothermal section at 1300°C, provided by Elliott [20], is shown in Figure 2.3. Another isothermal section at 1200°C, appeared in the literature [17], but it was found to be in disagreement with other equilibrium measurements of this system [19,20]. It is very important to note that thermodynamically

the formation of the  $\text{Cu}_2\text{O}$  phase is not possible under the conditions of copper converting until all of the  $\text{Cu}_2\text{S}$  phase is reacted completely. The other important point to note is that the sulphide phase, as well as the metal phase, have finite solubilities of oxygen.

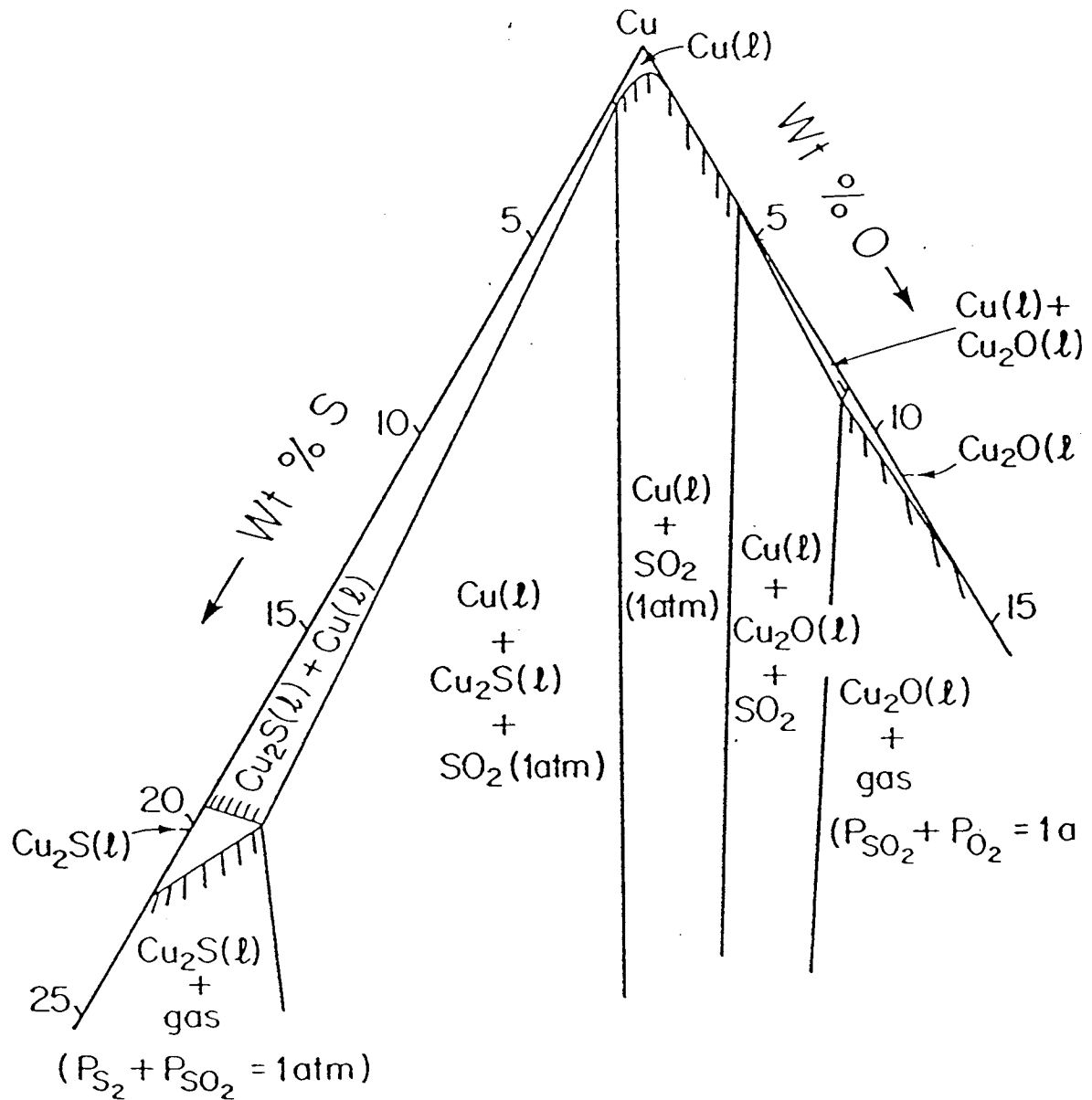


Figure 2.3. The 1300 °C isotherm of the Cu-O-S system, at 1 atm, (after Elliott [20]).

The Cu-S-O system can be divided into two distinct sub-systems: the copper sulphide system (ionic melt) and the copper system (neutral metallic melt). Due to the complexity of the thermodynamics of ionic melts, the thermodynamic behaviour of the sulphide system has not yet been fundamentally described. For example, it is not yet possible to carry out calculations of the equilibrium pressures of O<sub>2</sub> and SO<sub>2</sub> over the sulphide melt, based on the activities of Cu<sup>+</sup>, O<sup>2-</sup> and S<sup>2-</sup>.

The thermodynamic behaviour of the metallic phase has been described by Alcock [26]. The S and O dissolution in copper is described by Reaction (2.9) and the free energy of formation of this reaction is given by Equation (2.10).



$$\Delta G^\circ = 68367 - 37T \quad (2.10)$$

In order to correct for the interaction of sulphur and oxygen in copper, the free energy of mixing (given by Equation (2.11)) is subtracted from the free energy of formation of Reaction (2.9).

$$\delta\Delta G^\circ = RT \ln \left[ \gamma_{[S]_{((Cu))}} \cdot \gamma_{[O]_{((Cu))}}^2 \right] = 2RT(X_O \epsilon_S^O) = 4RT(X_S \epsilon_O^S) \quad (2.11)$$

The oxygen and sulfur contents of the metal and sulphide phases, as functions of SO<sub>2</sub> pressure and system temperature, have been measured by Schmiedl [19]. The measurements have also been expressed in mathematical form, by Schmiedl, and are as follows;

Metal Phase:

$$Wt \% O = 10^{(-1.38 - (1278/T))} \times P_{SO_2}^{1/2} \quad (2.12)$$

$$Wt \% Cu = 10^{(1.98 + (24/T))} \quad (2.13)$$

$$Wt\%S = 100 - Wt\%O - Wt\%Cu \quad (2.14)$$

Sulphide Phase:

$$Wt\%O = 10^{(-1.96+(1013/T))} \times P_{so_2}^{1/2} \quad (2.15)$$

$$Wt\%Cu = 79.61 + 0.26 \times 10^{-12} \times T^4 \quad (2.16)$$

$$Wt\%S = 100 - Wt\%O - Wt\%Cu \quad (2.17)$$

### 2.3. Gas-Liquid Interactions

A majority of the processes relevant to the extraction and refining of metals depend on mass transfer of the reacting species across an interface. Gas-liquid reactions can take place in many ways, e.g. superficial contact of a gas with a liquid surface via diffusion across a stagnant gas film, gas jets impinging on a liquid surface and gas bubbles rising through a liquid. In order to determine the rate of reaction, the mass transfer of species across the reaction interface must be considered. To illustrate some basic principles of mass transfer encountered in the analysis of metallurgical systems, consider the following hypothetical case in which an oxygen-inert gas mixture is in contact with a liquid metal Me (e.g. Fe, Cu, Mn,..) bath.

As the gas mixture comes in contact with the liquid metal surface, the oxygen dissolves in Me according to Reaction (2.18).



This process proceeds according to the following steps:

1. The gas phase mass transfer of the oxygen species to the liquid metal surface.
2. The chemical reaction at the interface which can be considered to be very fast, in most pyrometallurgical reactions.

### 3. The mass transfer of oxygen in the liquid metal phase.

Depending on the relative resistances to mass transfer in the gas and liquid phases, the rate of oxygen dissolution in the metal is, therefore, controlled by either mass transfer in one of the phases or simultaneously in both phases.

In order to determine the rate controlling step of the dissolution reaction, the following analysis can be carried out:

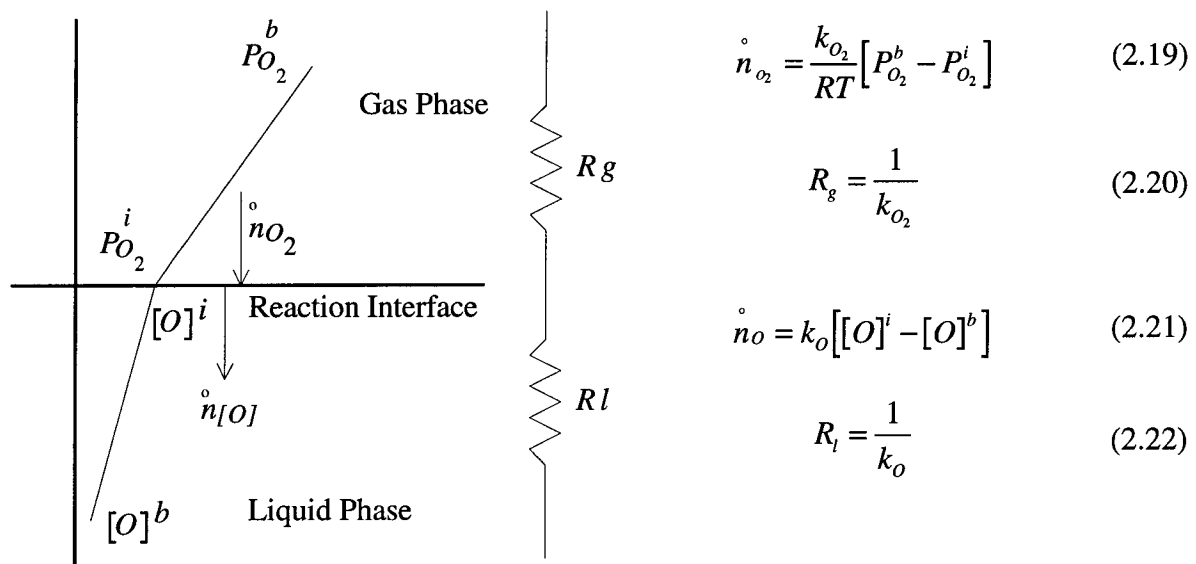


Figure 2.4. Schematic diagram of a hypothetical case of oxygen dissolution in a liquid metal bath,  $R_g$  and  $R_l$  are the gas phase resistance and the liquid phase resistance respectively.

#### Equilibrium at Phase Boundaries:

Because the chemical reaction is very fast and does not offer any resistance to the overall reaction rate, equilibrium conditions must prevail at the gas-liquid interface. This implies that the interfacial concentrations can be considered to be dictated by the thermodynamics of Reaction (2.18). Therefore, the relationship between the interfacial partial pressure of oxygen in the gas phase and the interfacial concentration of oxygen in the liquid phase can be derived from the equilibrium constant of the interface reaction, as follows:

$$P_{O_2}^i = \frac{[O]^{i^2}}{K'} \quad (2.23)$$

Stoichiometry:

The interface reaction dictates that the relationship between  $\dot{n}_{O_2}$  and  $\dot{n}_O$  is as follows:

$$\dot{n}_O = 2\dot{n}_{O_2} \quad (2.24)$$

Flux Equations:

The molar flux of  $O_2$  ( $\dot{n}_{O_2}$ ) in the gas phase is given by Equation (2.19) and the molar flux of O ( $\dot{n}_O$ ) in the liquid phase is given by Equation (2.21).

If the gas phase mass transfer resistance is negligible then the reaction rate is the molar transport rate of O in the liquid phase, as given by the following equation:

$$\dot{N}_O = k_o A \left[ \sqrt{K' P_{O_2}^b} - [O]^b \right] \quad (2.25)$$

If the liquid phase mass transfer resistance is negligible, the reaction rate can be described by the molar transport rate of  $O_2$  in the gas phase, as follows:

$$\dot{N}_O = 2A \frac{k_{O_2}}{RT} \left[ P_{O_2}^b - \frac{[O]^{b^2}}{K'} \right] \quad (2.26)$$

In most cases of gas phase mass transfer control, the interfacial partial pressure of  $O_2$  is negligible with respect to the bulk partial pressure of  $O_2$ , and can be ignored. Therefore, the rate expression can be described by Equation (2.27).

$$\dot{N}_O = 2A \frac{k_{O_2}}{RT} \cdot P_{O_2}^b \quad (2.27)$$

To determine the general rate equation for mass transfer control in both phases, the stoichiometry of the reaction is invoked as follows:

$$k_o[[O]^i - [O]^b] = 2 \frac{k_{o_2}}{RT} \left[ P_{o_2}^b - \frac{[O]^i}{K'} \right] \quad (2.28)$$

Equation (2.28) can be solved for  $[O]^i$ :

$$[O]^i = \frac{-RTK'k_o + \sqrt{[RTK'k_o]^2 + 8k_{o_2} [RTK'k_o][O]^b + 2K'k_{o_2} P_{o_2}^b}}{4k_{o_2}} \quad (2.29)$$

### Material Balance:

A molar balance on the bath yields the following:

$$\begin{aligned} & [\text{rate of } O \text{ input}] - [\text{rate of } O \text{ output} = 0] \\ & [\text{rate of } O \text{ generation} = 0] - [\text{rate of } O \text{ consumption} = 0] \\ & = \text{rate of } O \text{ accumulation} \end{aligned} \quad (2.30)$$

$$\dot{n}_o \cdot A = V \frac{d[O]^b}{dt} \quad (2.31)$$

Depending on the transport conditions, gas-liquid interactions can take place in different regimes. Although the mass transfer analysis is generally similar in most processes, as outlined above, it is the mass transfer coefficient<sup>2</sup> that determines the transport characteristics of the regime.

### **2.3.1. Superficial Gas-Liquid Contact**

Diffusion of solutes in a gas mixture through a stagnant gas film to a liquid surface is the most obvious type of superficial gas-liquid contact. Thus the reacting species transfer to the reaction interface driven by the concentration gradient, established by the interfacial reaction. Diffusion through a stagnant gas film in capillary tubes and around levitated

---

<sup>2</sup>Depending on the transport conditions, the mass transfer coefficient can be determined from: the film model, the surface renewal model, from empirical mass transfer correlations and/or from measurements, (refer to J. Szekely and N. J. Themelis, Rate Phenomena in Process Metallurgy [52]).



droplets, to study the kinetics of gas-liquid reactions has been adopted by several investigators [27-33]. In cases of heterogeneous reactions involving interfacial phenomena, e.g. interfacial turbulence or interfacial blockage, due to surface active solutes, however, diffusion tests are difficult to interpret. Furthermore, in systems with very fast liquid phase mass transfer, diffusion methods may create conditions of starvation in the gas phase.

### **2.3.2. Convective Gas-Liquid Contact**

Top-blown and bottom-blown jets in bath smelting are the most common metallurgical examples of gas-liquid convective transport. A very high degree of bath mixing and high reaction gas utilization are some of the advantages gained by adopting bottom-blown jetting methods. On the other hand, top-blown jetting systems are advantageous with respect to refractory wear and ease of maintenance. Due to its relevancy to the improvement of the current bath smelting processes and to the development of new bath smelting processes, several studies have been conducted to understand the fundamental and practical aspects of gas injection including top-blown jets [62-67].

#### **2.3.2.1. Gas Jets Impinging on Liquid Surfaces**

Owing to numerous advantages of top blown methods in metallurgical systems, the principle of lancing is employed in a variety of processes such as oxygen steel making, Worera and Mitsubishi processes. Gas jet impingement techniques can be categorized into three main types [41], according to their flow behaviour, as follows:

1. With low jet momentum, a classical wall jet pattern is formed including a slight surface depression (Figure 2.5a).
2. With increased jet momentum, a shallow depression forms in the liquid (Figure 2.5b); a splashing pattern develops.

3. With further increased jet momentum, much deeper penetration of the bath takes place. Thus the penetration or re-entrant mode (Figure 2.5c) is established.

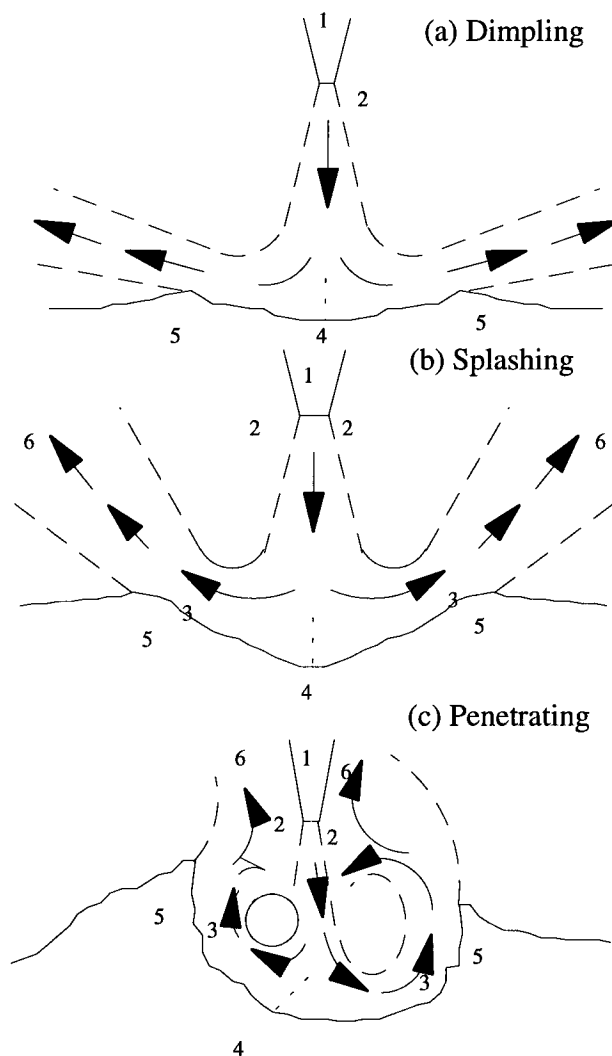


Figure 2.5. Comparative geometry of flow modes; (1) nozzle body; (2) entrainment region of the original jet; (3) entrainment region of the wall jet across the phase interface; (4) stagnation point of the original jet; (5) separation point of the wall jet; (6) two-phase exit flow, (after Molloy [41]).

There have been numerous studies on the behaviour of impinging gas jets [35-43,45-48,51-53], as a result of their high degree of relevancy to metallurgical processes.

Laboratory experiments that are carried out to study the kinetics of gas-liquid reactions, under top-blown conditions, often employ low momentum jets, which do not stir the bath

appreciably or penetrate the liquid surface. Due to its relevancy to the current work, the low momentum type of gas jetting will be the main focus of this discussion. Owing to the difficulties encountered in the kinetic measurements of metallurgical systems under actual operating conditions, room temperature models have been adopted by several investigators [35-36,38,40-42,44-45,49-50,54].

### 2.3.2.1.1. High Momentum Jetting Systems

One of the early models for the gas-liquid jetting systems is that of Wakelin and Lohe [38]. The geometry of the impingement area observed by Wakelin is shown in Figure 2.5. Using air-water, CO<sub>2</sub>-water, air-mercury and CO<sub>2</sub>-mercury systems, Wakelin investigated the effect of the jet characteristics on the size and shape of the depression formed in the liquid, the bath circulation, and the rate of mass transfer.

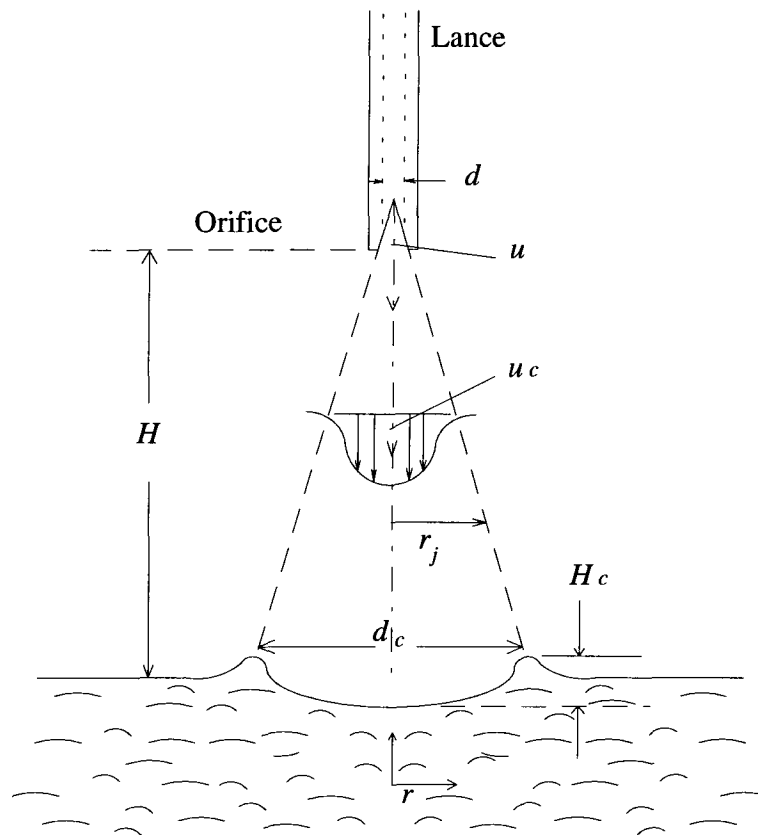


Figure 2.6. Model of impinging gas jet used by Wakelin (after Themelis and Szekely [52]).

Wakelin correlated the measured Sherwood number to the Reynolds number as follows:

$$Sh = a[Re(1 + Fr')]^n \quad (2.32)$$

where the gas phase mass coefficient can be calculated as follows:

$$k_g = \frac{2aD_{A-B}}{d_c} \left[ \frac{d_c K_{j,u} u d \rho_g}{4H\mu_g} \left( 1 + \frac{\rho_g u^2}{g(\rho_l - \rho_g)d} \frac{d_c}{2H_c} \right) \right]^n \quad (2.33)$$

The ratio of the depth to the diameter of the cavity can be determined from the following correlation:

$$\frac{H_c}{d} \left( \frac{H + H_c}{d} \right)^2 = \frac{K_{j,u}^2 M_j}{2\pi g \rho_l d^3} \quad (2.34)$$

where  $K_{j,u}$  is the jet constant for momentum transfer, defined as:

$$K_{j,u} = \frac{u_c y}{ur} \quad (2.35)$$

Experimental measurements using the above models yielded  $K_{j,u} \approx 15$  [52] and 12.5 [35].

Mass transfer correlations for an air jet impinging on water gave 6.57 and 0.43 for a and n respectively<sup>3</sup>.

This model provided a basis for experimentally obtaining empirical correlations that can be used to estimate the gas phase mass-transfer coefficient for high momentum jetting systems. The correlation obtained from the air-water system measurements which were conducted using high momentum jets of 8000 dynes, cannot be used in the calculation of the gas phase mass transfer coefficients of the system under study. In the present work, low momentum jets of approximately 3-25 dynes were applied. The extrapolation of this correlation, to calculate the gas phase mass-transfer coefficient for the conditions of jet

---

<sup>3</sup>A plot of  $Sh$  Vs  $Re(1 + K_{Fr})$  was provided for the mass transfer correlation for an air jet impinging on water [52]. The data were extracted from the graph and were used in the calculation of a and n, via regression analysis.

momentum of one to two orders of magnitude below its range would result in considerable error.

#### 2.3.2.1.2. Low Momentum Jetting Systems

In order to obtain valid kinetic measurements of gas-liquid reactions, starvation conditions of both reactants must be avoided. In the case of crucible-type laboratory tests, for the investigation of process kinetics, a sufficient amount of reactant gas must be delivered to the reaction interface, in order for the measurements to be valid. For a certain bath volume, the limiting gas flow rate of non-starvation conditions must be determined from preliminary tests<sup>4</sup>. In studying the kinetics of gas-liquid reactions, for experimental simplicity and higher accuracy of measurement, the use of low momentum jetting in such experiments has been adopted by several investigators [45-49,55-57].

Kikuchi et al. conducted several studies on top-blown lancing systems [45-48]. Their studies included room temperature and high temperature measurements of mass transfer as well as numerical simulations of crucible-type top lancing systems. Room temperature measurements of reaction rates of systems under conditions of gas phase mass transfer control yielded the formulation of several empirical correlations for the gas phase mass transfer coefficient. Room temperature experiments included: sublimation of naphthalene into a nitrogen stream; evaporation of pure liquid (toluene, water, and acetic acid were used respectively) into a nitrogen stream; absorption of ammonia from an ammonia-nitrogen stream into water. For the latter system the gas phase mass transfer coefficient ( $k_g$ ) was evaluated by eliminating the liquid phase mass transfer resistance. Figure (2.7) shows a summary of the experimental results. The reaction rate measurements permitted the correlation of the Sherwood number to the ratio of the radius of the reaction area and

---

<sup>4</sup>The limiting gas flow rate of non-starvation conditions in the gas phase is the gas flow rate at which the reaction gas utilization is 100%.

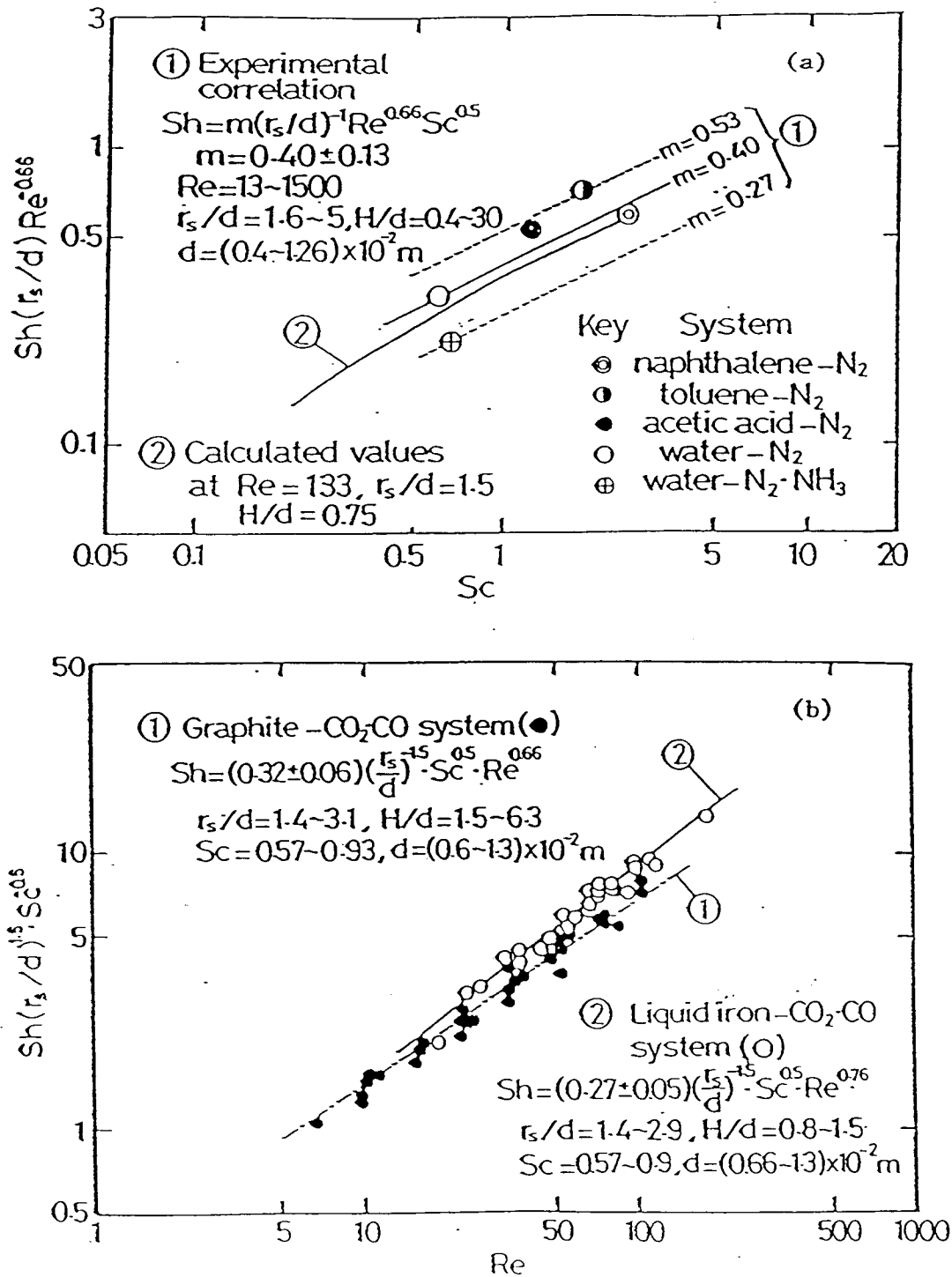


Figure 2.7. (a) Mass-transfer coefficient in gas phase at room temperature, (b) Mass-transfer coefficient in gas phase at elevated temperatures, (after Kikuchi et al. [48]).

the inside diameter of the lance, the Reynolds number, and the Schmidt number, as follows:

$$Sh = (0.40 \pm 0.13)(r_s/d)^{-1} Re^{0.66} Sc^{0.5} \quad (2.36)$$

Elevated temperature experiments included: the oxidation of graphite by CO<sub>2</sub>-CO gas mixtures and the decarburization of liquid iron by a CO<sub>2</sub>-CO gas mixture. The measurements yielded the following correlations:

$$Sh = (0.32 \pm 0.06)(r_s/d)^{-1.5} Re^{0.66} Sc^{0.5} \quad (2.37)$$

$$Sh = (0.27 \pm 0.05)(r_s/d)^{-1.5} Re^{0.76} Sc^{0.5} \quad (2.38)$$

In determining the rate controlling mechanism of a gas-liquid reaction, the above correlations can be used as a tool in the analysis of rate measurements. The above correlations indicate that for a gas-liquid reaction rate to be controlled by gas phase mass transfer, the relationship between the reaction rate and the gas flow rate (or *Re*), must yield an exponent of the gas flow rate (or *Re*) of approximately 0.66-0.76.

#### 2.4. Oxidation Kinetic Studies

In the past twenty-five years, fundamental research involving experimental measurements of the oxidation kinetics of metals and mattes has gained attention from metallurgical investigators [7,27-32,34,51,53,56-57,69-77]. Because the understanding of the oxidation kinetics of copper sulphide is paramount to the overall comprehension of the metallurgy of copper converting, many studies have been conducted [7,27,30-31,57,68-77].

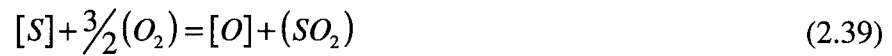
In order to study the kinetics of copper converting, Ashman et al. [7] constructed a mathematical model of the bubble formation at the tuyeres of a copper converter. Their kinetic studies suggested that the copper converter operation is gas-phase mass transfer limited.

Toguri and Ajersch [27] measured the weight change of molten samples of copper sulphide, during oxidation by Ar-O<sub>2</sub> gas mixtures, in capillary tubes. Their results indicated that the oxidation reaction of copper sulphide proceeds in two stages. The first stage is an unsteady state period in which the loss of sulphur from the melt, in the form of SO<sub>2</sub>, takes place. This loss of sulphur continues until the composition of the melt reaches the miscibility gap after which the melt loses weight at a constant rate (according to Reaction (2.4)) until the sulphide phase disappears. Their conclusion was that the rate of reaction is limited by gas diffusion.

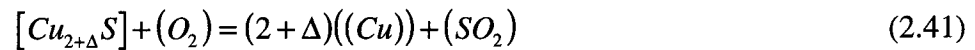
Rottmann and Wuth [71] studied the kinetics of copper matte conversion, under top-blown conditions involving a subsonic N<sub>2</sub>-O<sub>2</sub> gas jet. Their experimental approach consisted of the measurement of the bath weight as well as off-gas analysis. Their results confirmed that the oxidation reaction of molten copper sulphide proceeds in two kinetic stages. In the first stage, the bath is desulphurized and oxygen saturated (at about 0.6 wt%); In the second stage, the bath is oxidized by both the dissolved oxygen and incoming oxygen, according to Reaction (2.4). Their conclusion was that the reaction is driven by the gas diffusion through the gas boundary layer adjacent to the melt surface. However, according to the results of numerical analysis of the gas phase mass transfer of top-blown systems [47], the existence of a boundary layer is highly questionable. The analysis of Rottmann and Wuth, however, did not explain the different reactions that take place in the two stages.

The experiments of Jalkanen [57] consisted of the gravimetric measurement of 3- to 7-gram samples of copper sulphide under top-blown conditions of N<sub>2</sub>-O<sub>2</sub> gas mixtures. The experimental results confirm that the oxidation reaction of molten copper sulphide takes place in two stages. Jalkanen claims that the first stage corresponds to the saturation of the melt by oxygen and copper according to Reactions (2.39) and (2.40) respectively.





When the copper sulphide melt is saturated by both oxygen and copper, the conversion of copper sulphide into metallic copper (the second stage) takes place according to Reaction (2.41).



Jalkanen suggested that Reaction (2.41) may take place in several steps:

- oxygen adsorption into the melt surface according to following reaction:



- formation of an intermediate activated complex as follows:



- formation and desorption of sulphur dioxide as follows:



Jalkanen concluded that both mass transfer in the gas phase and the kinetics of Reaction (2.44) control the overall rate of copper sulphide oxidation.

Thus all of the above studies agree that the rate controlling mechanism of the oxidation reaction of molten copper sulphide is gas phase mass transfer but they did not underpin their findings with a mathematical analysis. Nor did they explain the mechanism by which blister copper is made.

In studying the kinetics of gas-liquid reactions, the effects of reaction gas flow rate and reaction gas composition on the reaction rates must be determined. In order for the reaction rate to be controlled by the gas phase mass transfer of oxygen to the melt surface, the following principal conditions must be satisfied:

1. The rate of oxygen reaction must be proportional to the oxygen bulk partial pressure, as described by the following equation:

$$\dot{N}_{O_2} = \frac{k_{O_2} A}{RT} P_{O_2}^b \quad (2.45)$$

2. The gas phase mass transfer coefficient and the reaction gas flow rate must have a relationship as follows:

$$k_{O_2} = aQ^n \quad (2.46)$$

, where  $a$  and  $n$  are constants. For top-blown jetting systems,  $n$  should have a value of approximately 0.6-0.8.

3. The reaction rate must not have a strong dependence on the reaction temperature
4. The rate of oxygen reaction must be independent of the concentrations of oxygen and any other reacting species in the bath.

## 2.5. Interfacial Phenomena

In describing the physical and chemical properties of a given phase, it must be recognized that the surface properties differ from those of the bulk. The interface between two interacting phases is not to be regarded as a simple geometrical plane, upon either side of which extend the interacting phases, but rather a complex part of the whole arrangement. In studying heterogeneous reaction systems, the consideration of interfacial effects is paramount to ensure the validity of the established results [55-56,80-104]. Depending on the reaction system, interfacial phenomena can have negative or positive effects on reaction rates [99]. Non-reacting surface-active solutes may cause a decrease of reaction rates by preventing the reactant species from transferring to the interface [56,84,99-102]. On the other hand, in some systems, surface tension-driven flows may enhance mass transfer by orders of magnitude [56].

## 2.5.1. Generation of Spontaneous Interfacial Motion

### 2.5.1.1. Driving Force

In some systems, it is known, that the surface tension is a strong function of surface-active solute concentration, electrical potential and/or temperature [83]. In liquid metal systems, surface-active solutes can either lower or raise the interfacial tension, as shown in Figure 2.8.

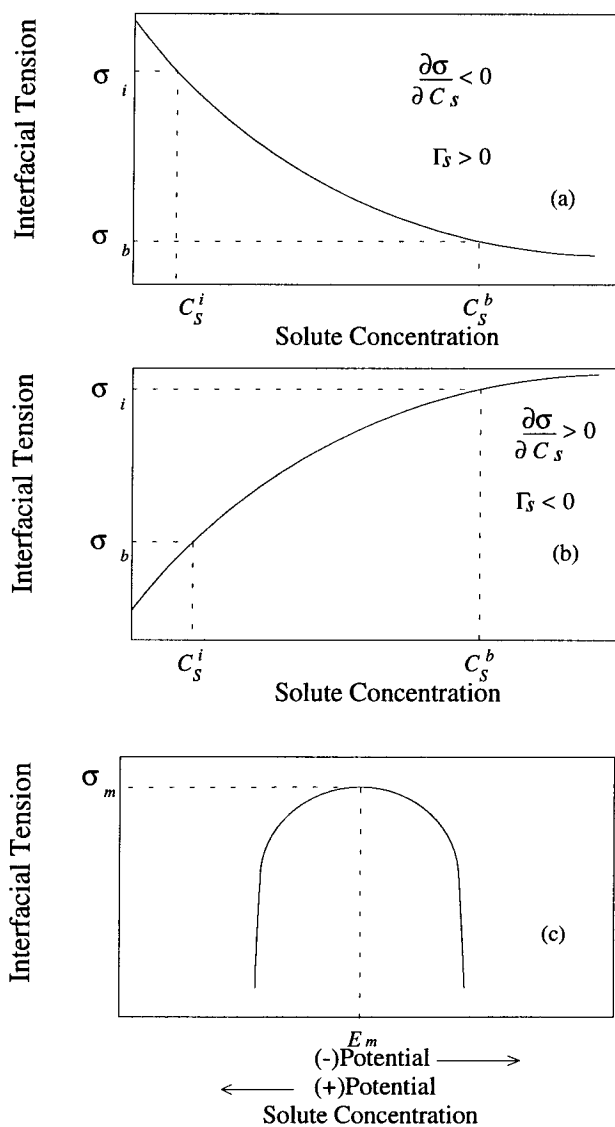


Figure 2.8. Type of adsorption at liquid-metal interfaces: (a), positive adsorption; (b) negative adsorption; (c), electrocapillary behaviour (after Brimacombe [83]).

The dependence of surface tension on the solute concentration is described by Equation (2.47), which is obtained from the Gibbs adsorption equation [83,86].

$$\left(\frac{\partial\sigma}{\partial C_s}\right)_{T,P} = -\Gamma_s \frac{RT}{C_s} \quad (2.47)$$

When two reacting phases are brought into contact, concentration gradients of surface-active solutes, along their interface, are established. Resulting interfacial tension gradients may cause the interface to move toward the region of high interfacial tension. In the case of oxygen and sulphur in copper, it is clear that positive adsorption is expected, as shown in Figures 2.9 and 2.10.

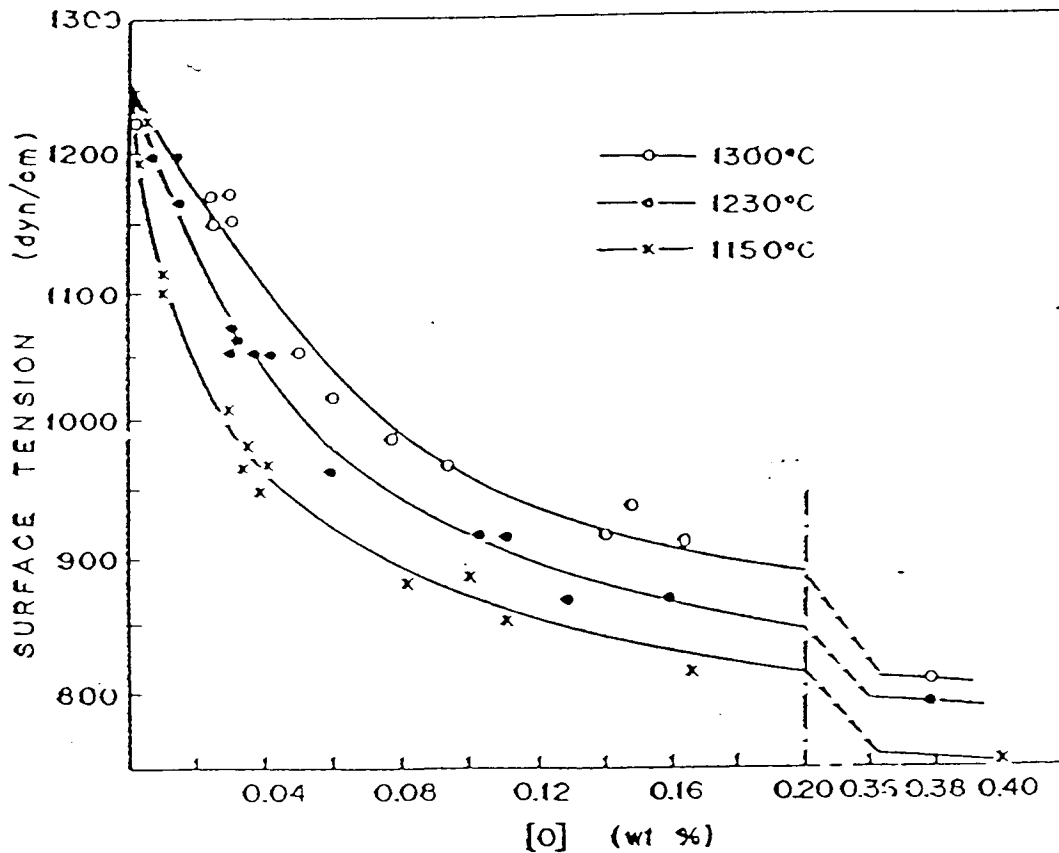


Figure 2.9. Effect of oxygen on the surface tension of liquid copper, (after Monma [87]).

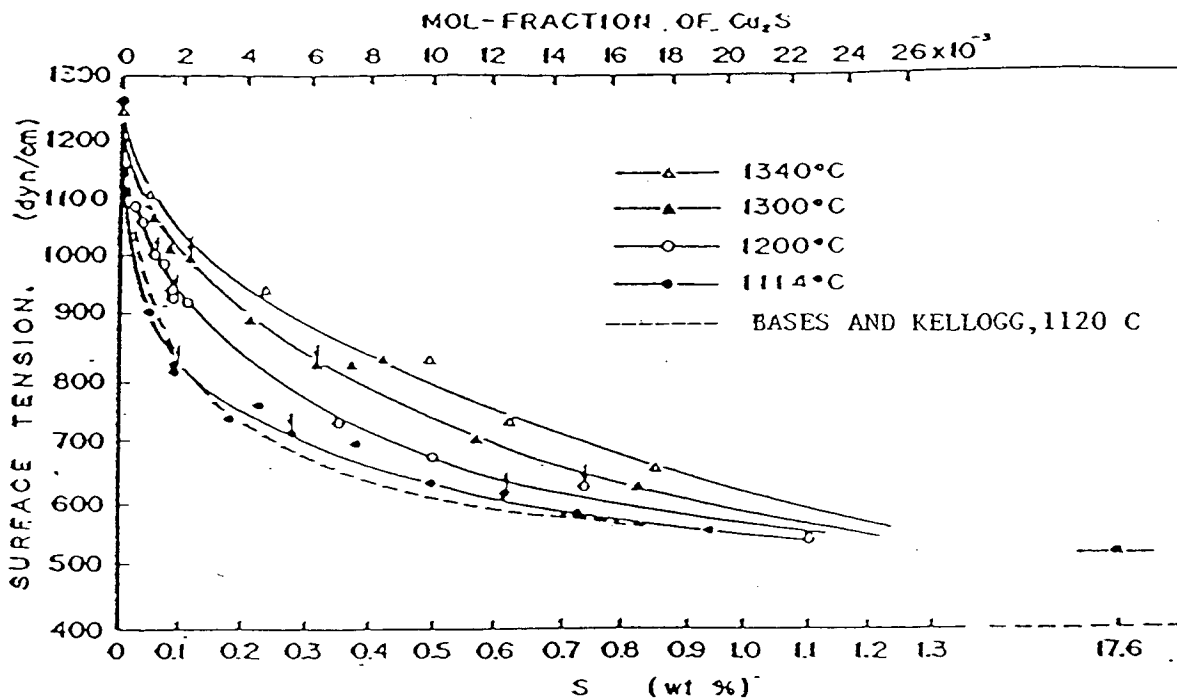


Figure 2.10. Effect of sulphur on the surface tension of liquid copper, (after Monma [87]).

It is very clear that the sulphur and oxygen have strong effects on the surface tension of molten copper. This is a strong indication that when investigating the oxidation kinetics of molten copper sulphide, the interfacial effects must not be ignored.

#### 2.5.1.2. Mechanism

Due to non-uniform mass transfer, in real systems, gradients of a surface-active solute along an interface are expected. In stirred systems these events can occur on a micro-scale by the essentially random penetration of eddies from the bulk of a fluid phase to an interface. Spontaneous motion may develop as a result of the concentration differences of the penetrating eddy and its surroundings, as shown in Figure 2.11.

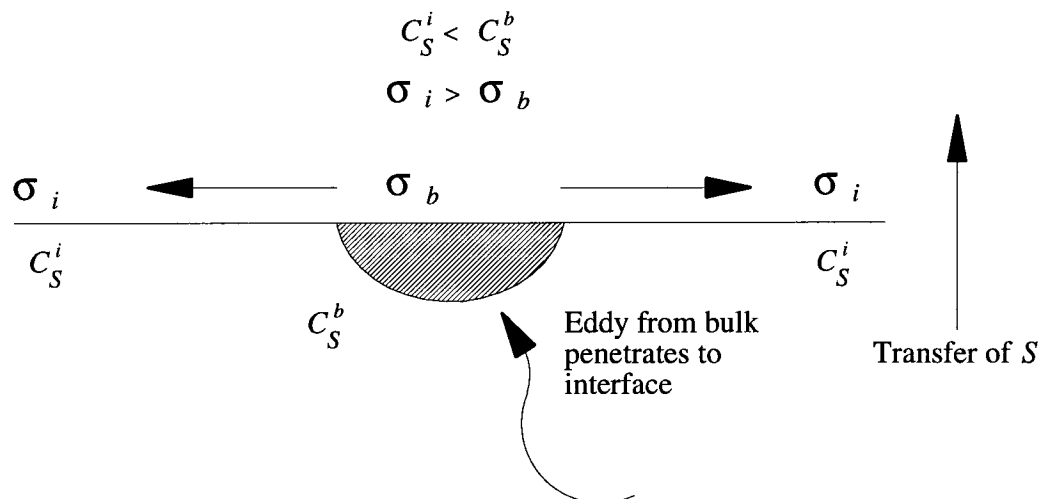


Figure 2.11. Interfacial motion generated on micro-scale due to eddy penetration (after Brimacombe [83]).

Also macro-scale non-uniform mass transfer of surface-active solute can generate interfacial turbulence at the mass transfer interface. A hypothetical example of macro-scale interfacial motion is the case of a solid  $\text{Cu}_2\text{S}$  piece partially immersed in molten copper, as shown in Figure 2.12. In this case, surface motion away from the solid  $\text{Cu}_2\text{S}$  is spontaneously generated. The experiments of Barton and Brimacombe indicated that interfacial turbulence is generated during the dissolution of solid  $\text{Cu}_2\text{S}$  in molten copper [85].

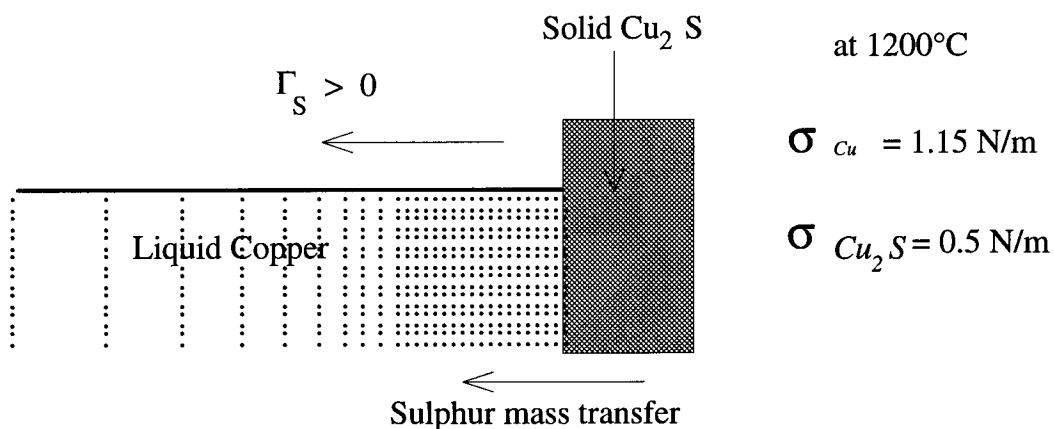


Figure 2.12. Interfacial motion generated on macro-scale by presence of partially immersed piece of  $\text{Cu}_2\text{S}$  in molten copper.

As shown in Figure 2.13, the effect of oxygen is expected to be similar to that of sulphur. The experiments of Barton and Brimacombe also indicated that interfacial turbulence can enhance the liquid phase mass transfer coefficient by at least one order of magnitude during the absorption of oxygen by liquid copper [56]. In those experiments Ar-O<sub>2</sub> gas mixtures were top blown onto molten copper baths. Measurements of surface velocity and of oxygen concentration in the bath were conducted to determine the effect of surface tension-driven flows on the kinetics of oxygen absorption by liquid copper. A copper oxide patch was observed beneath the oxygen lance, and the surface spreads rapidly outward as shown in Figure 2.13. Spreading of the copper surface in the presence of copper oxide can be described by the initial spreading coefficient, as follows:

$$S = \sigma_{Cu} - (\sigma_{oxide} + \sigma_{oxide/Cu}) \quad (2.48)$$

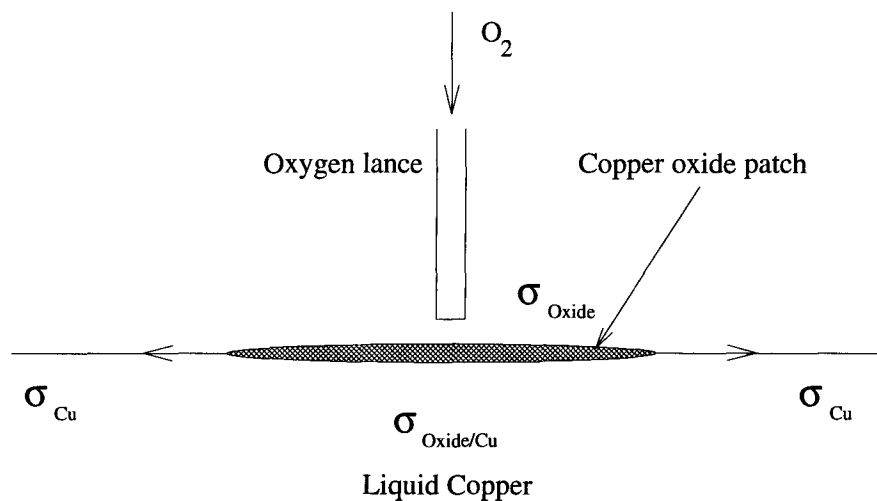


Figure 2.13. Mechanism of copper oxide patch spreading on the liquid copper surface, (surface spreads if  $\sigma_{Cu} > \sigma_{Oxide} + \sigma_{Cu/Oxide}$ ).

Having reviewed the practical implications of the effects of oxygen and sulphur on the surface tension of liquid copper, separately, it becomes very clear that their simultaneous effect is of a very similar nature. Thus, when investigating the oxidation kinetics of molten copper sulphide, the effect of surface-tension driven flows must be considered.

### **3. Objectives and Scope**

The understanding of the oxidation kinetics of molten copper sulphide is highly important to the overall understanding of copper converting. The high oxygen utilization of the copper converter and the findings of earlier studies indicate that the rate controlling mechanism of the oxidation reaction of molten copper sulphide is gas phase mass transfer. There are, however, fundamental discrepancies with respect to the chemistry of the copper-making stage. Earlier studies indicated that the oxidation of molten copper sulphide takes place in two stages. The measurements of Rottmann and Wuth [71] indicated that the ratio of the moles of reacted oxygen to the moles of evolved sulphur dioxide are greater than unity during the primary stage and less than unity (approximately 0.9) during the secondary stage. Therefore, it is clear that neither Reaction (2.4) nor Reaction (2.5) can be the reactions during the primary stage. According to the stoichiometry of Reaction (2.2), the ratio of oxygen to sulphur dioxide is  $3/2$ . This may suggest that Reaction (2.2) is the primary reaction; however, the thermodynamics of this system indicates that the formation of  $\text{Cu}_2\text{O}$  is not possible before the total oxidation of  $\text{Cu}_2\text{S}$ . Furthermore, the formation of solid  $\text{Cu}_2\text{O}$  results in surface blockage and likely cessation of the oxidation reaction. Therefore Reaction (2.2) is not the secondary copper-making reaction, as claimed by all of the investigators. It also is clear that treating this system as an aggregate of neutral compounds results in a fundamental dilemma in characterizing the form of the dissolved oxygen<sup>5</sup>: it is well known that sulphide melts are ionic in nature [24-25,115]. Therefore, in order to correctly deduce the chemical reactions that take place during the copper-making stage, the electrochemical treatment of this system must be adopted rather than the conventional (neutral compounds) treatment adopted by previous investigators.

---

<sup>5</sup>Since the ratio of the moles of reacted  $\text{O}_2$  to the moles of evolved  $\text{SO}_2$  is greater than one, some of the oxygen must dissolve in the melt.



Although all of the previous investigators have concluded that the rate controlling mechanism of the oxidation reaction of molten copper sulphide is gas phase mass transfer, Jalkanen [57] has suggested that the rate of chemical reaction may be rate limiting as well. None of the experimental studies provided any results of the reaction gas flow rate effect on the reaction rates. Perhaps this has not been possible in experiments involving small bath size (3-7 grams [57]) and in the case of diffusion testes (0.1-0.15 grams [27]). As explained in Section 2.4, in studying the kinetics of gas-liquid reactions, it is vital that the effect of reaction gas flow rate be determined.

Earlier studies revealed that the effect of interfacial phenomena in copper baths must be considered when investigating gas-liquid or solid-liquid reaction kinetics. It has been established that surface tension-driven flows have a profound effect on the kinetics of oxygen absorption by molten copper. The effect of interfacial phenomena on the oxidation kinetics of liquid mattes has not been investigated yet. In the light of this discussion, the objectives of the present work can be outlined as follows:

1. To elucidate further the rate controlling mechanism of the oxidation reaction of molten copper sulphide.
2. To investigate the role of spontaneous interfacial motion in the oxidation reaction of molten copper sulphide.
3. To formulate a mathematical model that can provide the fundamental evidence in support of the experimental findings.
4. To extend the understanding of the oxidation kinetics of molten copper sulphide to the copper-making stage in the Peirce-Smith converter.

### 3.1. Experimental Objectives

In order to determine the rate controlling mechanism of the oxidation reaction of molten copper sulphide, the following experimental objectives were pursued:

1. A series of laboratory tests was conducted to determine the rates of reactions of molten copper sulphide baths.
2. With the reaction gas composition, the melt volume, and the reaction temperature fixed, a series of tests was carried out for a gas flow rate range of 1-4 l/min.
3. Fixing all other variables, a series of tests was conducted for a reaction gas composition in the range of 20-80% O<sub>2</sub>.
4. Similarly with respect to bath temperature, reaction rates at 1200-1300 °C were determined.
5. To investigate the role of liquid phase mass transfer resistance in the oxidation kinetics, an artificially invoked mixing test was conducted in which the bubbling of argon gas in the bath during oxidation was adopted.
6. In order to determine the effect of surface tension-driven flows on the reaction kinetics, photography and direct observations of the melt surface were carried out.
7. Microscopic examinations of frozen melt samples, at pre-defined reaction conditions, were undertaken to aid in the analysis of the reaction rate results.

### **3.2. Theoretical Objectives**

In order to confirm the findings of this work, a mathematical model was formulated and validated against the experimental results. Based exclusively on gas phase mass transfer and the electrochemical behaviour of the melt, the model was constructed to achieve the following objectives:

1. To predict, within an acceptable degree of error, the measured bath sulphur and oxygen molar contents for the two stages and their time durations.
2. To predict, within a reasonable margin of error, the molar reaction rates of the sulphur and oxygen as functions of reaction gas flow rate, reaction gas composition and bath temperature.

Based on the model predictions, the reason for the existence of two stages rather than one was determined, and the rate controlling mechanism of the oxidation reaction of molten copper sulphide was confirmed. The electrochemical reactions that take place during the two stages were inferred.

## **4. Experimental**

### **4.1. Experimental Apparatus**

In order to achieve the experimental objectives, the experimental equipment was designed and built for use in all of the laboratory tests. The equipment consisted of: a reactor, gas drying and control system, gas analysis system, gravimetric measurement system equipped with a data acquisition system, and the melt surface photography system.

#### **4.1.1. Reactor**

The reactor, shown in Figure 4.1, consisted of a vertical tube resistance furnace, with a reaction tube, heating elements and layers of insulation contained in a steel frame. In the core of the reactor, an alumina<sup>6</sup> reaction tube, with dimensions of 57 mm inside diameter, 64 mm outside diameter and 762 mm length, was located. Water-cooled brass couplings were used for the support and mounting of the reaction tube to the steel frame. Vacuum greased fluorocarbon O-rings were used to seal the reaction tube to the brass couplings<sup>7</sup>. Insulating alumina bricks were used for the inner portion of the insulation, immediate to the heating elements, and firebricks were used for the outer portion, between the insulating alumina brick layer and the steel frame<sup>8</sup>. Porcelain wool was used to fill the gaps between the bricks.

Four 2-shank KANTHAL SUPER heating elements were carefully mounted around the reaction tube and connected in series. The heating elements were connected to a 5 kW power-supply<sup>9</sup>. Using this set-up, approximately 40 mm of  $\pm 0$  °C hot zone was obtained.

---

<sup>6</sup>99.7% recrystallized alumina was used in all of the reactor components that are within and including the reaction tube.

<sup>7</sup>To prevent the corrosion of the inside surface of the brass coupling, due to the long term exposure to SO<sub>2</sub>, the inside surface of the brass coupling was vacuum greased.

<sup>8</sup>Reactor insulating materials properties are provided in Appendix A.

<sup>9</sup>For more details about the electrical circuit of the power-supply, refer to Figure A.1 in Appendix A.

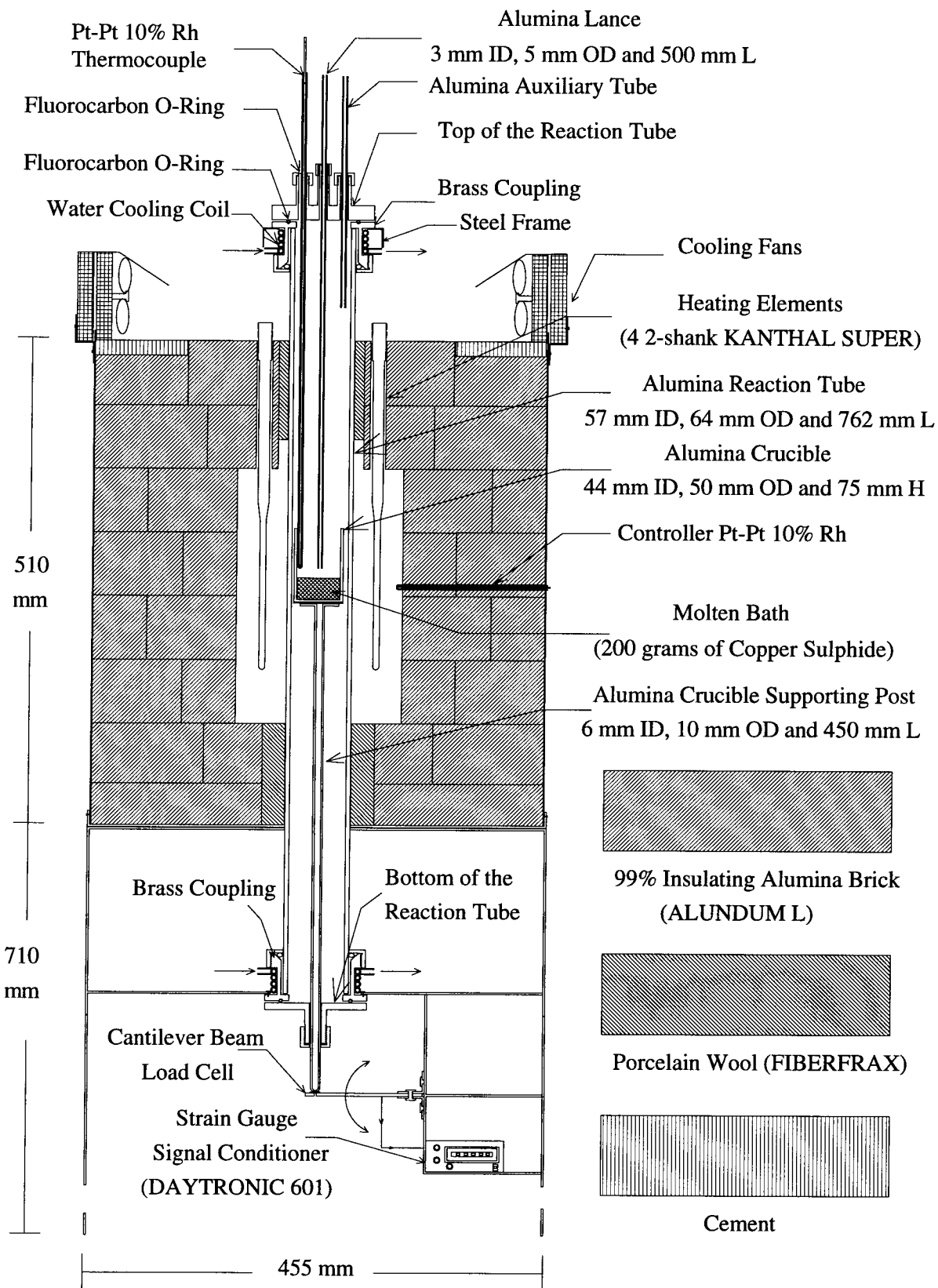


Figure 4.1. Cross-sectional view of the reactor.

To maintain constant electrical conductivity of the electrical connectors of the heating elements, two electric fans were used to cool the exposed portions of the heating elements.

Approximately 200-gram samples of molten copper sulphide were held in cylindrical, flat bottom, alumina crucibles of approximately 44 mm inside diameter, 50 mm outside diameter and 75 mm height. The crucible supporting post, shown in Figure 4.2, consisted of a closed end alumina tube (6 mm I.D., 10 mm O.D. and 450 mm long) attached to an alumina disc (40 mm in Dia and 3 mm thick), with high temperature ceramic cement.

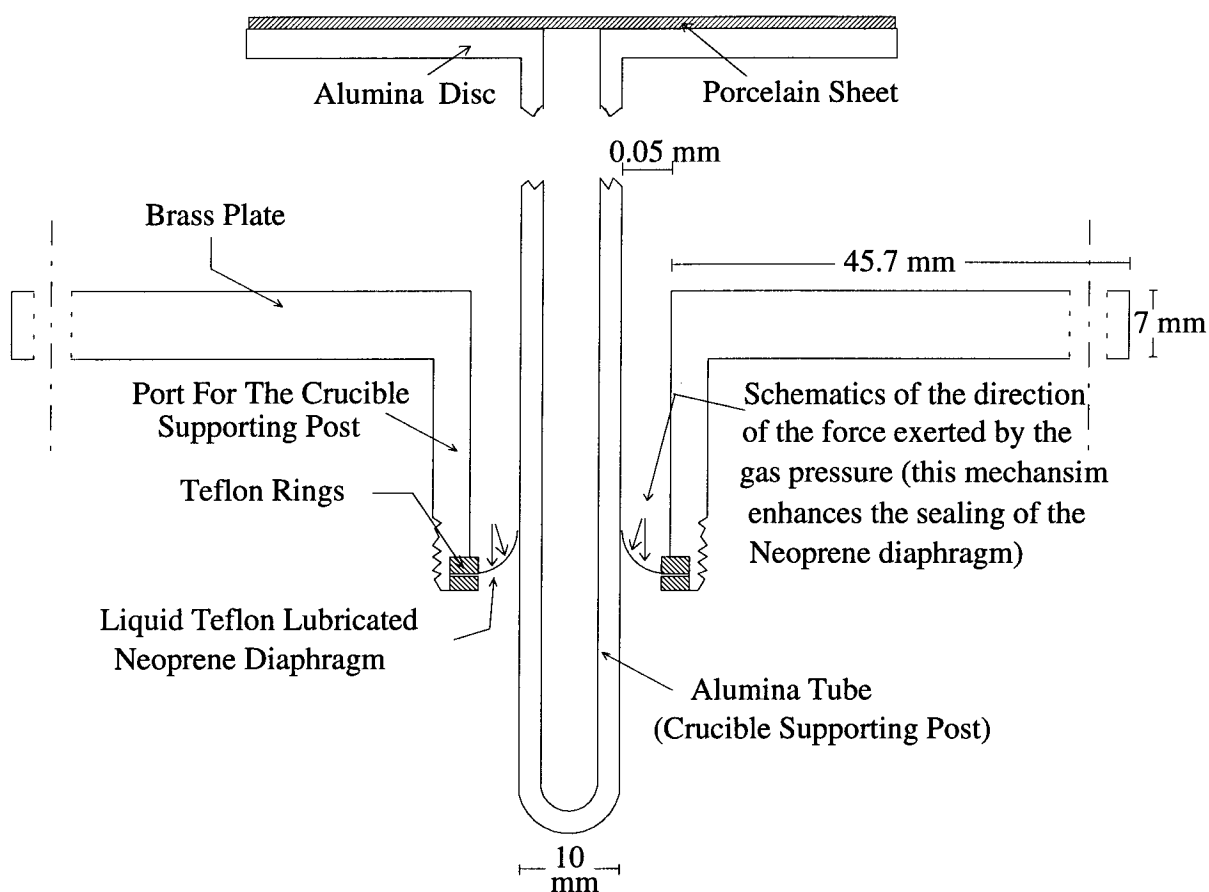


Figure 4.2. Sectional view of the bottom of the reaction tube, including the crucible supporting system. Note that the scale is offset to show the rubber diaphragm sealing arrangement.

A thin sheet of porcelain wool was used as an insulator between the bottom of the crucible and the alumina disc<sup>10</sup>.

The bottom of the reaction tube consisted of a brass plate with a port for the crucible supporting post. For safety reasons and for the purpose of analyzing the off-gas, the system had to be very tightly sealed. A neoprene diaphragm arrangement was used to seal the bottom of the reactor, as shown in Figure 4.2.

The top of the reaction tube, shown in Figure 4.3, consisted of ports for the lance, the auxiliary tube and the thermocouple sheath, the off-gas outlet pipe, and two viewing ports. The alumina tubes were fitted and sealed in the ports by O-rings. Due to the condensation of water vapor on the lower surface of the viewing port, the ability to clean the surface easily without allowing a large amount of gas to escape, required the viewing ports to be equipped with shutters, as shown in Figure 4.3. The off-gas outlet pipe, permanently attached to the top of the reaction tube, consisted of a copper pipe of 6 mm inside diameter, 8 mm outside diameter, and 400 mm length.

---

<sup>10</sup>Due to the release of the heat of fusion of the solidifying bath, during the withdrawal of the crucible, the alumina disc was susceptible to cracking as a result of its low thermal shock resistance.

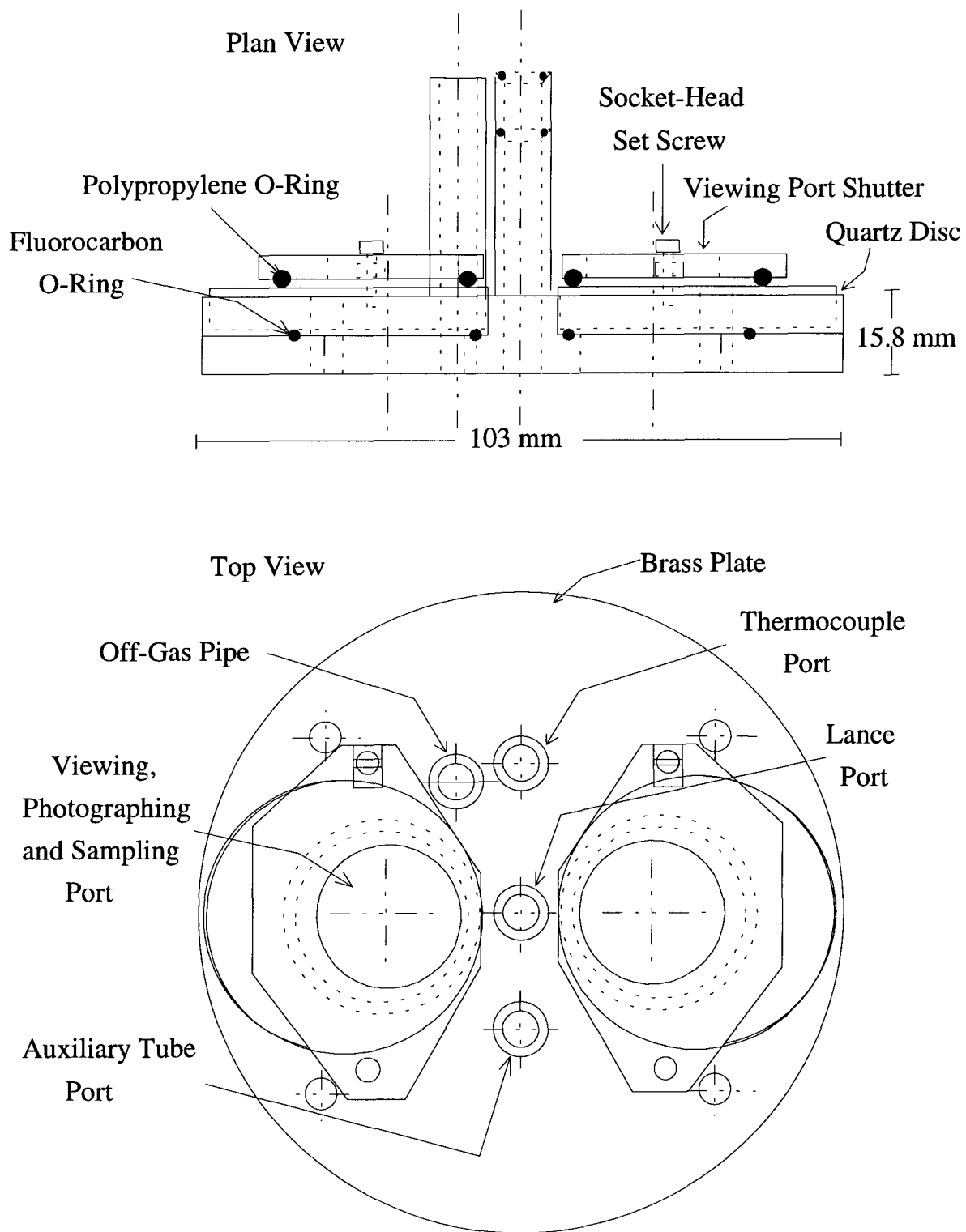


Figure 4.3. Schematic diagram of the top of the reaction tube.



### 4.1.2. Gas Drying And Control System

To control the gas flow rate and composition, and to reduce its moisture content<sup>11</sup>, the gas control and drying system, shown in Figure 4.4, consisted of gas drying columns, rotameters, pressure gauge, mercury manometer and thermometer. Polyflow lines were used to connect the components of the gas control and drying system.

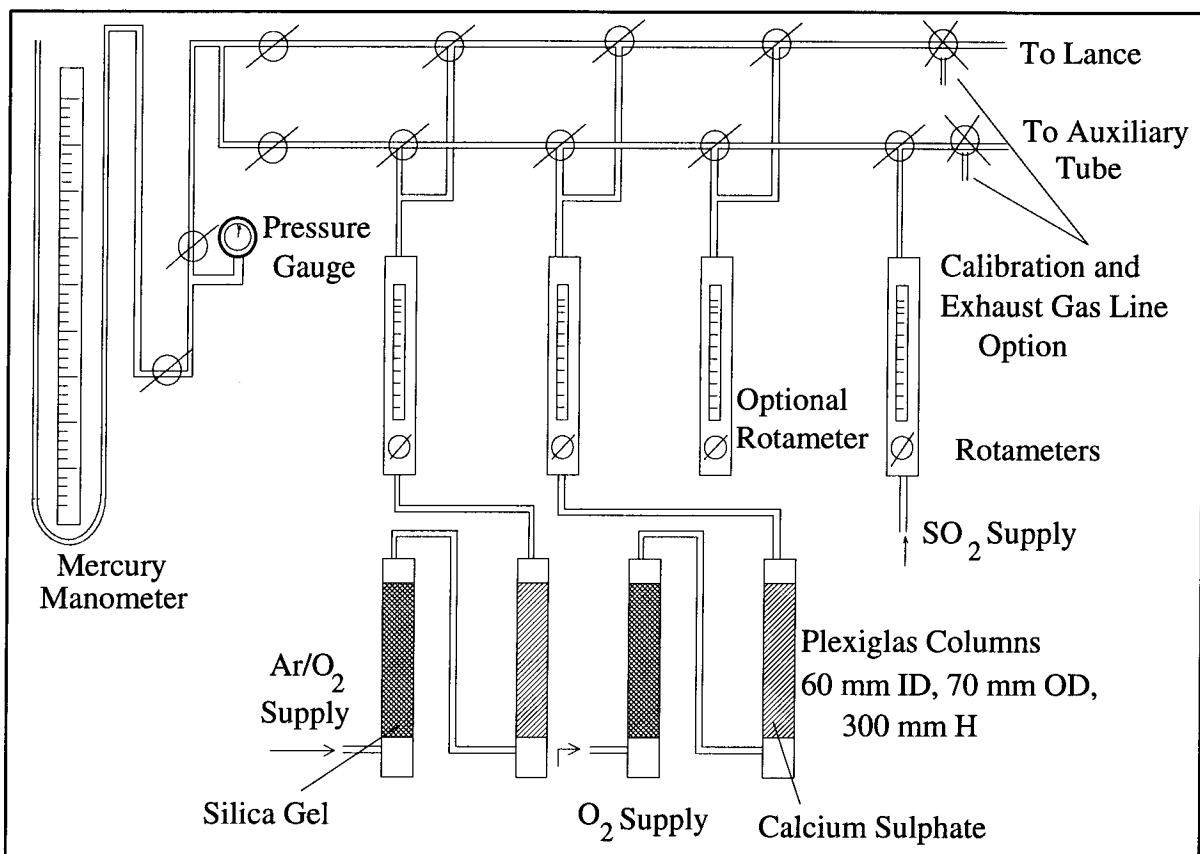


Figure 4.4. Schematic diagram of the gas train (not to scale).

### 4.1.3. Gas Analysis System

Manual measurements of the reaction rates were conducted by the use of an  $\text{SO}_2$  gas absorber and a soap bubble meter. Due to its simplicity, the manual measurement system was found to be very reliable and more accurate than gravimetric measurement.

However, gravimetric measurement was found to provide a general support to the manual

<sup>11</sup>Water vapor, in the reaction gas, condenses on the inner surface of the quartz discs and prevents surface observations.

measurement. The gas analysis consisted of the determination of the amount of sulphur removed from the bath by the use of the  $\text{SO}_2$  absorber and of the amount of unreacted oxygen using a soap bubble meter.

#### 4.1.3.1. $\text{SO}_2$ Absorber

The  $\text{SO}_2$  gas absorber consisted of approximately 3 liters of 5%  $\text{H}_2\text{O}_2$  solution vigorously mixed in a Plexiglas column, as shown in Figure 4.5.

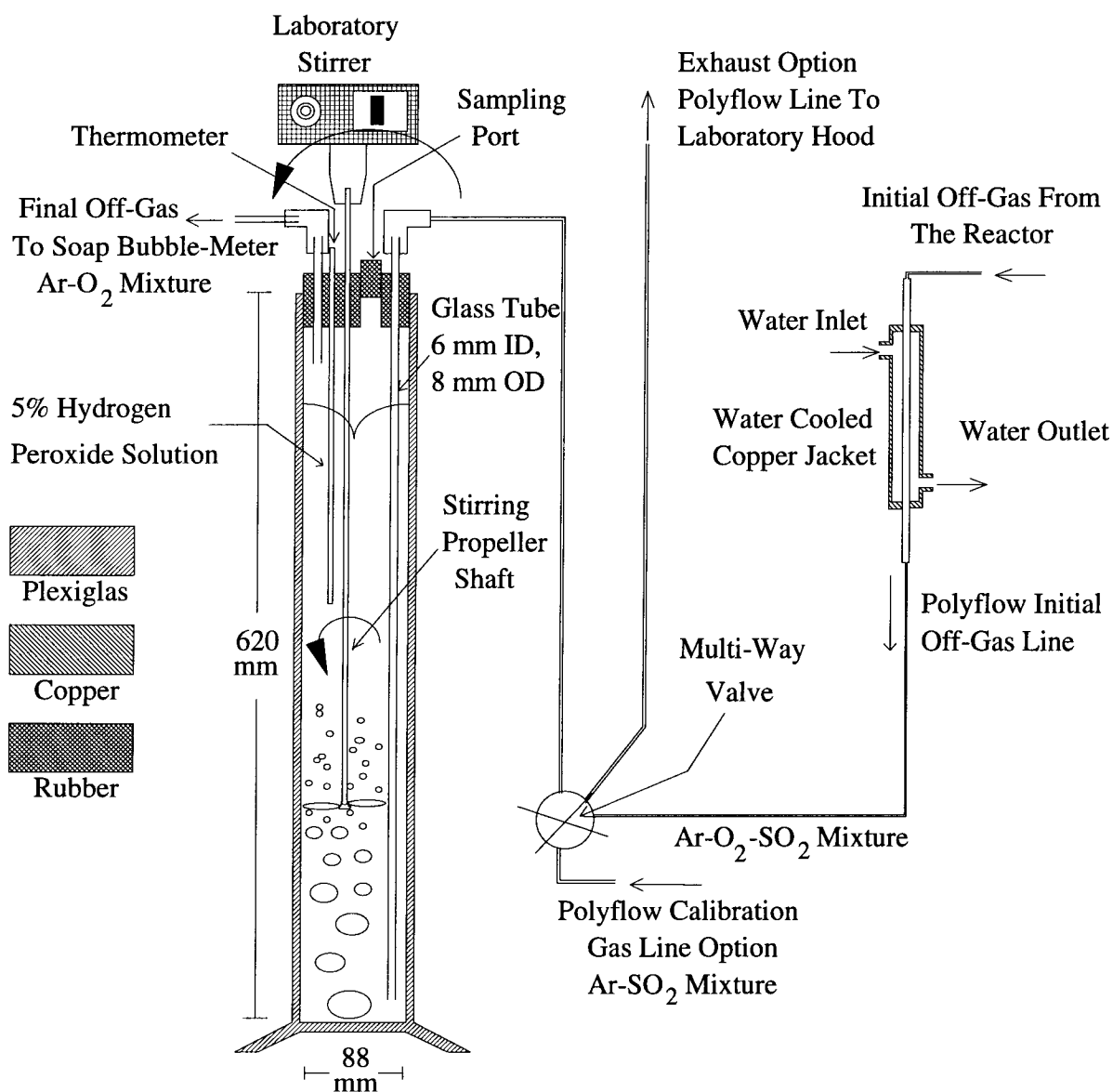


Figure 4.5. Schematic diagram of the off-gas analysis system, not including the soap bubble meter.

In order to reduce the temperature of the off-gas before introducing it to the absorber, it was passed through a 300 mm long water-cooled copper jacket, as shown in Figure 4.5. To determine the amount of  $\text{SO}_2$  absorbed, a sampling port with a rubber stopper was constructed in the master rubber stopper of the absorber. Using a 5-ml pipet, samples were extracted through the sampling port, at specific intervals of reaction time. During the time of the final gas flow rate measurement, using the soap bubble meter, the sampling port was sealed to prevent escape of the final off-gas. Due to the high aspect ratio of the absorber, vigorous mixing of the solution had to be ensured for the extraction of representative samples. In order to achieve simultaneous mixing and sealing of the absorber, the stirrer shaft had to be sealed to the rubber stopper as shown in Figure 4.6.

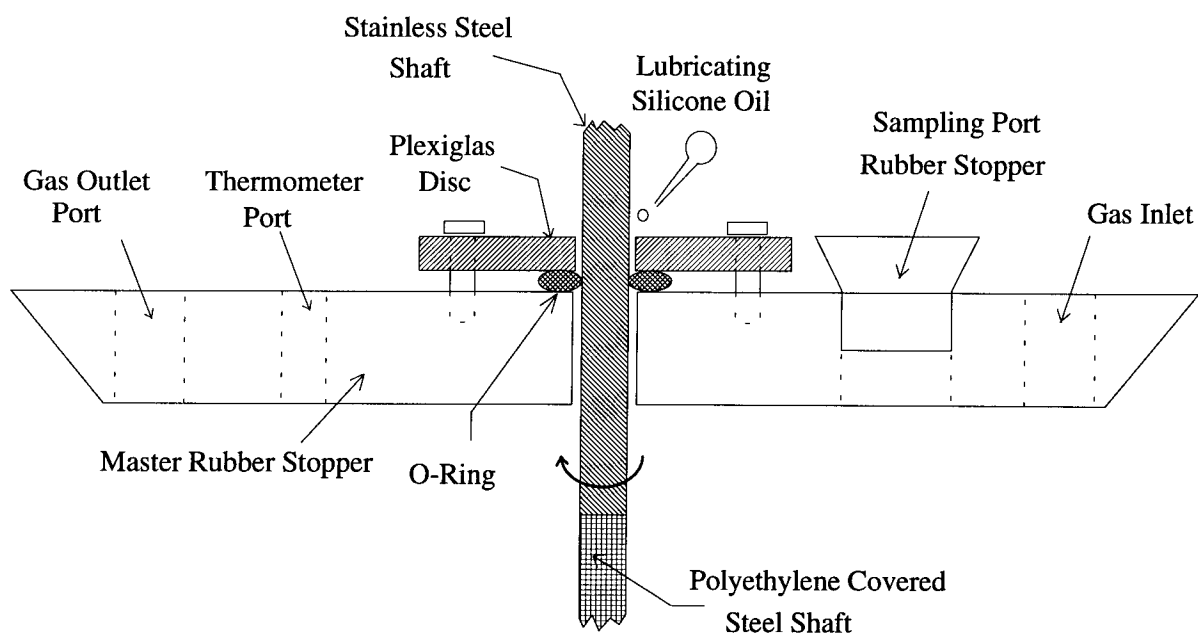
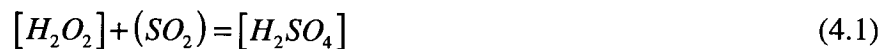


Figure 4.6. Schematic diagram of the absorber rubber stopper (not to scale).

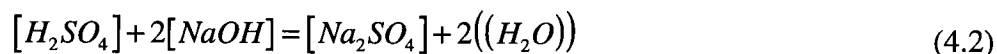
Once the bubbles come in contact with the hydrogen peroxide solution, the  $\text{SO}_2$  is absorbed from the bulk gas according to the following reaction:



To ensure high SO<sub>2</sub> absorption efficiency, vigorous mixing, a high aspect ratio of 6 and a sufficient amount of the 5% H<sub>2</sub>O<sub>2</sub> solution were adopted. It is well known that the rate of Reaction (4.1) is very fast [44]. Hence, in such a system, the rate must be bubble volume limited i.e. the smaller the average bubble size, the higher is the absorption efficiency. Vigorous mixing of the solution and the introduction of the gas at the wall of the absorber caused the gas bubbles to disintegrate to a small size and to be retained in the region of the propeller, as shown in Figures 4.5 and 4.8, thereby increasing their retention time and ensuring complete absorption of the SO<sub>2</sub>. The high aspect ratio was also important in achieving the high absorption efficiency.

The total possible amount of SO<sub>2</sub> that might be evolved from the oxidation of 200 grams of Cu<sub>2</sub>S is approximately 1.257 moles. Therefore, according to Reaction (4.1), the corresponding amount of H<sub>2</sub>O<sub>2</sub> required is also 1.257 moles. However, to ensure complete SO<sub>2</sub> absorption, 3 liters of 5% H<sub>2</sub>O<sub>2</sub> solution system was utilized i.e. approximately 4.4 moles of H<sub>2</sub>O<sub>2</sub>.

To determine the amount of SO<sub>2</sub> absorbed, the samples were titrated with 0.1 N NaOH standard solution, according to Reaction (4.2). Thus the moles of SO<sub>2</sub> were calculated, accordingly, from Equation (4.3).



$$N_{SO_2} = \frac{V_{NaOH} N_{NaOH}}{2V_s} \cdot V_a \quad (4.3)$$

To test the absorber performance, an Ar-SO<sub>2</sub> gas mixture was admitted at a constant flow rate and composition for approximately 60 minutes. Samples were obtained at pre-defined intervals of time and the amount of SO<sub>2</sub> absorbed was determined by acid-base titration. The measured absorbed SO<sub>2</sub> was found to be in agreement with the admitted amount as shown by Figure 4.7.

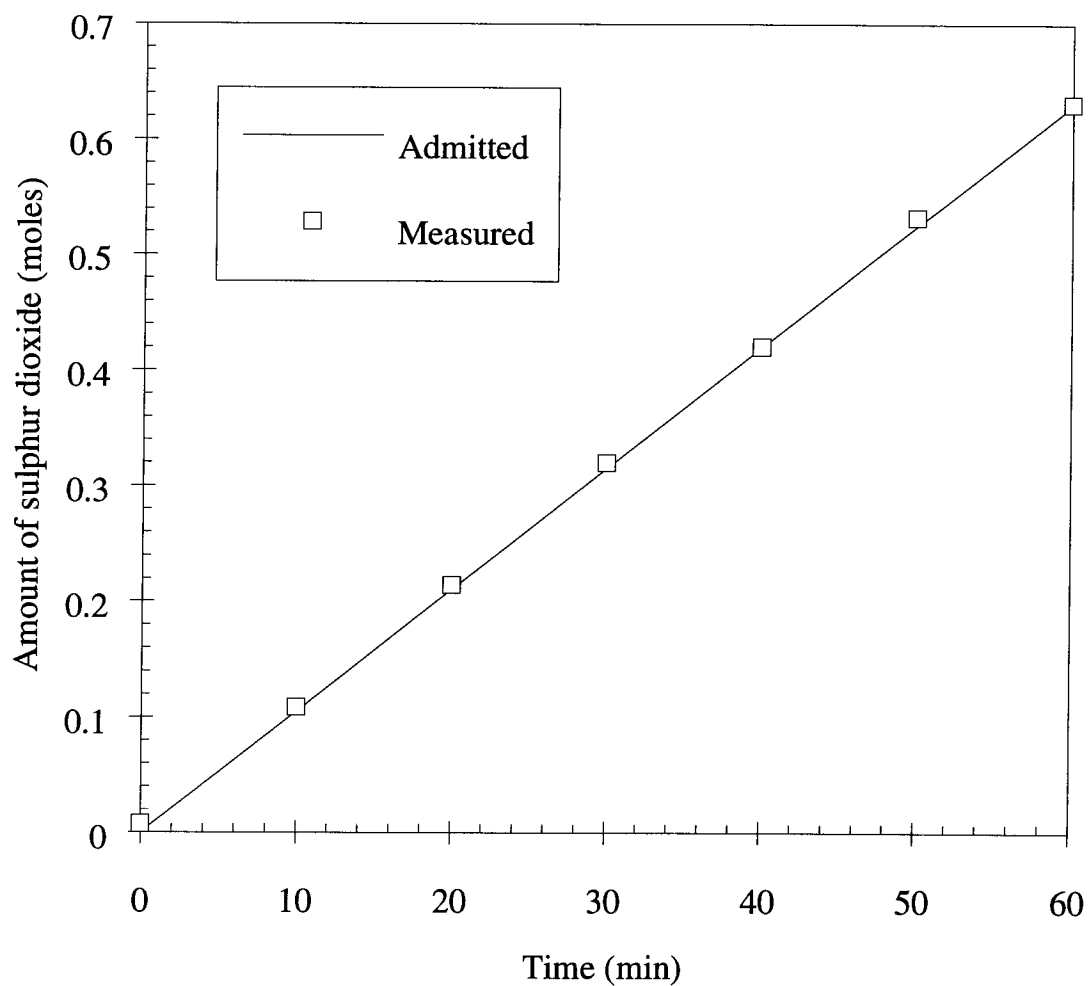


Figure 4.7. Plot of the amount of  $\text{SO}_2$  absorbed as a function of time for a test of 2 l/min of 13 %  $\text{SO}_2$  and 87% Ar at 23 °C.

The absorber performance was also tested by admitting approximately 260 ml/min of pure  $\text{SO}_2$ . The gas flow rate from the absorber was found to be approximately 0 ml/min. The gas bubbles were observed to diminish in size as they traveled upward to the solution surface, as shown in Figure 4.9.

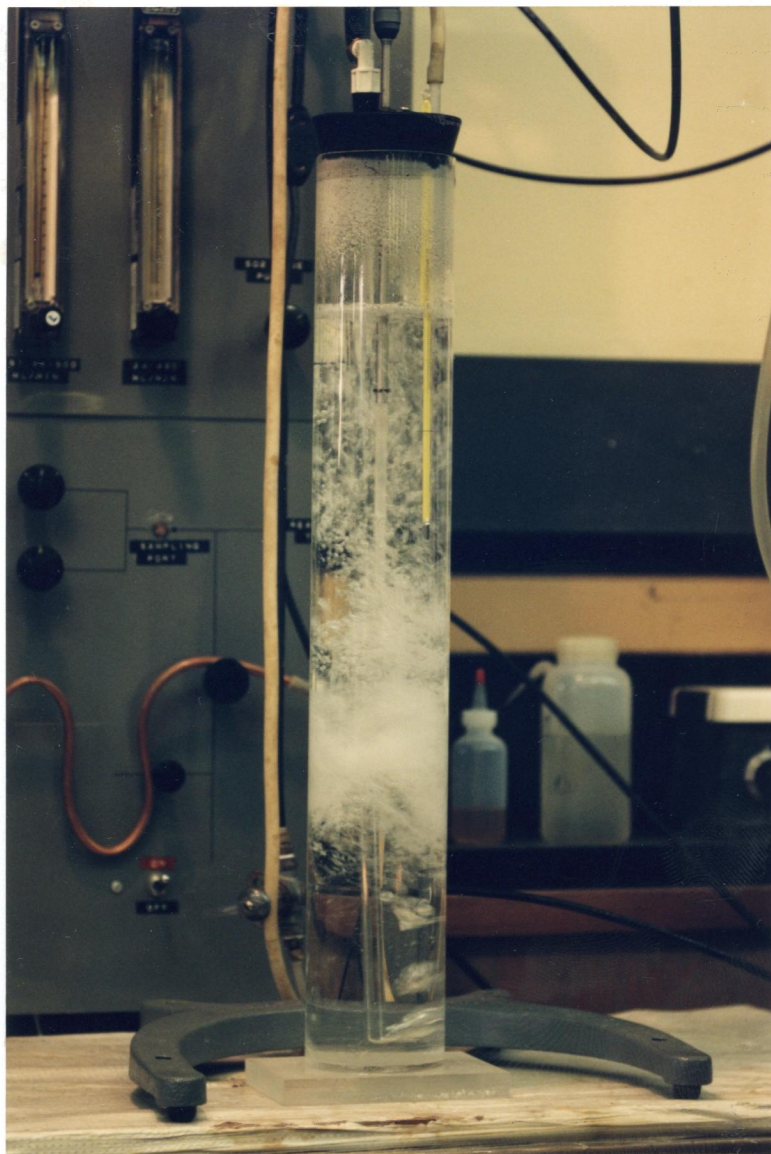


Figure 4.8. Photograph of the SO<sub>2</sub> absorber with a gas flow rate of 2 l/min, 13 % SO<sub>2</sub> and 87 % Ar. Note the vigorous mixing attained by the design of the absorber.

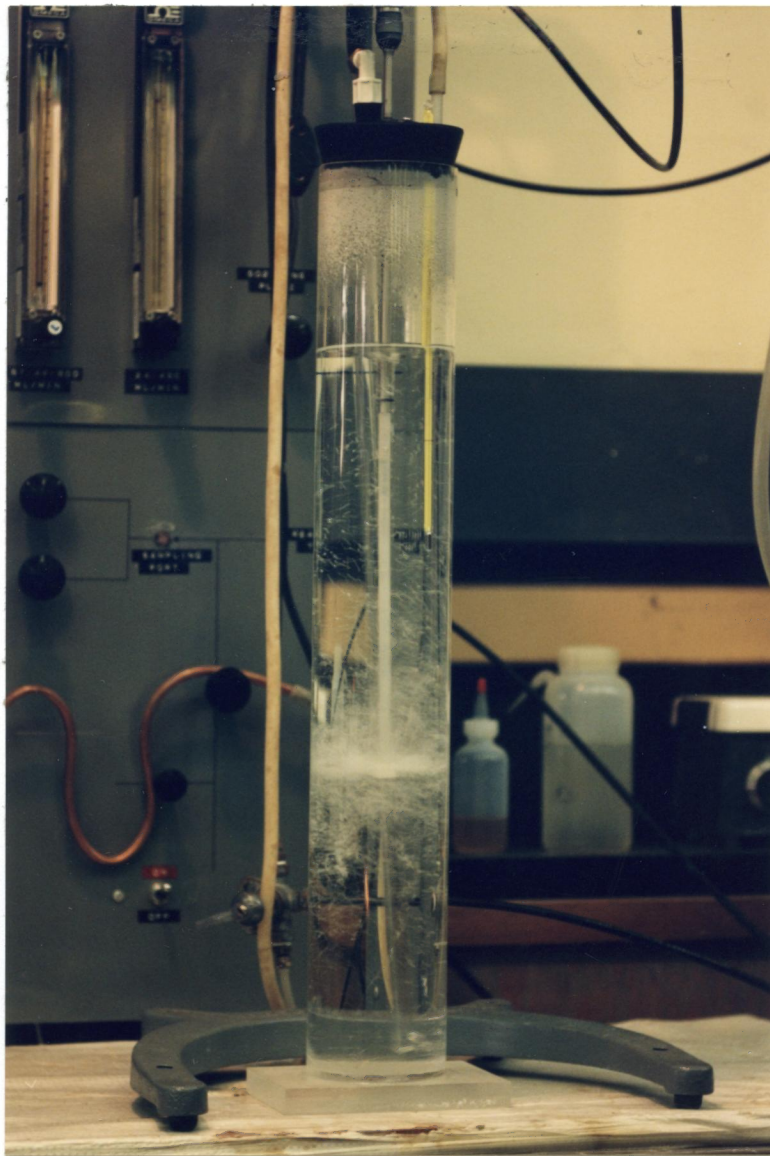


Figure 4.9. Photograph of the  $\text{SO}_2$  absorber with a gas flow rate of 260 ml/min pure  $\text{SO}_2$ .

To determine the validity of the kinetic measurements, the following calibration procedure was performed both before and after each run:

1. An Ar- $\text{SO}_2$  gas mixture with a gas flow rate and composition close to that of the expected off-gas (assuming 100 % oxygen utilization), was admitted for a period of 10 min.

2. A sample was obtained and the amount of SO<sub>2</sub> absorbed was determined by titration and compared to the admitted amount.
3. The final off-gas flow rate was measured by the soap bubble meter and compared to the above results.
4. The final off-gas was tested by smell to detect any residual SO<sub>2</sub>.
5. If the above results were found to be consistent and the absorber efficiency was found to be very close to 100 %, the results of the respective run were accepted<sup>12</sup>.

#### 4.1.3.2. Final Off-Gas Flow Rate Measurement

In order to determine the final off-gas flow rate accurately, an appropriate size of the soap bubble meter was selected, for the given reaction conditions. Using a stop watch, the time that a soap bubble takes to travel over a certain height of the graduated cylinder was determined. To determine the gas flow rate, the volume was divided by the measured time.

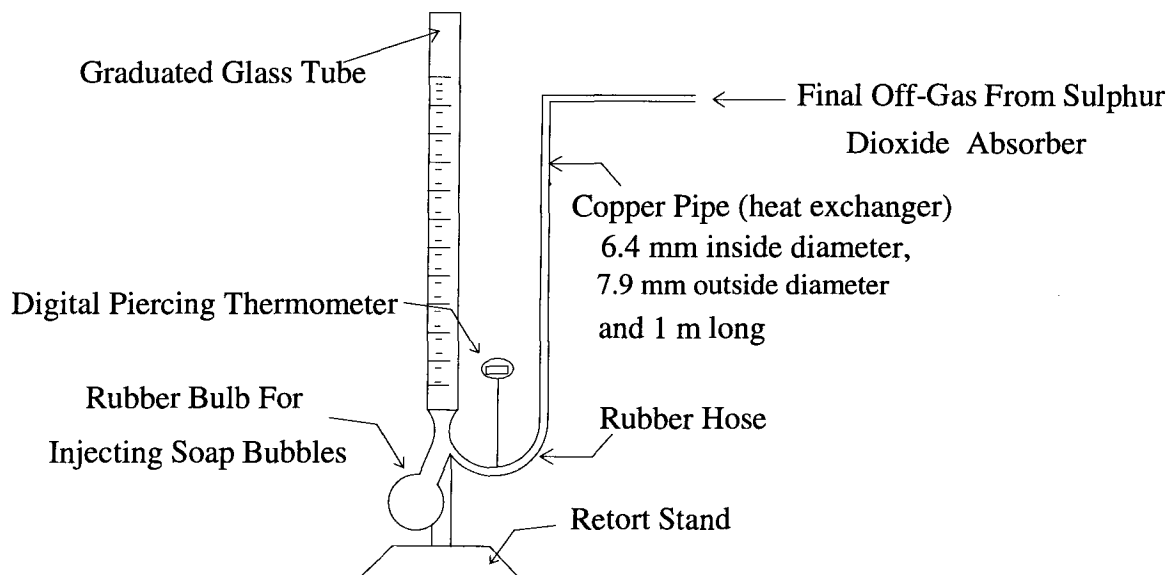


Figure 4.10. Schematic diagram of the soap bubble meter.

<sup>12</sup>Due to the low percentage of rejection, approximately 3% for the entire program, the SO<sub>2</sub> absorber was considered to be very effective.



To ensure accurate measurements, graduated tubes that resulted in relatively low bubble velocities, of approximately 20-50 mm/sec, were used. Depending on the expected final off-gas flow rate, the size of the soap bubble meter was selected. For final off-gas flow rates of  $\geq 2$  l/min, a 500-ml graduated tube was selected and for the measurement of final off-gas flow rates of  $< 2$  l/min, a 250-ml graduated tube was used.

#### 4.1.4. Gravimetric Measurement System

In order to obtain automatic measurement of the bath weight, a gravimetric measurement system, consisting of weighing and recording devices, was custom assembled from a load cell and a data acquisition system.

The load cell consisted of a cantilever beam that was made of a  $3 \times 19 \times 120$  mm steel bar, four temperature compensated strain gauges and strain gauge signal conditioner, assembled as shown below.

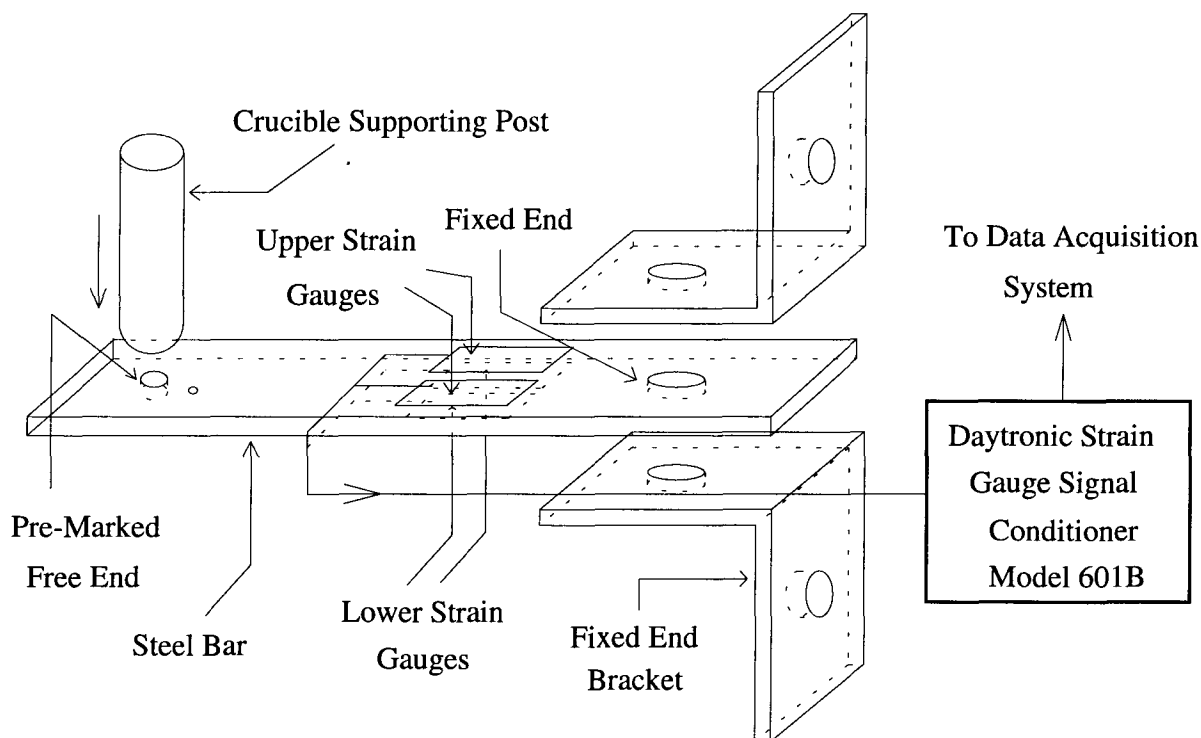


Figure 4.11. Schematic diagram of the load cell<sup>13</sup>.

<sup>13</sup>For more details about the electric circuit and the components of the load cell, refer to Appendix A.

The data acquisition system was comprised of a 286 IBM PC equipped with CIO-AD08 data acquisition board with a total of 32 channels, data acquisition program and a spreadsheet program.

The crucible supporting post was placed on the pre-marked free end of the cantilever beam, as shown in Figure 4.11. The fixed end of the cantilever beam was attached to the support frame by means of the fixed end brackets such that the beam could swing to the side to permit removal of the crucible at the end of a run.

As mentioned earlier, the gravimetric measurement was found to be less reliable than the manual gas analysis to characterize the reaction rate. This is due to the fact that when placing the alumina post on the load cell, it was difficult to determine whether it was completely free<sup>14</sup>. It was only after 10 minutes of the reaction time that the visual display of the gravimetric measurement on the PC screen, indicated if the measurement was successful. The gravimetric measurement, therefore, was used only as a general check on the validity of the results of the manual gas analysis. The rate of bath weight change was exclusively used in comparing the gas analysis results to the gravimetric measurement results. The overall rate of bath weight change was obtained by performing linear regression of the bath weight with time. Statistically, the validity of this regression was dependent on the number of data collected over relatively long periods of time. This was often possible during the secondary stage only. In most of the runs, during the primary stage, it was not possible to obtain reliable results.

---

<sup>14</sup>Success of the measurements was contingent upon the crucible being concentric with respect to the reaction tube. On occasion, however this was difficult to accomplish because of the nature of the crucible supporting post. Due to manufacturing defects, the alumina tubes, used in making the crucible supporting posts were often warped at the bottom (in the vicinity of the bottom of the reaction tube). Because the gravimetric measurement system was added to the apparatus at a later stage of the experimental program, it was not possible to modify some key components of the apparatus to eliminate all of the problems associated with the gravimetric measurement system. For a newly designed apparatus, however, the elimination of these problems can be achieved.

Standard weights were used in the calibration of the load cell before and after each run. An average equation for the relationship of the weight and the load cell reading was obtained to convert the load cell response to weight measurement. As the relationship between the weight and load cell reading is linear, as shown by Figure 4.12, a typical equation for the best line can be calculated as follows:

$$W = 87 + 82R_s \quad (4.4)$$

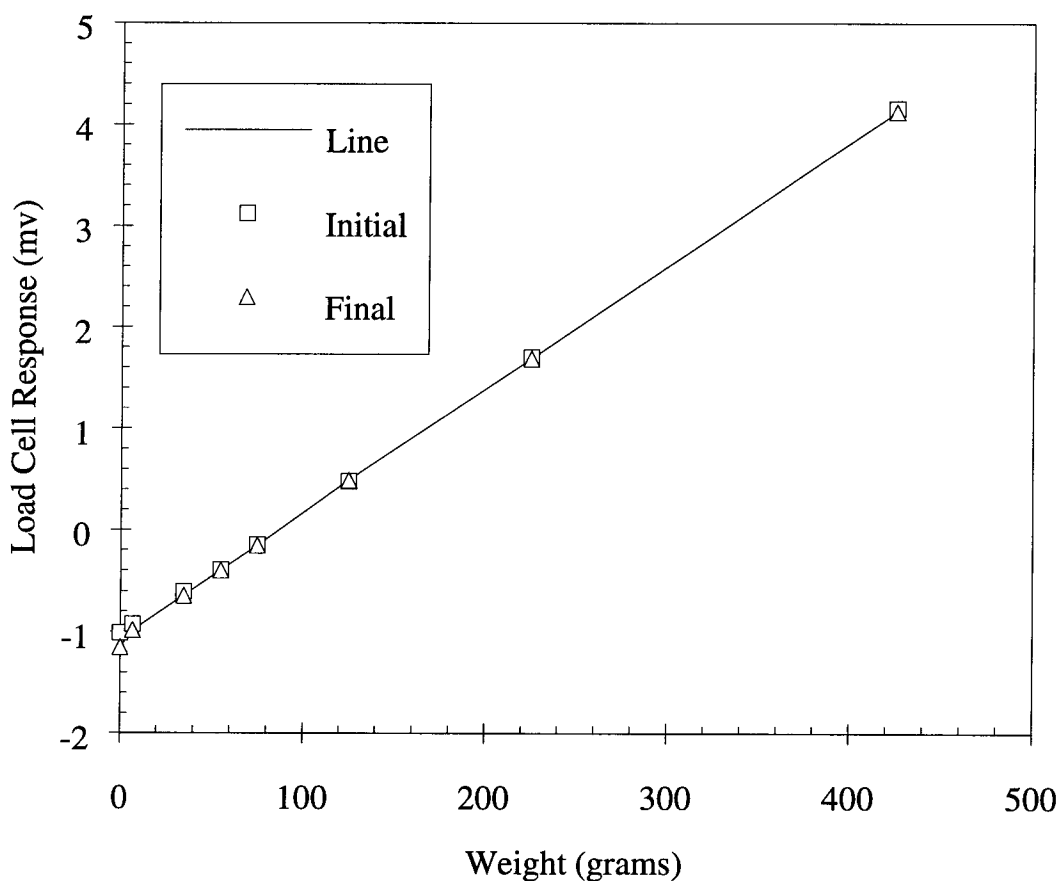


Figure 4.12. Load cell calibration plot obtained with standard weights.

The load cell response, during the reaction time, was recorded by the data acquisition system and stored in a spreadsheet. The millivolt readings were converted by the calibration equation of the respective run.

Constant load cell reading for a period of time or permanently until the end of a run was observed to take place during some experiments. This indicated that due to some mechanical interference in the weighing system, the load cell was not measuring the full weight. Then depending on how long this interference took place, the measurement was either completely discarded or the straight line segments were used to calculate an average value for the rate of weight change. Due to the stabilization process that the system undergoes, as a result of the internal pressure change<sup>15</sup> at the beginning of the reaction, the measurements that were obtained during the first minute were discarded. For the secondary stage, reading for at least 10 minutes was taken as a valid measurement. To determine the validity of the measurement and its time domain the sample weight was plotted against time and examined visually. Using the least squares method [105], linear equations for weight as a function of time, were calculated for the linear portions of the measurement. To determine the rate of weight change, the equations were differentiated with respect to time as follows:

$$\dot{W} = \frac{dW}{dt} = \frac{d}{dt}[a + bt] = b \quad (4.5)$$

#### 4.1.5. Optical Photography System

In optimizing the furnace parameters, the volume of the reaction tube was kept to a minimum in order to minimize the gas measurement time lag. This resulted in relatively small view ports, of approximately 20 mm in diameter. In order to photograph the melt surface, of approximately 44 mm, the need to design a specific optical system was inevitable. The variable focal length optical system consisted of a 45° mirror to reflect the image horizontally, a focusing macro-lens and a magnifying eyepiece, as shown in

---

<sup>15</sup>As a result of passing the off-gas through the SO<sub>2</sub> absorber, the pressure head of the solution of the absorber increased the internal pressure of the reactor in a non-steady state manner at the beginning of the reaction.

Figure 4.13. This system of lenses was installed on a 35 mm camera with the use of a bellows.

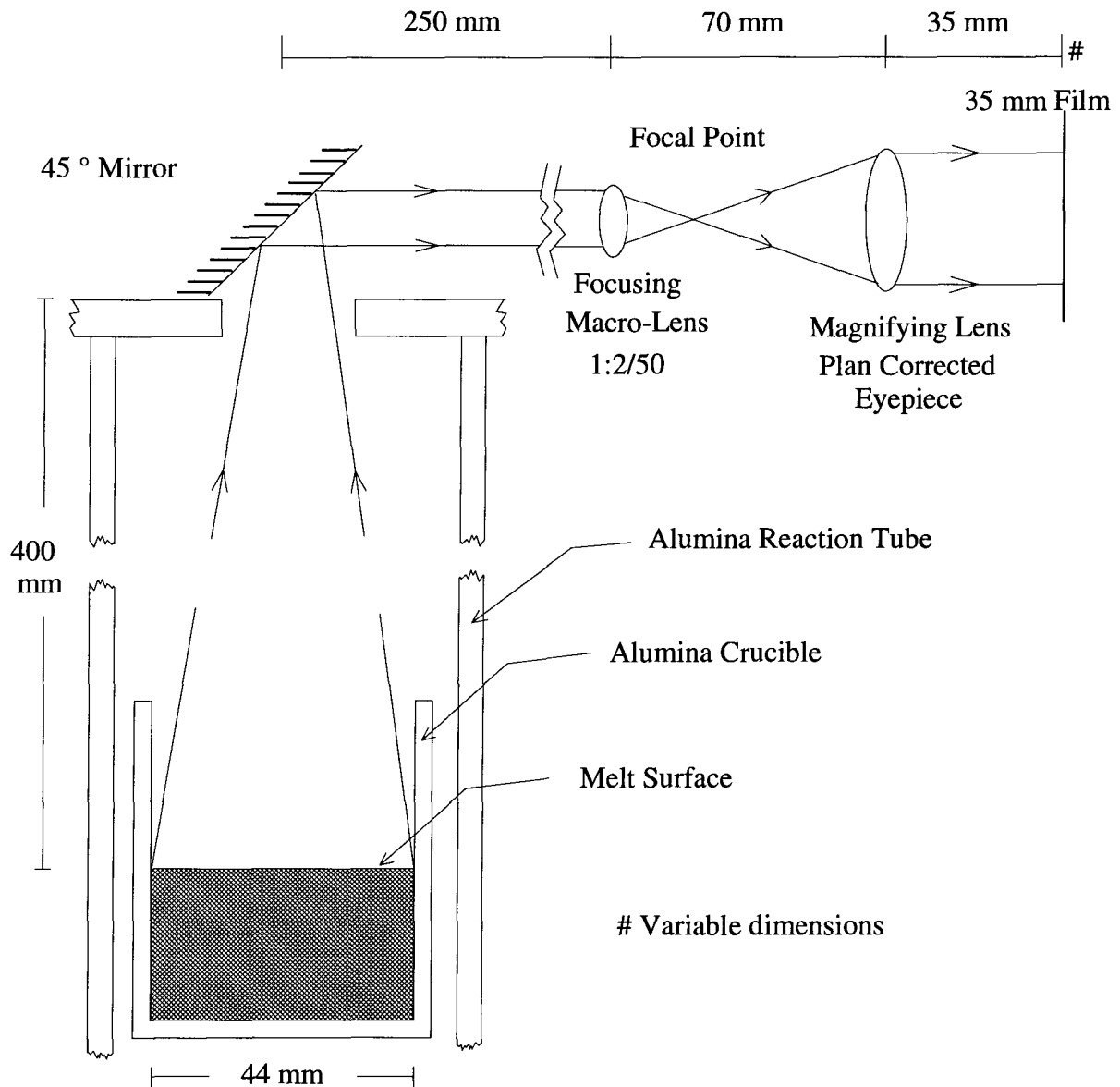


Figure 4.13. Schematic diagram of the optical system used in the photography of the melt surface. The lenses were mounted and enclosed within a system of bellows.

## 4.2. Material

### 4.2.1. Copper Sulphide

#### 4.2.1.1. Supplied Copper Sulphide

Approximately 99.5% copper sulphide, monoclinic  $\text{Cu}_2\text{S}$  (-200 mesh) supplied and certified by Cerac Inc. was used for all of the runs except for the first 5 runs. The chemical analysis given in Table 4.1 indicated that the impurities are negligible in quantity.

Table 4.1. Trace analysis (wt%) of supplied copper sulphide.

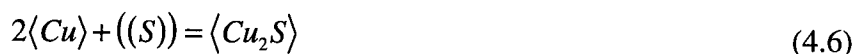
Ag	< 0.01
Al	< 0.01
Ca	< 0.01
Cr	< 0.01
Fe	< 0.01
Mg	< 0.01
Mn	< 0.01
Ni	< 0.01
Pb	< 0.01
Si	< 0.01
Sn	< 0.01
Ti	< 0.01
Zr	< 0.01

#### 4.2.1.2. Prepared Copper Sulphide

For the preliminary runs (the first 5 runs), prepared  $\text{Cu}_2\text{S}$  was made of 99.9 % pure copper powder and laboratory reagent grade elemental sulphur. Approximately 1590 grams of copper were well mixed with approximately 410 grams of sulphur<sup>16</sup> in a graphite-clay crucible. The crucible was then placed in a larger graphite crucible, to

<sup>16</sup>In order to compensate for the loss of sulphur during the  $\text{Cu}_2\text{S}$  reaction, approximately 2 % excess sulphur was used.

avoid damaging the furnace material in case of spillage. The crucible was then covered with a graphite lid and placed in a preheated muffle furnace, at approximately 400°C, for approximately 3.5 hours. To minimize sulphur evaporation prior to its reaction with copper, the reaction was allowed to take place at a temperature of 50 °C below the boiling point of elemental sulphur, according to Reaction (4.6). To prevent excessive reaction of oxygen with the copper sulphide, argon gas at a flow rate of approximately 200 ml/min was passed through the furnace.



In order to homogenize the copper sulphide by melting according to Reaction (4.7), the crucible was then placed in another preheated muffle furnace, at approximately 1200 °C, with argon atmosphere, for approximately thirty minutes. The crucible was then carefully removed from the furnace and placed on a steel plate, to slow cool. The copper sulphide ingot then was removed from the crucible and crushed into small granules, for use. However, due to the difficulties in reparing the same composition and the cost of chemical analysis, the use of prepared copper sulphide was terminated.



#### 4.2.2. Gases

Ar-O<sub>2</sub> mixtures were used for most of the runs, except for a run to investigate the effect of reaction gas carrier type, where a N<sub>2</sub>-O<sub>2</sub> mixture was utilized. Ar-SO<sub>2</sub> gas mixtures were employed for the calibration of the gas analysis system. The impurity specifications of these gases are as given in Table 4.2. In order to reduce the moisture content of the gases, they were passed through silica gel and CaSO<sub>4</sub> columns before being admitted into the reaction tube, as shown in Figure 4.4.

Table 4.2. Impurity specifications of gases in ppm.

Gas	Minimum Purity	N <sub>2</sub>	O <sub>2</sub>	H <sub>2</sub> O	CO <sub>2</sub>	THC	Kr	Ar
O <sub>2</sub> (U H P)	99.995%	< 40		< 5	< 1	< 1	< 15	< 15
N <sub>2</sub> (U H P)	99.999%		< 5	< 5	< 1	< 1		< 25
Ar (Pre-purified)	99.998%		< 3	< 5				
SO <sub>2</sub> (Anhydrous)	99.98%							

#### 4.2.3. Hydrogen Peroxide Solution

To prepare approximately 5% H<sub>2</sub>O<sub>2</sub> solution for the absorption of SO<sub>2</sub>, approximately 2500 ml of de-ionized water was added to 500 ml of 30% H<sub>2</sub>O<sub>2</sub> solution, for which the chemical analysis is given in the Table 4.3. Due to their insignificant concentrations in the supplied hydrogen peroxide solution, the impurities were ignored in the determination of the amount of SO<sub>2</sub> absorbed.

Table 4.3. Maximum limits of impurities for the 29.0-32.0 % hydrogen peroxide solution (supplied by BDH).

Impurity	Maximum Concentration
Residue after evaporation	0.002 %
Titratable acid	0.006 meq/g
Chloride (Cl)	3 ppm
Nitrate (NO <sub>3</sub> )	2 ppm
Phosphate (PO <sub>4</sub> )	2 ppm
Sulphate (SO <sub>4</sub> )	5 ppm
Ammonium (NH <sub>4</sub> )	5 ppm
Heavy metals (Pb)	1 ppm
Iron (Fe)	0.5 ppm



#### 4.2.4. Titration Reagents

Approximately 0.1 N NaOH standard solution was used in the acid-base titration of the samples obtained from the gas absorber. The NaOH standard solution was prepared by dissolving pre-weighed amounts of reagent grade solid sodium hydroxide in de-ionized water and storing it in plastic bottles. The NaOH solution was then standardized by potassium hydrogen phthalate ( $\text{KHC}_8\text{H}_4\text{O}_4$ ) [106] and labeled for use. The chemical analysis given in Table 4.4 indicated that after standardizing the prepared solution, the effect of impurities in the solid hydroxide can be ignored.

Table 4.4. Maximum limits of impurities for the 98.0 % sodium hydroxide pellets (supplied by BDH).

Impurity	Maximum Concentration (%)
Water insoluble matter	0.01
Carbonate ( $\text{Na}_2\text{CO}_3$ )	1.0
Chloride (Cl)	0.005
Phosphate ( $\text{PO}_4$ )	0.001
Silicate ( $\text{SiO}_2$ )	0.01
Sulphate ( $\text{SO}_4$ )	0.005
Aluminum (Al)	0.001
Calcium (Ca)	0.002
Copper (Cu)	0.0005
Iron (Fe)	0.0005
Lead (Pb)	0.0005
Nickel (Ni)	0.0005
Potassium (K)	0.05
Nitrogen Compounds (N)	0.0005

Approximately 0.1 % phenolphthalein was used as an indicator for the acid-base titration. The indicator was prepared by dissolving the solid in 80 % ethyl alcohol [106].

All glassware was cleaned with the use of laboratory glassware cleaning solution and soap. The cleaning solution was prepared by mixing 10-15 grams of potassium dichromate ( $K_2Cr_2O_7$ ) with about 15 ml water, in a 500 ml heat resistant conical flask. Enough concentrated sulphuric acid was added slowly, until all of the forming solid was dissolved. The solution was discarded when it acquired a green color [108].

### **4.3. Experimental Procedure**

#### **4.3.1. Oxidation Rate Measurement**

To measure the rate of oxidation of the molten copper sulphide bath, the following steps were followed :

1. Before each run, a complete leak test was performed on all of the couplings, polyflow fittings and valves. Leak tests were performed by pressurizing the system and testing for leaks by the use of bubbling soap. The gas supplies were also checked to ensure sufficient supply for the run.
2. Approximately 200 grams of the solid  $Cu_2S$  were weighed in an alumina crucible. The crucible was then carefully placed at the bottom of the reaction tube, on the alumina supporting post. The bottom of the post was placed on a laboratory jack, which was used to push up the post until the crucible was located at a pre-defined position, in the hot zone. To avoid thermal shock, the crucible was pushed at a rate of approximately 10 mm/min. During the preheating and melting of the sulphide sample, approximately 50 ml/min of argon was introduced through the preheating tube.
3. During the melting of the sulphide sample, the load cell and gas absorber were calibrated, and the data acquisition system was activated.

4. After the calibration of the load cell, the jack was removed and the alumina post was carefully placed on the marked end of the load cell as shown in Figures 4.1 and 4.11.
5. After ensuring that the sample was completely molten, by surface observation and from the temperature, the reaction gas flow rate and composition were adjusted to the desired levels, and the thermocouple was lifted from the bath to the vicinity of the lance nozzle<sup>17</sup>. The reaction gas was then admitted to the reaction tube, through the lance, and the data collection proceeded immediately.
6. The data collection was done via two independent sources: the gas analysis for SO<sub>2</sub> and O<sub>2</sub>, and the gravimetric measurement of the bath weight.
7. Due to the corrosive nature of copper oxide, the reaction was terminated just before Cu<sub>2</sub>O began to form. As the oxidation reaction of molten copper sulphide ended, the spontaneous motion of the surface was observed to cease.
8. The final calibration of the gas absorber and the load cell were carried out.
9. The temperature of the system was recorded throughout the run by the data acquisition system and stored in a spread sheet. Using the mercury manometer, the pressure of the system was monitored periodically throughout the run and an average value was recorded.
10. The load cell was released and swung to the side for removal of the crucible.
11. The crucible supporting post was then placed on the laboratory jack. The jack was then lowered at the rate of approximately 10 mm/min. This was

---

<sup>17</sup>Due to the intensity of the oxidation reaction, corrosion of the thermocouple sheath and the platinum thermocouple was found to take place if the same thermocouple sheath was used in more than one run, with its tip immersed in the melt.

important to avoid the rapid release of the heat of fusion, which started at approximately mid-distance from the bottom of the reaction tube.

12. The crucible was removed after it reached the bottom of the reaction tube. Once the temperature of the crucible reached room temperature, its weight was determined and recorded.
13. All of the glassware was washed and prepared for the next run.

#### 4.3.1.1. Gas Analysis

In order to determine the amount of sulphur removed from the bath as a function of time, samples were extracted from the gas absorber, at pre-defined time intervals, with a 5-ml pipet. The samples were stored in pre-labeled 250-ml conical flasks, until the end of the run. Due to the exothermic nature of the absorption reaction, the temperature of the solution was observed to increase at a constant rate. This was used as another indicator of the efficiency of the absorber in a particular run. For each sample obtained, the temperature of the absorption solution was recorded. The amount of sulphur dioxide absorbed was determined by the acid-base titration of the individual samples, using 0.1 N NaOH standard solution [107]. Since the molar ratio of sulphur to sulphur dioxide is unity, the number of moles of sulphur removed from the bath is the same as the moles of sulphur dioxide absorbed.

To determine the amount of unreacted oxygen in the off-gas, the soap bubble meter was used to measure the off-gas flow rate. For each absorber sample obtained, at least four volumetric flow rate measurements were made. Due to the increase of the temperature of the absorption solution, the temperature of the gas was expected to deviate from room temperature, as it left the absorber. In order to avoid temperature effects, the temperature of the gas inside the rubber hose, leading to the soap bubble meter, was recorded for each set of measurements.

#### 4.3.1.2. Gravimetric Measurement

This measurement was used to verify and support the gas analysis measurement. The reaction system weight was performed automatically, using the data acquisition system. The numerical load cell response was converted to weight using the calibration equation.

#### **4.3.2. Microscopic Examination of Frozen Melt Samples**

For further validation of the kinetic measurements, melt samples of known reaction were obtained and microscopically examined. U-shaped quartz tubes with an approximate inside diameter of 5 mm were used to obtain approximately 4- 7-gram samples at specific intervals of reaction time. To minimize post sampling reaction, the samples were immediately quenched in an ice bath. The samples were sectioned, hot-mounted and polished using 5  $\mu\text{m}$  and 1  $\mu\text{m}$  alumina polishing powder. The samples were then examined with an optical microscope to assess copper droplets, gas bubbles and the phases present.

#### **4.3.3. Surface Observation**

Surface observations were primarily undertaken to investigate the effect of surface-tension driven flows on the reaction kinetics. The observations included the qualitative measurement of surface movement, gas bubbles rising from the melt and surface velocity, under different reaction conditions. The surface observations also served as an indication of the state of reaction and its termination. Using a 35-mm camera and the optical system presented above, some runs were conducted to obtain photographic evidence of the visual observations. Photographs were taken of the melt surface under specific reaction conditions.

## 5. Experimental Results and Discussion

### 5.1. Oxidation Rate Results

#### 5.1.1. Gas Analysis Data

##### 5.1.1.1. Sulphur and Sulphur Dioxide Analyses

The gas flows, which were characterized to determine the oxidation kinetics of molten  $\text{Cu}_2\text{S}$ , are shown schematically in Figure 5.1. Typical results of the gas analysis, for each run, are plotted against time, in Figures 5.2-5.3. Because all of the  $\text{SO}_2$  is absorbed by the  $\text{H}_2\text{O}_2$  solution, the moles of sulphur in the bath,  $N_s(t)$ , can be calculated from the moles of  $\text{SO}_2$ ,  $N_{\text{SO}_2}(t)$ , absorbed as follows:

$$N_s(t) = N_s^i - N_{\text{SO}_2}(t) \quad (5.1)$$

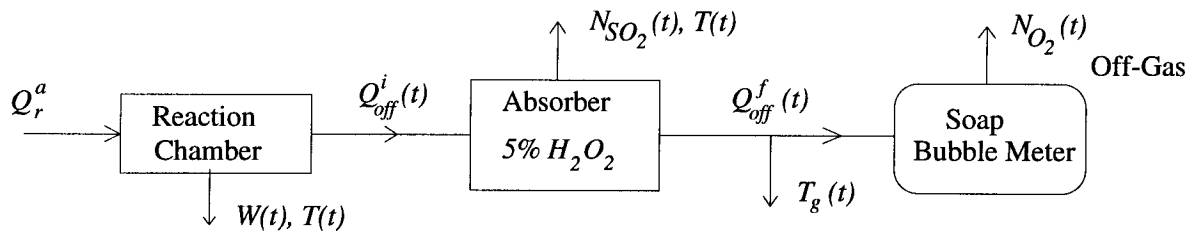


Figure 5.1. Gas flows in the oxidation experiments.

Figure 5.2 reveals that there are two distinct stages, primary and secondary, for the formation of  $\text{SO}_2$ . In order to determine the rates of  $\text{SO}_2$  formation and the time domains of the two stages, the following analysis was carried out:

1. The time domains of the two stages were determined, as a first approximation, by visualization of the  $\text{SO}_2$  vs. time graphs.
2. Since the time dependence of the two stages appears to be linear, a linear equation for each stage was calculated, via regression analysis; and the transition time was calculated by equating the two equations. If the calculated transition time was found to be within the time domain of the adjacent two

measured points, the equations were accepted. If the calculated transition time was found to be closer to another measured value, the linear equations were recalculated, based on the new designated values. This procedure was iterated until the best agreement between the measured and calculated values was achieved. Once the equations were accepted, the slopes of the equations were regarded as the measured  $\text{SO}_2$  molar rates.

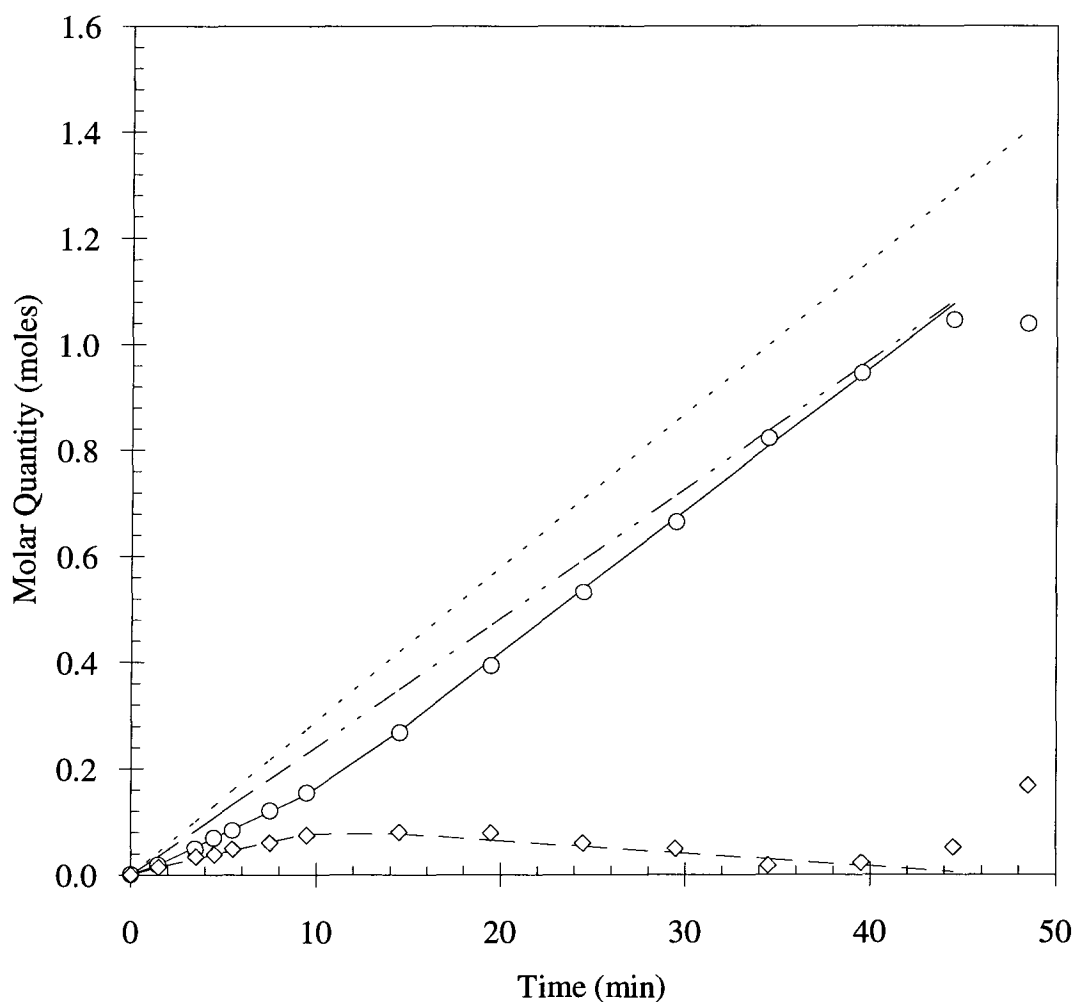


Figure 5.2. Moles of reaction gas and off-gas as a function of time, for the experimental conditions of: 200 grams of  $\text{Cu}_2\text{S}$ , 2 l/min of 35%  $\text{O}_2$  and 65% Ar, at 1200 °C; ——— regression line for the absorbed  $\text{SO}_2$ ; ○ measured absorbed  $\text{SO}_2$ ; - - - regression line for the dissolved  $\text{O}_2$ ; ◇ dissolved oxygen by difference; - · - · - reacted oxygen; · · · · · admitted  $\text{O}_2$ .

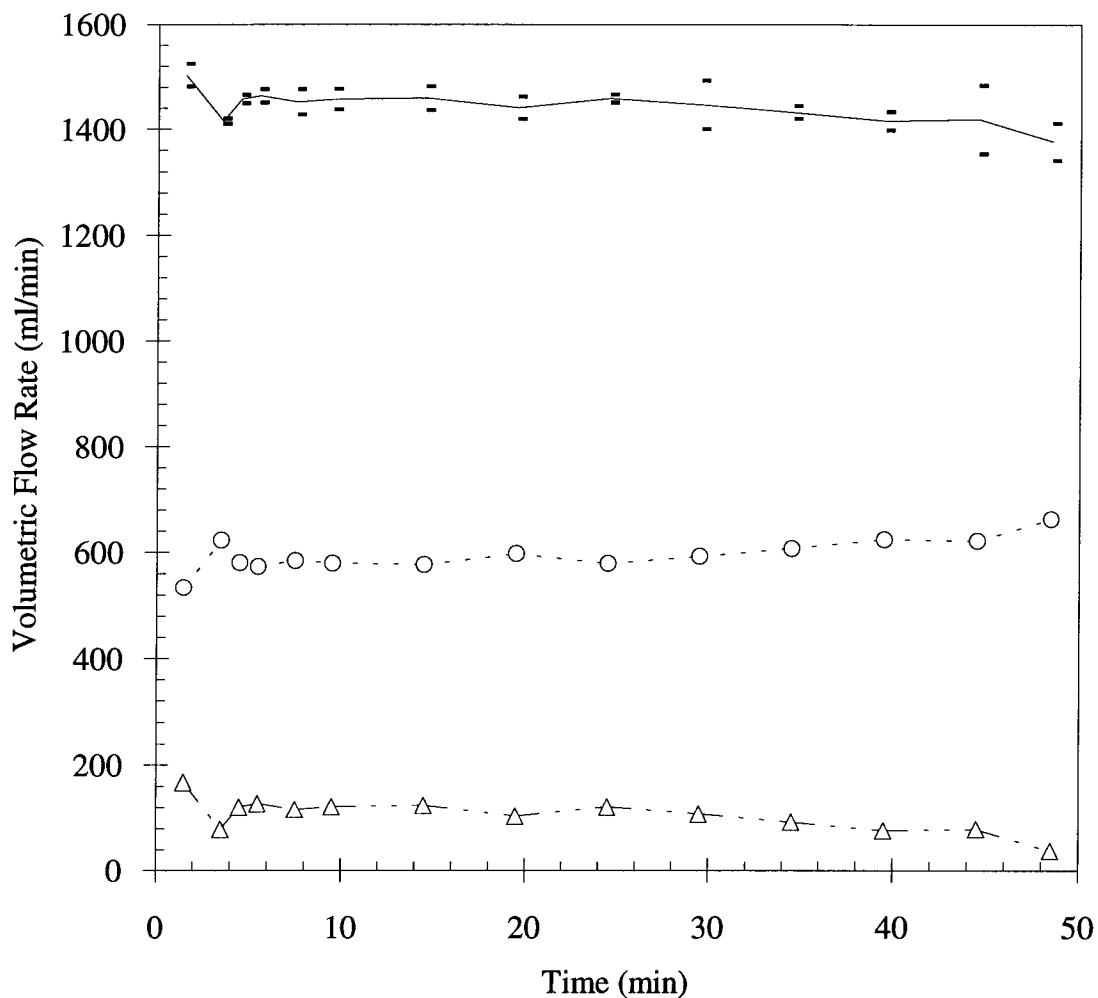


Figure 5.3. The final volumetric off-gas flow rate as a function of time for the experimental conditions of : 200 grams of  $\text{Cu}_2\text{S}$ , 2 l/min of 35%  $\text{O}_2$  and 65% Ar, at 1200  $^\circ\text{C}$ ; — measured final flow rate; - -  $\circ$  - - reacted oxygen flow rate; -  $\Delta$  - unreacted oxygen flow rate.

Assuming that the reaction takes place uniformly over the melt surface area, the  $\text{SO}_2$  molar fluxes were calculated by dividing the  $\text{SO}_2$  molar rates by the crucible cross-sectional area, as follows:

$$\dot{n}_{\text{SO}_2} = \frac{\dot{N}_{\text{SO}_2}}{A} \quad (5.2)$$



### 5.1.1.2. Oxygen Analysis

The amount of oxygen dissolved in the bath as a function of time was determined from the measured SO<sub>2</sub> and the final off-gas flow rate measurement by the following procedure.

The admitted volumetric gas flow rate,  $Q_r^a$ , was composed of argon,  $Q_{Ar}$ , and oxygen,  $Q_{O_2}^a$ , as follows:

$$Q_r^a = Q_{O_2}^a + Q_{Ar} \quad (5.3)$$

The volumetric off-gas flow rate,  $Q_{off}^i(t)$ , varies with time, with an unknown quantity of SO<sub>2</sub>,  $Q_{SO_2}(t)$ , unreacted O<sub>2</sub>,  $Q_{O_2}^u(t)$ , and Ar, as described by the following equation.

$$Q_{off}^i(t) = Q_{Ar} + Q_{O_2}^u(t) + Q_{SO_2}(t) \quad (5.4)$$

After the SO<sub>2</sub>, the volumetric off-gas flow rate,  $Q_{off}^f(t)$ , also varies with time, with an unknown quantity of unreacted O<sub>2</sub> and Ar, as described by the following equation.

$$Q_{off}^f(t) = Q_{Ar} + Q_{O_2}^u(t) \quad (5.5)$$

Having defined the volumetric flow rate equations, the calculation of the volumetric flow rate of unreacted oxygen can be readily carried out. Since the gas temperature was not constant, this calculation was based on molar flow rates rather than volumetric flow rates. Assuming that the gas mixture is ideal, the final volumetric gas flow rate can be converted to molar flow rate as follows<sup>18</sup>:

$$\dot{N}_{off}^f(t) = \frac{Q_{off}^f(t)P}{RT_g(t)} \quad (5.6)$$

Therefore the unreacted molar flow rate of oxygen can be determined from Equation (5.7).

---

<sup>18</sup>Note that the molar flow rate of Ar,  $\dot{N}_{Ar}$ , is calculated from the rotameter reading (volumetric flow rate) which was calibrated at room temperature. There may be a difference between the temperature of the measurement of the final off-gas flow rate and the rotameter calibration temperature.

$$\dot{N}_{O_2}^u(t) = \dot{N}_{off}^f(t) - \dot{N}_{Ar} \quad (5.7)$$

The molar flow rate of unreacted oxygen is converted to volumetric flow rate as follows:

$$Q_{O_2}^u(t) = \frac{\dot{N}_{O_2}^u(t)RT_g(t)}{P} \quad (5.8)$$

A molar balance on the oxygen yields the following.

$$Q_{O_2}^r(t) = Q_{O_2}^a - Q_{O_2}^u(t) \quad (5.9)$$

To determine the molar rate of reacted oxygen, the volumetric flow rate of oxygen is converted to molar rate, according to the following equation.

$$\dot{N}_{O_2}^r(t) = \frac{Q_{O_2}^r(t)P}{RT_g(t)} \quad (5.10)$$

This molar flow rate of reacted oxygen is calculated from the measured final off-gas flow rate, for specific intervals of reaction time. The integrated measured molar flow rate of reacted oxygen is described as follows:

$$N_{O_2}^r(t) = N_{O_2}^r(t_1) + \int_{t_1}^{t_2} \dot{N}_{O_2}^r(t_{1-2}) dt \quad (5.11)$$

To determine the molar flux of reacted oxygen, linear regression was applied to the data obtained from Equation (5.11). The molar rate of reacted oxygen was found to be constant throughout the reaction duration, as shown in Figures 5.2-5.3. Hence for simplicity, the function of time notation, (t), is dropped. The oxygen molar flux was calculated by dividing the calculated molar flow rate of reacted oxygen by the cross-sectional area of the crucible ( for notational simplicity, from this point on, the superscript r is dropped), as follows:

$$\dot{n}_{O_2} = \frac{\dot{N}_{O_2}}{A} \quad (5.12)$$

Since the oxygen reacted must be removed in the form of SO<sub>2</sub> or dissolved in the bath, the oxygen dissolved in the bath can be determined by a material balance on the oxygen as follows:

$$N_{[O]}(t) = 2[N_{O_2}^r(t) - N_{SO_2}(t)] \quad (5.13)$$

Assuming plug flow conditions, the real time in the reaction was calculated by subtracting the time needed for a given flow rate of gas to travel the distance from the reaction surface to the gas absorber ( the volume of the off-gas line was approximately 1 liter and the employed range of volumetric flow rate was 1-4 l/min which resulted in a time lag of 15-60 s).

In order to study the reaction kinetics, the measured sulphur and oxygen contents in the bath were plotted on graphs such as that of Figure 5.4. Comparing the closeness of the measured values to the regression lines, the sulphur analysis exhibits less scatter than the oxygen analysis. From Figure 5.4, the sulphur and oxygen contents in the bath vary linearly with respect to time. Thus the rate at which the sulphur is removed from the bath is constant, but different in the two regimes. Similarly, the respective rate of oxygen dissolution in the bath is also constant over the primary and secondary stages. In trying to understand the reaction mechanism, the oxygen behaviour is obviously the first clue. As shown in Figure 5.4, the amount of dissolved oxygen increases linearly to a certain value at the transition time, and then decreases to a minimum value, at the final reaction time.

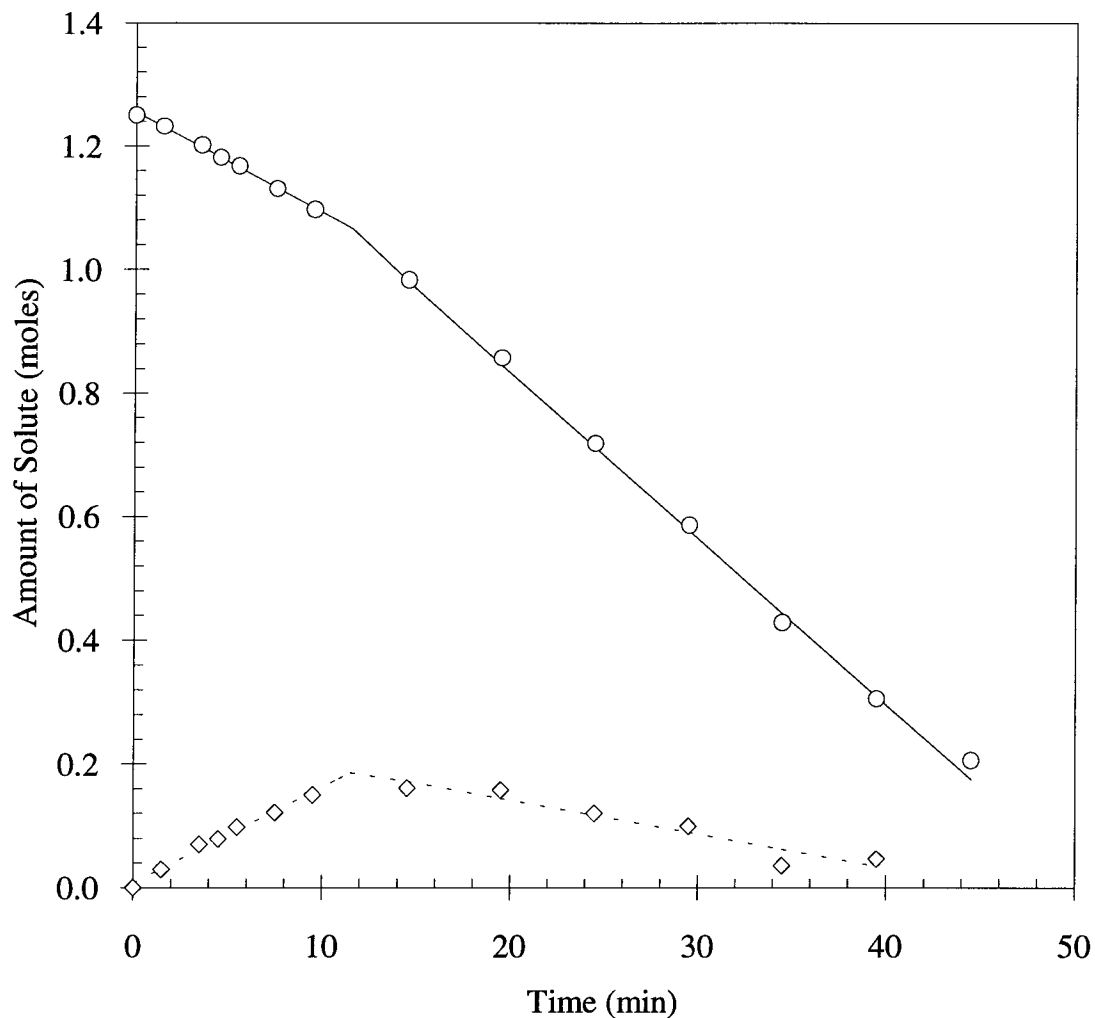


Figure 5.4. The molar sulphur and oxygen contents of the bath as a function of time, for the experimental conditions of: 200 grams of  $\text{Cu}_2\text{S}$ , 2 l/min of 35%  $\text{O}_2$  and 65% Ar, at 1200 °C; — regression line for the amount of sulphur in the bath;  $\circ$  measured amount of sulphur in the bath; - - - regression line for the amount of dissolved oxygen in the bath;  $\diamond$  determined amount of dissolved oxygen.

#### 5.1.1.3. Overall Reaction Rate

Further analysis of the reaction kinetic data can be accomplished by examining the bath weight change with respect to time. The rate of weight change of the bath,  $\dot{W}$ , can be related to the rate of sulphur dioxide evolved from the bath,  $\dot{N}_{\text{SO}_2}$ , and the rate of oxygen reacted,  $\dot{N}_{\text{O}_2}$ , as follows:

$$\dot{W} = \dot{N}_{O_2} M_{O_2} - \dot{N}_{SO_2} M_{SO_2} \quad (5.14)$$

In order to study the oxygen and sulphur behaviour simultaneously, the bath weight was plotted for each run in graphs typical of that shown in Figure 5.5.

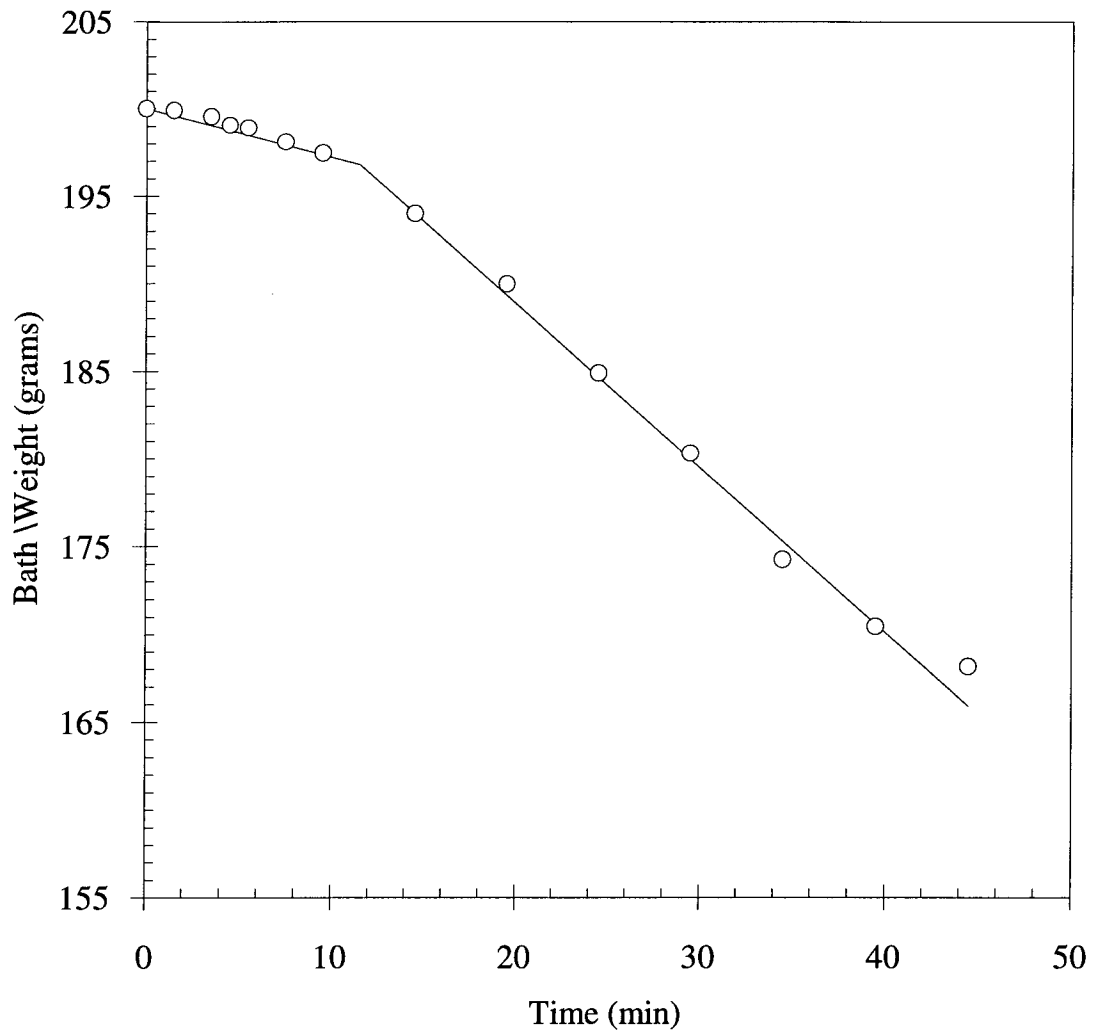


Figure 5.5. Change of bath weight with time for the experimental conditions of: 200 grams of  $Cu_2S$ , 2 l/min of 35%  $O_2$  and 65% Ar, at 1200 °C; — calculated from Equations (5.15) and (5.16); ○ calculated from Equation (5.17).

The sample weight was calculated by integrating the rate of weight change with respect to time, as given by Equations (5.15) and (5.16) by using the determined amounts of oxygen and sulphur as given by Equation (5.17)<sup>19</sup>.

$$W_{ga}^p(t) = W_{ga}(0) + \left[ \dot{N}_{O_2}^p M_{O_2} - \dot{N}_{SO_2}^p M_{SO_2} \right] \cdot t \quad (5.15)$$

$$W_{ga}^s(t) = W_{ga}(t^*) + \left[ \dot{N}_{O_2}^s M_{O_2} - \dot{N}_{SO_2}^s M_{SO_2} \right] \cdot (t - t^*) \quad (5.16)$$

$$W_{ga}(t) = W(0) + \left[ N_{O_2}(t) M_{O_2} - N_{SO_2}(t) M_{SO_2} \right] \quad (5.17)$$

### 5.1.2. Gravimetric Measurement Data

The sample weight measurement, determined gravimetrically with the load cell arrangement, was plotted against time for each successful experiment, an example of which is shown in Figure 5.6. Applying the least squares method, the rate of weight loss in the two stages and the reaction transition time were determined. The reaction transition time is the time at which the rate of sulphur dioxide formation changes. In the gravimetric measurement, the reaction transition time is the time at which the rate of weight loss changes.

---

<sup>19</sup>Note that Equations (5.15) and (5.16) describe the regression lines obtained from the measured results and Equation (5.17) represent the individual measured data points.

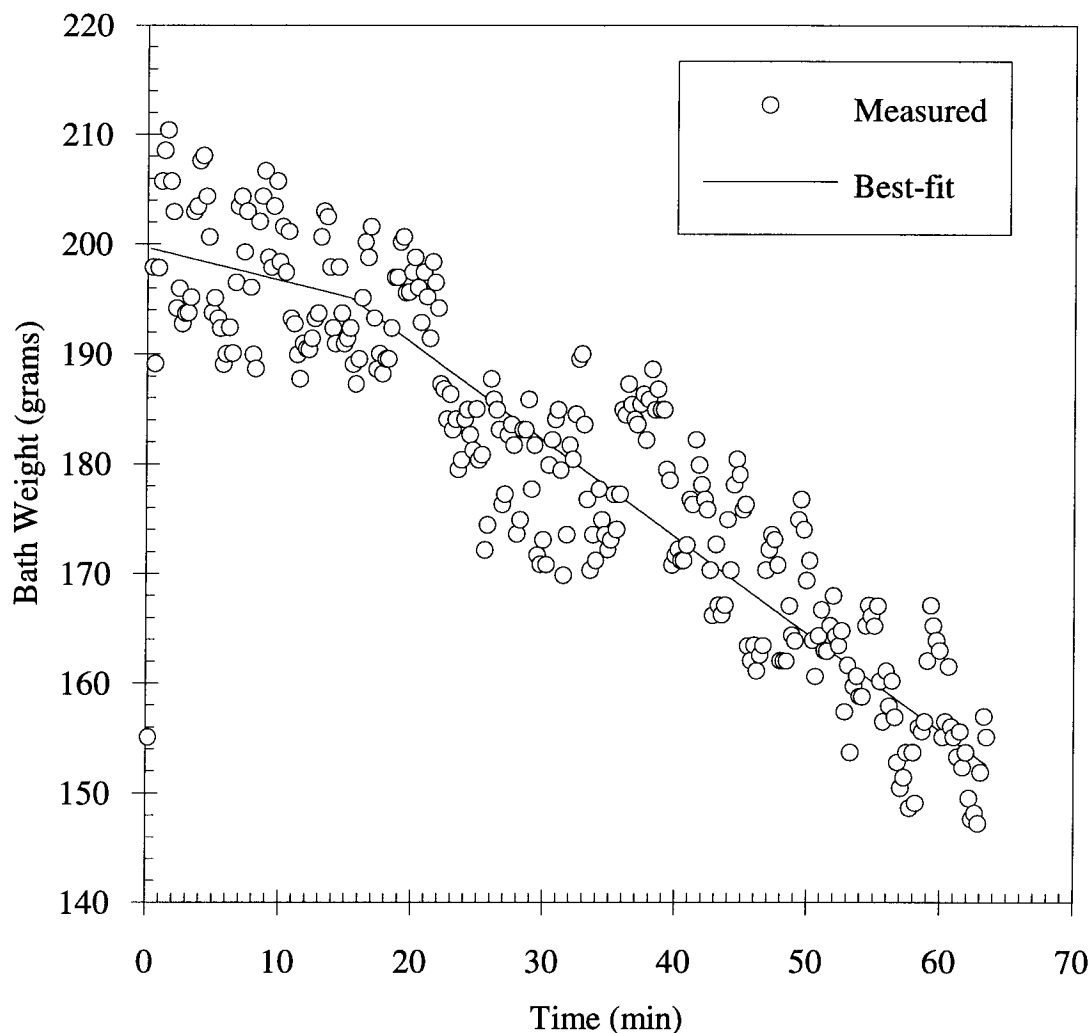


Figure 5.6. Gravimetric plot of bath weight against time for the experimental conditions of : 200 grams of  $\text{Cu}_2\text{S}$ , 2 l/min of 22%  $\text{O}_2$  and 78% Ar, at 1200 °C.

### 5.1.3. Summary of the Oxidation Rate Results

#### 5.1.3.1. Oxidation Rates

The raw data for each run consisted of: a complete description of the experimental conditions and parameters, the gas absorber sampling time, the  $\text{SO}_2$  absorbed and the final off-gas volumetric flow rate. Tables containing the gas analysis data for all of the experimental runs are provided in Appendix B. The experimental program included the

investigation of the influence of several variables-gas flow rate, gas composition, reaction temperature and bath mixing- on the oxidation rate of the molten  $\text{Cu}_2\text{S}$  bath. A summary of the measured reaction rates is presented in Appendix B as well.

#### 5.1.3.1.1. Effect of Admitted Gas Flow Rate

The rate of oxygen reaction,  $\dot{N}_{\text{O}_2}$ , was found to be a power function of the total reaction gas volumetric flow rate, as shown in Figure 5.7.

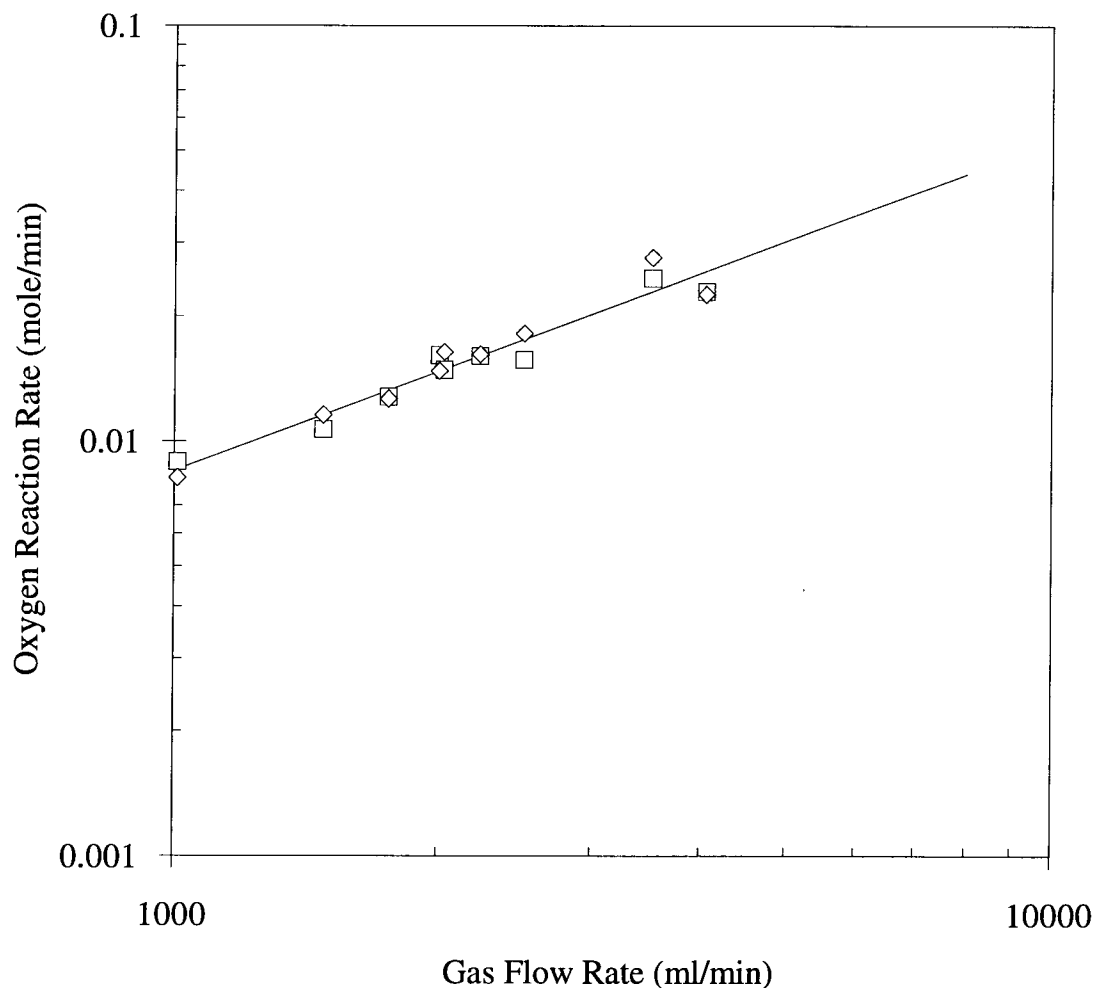


Figure 5.7. Oxygen reaction rate ( $\dot{N}_{\text{O}_2}$ ) as a function of reaction gas volumetric flow rate,  $Q$ , (total admitted flow rate); for the experimental conditions of 200-gram samples, 1200 °C, average pressure of 1.08 atm and 23 %  $\text{O}_2$ ; — regression curve ( $=3.59 \times 10^{-5} Q^{0.79}$ );  $\square$  primary measured;  $\diamond$  secondary measured.



From a least squares fit, the average exponent on the admitted gas flow rate, obtained from the results of both stages, is 0.79, which is similar to other systems in which gas phase mass transfer control prevails [48]. Interestingly the oxygen reaction rate is the same in the primary and secondary stages.

Figure 5.8 shows a log-log plot of rate of sulphur removal from the bath,  $\dot{N}_s$ , against admitted gas flow rate. As already observed, the rate is faster in the secondary stage.

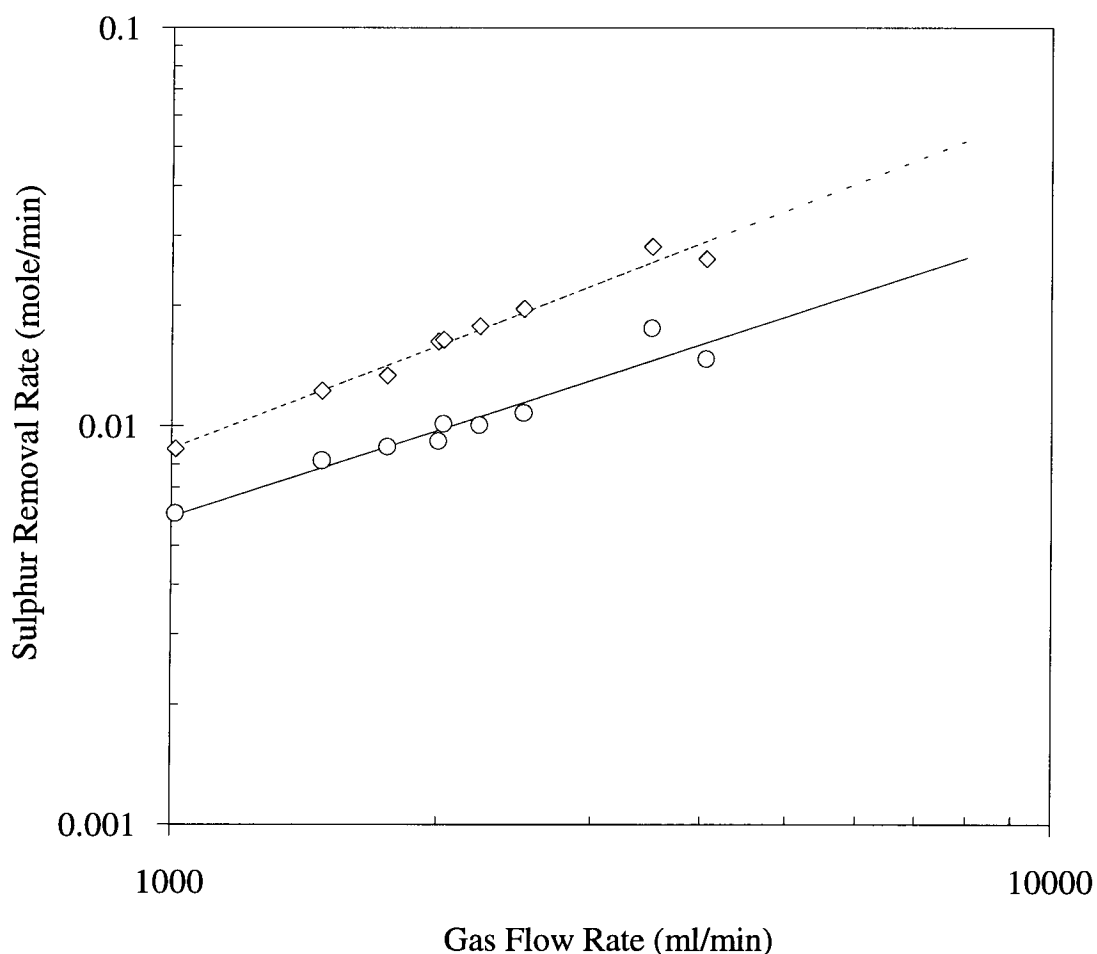


Figure 5.8. Sulphur removal rate ( $\dot{N}_s$ ) as a function of reaction gas volumetric flow rate; for the experimental conditions of 200 gram samples, 1200 °C, average pressure of 1.08 atm and 23 % O<sub>2</sub>; — primary regression curve ( $= 4.15 \times 10^{-5} Q^{0.72}$ ); ○ primary measured; - - - secondary regression curve ( $= 2.39 \times 10^{-5} Q^{0.85}$ ); ◇ secondary measured.

Exponents on the gas flow rate were calculated to be 0.72 and 0.85 for the primary and secondary stages respectively, close to that obtained from the oxygen reaction rate, Figure 5.7.

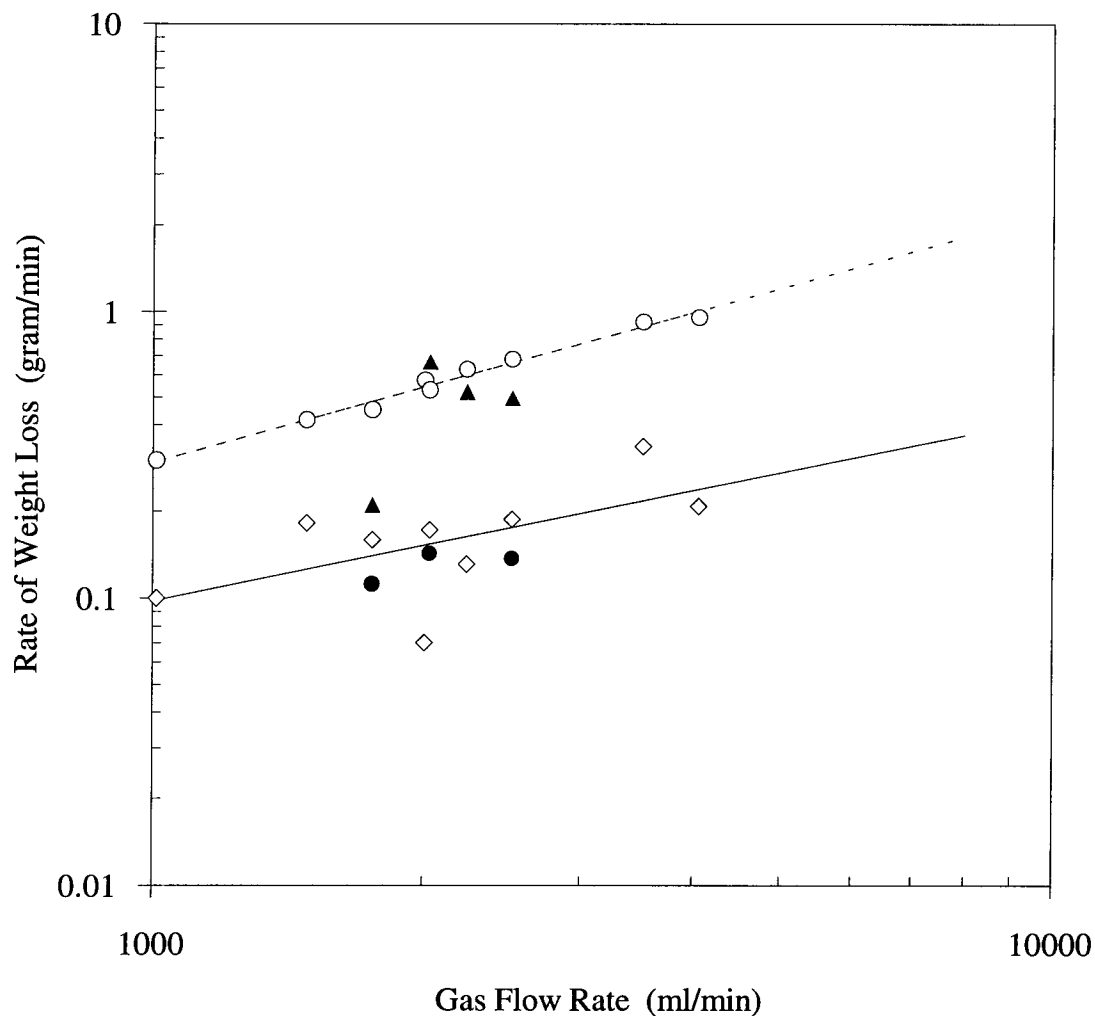


Figure 5.9. Sulphur removal rate ( $\dot{N}_S$ ) as a function of reaction gas volumetric flow rate; for the experimental conditions of 200-gram samples, 1200 °C, average pressure of 1.08 atm and 23 % O<sub>2</sub>; — primary regression curve ( $= 1.2 \times 10^{-3} Q^{0.63}$ );  $\diamond$  primary obtained from gas analysis;  $\bullet$  primary obtained from gravimetric measurement; - - - secondary regression curve ( $= 0.71 \times 10^{-3} Q^{0.87}$ );  $\circ$  secondary obtained from gas analysis;  $\blacktriangle$  secondary obtained from gravimetric measurement.

In Figure 5.9, the combined behaviour of the oxygen reaction rate and the rate of sulphur removal (overall reaction rate) with respect to gas flow rate are shown based on gas

analysis and gravimetric measurement. The exponents on the gas flow rate were found to be 0.63 and 0.87 for the primary and secondary stages respectively.

#### 5.1.3.1.2. Effect of Gas Composition

Figure 5.10 shows the influence of oxygen partial pressure in the admitted reaction gas on the overall oxygen reaction rate. As expected in the case of gas phase mass transfer control, the reaction rate depends linearly on the partial pressure of oxygen in the reaction gas. From Figure 5.10, the slope of the rate of oxygen reacted with respect to the oxygen pressure is  $k_{O_2}A/RT$ .

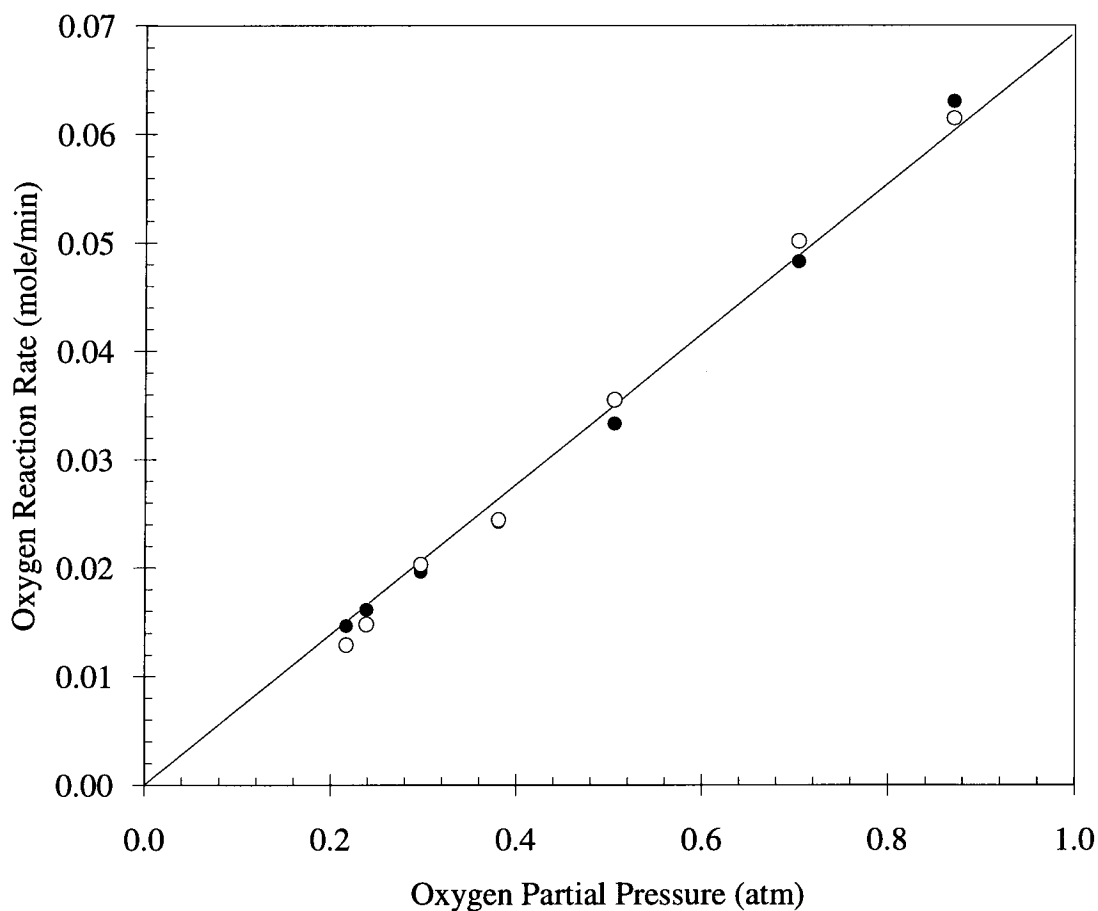


Figure 5.10. Oxygen reaction rate as a function of oxygen partial pressure for the experimental conditions of: 1200 °C and 2000 ml/min; ——— calculated from regression line ( $=0.096P_{O_2}$ ); ● primary measured; ○ secondary measured.

Similarly, the rate of sulphur removal is plotted against the partial pressure of oxygen in Figure 5.11. It can be readily seen that the rate of sulphur removal is directly proportional to the partial pressure of oxygen. This is an indication that the sulphur removal rate is driven by the rate of oxygen transfer in the gas phase.

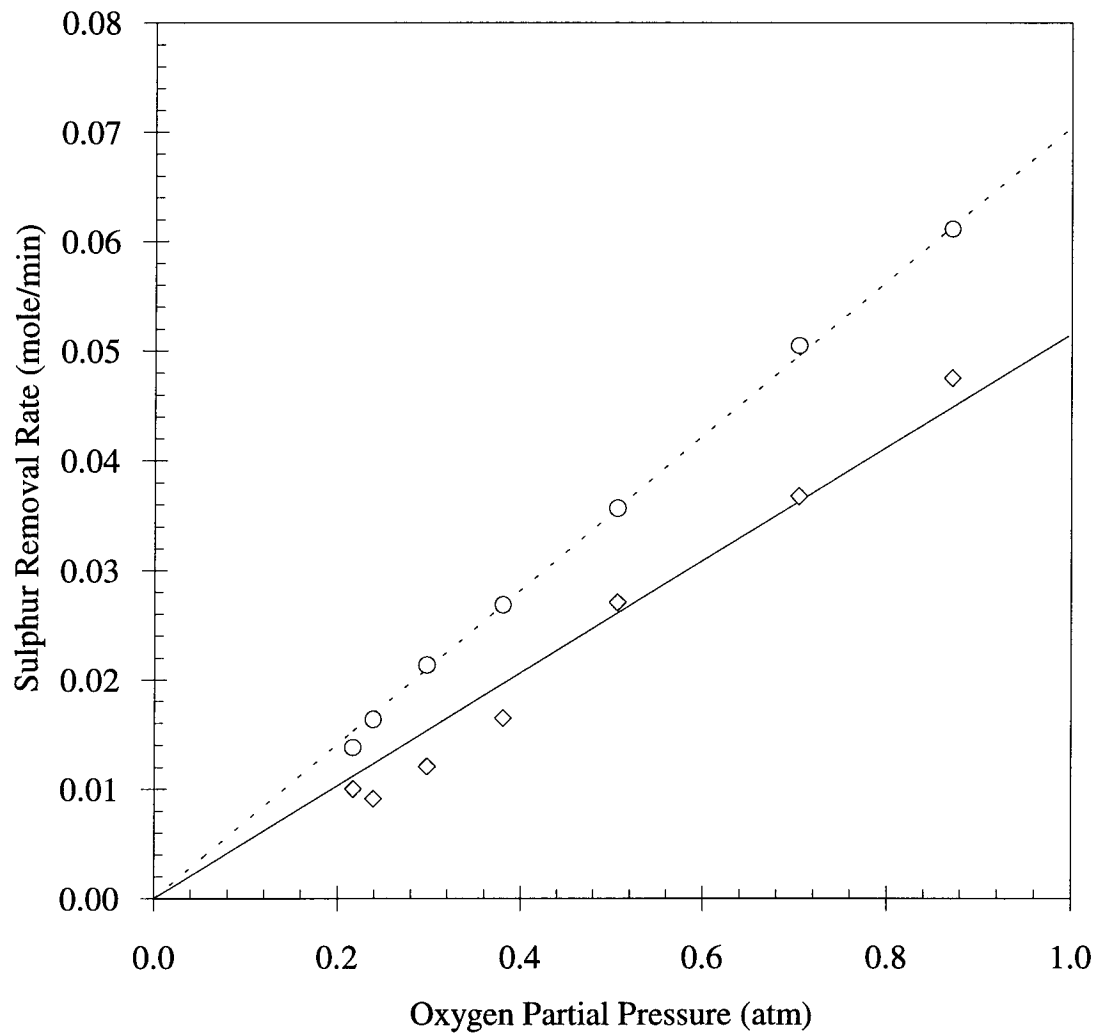


Figure 5.11. Sulphur removal rate as a function of oxygen pressure for the experimental conditions of: 1200 °C and 2000 ml/min; — primary calculated from regression line ( $=0.052P_{O_2}$ );  $\diamond$  primary measured; - - - primary calculated from regression line ( $=0.07P_{O_2}$ );  $\circ$  secondary measured.

It can be seen that the slope of the sulphur removal rate with respect to the oxygen pressure is  $k_{O_2}/\alpha RT$ , where  $\alpha$  is a stoichiometric factor. From linear regression, the slope of the secondary rate of sulphur removal was found to be approximately 1.3 times that in the primary stage.

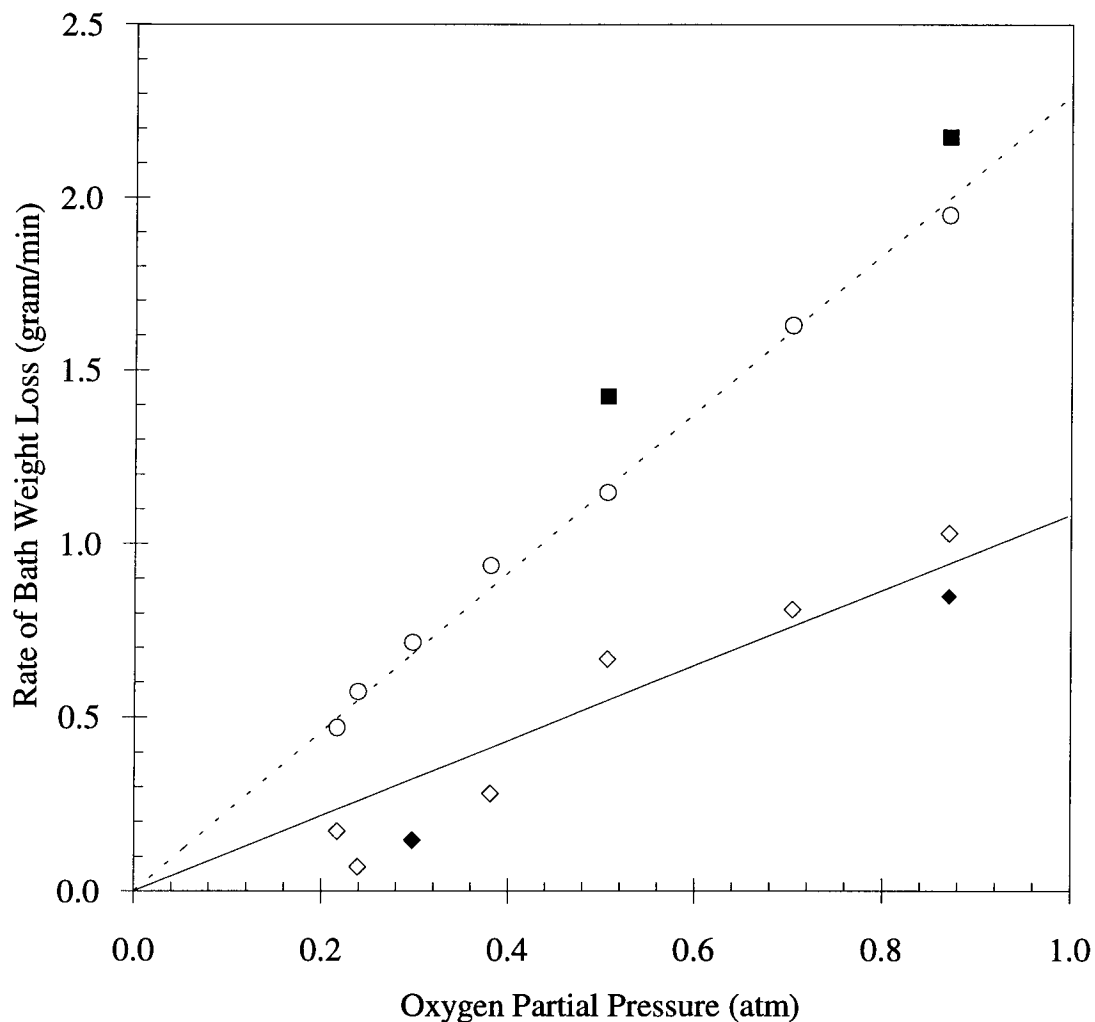


Figure 5.12. Rate of weight loss ( $\dot{W}$ ) as a function of oxygen pressure for the experimental conditions of: 1200 °C and 2000 ml/min; — primary calculated from regression line ( $=1.08P_{O_2}$ );  $\diamond$  primary obtained from gas analysis measurements;  $\blacklozenge$  primary obtained from gravimetric measurements; - - - primary calculated from regression line ( $=2.29P_{O_2}$ );  $\circ$  secondary obtained from gas analysis measurements;  $\blacksquare$  secondary obtained from gravimetric measurements.

The rate of bath weight loss is plotted against the oxygen partial pressure in Figure 5.12. As expected, a linear relationship was found for both the primary and secondary stages. Due to its relatively short time duration, the primary stage yielded measurements with greater experimental error than the secondary stage.

#### 5.1.3.1.3. Effect of Temperature

Processes in which the overall reaction kinetics are limited by the rate of chemical reaction are strongly dependent on temperature [118]. When studying the effect of temperature on reaction rates, it is customary to express them in the form of the Arrhenius relationship. The logarithm of the oxygen reaction rate is plotted vs.  $1/T$  in Figure 5.13, from which it is clear that the oxygen reaction rate is effectively independent of temperature. This was also confirmed from the statistical F test, at the 5% level of significance, which resulted in  $F_{\text{calculated}} = 2.4 \times 10^{-2}$  and  $F_{\text{significance}} = 0.88$ , thus indicating that the overall relationship is not significant at the 95% confidence limit [119]<sup>20</sup>.

The dependence of the sulphur removal rate on the inverse of temperature is shown in Figure 5.14. In the primary stage, a small activation energy of approximately  $37 \pm 17$  kJ/mole is calculated; this value is low compared to the activation energy range of 50 to 500 kJ/mole more typical of chemical reaction control [118]. For the secondary sulphur removal rate, however, as shown in Figure 5.14, the relationship appears to be statistically insignificant which means that the secondary removal rate of sulphur is effectively independent of temperature.

---

<sup>20</sup>The significance of expressing the measured oxygen reaction rate in terms of this relationship was checked by the F test, where  $F_{\text{calculated}}$  is obtained from the ratio of the sum of the squares of the deviations accounted for by the regression to the error variance; and  $F_{\text{significance}}$  is obtained from the probability distribution of variance ratio F at an acceptable level of confidence. For the applicability of the relationship to the measured data to be valid, the calculated value of F must be greater than the value obtained from the probability distribution curve.

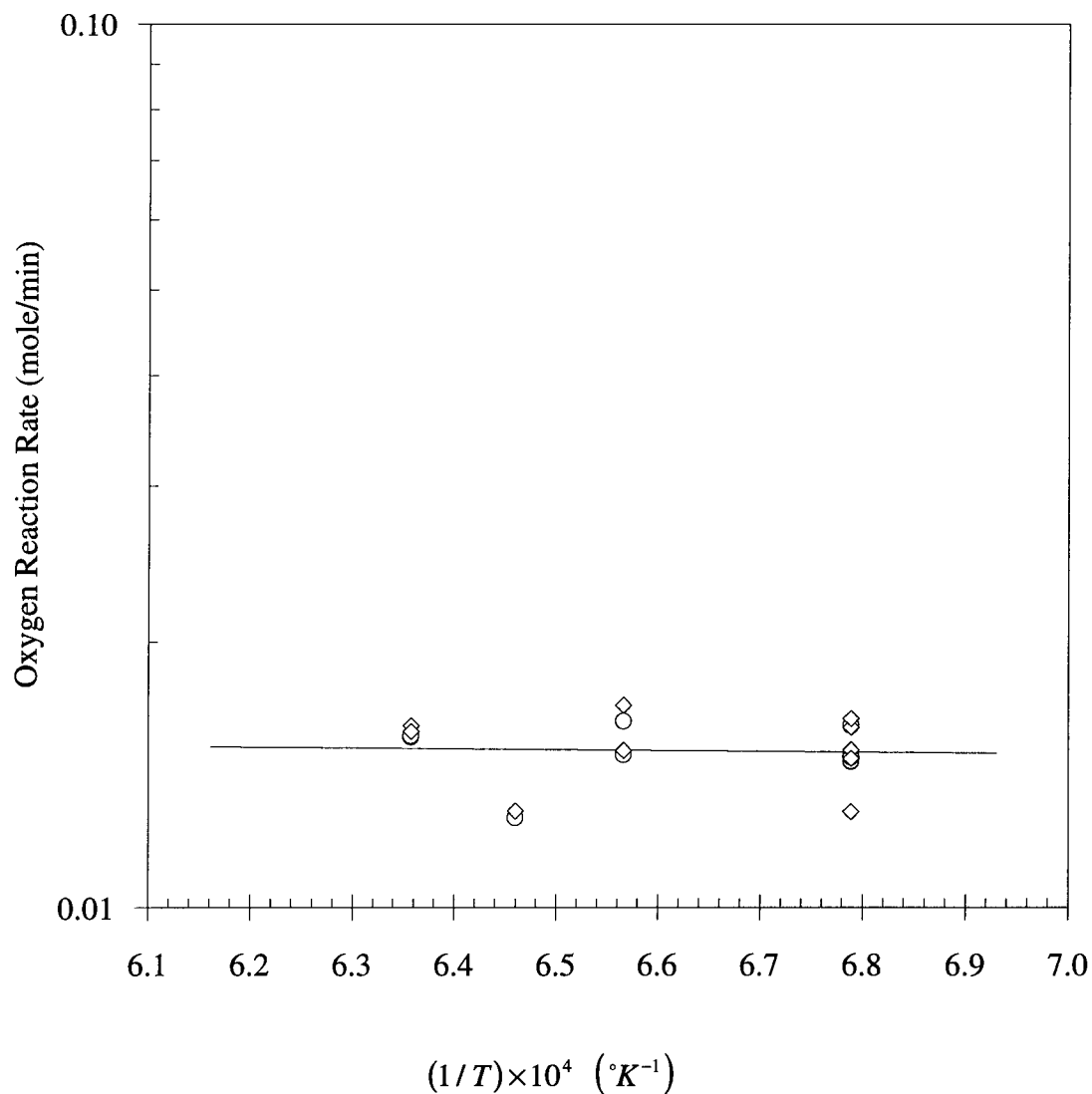


Figure 5.13. Oxygen reaction rate as a function of temperature for the experimental conditions of: 2000 ml/min of 20-23%  $\text{O}_2$  and average pressure of 1.08 atm; — primary calculated from regression curve ( $= 0.018 \exp -(1.9 \text{ kJ/mole})/0.0083144T$ ,  $F_{\text{cal}} = 2.4 \times 10^{-2}$  and  $F_{5\% \text{sig}} = 0.88$ );  $\circ$  primary measured;  $\diamond$  secondary measured.

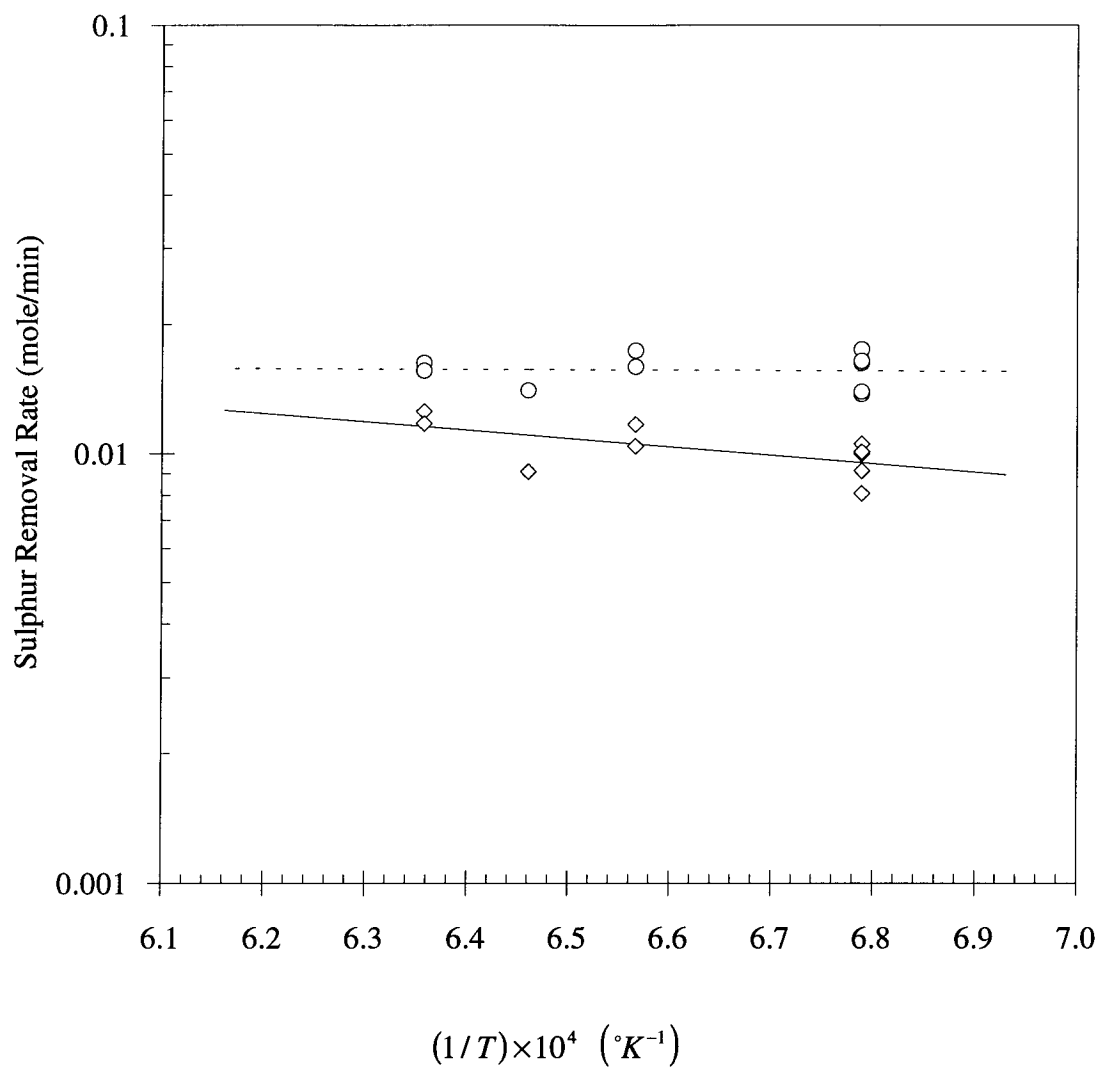


Figure 5.14. Sulphur removal rate as a function of temperature for the experimental conditions of: 2000 ml/min of 20-23%  $O_2$  and average pressure of 1.08 atm; — primary calculated from regression curve ( $= 0.2 \exp -(37 \text{ kJ/mole})/0.0083144T$ ,  $F_{\text{cal}} = 5$  and  $F_{5\% \text{sig}} = 0.06$ ); - - - secondary calculated from regression curve ( $= 0.018 \exp -(1.9 \text{ kJ/mole})/0.0083144T$ ,  $F_{\text{cal}} = 1.8 \times 10^{-2}$  and  $F_{5\% \text{sig}} = 0.89$ )  $\diamond$  primary measured;  $\circ$  secondary measured.



#### 5.1.3.1.4. Effect of Bath Mixing

Although all of the experimental results indicated that the rate limiting step of the oxidation reaction is gas phase mass transfer, the liquid phase mass transfer resistance contribution, if any, needed to be investigated. In order to examine the transport conditions of the liquid phase, a test during which the bath was mixed by injecting approximately 77 ml/min of Ar was conducted. Figure 5.15 shows a comparison of the bath mixing run to a normal run. The bath weight change is seen to be almost identical; thus the liquid phase mass transfer resistance has a negligible contribution to the overall reaction rate. Interestingly the disruption of the bath surface by the gas bubbles appears to have no significant effect on interfacial area.

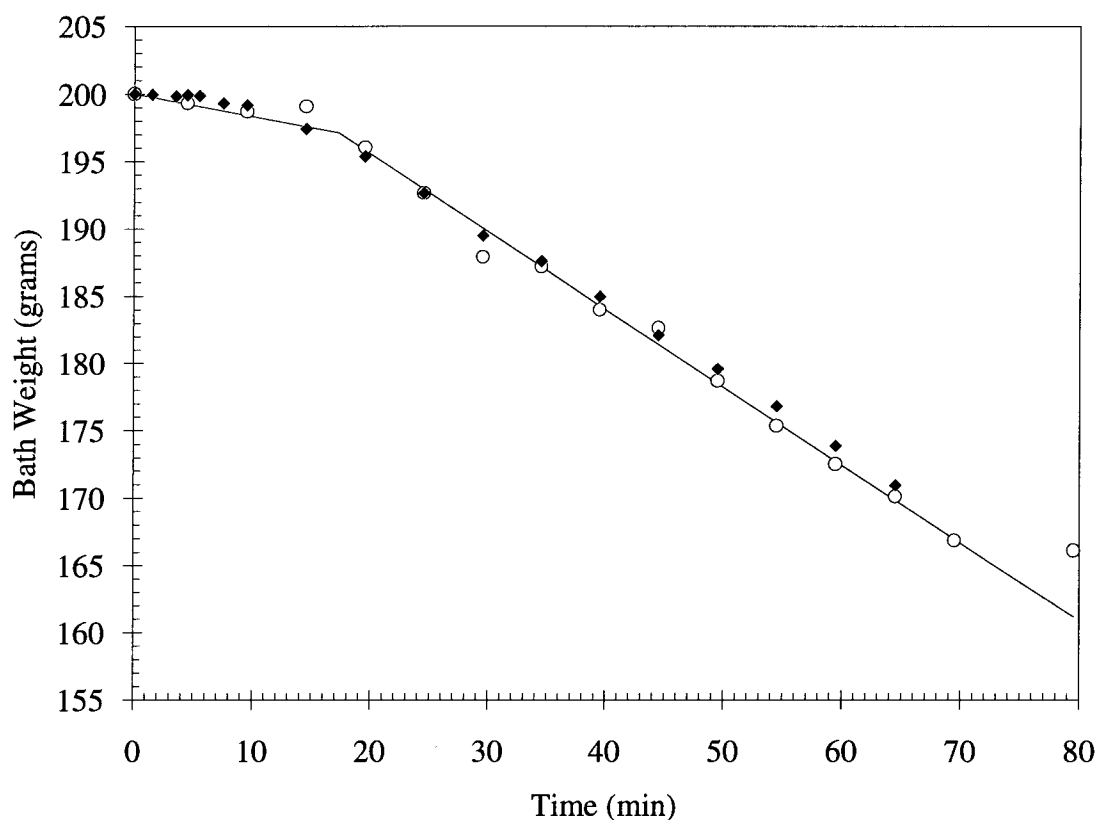


Figure 5.15. Bath weight as a function of time for the experimental conditions of: 1200 °C, average pressure of 1.08 atm and 22 % O<sub>2</sub>; ○ no mixing, 2006 ml/min; ◆ mixing with 77 ml/min of Ar, 2032 ml/min.

### 5.1.3.2. Reaction Transition Characteristics

The measured transition characteristics (sulphur and oxygen contents in the bath and degree of desulphurization in wt% at the transition) and the molar ratios of reacted oxygen to sulphur removed in the primary and secondary stages are presented in Table 5.1.

Table 5.1. Reaction transition characteristics and the molar ratios of reacted oxygen to removed sulphur.

Run	$Q_r^a$ (ml/min)	%O <sub>2</sub>	T (°C)	[%S] <sup>*</sup>	[%O] <sup>*</sup>	$d_s^*$ (%)	$\alpha^p$	$\alpha^s$
4	922	26	1200	18.09		17.02		
5	922	26	1200	16.95		20.37		
6	922	26	1200	17.48		16.26		
7	922	26	1200	16.63	1.62	19.76	1.5	0.97
8	1010	24	1200	16.75	1.67	18.97	1.5	0.93
9	1480	22	1200	17.27	1.04	16.57	1.3	0.94
10	2078	20	1200	16.92	1.43	18.23	1.4	1.08
11	1987	22	1200	16.90	1.74	18.01	1.5	0.94
12	1579	24	1200	16.77		20.00		
13	1521	20	1200	17.75	1.73	13.04	1.7	0.99
14	1532	21	1200	15.92	2.55	20.83	1.6	0.97
15	2006	22	1200	17.56	1.54	14.35	1.8	0.91
16	2510	23	1200	17.13	1.20	17.25	1.5	0.92
17	1755	22	1200	16.52	1.37	20.60	1.4	0.95
18	2234	23	1200	17.02	1.41	17.64	1.6	0.91
19	3015	23	1200	18.35	0.40	11.00	1.3	1.00
21	4055	22	1200	16.71	1.62	19.25	1.6	0.86
22	2000	27	1200	17.06	1.40	17.47	1.6	0.95
23	2000	35	1200	16.37	1.46	21.37	1.5	0.91
24	2000	46	1200	16.46	0.82	21.50	1.2	1.00
25	2000	64	1200	16.38	1.03	21.72	1.3	1.00
27	2000	23	1250	17.17	1.25	16.97	1.4	0.95
28	2000	23	1300	16.76	1.13	19.45	1.3	1.01
29	1994	21	1275	16.21	1.36	22.43	1.4	0.92
30	2000	22	1300	16.38	1.05	21.72	1.3	0.99
31	2000	22	1250	17.00	1.16	18.06	1.4	0.98
33	3493	27	1200	16.65	1.24	19.97	1.3	1.06
34	2000	78	1200	16.08	1.30	23.19	1.3	1.01
36	2032	22	1200	17.32	1.50	15.81	1.5	1.00
37	2000	21	1200	17.60	1.50	14.18	1.8	0.91
41	3516	24	1200	17.04	1.50	17.46	1.4	0.98

Thus the reaction transition characteristics seem to be independent of the reaction conditions. The average weight percents of sulphur and oxygen in the bath at transition from the primary to the secondary stage were found to be  $16.94 \pm 0.10\%$  and  $1.37 \pm 0.07\%$  respectively. These values compare favorably with the equilibrium values of 17.7 and 1.47% for sulphur and oxygen dissolved in  $\text{Cu}_2\text{S}$  respectively, at  $1200^\circ\text{C}$  and 1 atm [19]. This is strong evidence that the melt, during the primary stage, is a single copper sulphide phase i.e.  $\text{Cu}_2\text{S}$  becoming saturated with dissolved oxygen.

The ratios of the rate of reacted oxygen to the rate of evolved sulphur dioxide, during the primary,  $\alpha^p$ , and secondary stages,  $\alpha^s$ , are another important lead to the understanding of the reaction mechanism. The average measured ratio of the rate of reacted oxygen to the rate of evolved sulphur dioxide was found to be  $1.46 \pm 0.03$  and  $0.96 \pm 0.052$ , for the primary and secondary stages respectively.

In studying these results, the reaction mechanism is suggested to be as follows:

Primary Stage:

- Since  $\alpha^p > 1$ , (see Table 5.1) part of the reacted oxygen is dissolved in the melt and the rest is reacted with sulphur to form  $\text{SO}_2$ .
- Because  $\alpha^p > 1$  while the melt consists of a single phase, the primary oxidation reaction is likely to be:



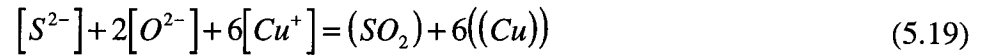
Secondary Stage:

- Because  $\alpha^s < 1$ , during the secondary stage, the amount of sulphur removed from the bath is greater than that of its reacted oxygen equivalent<sup>21</sup>. This in turn suggests that the sulphur removal, during the secondary stage, takes place

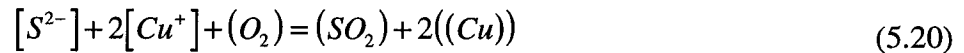
---

<sup>21</sup>Assuming that the sulphur removed from the bath is only in the form of  $\text{SO}_2$ .

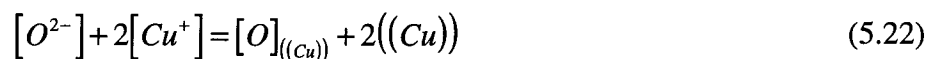
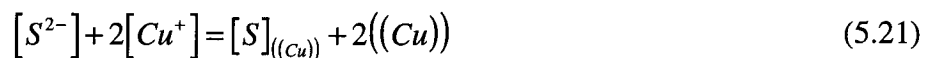
at the melt surface, according to Reaction (5.18), and in the melt according to Reaction (5.19).



If  $\alpha^s = 1$ , then the rate of oxygen reaction is equal to the rate of sulphur removal according to Reaction(5.20). This also implies that blister copper does not contain any sulphur or oxygen.



- It is apparent that the making of copper is accompanied by the simultaneous dissolution of sulphur and oxygen. Since the sulphide melt is ionic and the copper phase is metallic, the process of oxygen and sulphur dissolution in copper must be accompanied by electron transfer by further copper making, according to Reactions (5.21-5.22). This is supported by the fact that the equilibrium metal phase composition is approximately 98.89% Cu, 0.95% S and 0.16% O.



In summary, during the primary stage, the melt is partially desulphurized and becomes oxygen saturated according to Reaction (5.18). During the secondary stage, the making of the metal phase takes place, according to Reactions (5.18), (5.19), (5.21) and (5.22).

## 5.2. Micro Examination Of The Melt Samples

In studying heterogeneous kinetics, it is important that a physical examination of the reaction system is carried out, however possible. The reaction rate results indicated that, during the primary stage, there is only one reaction site (at the melt surface according to Reaction (5.18)), and during the secondary stage, there are two reaction sites (at the melt surface according to Reaction (5.18) and in the melt according to Reactions (5.19), (5.21) and (5.22)). This implies that, during the primary stage, the melt consists only of the sulphide phase, and, during the secondary stage, the melt consists of the sulphide phase, the metal phase and the rising gas bubbles. In order to further investigate the validity of these results, melt samples were extracted at specific reaction conditions. These samples were sectioned, polished, examined via optical microscopy (magnification range of 80-400X), and photomicrographed. In order to correlate these observations to the reaction rate results, this examination included the investigation of the existence of copper droplets, the traces of gas bubbles and phase constitutions.

As mentioned above (see also Section 2.2), the melt initially consists of the single  $\text{Cu}_2\text{S}$  phase. As the reaction proceeds, during the primary stage, the melt is partially desulphurized and oxygen saturated until its composition reaches approximately (80.83% Cu, 17.7% S and 1.47% O, at 1200 °C and 1 atm [19]).

Figures 5.16 and 5.17<sup>22</sup> show photomicrographs of polished bath samples at 7 min of reaction time from the primary stage. Although metal (pink) precipitates are evident around the solidifying grains of the sulphide (green) and there are traces of gas bubbles (black), the morphology of the metal phase and the average size of the gas bubbles suggest that they result from the cooling process during the quenching of the sample. As discussed in Section 4.3.2, quartz tubes were used in the sampling of the melt. Hence, it

---

<sup>22</sup>All of the photomicrographs are for the experimental conditions of: 200 grams of  $\text{Cu}_2\text{S}$ , at 1200 °C and 1 atm, 2 l/min of 22%  $\text{O}_2$  and 78% Ar.

is impossible to completely prevent post reaction changes, during quenching<sup>23</sup>. In the absence of vertical sections of the Cu-S-O ternary system, it is not possible to account for the gas bubbles. However, it is just as useful to consider the binary Cu-S system; *ignoring the effect of oxygen*, for compositions slightly below the exact stoichiometry of  $\text{Cu}_2\text{S}$ , the melt cooled under equilibrium conditions, will decompose to  $\text{Cu}_2\text{S}$  ( $\gamma$ ) and liquid copper, at the liquidus temperature of 1105 °C, and to  $\text{Cu}_2\text{S}$  ( $\gamma$ ) and solid copper, at the eutectic temperature of 1067 °C.

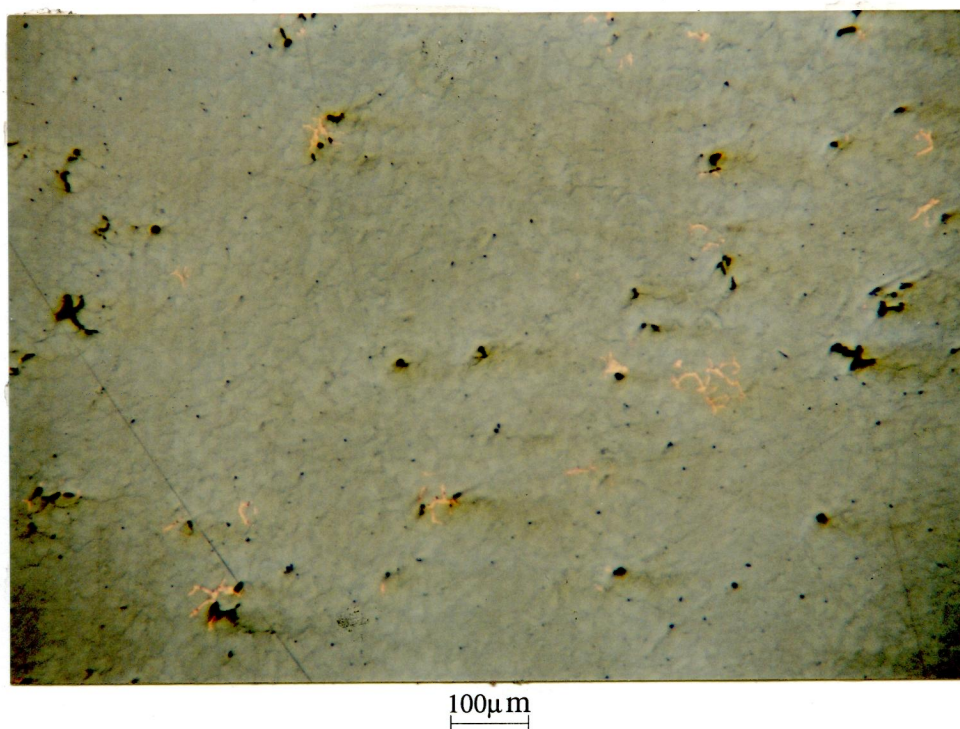


Figure 5.16. Photomicrograph of polished section of frozen melt sample, at 7 min of reaction time (during the primary stage); green is sulphide; pink is metallic; black is gas.

---

<sup>23</sup>Compared to other ceramics, quartz has a relatively high resistance to thermal shock. Its relatively low thermal conductivity, however, retards the quenching process.

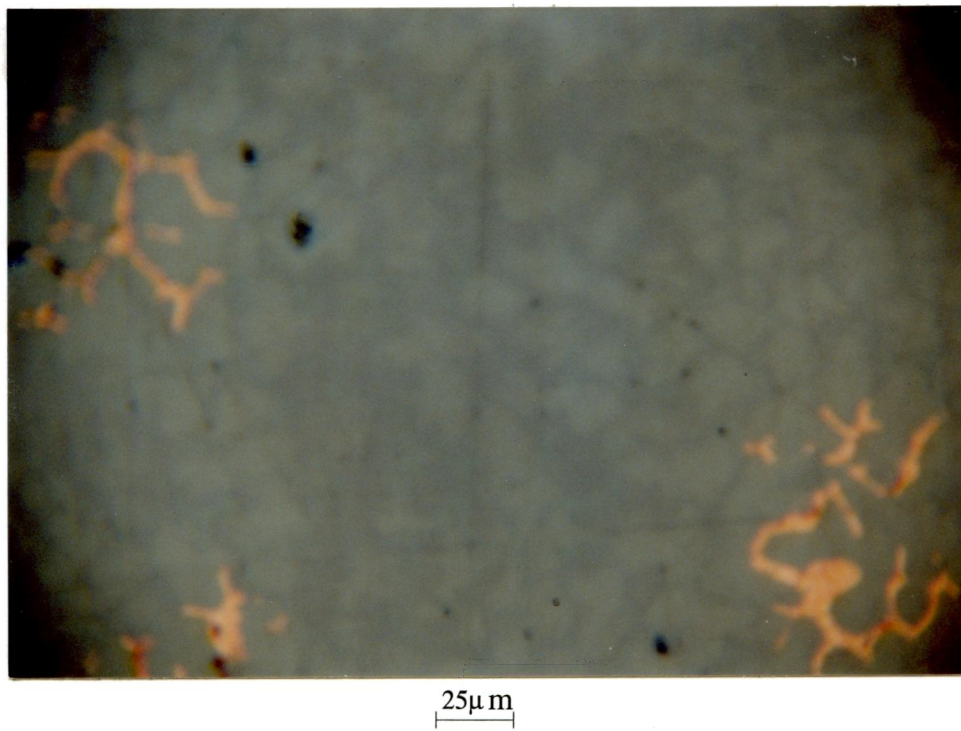


Figure 5.17. Photomicrograph of polished section of frozen melt sample, at 7 min of reaction time (during the primary stage).

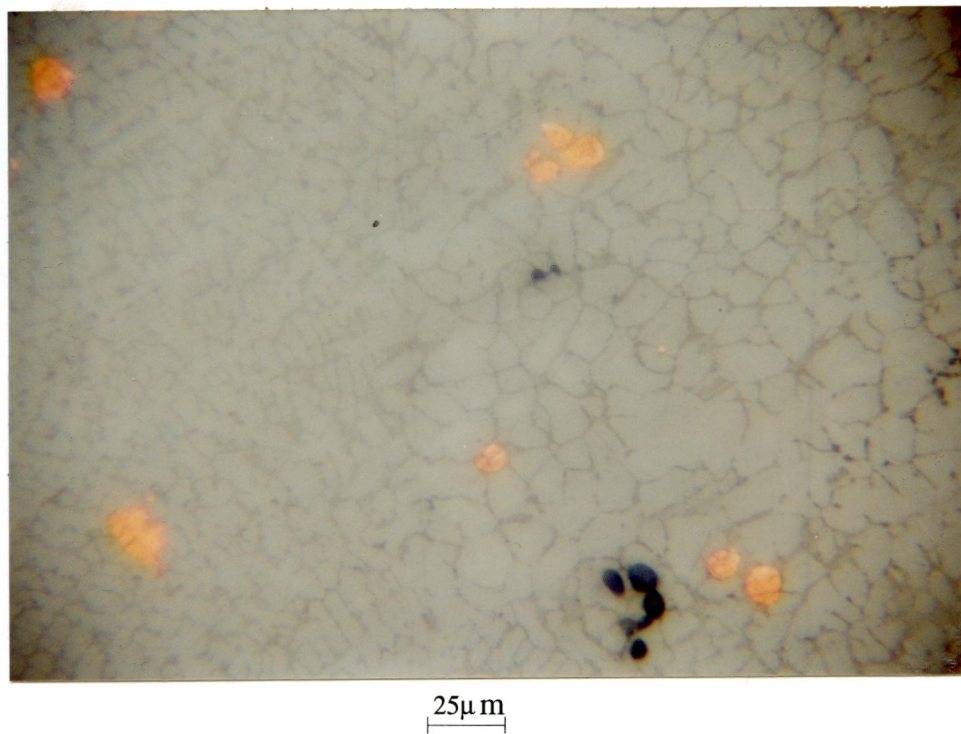
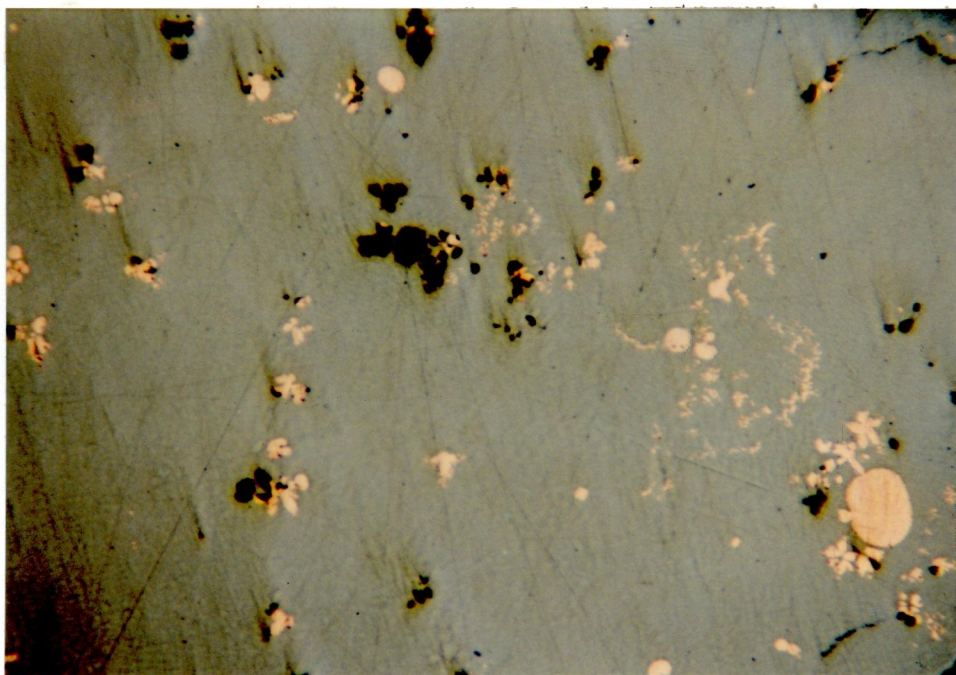


Figure 5.18. Photomicrograph of polished section of frozen melt sample, at 15 min of reaction time (1 min after the copper droplets and SO<sub>2</sub> gas bubbles start to form in the melt).

The reaction rate results indicated that the transition time for 2 l/min of 22% O<sub>2</sub> and 78% Ar, at 1200 °C, is approximately 14 min (refer to Figure 5.6). This means that before 14 min, there should be no copper and gas bubble formation in the melt. At 14 min the secondary stage commences, for which Reactions (5.19), (5.21) and (5.22) proceed in the melt, thereby forming copper droplets and SO<sub>2</sub> gas bubbles, as can be seen in Figures 5.18-5.23.

It is evident that the metal phase, at 15 min of elapsed reaction time, is in the form of droplets, of  $11\pm 1\mu\text{m}$  average diameter, as shown in Figure 5.18, rather than precipitates around the sulphide grain boundaries, as shown in Figure 5.17. This is an indication that the copper formed after 15 min is the result of the oxidation reaction, rather than the result of the slow quenching process.



100 $\mu\text{m}$

Figure 5.19. Photomicrograph of polished section of frozen melt sample, at 25 min of reaction time.



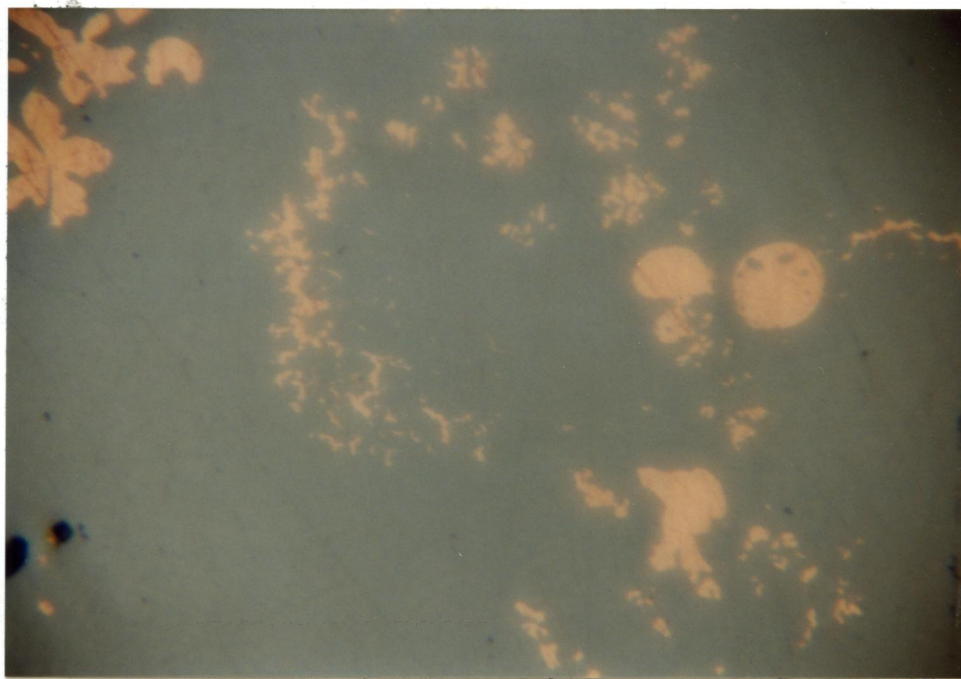


Figure 5.20. Photomicrograph of polished section of frozen melt sample, at 25 min of reaction time.

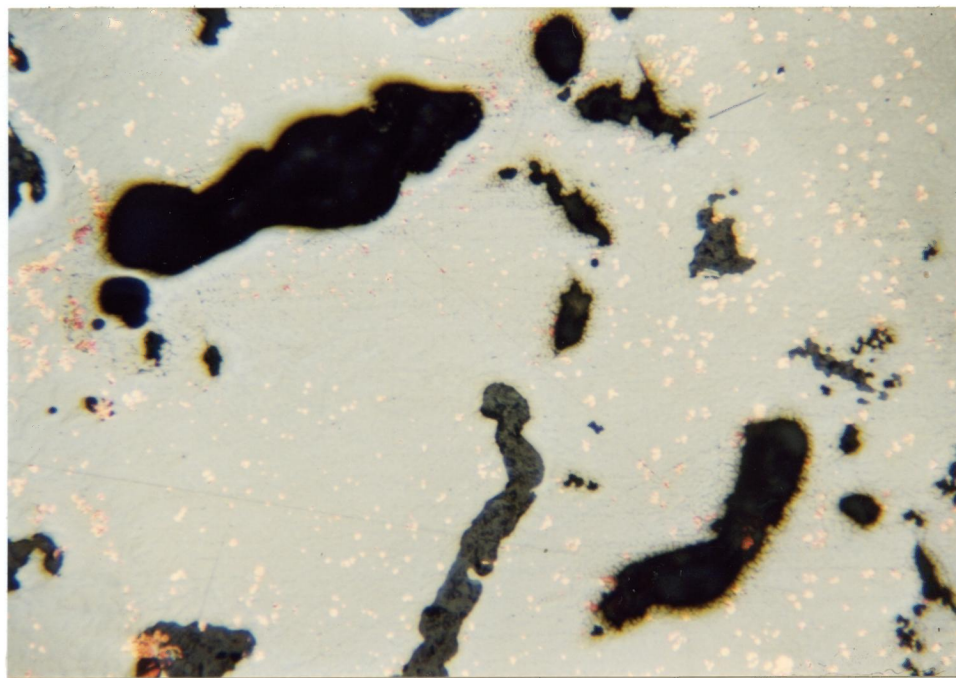


Figure 5.21. Photomicrograph of polished section of frozen melt sample, at 35 min of reaction time.

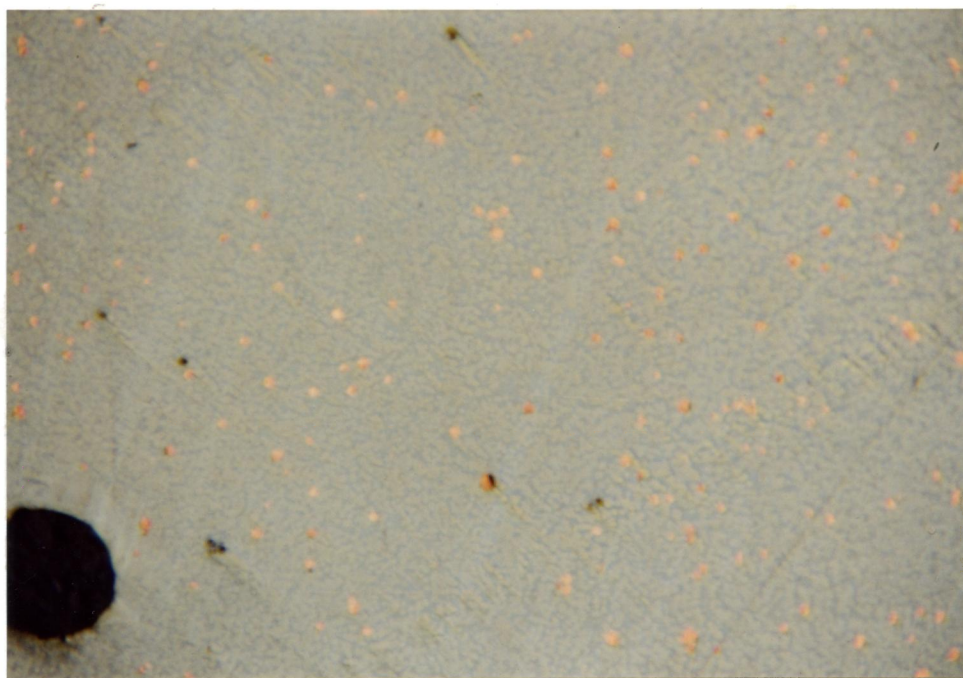


Figure 5.22. Photomicrograph of polished section of frozen melt sample, at 40 min of reaction time.

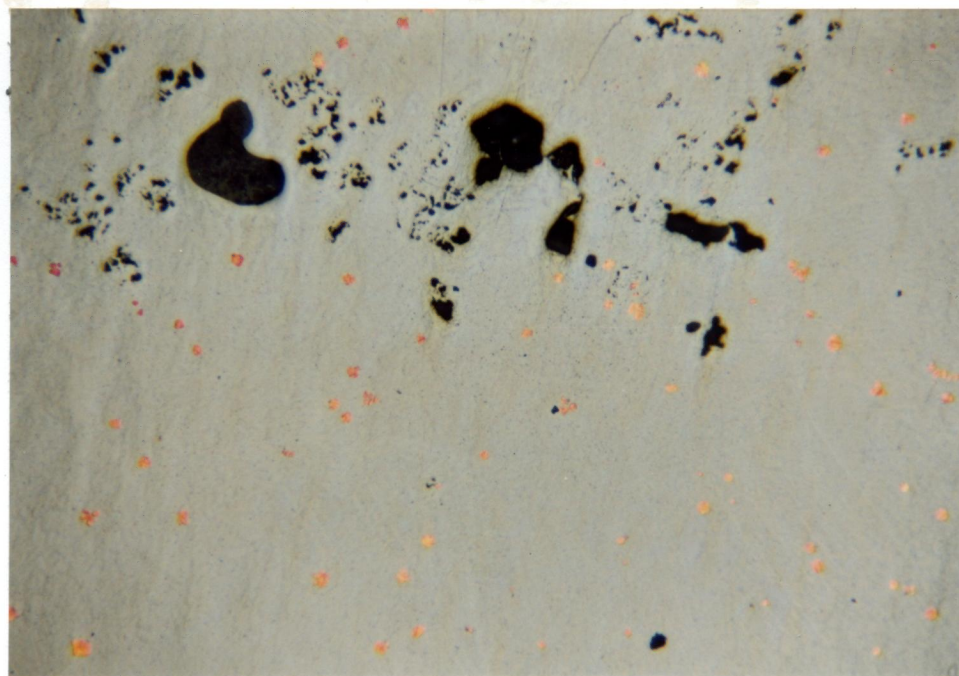
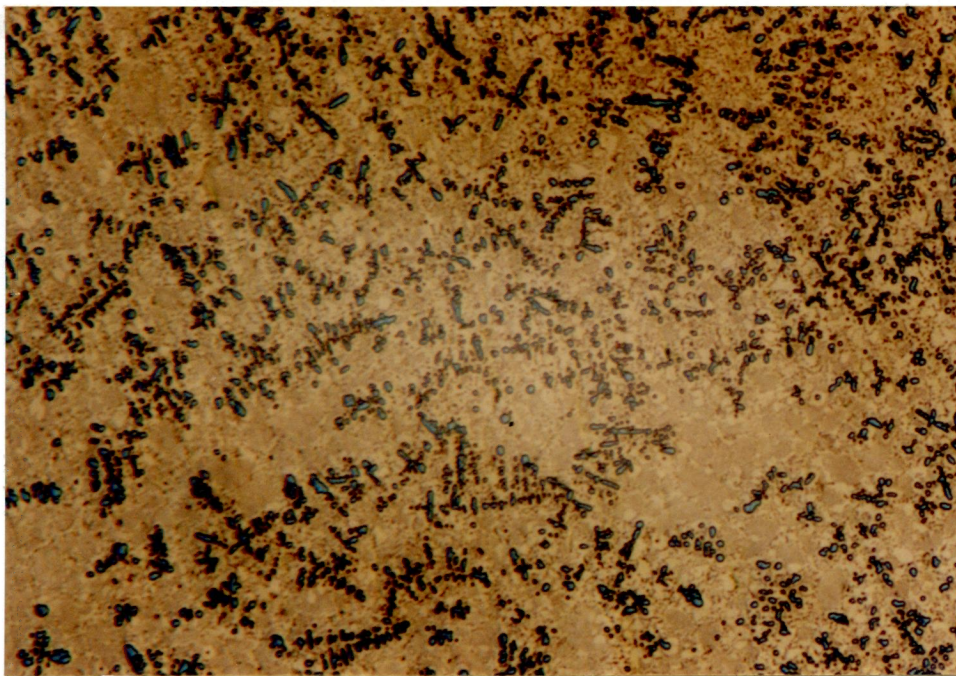


Figure 5.23. Photomicrograph of polished section of frozen melt sample, at 50 min of reaction time.

After 25 min of reaction time, the quantity of copper and gas bubbles increases, as shown in Figure 5.19. The average copper droplet diameter, of  $26 \pm 3 \mu\text{m}$  appears to be larger as the reaction time elapses. The other important point to note is that there are two types of copper formation: the large copper droplets, and small random copper droplets that are associated with the gas bubbles. As suggested by Reactions (5.19), (5.21) and (5.22), the latter are expected, since they share common reaction sites. The shape of the small copper droplets appear to be random, unlike the large copper droplets, which are spherical. Because the melt is spontaneously mixed as a result of surface-tension driven flows and gas evolution, evidently the small copper droplets agglomerate to form the larger droplets, as shown in Figures (5.19) and (5.20). From surface observations during the secondary stage, small numbers of gas bubbles were observed to rise randomly from the melt on a continuous basis and large quantities, in a boiling fashion, on a less frequent basis. Due to the fluid dynamics of the system, the size and quantity of gas bubbles with respect to time cannot be traced in a similar way to the copper droplets. However, when the sample was extracted just before an incident of intense boiling, in a coincidental manner, a large quantity of gas was found to be contained by the melt, as shown in Figure 5.21.

Due to the density difference between the metal phase ( $7.9 \text{ g/cm}^3$ ) and the sulphide phase ( $5.5 \text{ g/cm}^3$ ) [113], the copper droplets coalesce and settle to the bottom of the crucible. The gas bubbles coalesce and rise to the melt surface continuously as well. However, as mentioned previously, occasionally intense boiling was observed to occur at the melt surface. During the secondary stage, the appearance of the sulphide phase remained unchanged until its complete depletion, as shown in Figures 5.18-5.23. Once the sulphide phase was completely consumed, at the end of the secondary stage, the composition of the melt approaches that of the metal phase, viz. approximately 98% Cu, 0.95% S and 0.16% O, at  $1200 \text{ }^\circ\text{C}$  and 1 atm [19]. As shown in Figures 5.24 and 5.25, towards the end of

secondary stage, the melt becomes predominately metallic (brown) containing the remaining sulphide phase (blue). Referring to the Cu-S binary, *ignoring the effect of oxygen*, at 1200 °C, for compositions of less than 1.4% S, the melt consists of the liquid copper phase such as that shown in Figure 5.26. In Figure 5.26, a polished section of 99.99% pure copper is shown to illustrate the apparent microstructural differences between pure copper and the copper produced at the end of the secondary stage. For compositions of greater than 1.4% S, the melt consists of the liquid copper and liquid copper sulphide phases. Rapid quenching of the 1.4% S sample should result in the suppression of any sulphide phase segregation, which takes place in the case of equilibrium cooling. However, due to the use of quartz tubes in the sampling of the melt, the rate of cooling of the sample, during quenching, appears to have been relatively slow. As shown in Figure 5.24, the dendritic precipitate of the  $\text{Cu}_2\text{S}$  phase (green/blue), in the matrix of the metal phase (light brown), is the result of equilibrium cooling.



125 $\mu\text{m}$

Figure 5.24. Photomicrograph of polished section of frozen melt sample, at 60 min reaction time (final reaction time is 70 min).

This indicates that the sample was quenched at a relatively low rate of cooling. Thus it is apparent that the melt consists only of the metal phase, at the sampling time. At the final reaction time, the composition of the melt is very close to blister copper, of 98.5-99.5% Cu. The compositional effect on the phase constitutions of the metal phase is shown in Figures 5.25-5.26.

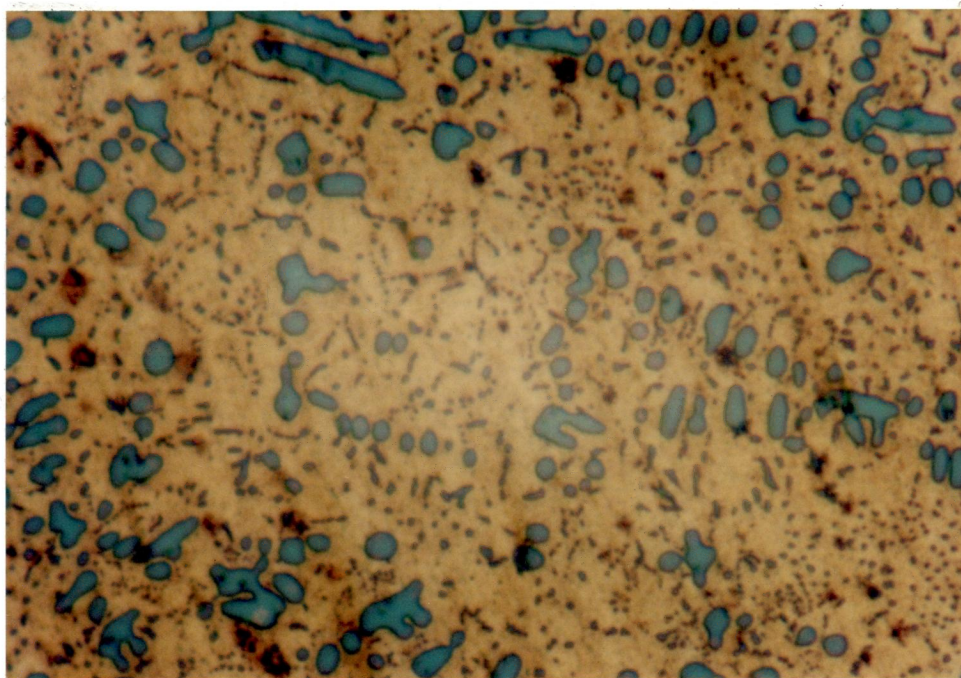


Figure 5.25. Photomicrograph of polished section of frozen melt sample, at 60 min reaction time (final reaction time is 70 min).

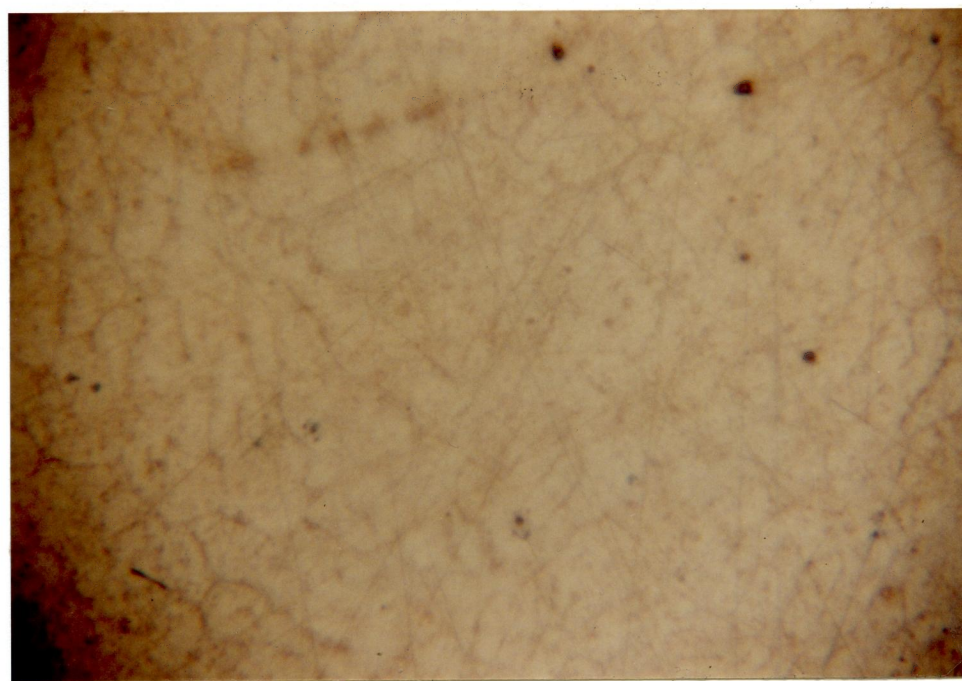


Figure 5.26. Photomicrograph of polished section of a 99.99% Cu standard sample.

### 5.3. Observations of the Bath Surface

Surface observations were useful, not only to investigate the Marangoni effect and gas bubbles eruptions, but also to gather more qualitative data about the reaction kinetics, and to aid in the termination of the reaction because surface-tension driven flows were observed to cease at the end of the secondary stage.

When the copper sulphide bath completely melted under argon, a thin liquid opaque film, easily broken by movement, was observed to cover the stagnant melt surface evenly, with the exception of some random shiny areas which appeared to be the sulphide melt, as shown in Figure 5.27.

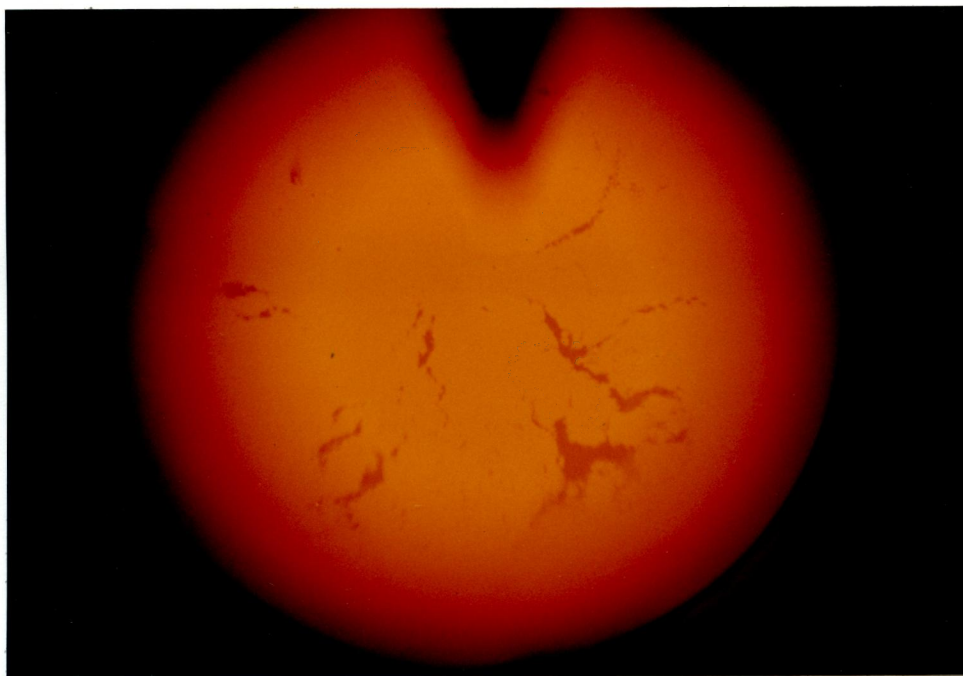


Figure 5.27. Bath surface, at 1200 °C with top-lancing at 2 l/min of Ar; the black triangular area at the top is the tip of the lance appearing out of focus; the right and left bottom segments of a ring are the inner rim of the crucible; the area within is the opaque film covering most of the melt except some random more shiny areas (the sulphide melt surface). Note the absence of surface movement, due to the gas impingement on the surface.

Although its chemical composition is unknown, the opaque film appeared to be immiscible with respect to the sulphide melt. Due to the apparent difference between its

emissivity and the emissivity of the copper sulphide melt, this film was used as an additional indicator of the surface motion. Upon admittance of the reaction gas, the surface of the sulphide melt (shiny area) was immediately uncovered in the area beneath the lance, as shown in Figure 5.28, after which the film moved outwardly from the area beneath the lance towards the crucible wall, as shown in Figure 5.29. As the reaction proceeded, the outline of the exposed and covered sulphide surface was observed to increase in diameter, in a vibrating fashion, as shown in Figure 5.29. The spontaneous motion of the melt surface from the center of the crucible to the wall was observed to increase, as shown in Figures 5.28-5.32.

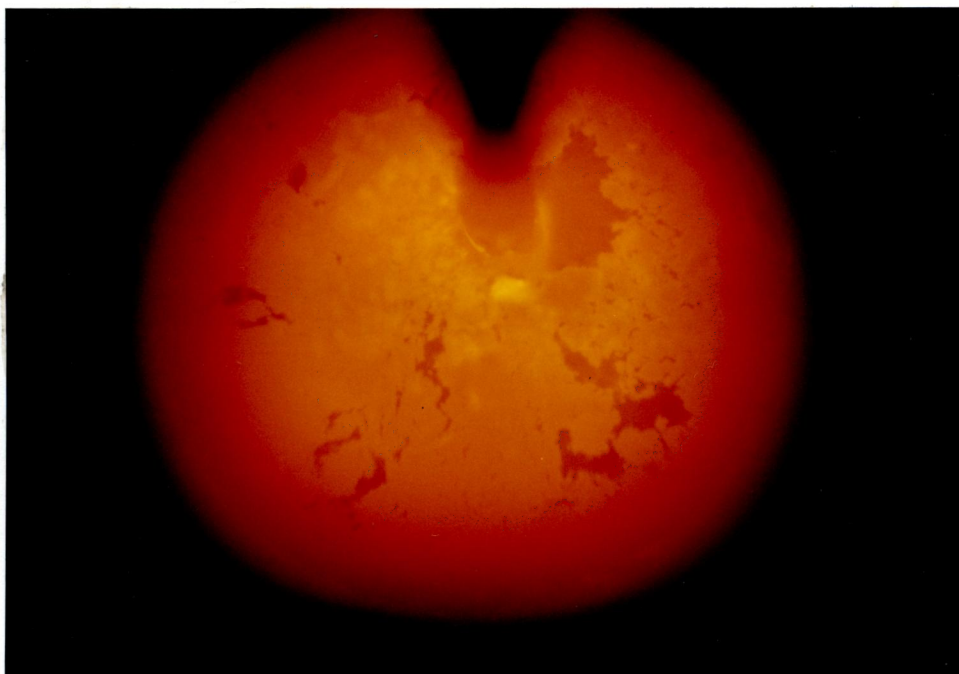


Figure 5.28. Photograph of the bath surface at the same time of the admittance of the reaction gas; the sulphide melt surface is starting to be exposed in the area beneath the lance (slightly above the center of the crucible); for the experimental conditions of 200 grams of  $\text{Cu}_2\text{S}$ , at  $1200\text{ }^\circ\text{C}$ , and under the top-lancing of 2 l/min of 80%  $\text{O}_2$  and 20% Ar.



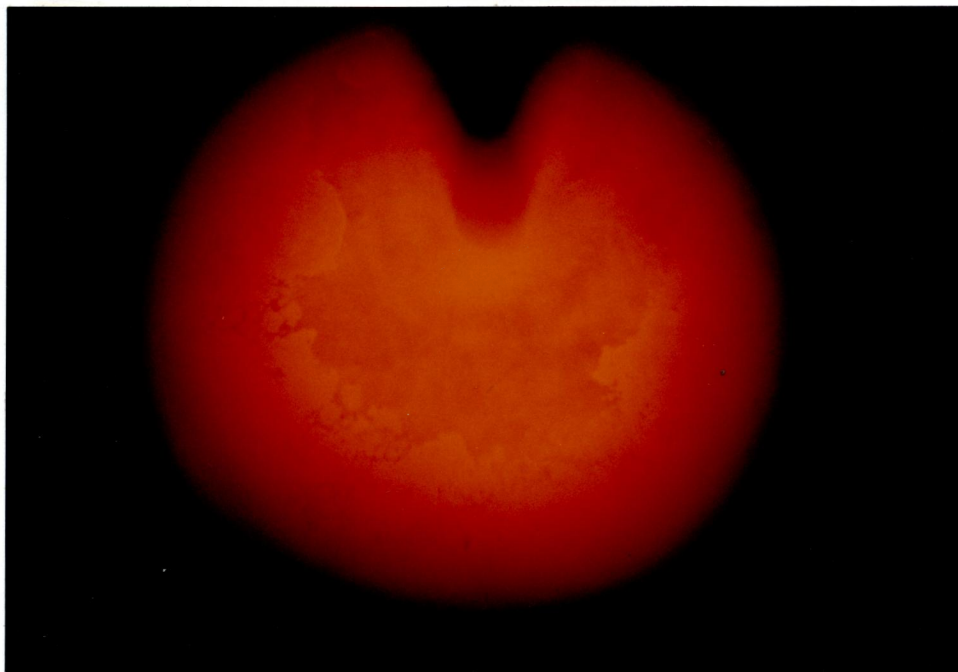


Figure 5.29. Photograph of the surface of the bath at approximately 60 s, after the initiation of the reaction. The film is pushed away from the center of the crucible to the wall, as seen by the further exposure of the sulphide shiny surface.

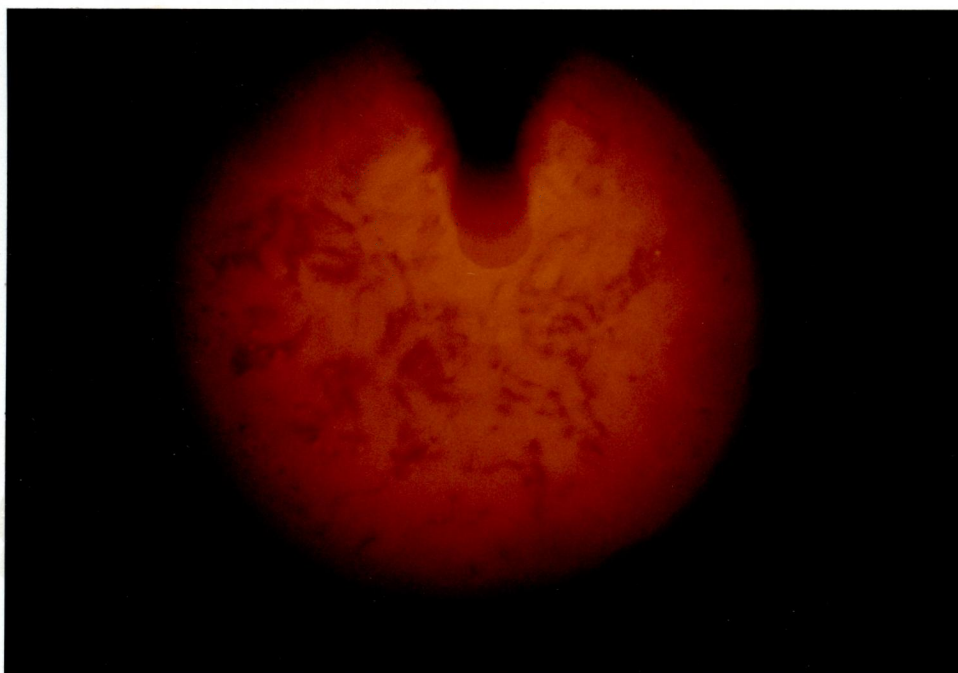


Figure 5.30. Photograph of the surface at approximately 3.5 min; spontaneous wavy motion of the melt surface is fully developed and the film is entirely pushed towards the crucible wall, as seen by the full exposure of the sulphide surface. The difference in the color of the surface is due to its wavy motion.

Once the spontaneous surface motion was fully developed, it continued throughout the duration of the reaction time, as shown in Figures 5.30-5.32. The speed at which the surface moved, due to the effect of surface tension, was observed to be apparently high enough to cause the stirring of the whole bath. Due to the motion of the melt surface, the thermocouple sheath, when immersed in the melt, was observed to continuously vibrate about its vertical axis, in a pendulum-like motion, creating a clinking noise. Because the eruption of gas bubbles from the melt surface occurred only during the secondary stage, the high degree of turbulence is attributed mainly to surface tension-driven flows. In studying the effects of reaction gas flow rate, reaction gas composition, and reaction temperature, the general behaviour of the melt surface was observed to be the same. However, the speed at which the surface moved was observed to be faster with higher reaction flow rate and composition, as shown in Figures 5.31 and 5.32. On the other hand, the effect of temperature was not detectable.

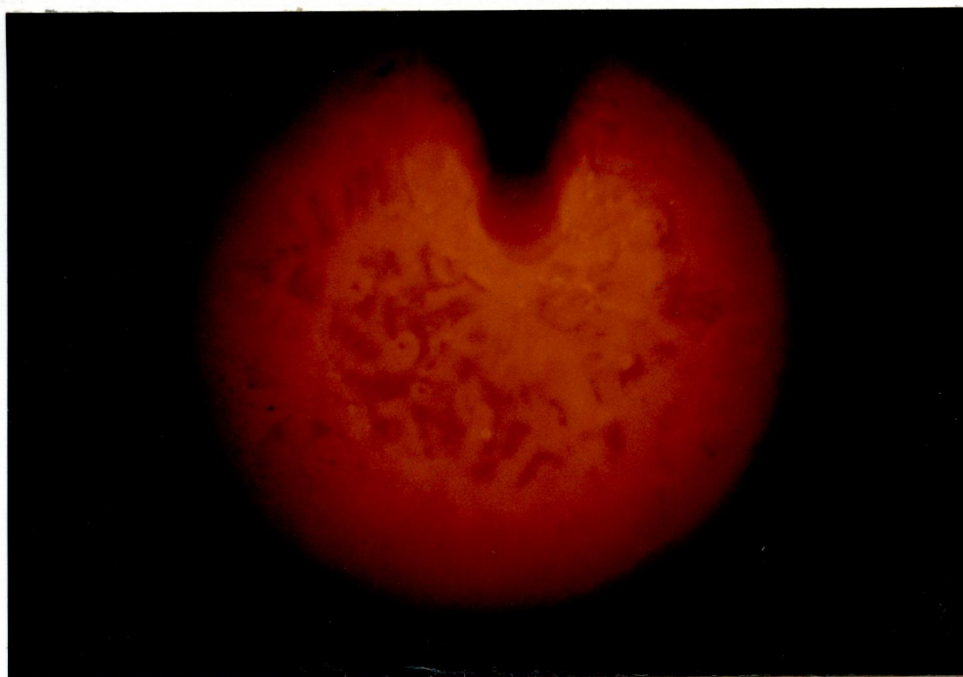


Figure 5.31. Photograph of the surface of the bath at approximately 5 min; the oxidation rate results indicated that the transition time for these experimental conditions was 5 min. Note that the film is entirely pushed away from the center of the crucible to the wall.

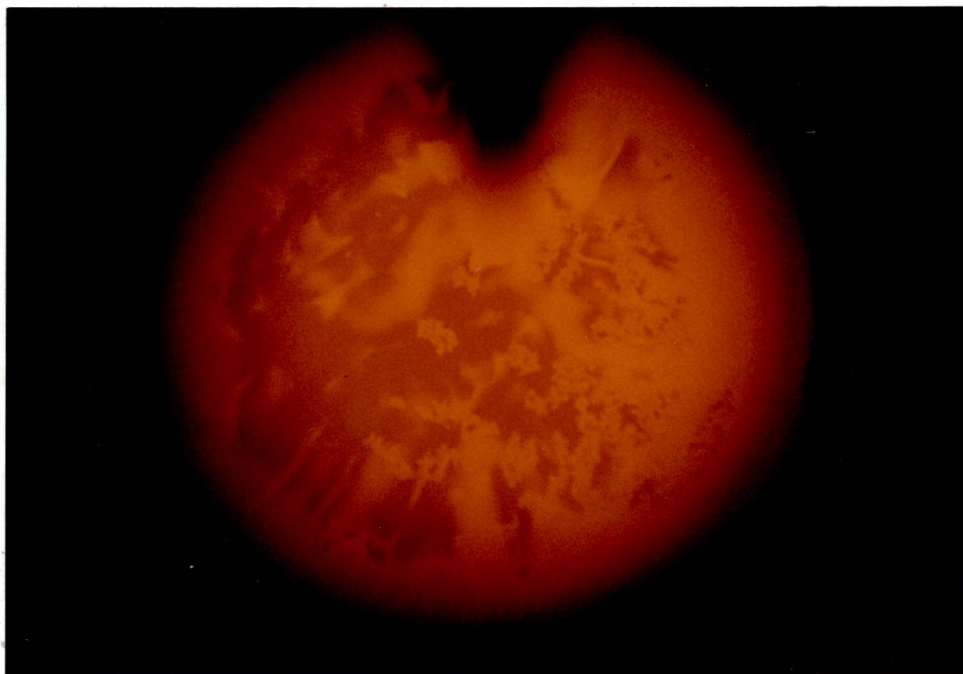


Figure 5.32. Photograph of the surface of the melt at approximately 21 min; spontaneous wavy motion of the melt surface continues throughout the duration of the reaction time. The oxidation rate results indicated that the final reaction time for these experimental conditions was 22 min.

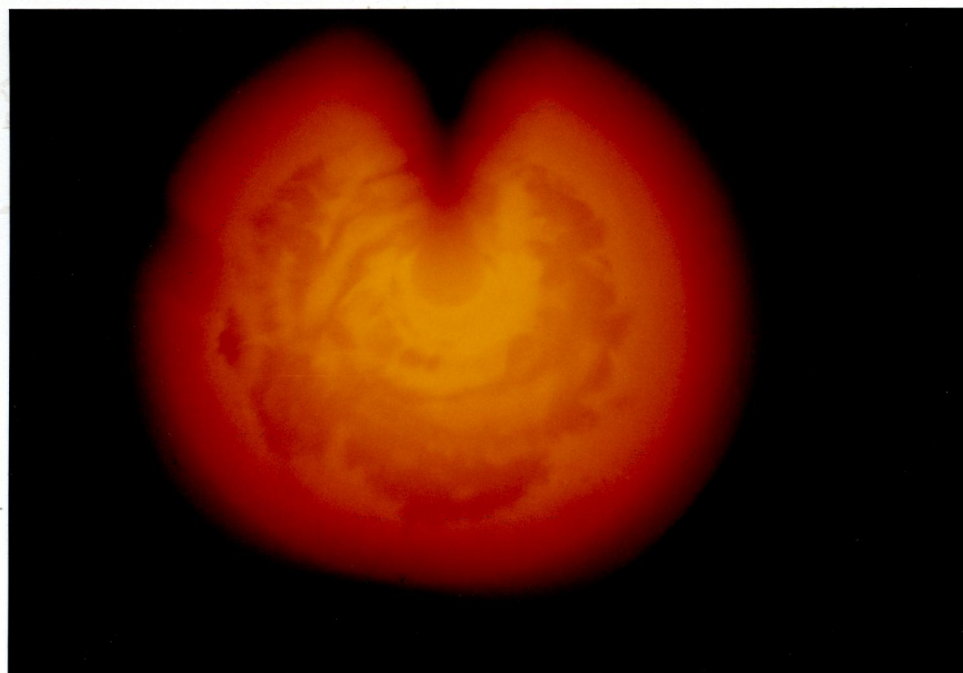


Figure 5.33. Photograph of the surface of the melt at approximately 20 min for the experimental conditions of 200 grams of  $\text{Cu}_2\text{S}$ , at  $1200\text{ }^\circ\text{C}$ , and under the top-lancing of 2 l/min of 22%  $\text{O}_2$  and 78% Ar. The transition and the final reaction times for these experimental conditions are 14 and 70 min respectively.

At the end of the oxidation reaction, the surface movement was observed to completely cease, and the film was observed to be pushed to the crucible wall (no surface spreading is occurring which may be the result of surface tension effects), as shown in Figure 5.34.

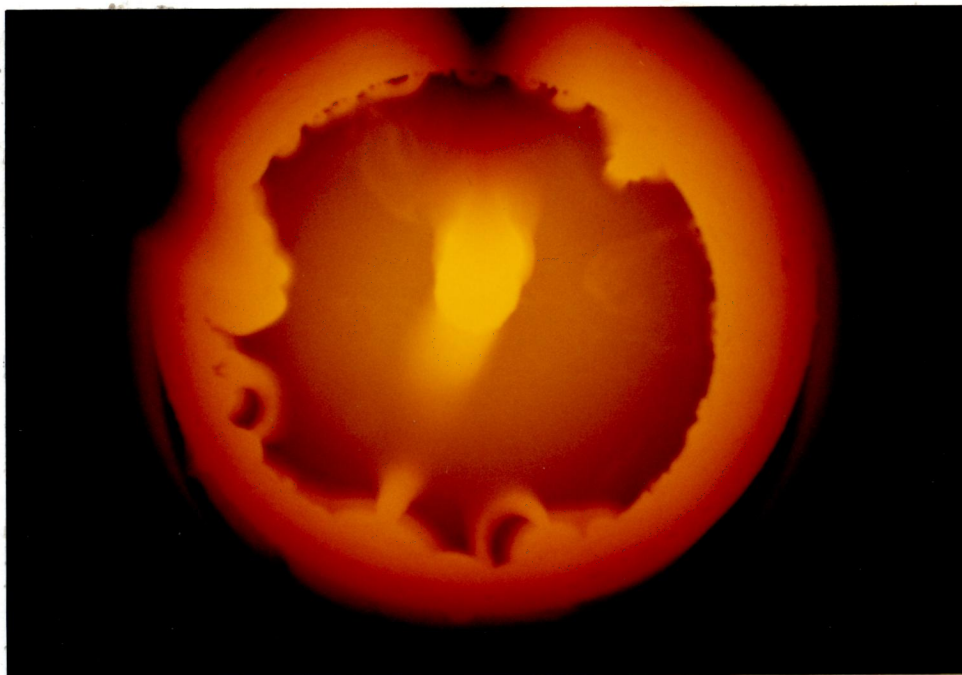


Figure 5.34. Photograph of the surface of the melt at approximately 10 min after the end of reaction. At the end of the secondary stage, the surface movement completely ceases. Note the difference in emissivity between the copper surface (shiny reflecting the lance nozzle at slightly above the center of the melt) and the emissivity of the film, at the crucible wall.

During the secondary stage, bubbles were observed to erupt from the melt surface in a continuous fashion. Occasional intense boiling was observed to occur at the melt surface as shown in Figure 5.35. The intensity and the frequency of boiling were observed to increase with increasing reaction gas flow rate and oxygen content, as shown in Figures 5.35 and 5.36.

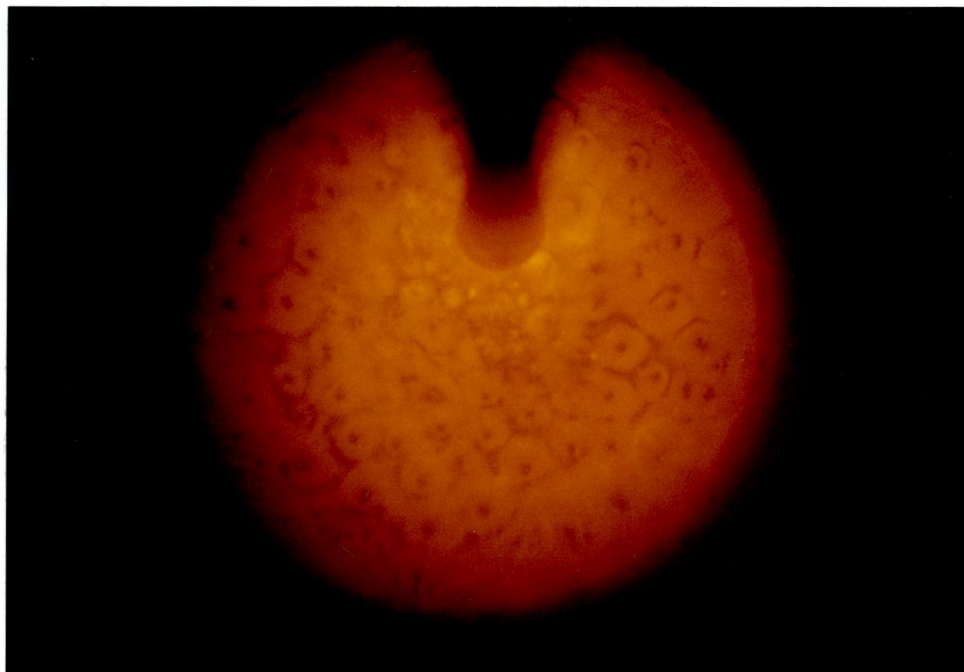


Figure 5.35. Photograph of the surface of the melt at approximately 14.5 min, under the top-lancing of 2 l/min of 80% O<sub>2</sub> and 20% Ar. Intense boiling at the melt surface, caused by the eruption of SO<sub>2</sub> gas bubbles, as a result of the melt reactions.

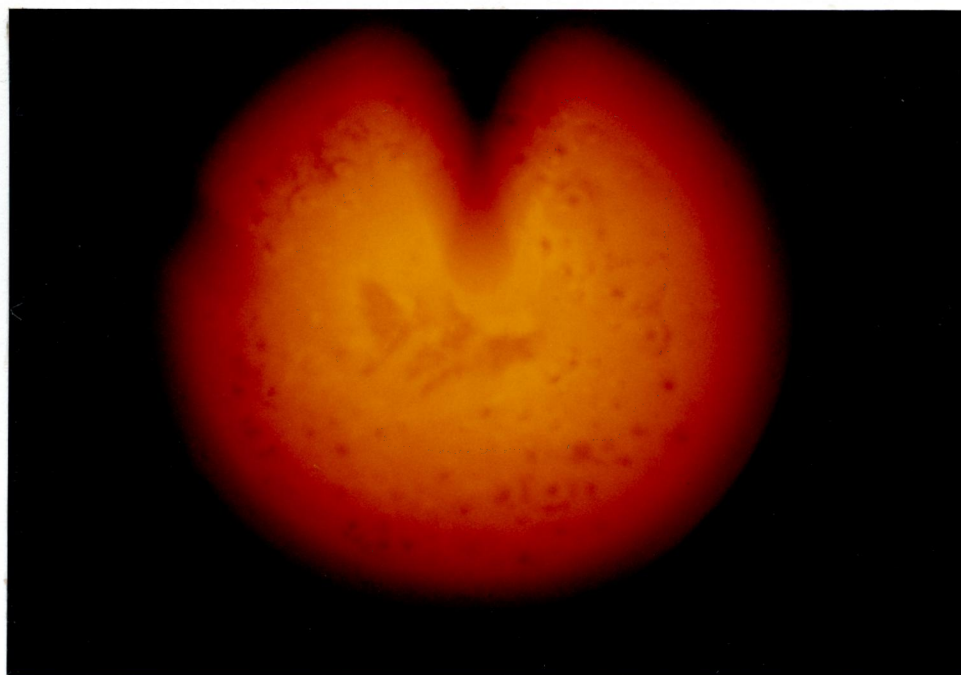


Figure 5.36. Photograph of the surface of the melt at approximately 14.5 min, under the top-lancing of 2 l/min of 80% O<sub>2</sub> and 20% Ar. Intense boiling at the melt surface, caused by the eruption of SO<sub>2</sub> gas bubbles, as a result of the melt reactions.

The frequent intense boiling indicates that as the number of gas bubbles increases, the bubbles coalesce and rise to the melt surface, causing the interruption of surface-tension driven flow. As discussed in Chapter 6, the effect of this phenomenon, on the transport conditions, was relatively strong. The break-up of the melt surface causes an increase in the interfacial area, while the increased surface turbulence causes the enhancement of the transport conditions.

## 6. Gas Phase Mass Transfer

### 6.1. Mathematical Analysis for Mass-Transfer Coefficient

To obtain mass-transfer coefficients from the experimental data, the following mathematical analysis was undertaken.

#### 6.1.1. Material Balance

As the reaction takes place, sulphur is removed from the bath in the form of SO<sub>2</sub>, thereby changing the bath sulphur content. The sulphur molar balance on the bath yields the following.

$$\begin{aligned} & [\text{rate of } S \text{ input} = 0] - [\text{rate of } S \text{ output}] - \\ & [\text{rate of } S \text{ consumption} = 0] + [\text{rate of } S \text{ generation} = 0] \\ & = \text{rate of } S \text{ accumulation} \end{aligned} \quad (6.1)$$

$$-\dot{n}_{SO_2} \cdot A = \frac{dN_S}{dt} \quad (6.2)$$

#### 6.1.2. Flux Equation:

As shown in Figures 5.10, 5.11 and 5.12, the response of the reaction rates to oxygen content in the gas is characteristic of gas phase mass transfer control. The results shown in Figure 5.16 also reveal that the liquid phase mass transfer resistance is negligible.

Thus the rate of reaction can be described by the oxygen molar flux, as follows:

$$\dot{n}_{O_2} = \frac{k_{O_2}}{RT} \cdot [P_{O_2}^b - P_{O_2}^i] \quad (6.3)$$

#### 6.1.3. Equilibrium At Phase Boundaries:

If the chemical reaction rate is fast, the interfacial partial pressure of oxygen must be that of the equilibrium oxygen pressure, dictated by Reaction (5.18). There are no available equilibrium data for this reaction; however, since the intercepts of the regression lines in

Figures 5.10, 5.11 and 5.12 are approximately zero, the partial pressure of oxygen must be negligible in magnitude, compared to the bulk partial pressure of oxygen.

#### 6.1.4. Stoichiometry:

The molar ratio of reacted oxygen to evolved sulphur dioxide,  $\alpha$ , is calculated as follows:

$$\alpha = \frac{\dot{N}_{O_2}}{\dot{N}_{SO_2}} \quad (6.4)$$

During the primary stage, the sulphur removal takes place only as a result of Reaction (5.18). Since  $\alpha^p$  is very close to 1.5, thus

$$\dot{n}_{SO_2}^p = \frac{2}{3} \frac{k_{O_2}}{RT} \cdot P_{O_2}^b \quad (6.5)$$

During the secondary stage, the experimental results indicate that the ratio of the  $O_2$  molar flux to the secondary  $SO_2$  molar flux, is approximately 0.96. The corresponding equation for the molar flux of  $SO_2$  in the secondary stage is, therefore, described as follows:

$$\dot{n}_{SO_2}^s = \frac{1}{0.96} \frac{k_{O_2}}{RT} \cdot P_{O_2}^b \quad (6.6)$$

#### 6.1.5. Solution:

In order to develop an expression for the sulphur content of the bath, the first order differential equation ( Equation (6.2)) is solved by substituting for the respective flux equations, and integrating between the following limits:

$$\begin{aligned} t = 0, \quad N_S &= N_S^i \\ t = t^*, \quad N_S &= N_S^* \end{aligned}$$

For the primary stage the resulting integration is:



$$\int_{N_s^i}^{N_s} dN_s = -\frac{2 k_{O_2}}{3 RT} A \cdot P_{O_2}^b \int_0^t dt \quad (6.7)$$

$$N_s = N_s^i - \frac{2 k_{O_2}}{3 RT} A P_{O_2}^b \cdot t \quad (6.8)$$

Similarly, the secondary stage expression is derived as follows:

$$N_s = N_s^* - \frac{1 k_{O_2}}{0.96 RT} A P_{O_2}^b [t - t^*] \quad (6.9)$$

where  $t^*$  is the transition time. Thus with gas phase mass transfer control, the bath sulphur content varies linearly with time. In general terms,

$$N_s = a + bt \quad (6.10)$$

When compared to Figure 5.4 which exhibits a linear relationship between the measured moles of sulphur in the bath and time, clearly the oxidation of molten  $Cu_2S$  is controlled by gas phase mass transfer of oxygen to the melt surface.

## 6.2. Experimental Gas Phase Mass-Transfer Coefficient

The gas phase mass-transfer coefficient is calculated from the slope of the plot of sulphur molar content in the bath vs. time, as follows:

$$k_{O_2}^p \approx \frac{\alpha^p RT}{A P_{O_2}^b} \frac{\Delta N_s^p}{\Delta t} \quad (6.11)$$

$$k_{O_2}^s \approx \frac{\alpha^s RT}{A P_{O_2}^b} \frac{\Delta N_s^s}{\Delta t} \quad (6.12)$$

Figure 6.1 shows the effect of admitted gas flow rate on the gas phase mass-transfer coefficient.

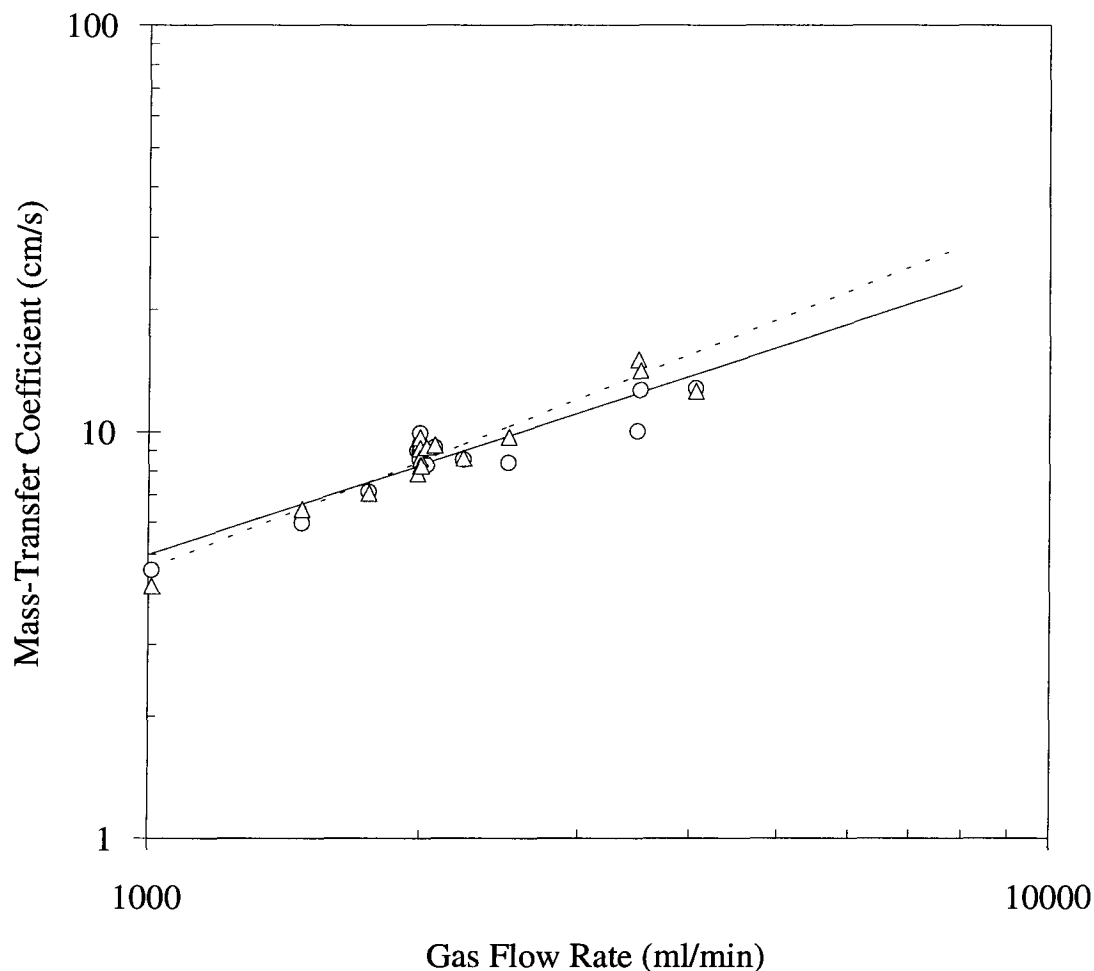


Figure 6.1. The gas phase mass-transfer coefficient as a function of gas flow rate for the experimental conditions of 200 grams of  $\text{Cu}_2\text{S}$  at 1200 °C, 1.084 atm, 3 mm inside diameter lance, 44 mm diameter of the interfacial reaction area and 10 mm distance from the nozzle to the reaction surface;  $\circ$  primary measured;  $\triangle$  secondary measured; — primary calculated from regression curve ( $= 0.03 Q^{0.73}$ ); - - - secondary calculated from regression curve ( $= 0.01 Q^{0.88}$ ).

Although the measured oxygen fluxes for the two stages appear to be identical, their corresponding gas phase mass-transfer coefficients seem to be slightly different. It can be seen that this is similar behaviour to the reaction rates, which exhibited greater exponents for the secondary stage (see Section 5.1.3). The exponents indicate that the relationship between the gas phase mass-transfer coefficient and the gas flow rate, is stronger in the

secondary stage than in the primary stage likely because during the former, gas bubbles erupt from the melt surface (see Figure 5.35 and 5.36), thereby increasing the gas/liquid interfacial area. Due to the difficulty of estimating the changes in the reaction interfacial area, it is not possible to account for this effect. Surface observations of the melt indicated that the frequency of gas bubbling and the interfacial turbulence were enhanced by an increase in the gas flow rate and the oxygen concentration in the gas.

In Figure 6.2, the gas phase mass-transfer coefficient is plotted against the partial pressure of oxygen, from which it appears that there is a slight dependence on the oxygen content.

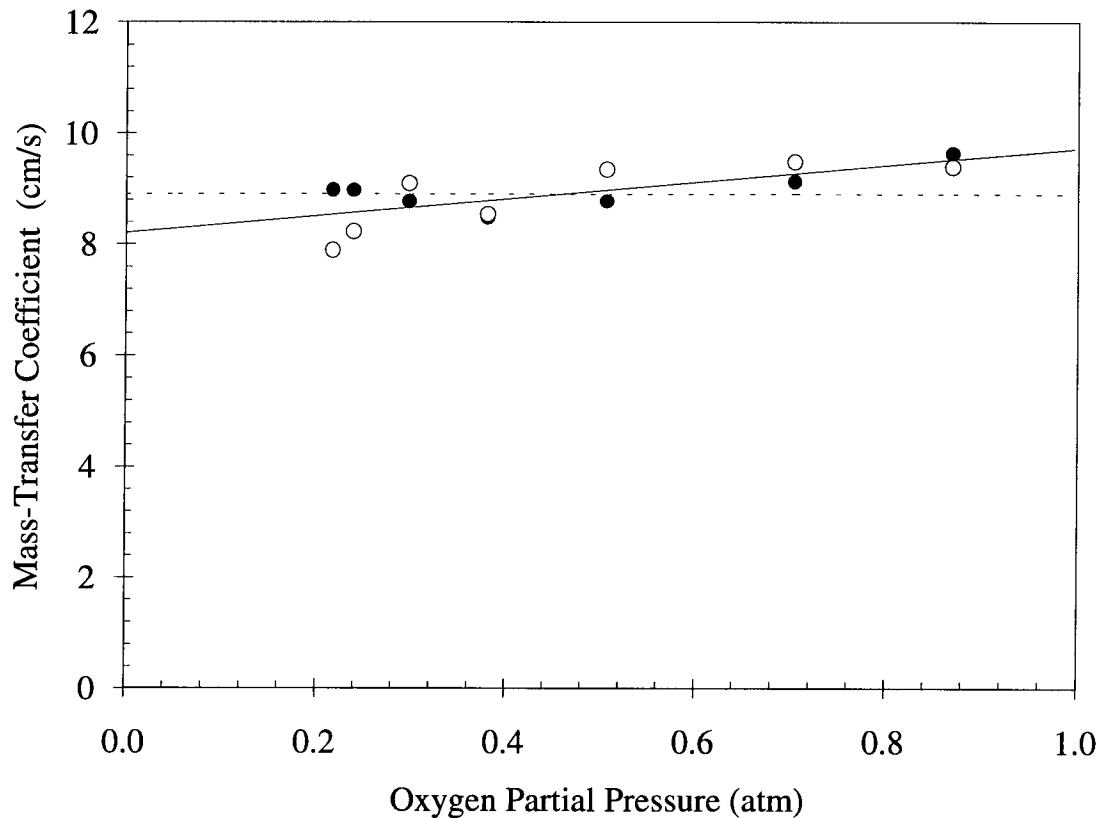


Figure 6.2. The gas phase mass-transfer coefficient vs. the partial pressure of oxygen for the experimental conditions of 200 grams of  $\text{Cu}_2\text{S}$ , average system pressure of 1.09 atm, 3 mm inside diameter lance, 44 mm diameter of the interfacial reaction area and 10 mm distance from the nozzle to the reaction surface; ● primary measured; ○ secondary measured; — regression line (Equation (5.15)); - - - - - average.

Under normal conditions, the gas phase mass-transfer coefficient is effectively independent of the oxygen concentration in the gas phase; however, owing to the Marangoni effect, the gas phase mass transfer coefficient slightly increases with increasing oxygen content in the reaction gas.

$$k_{O_2} = (8.2 \pm 0.2) + (1.5 \pm 0.3)P_{O_2}^b \quad (6.13)$$

The average gas phase mass-transfer coefficient, from the primary and secondary stages, is plotted against the inverse of temperature in Figure 6.3, from which it is clear that the gas phase mass-transfer coefficient has a slight positive dependence on temperature.

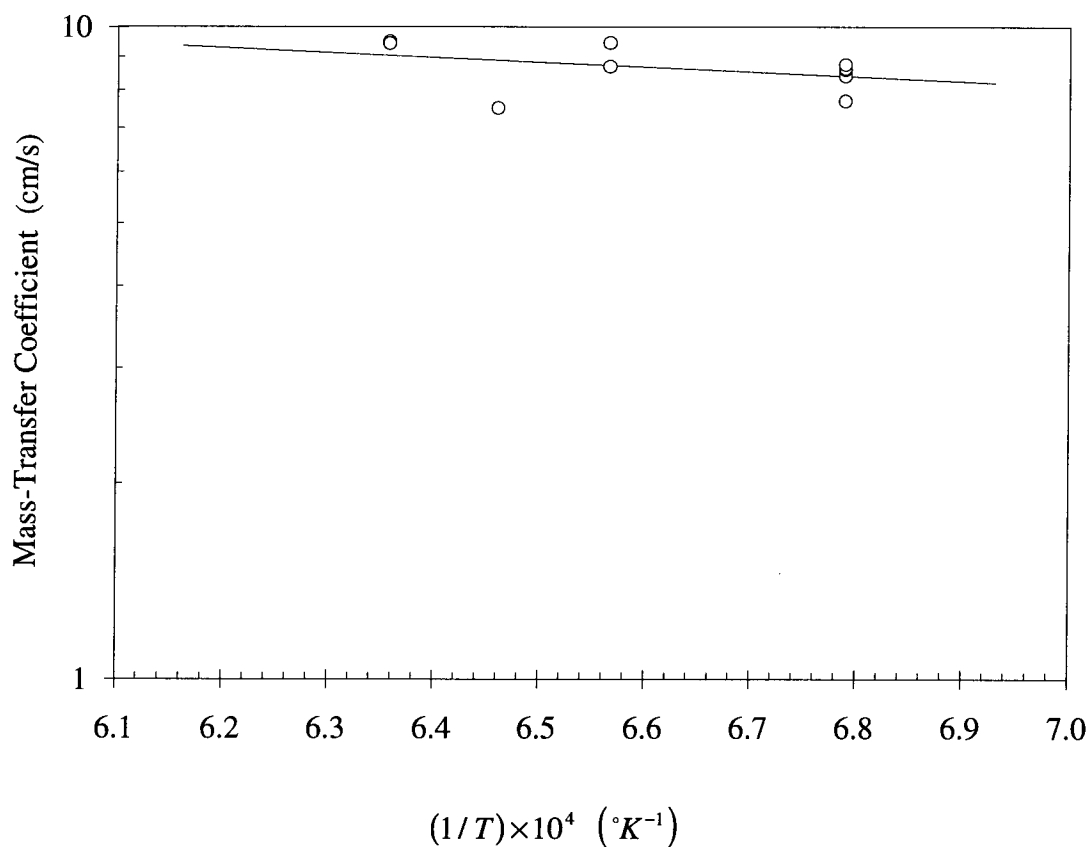


Figure 6.3. The gas phase mass-transfer coefficient vs. the inverse of temperature for the experimental conditions of: 2000 ml/min of 20-23% O<sub>2</sub> and average pressure of 1.08; ○ mean of the measured primary and secondary; — regression curve (Equation (6.14)).

From least squares, the Arrhenius relationship, described by Equation (6.14), yielded an activation energy of  $14 \pm 12$  kJ/mole, which is a characteristic of mass transfer.

$$\ln k_{O_2} = \ln(3.3 \pm 0.9) - \left[ \frac{14 \pm 12 \text{ kJ / mole}}{0.0083144 \text{ kJ / }^\circ\text{K. mole}} \right] \frac{1}{T} \quad (6.14)$$

### 6.3. Gas Phase Mass-Transfer Correlation

The gas phase mass-transfer coefficient is empirically<sup>24</sup> related to the transport conditions of the system via the Sherwood number,  $Sh$ . As discussed in Section 2.3.2.1.2, for laminar top-blown systems,  $Sh$  is related to the Schmidt number,  $Sc$ , and the Reynolds number,  $Re$ , as follows [48]<sup>25</sup>:

$$Sh = m(r_s/d)^{n_s} Re^{n_{re}} Sc^{n_{sc}} \quad (6.15)$$

Figure 6.4 shows a logarithmic plot of  $Sh$  against  $Re$  based on the results of this study. For constant  $Sc$  and  $(r_s/d)$ , the exponents of  $Re$  are 0.73 and 0.88 for the primary stage and secondary stage respectively, as described by Equations (6.16) and (6.17), which indicate that the empirical relationships of the  $Sh-Re$  are identical to the empirical relationships of the  $k_{O_2} - Q$ .

$$Sh^p = 0.03 Re^{0.73} \quad (6.16)$$

$$Sh^s = 0.02 Re^{0.88} \quad (6.17)$$

---

<sup>24</sup>The transport properties of the gas are considered to be those of the reaction gas mixture, for which the calculation procedures are presented in Appendix C.

<sup>25</sup>The Sherwood number,  $Sh$ , is the ratio of the total mass transfer to the mass transfer by molecular diffusion; the Schmidt number,  $Sc$ , is the ratio of the momentum diffusivity to the molecular diffusivity and the Reynolds number,  $Re$ , is the ratio of the inertia force of a fluid to the viscous force.

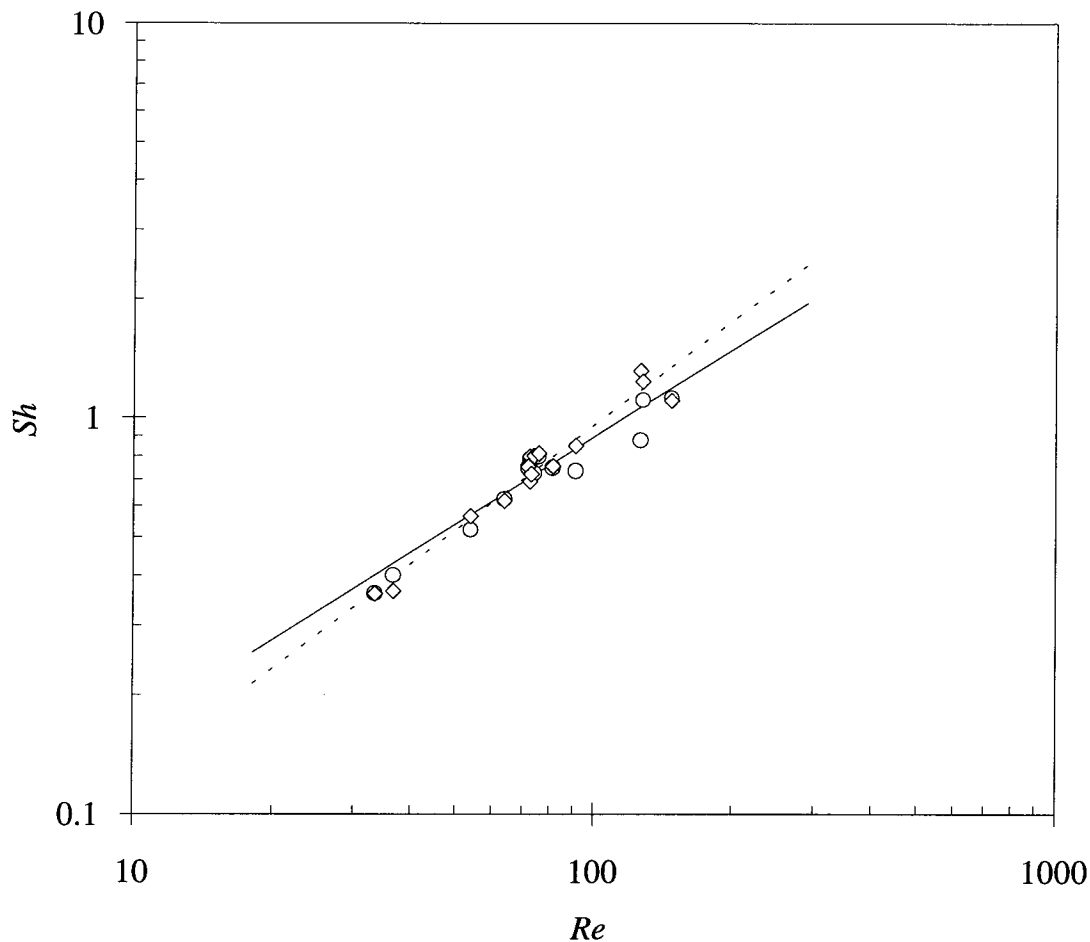


Figure 6.4. The Sherwood number as a function of the Reynolds number for the top-blown conditions of 200 grams of  $\text{Cu}_2\text{S}$  at 1200 °C, 1.084 atm, 3 mm inside diameter lance, 44 mm diameter of the interfacial reaction area and 10 mm distance from the nozzle to the reaction surface and  $Sc = 0.57$ ;  $\circ$  primary measured;  $\triangle$  secondary measured; — primary calculated from regression curve ( $= 0.03 Re^{0.73}$ ); - - - secondary calculated from regression curve ( $= 0.02 Re^{0.88}$ ).

From boundary-layer theory [120], and in most mass transfer correlations, the exponent of the Schmidt number,  $n_{Sc}$ , is of the order of 1/5-1/3. Since the Schmidt number is a function of the physical properties of the fluid involved in mass transfer, at room temperature, the range of  $Sc$  is high enough (0.05-5) to allow the determination of its exponent more accurately from measurements. However, in high temperature systems, the Schmidt number is only of the order of 0.57-0.9 [48] (in the case of  $\text{O}_2\text{-Ar/N}_2$  gas

mixtures at 1200-1300 °C, it is 0.57-0.61). In their evaluation of the Sherwood number at high temperature, Taniguchi et al. [48] assumed that  $n_{sc} = 0.5$ . Similarly, their results gave the best fit when the exponent of  $(r_s/d) \cdot n_s$ , was -1 for room temperature systems and -1.5 for the high temperature systems. Figure 6.5 shows a plot of  $Sh(r_s/d)^{1.5} Sc^{-0.5}$  against  $Re$  from the experimental results obtained in this study.

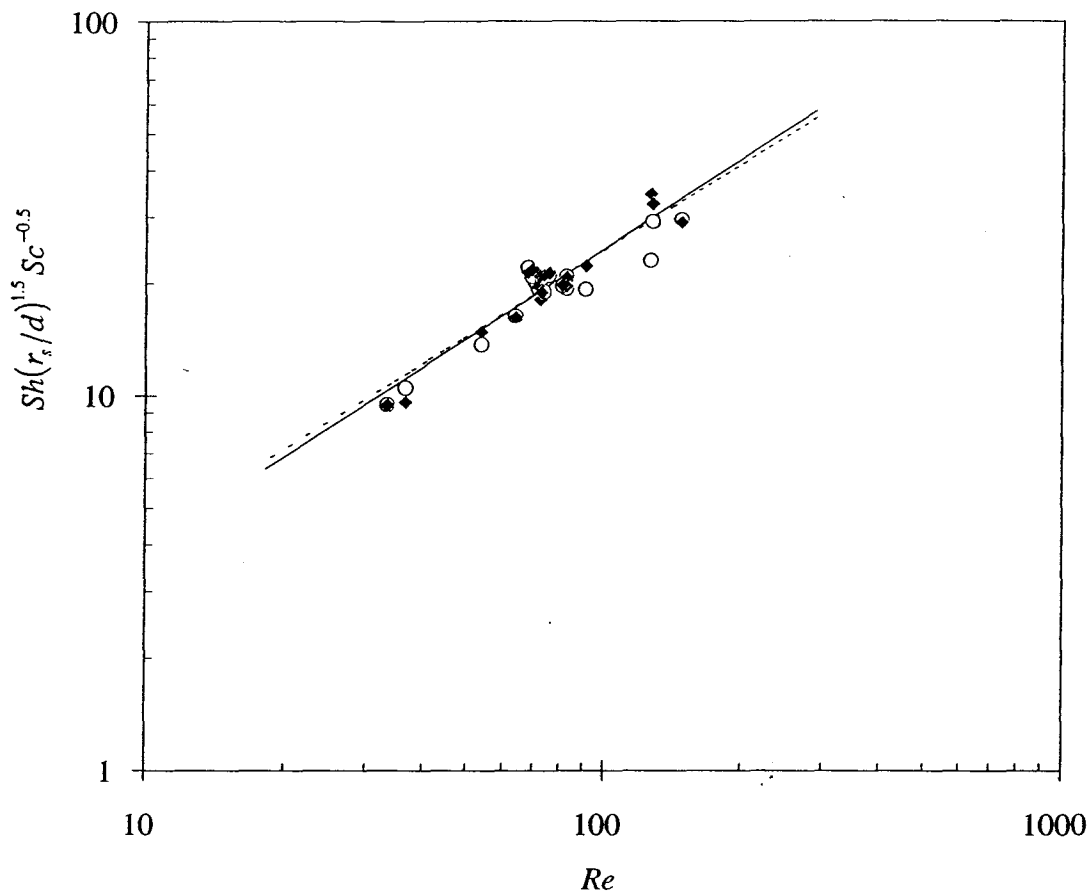


Figure 6.5.  $Sh(r_s/d)^{1.5} Sc^{-0.5}$  plotted against the Reynolds number for top-blown conditions of  $O_2$ -Ar/ $N_2$  onto molten  $Cu_2S$  bath, at 1200-1300 °C, 1.084 atm,  $0.56 \leq Sc \leq 0.63$ ,  $7 \leq r_s/d \leq 11$ , 2-3 mm inside diameter lance, 44 mm diameter of the interfacial reaction area and 10 mm distance from the nozzle to the reaction surface;  $\circ$  primary measured;  $\blacklozenge$  secondary measured; ——— calculated from regression curve ( $Sh = (0.64 \pm 0.07)(d/r_s)^{1.5} Sc^{0.6} Re^{(0.79 \pm 0.06)}$ ); - - - - secondary calculated from regression curve ( $Sh = (m = 0.74) ((d/r_s)^{1.5} Sc^{0.5} Re^{0.76}$ , from decarburization of liquid iron, after Taniguchi et al. [48])).

The resulting correlation is as follows:

$$Sh = (0.64 \pm 0.07)(r_s/d)^{-1.5} Sc^{0.5} Re^{(0.79 \pm 0.06)} \quad (6.18)$$

By comparison Taniguchi et al. [48] found the exponent of  $Re$  to be 0.66 for room temperature systems and 0.76 obtained from the rate of decarburization of liquid iron, (of greater than 0.2 wt% carbon). The results presented in Figure 6.5 clearly agree with the experimental measurements of Taniguchi et al. for  $Re = 13-1500$ ,  $r_s/d = 1.6-5$  and  $H/d = 0.4-30$ , for which ( $Sh = m (r_s/d)^{-1.5} Sc^{0.5} Re^{0.76}$ ). In the system under study these values are  $Re = 33-147$ ,  $r_s/d = 11-7.3$  and  $H/d = 3.33-5$ , and the value for  $m$  that gives the best agreement is 0.74. As shown in Figure 2.7 (a),  $m$  appears to vary slightly with the type of system. For the water-N<sub>2</sub>-NH<sub>3</sub> system, it is 0.27 and it is 0.53 for the toluene-N<sub>2</sub> system. Although the exponents of the correlation obtained from the decarburization of liquid iron are closer to those of the current system,  $m$  appears to differ greatly. For the decarburization of liquid iron,  $m = 0.27 \pm 0.05$ , while it was found to be  $0.74 \pm 0.01$  for the current system.

For the purpose of analyzing the oxidation kinetics of molten Cu<sub>2</sub>S, Equation (6.18) was used in the prediction of the gas phase mass-transfer coefficient. Since all of the apparently relevant parameters are in agreement with those obtained from systems of gas mass transfer control [45-48], this correlation was accepted in the prediction of the gas phase mass-transfer coefficient.

Table 6.1 shows the effect of lance diameter on the gas phase mass-transfer coefficient. The lance nozzle-diameter appears to be an important parameter in the gas phase mass-transfer. Where a 33% decrease in the diameter results in an approximately 20% increase in the gas phase mass-transfer coefficient, the correlation provides a better prediction when  $n_{sc}$  is -1.5 than when it is -1, as shown in Table 6.1.



Table 6.1. The effect of the lance diameter on the gas phase mass transfer coefficient. These runs were conducted at 1200 °C and average oxygen content of 21%.

$Q_r^a$	d	$r_s/d$	$H/d$	$k_{O_2}$ $m = 0.64, n_s = -1.5$ and $n_{Re} = 0.79$	$k_{O_2}$ $m = 0.25, n_s = -1$ and $n_{Re} = 0.78$	$k_{O_2}^p$ measured	$k_{O_2}^s$ measured
(ml/min)	(mm)			(cm/s)	(cm/s)	(cm/s)	(cm/s)
1480	3	7	3	6.57	6.49	5.95	6.45
1520	2	11	5	7.57	23.12	7.42	7.40

#### 6.4. Sensitivity Analysis of the Effect of the Interfacial Area on Gas Phase Mass-Transfer Coefficient

In top-blown systems, the reaction interfacial area is a function of the flow characteristics of the jet and the diameter of the crucible. For highly turbulent systems, the reaction interfacial area may be considered to be the area of the paraboloid, outlined by the jet impingement area, as follows:

$$A = \frac{\pi}{6} \left[ [1 + 4H_c]^{3/2} - 1 \right] \quad (6.19)$$

In laminar flow systems in a certain crucible diameter range, the reaction interfacial area is assumed to be the cross-sectional area of the crucible. The experimental measurements and the numerical computations of Taniguchi et al. [47-48] revealed that for laminar flow conditions, the reaction interfacial area can be assumed to be the cross-sectional area of the crucible, as shown in Figure 6.6. From a numerical solution of the gas phase flow equations, and from visualizing the flow pattern of the gas phase by a tracer (TiCl<sub>4</sub>) [47], it was deduced that this assumption was acceptable.

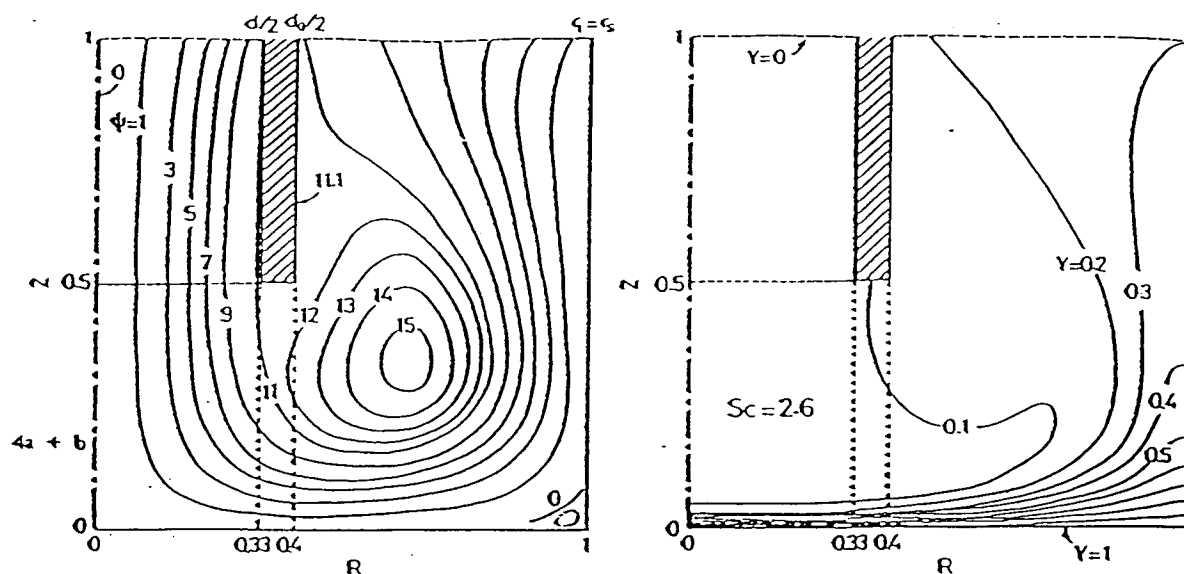


Figure 6.6. Computed streamline patterns and concentration profiles at  $u = 200$  m/c (laminar flow) (after Taniguchi et al. [48]); (a) streamline patterns  $\psi$ , (b) concentration profiles  $Y$ .

From Equation (6.18), the variation in the predicted gas phase mass-transfer coefficient is related to the variation in the reaction interfacial area as follows:

$$\delta k_{O_2} = \left| -\frac{3}{4} (0.64) \pi^{3/4} D_{O_2-Ar} \sqrt{dSc} Re^{0.79} \right| \frac{\delta A}{A^{7/4}} \quad (6.20)$$

The variation in the experimentally determined gas phase mass-transfer coefficient is related to the variation in the interfacial reaction area as follows:

$$\delta k_{O_2} = \left| -\frac{\dot{N}_{O_2} RT}{P_{O_2}^b} \right| \frac{\delta A}{A^2} \quad (6.21)$$

Due to the rising gas bubbles frequently erupting from the melt during the secondary stage, the reaction interfacial area may vary to an uncertain extent. In order to investigate the effect of this possible variation on the gas phase mass-transfer coefficient, a

sensitivity analysis was carried out using Equations (6.20) and (6.21). The results are shown in Figure 6.7 and indicate that a 20% variation in the area, results in approximately 15% and up to 21% uncertainties in the estimation of the measured and predicted gas phase mass-transfer coefficients respectively.

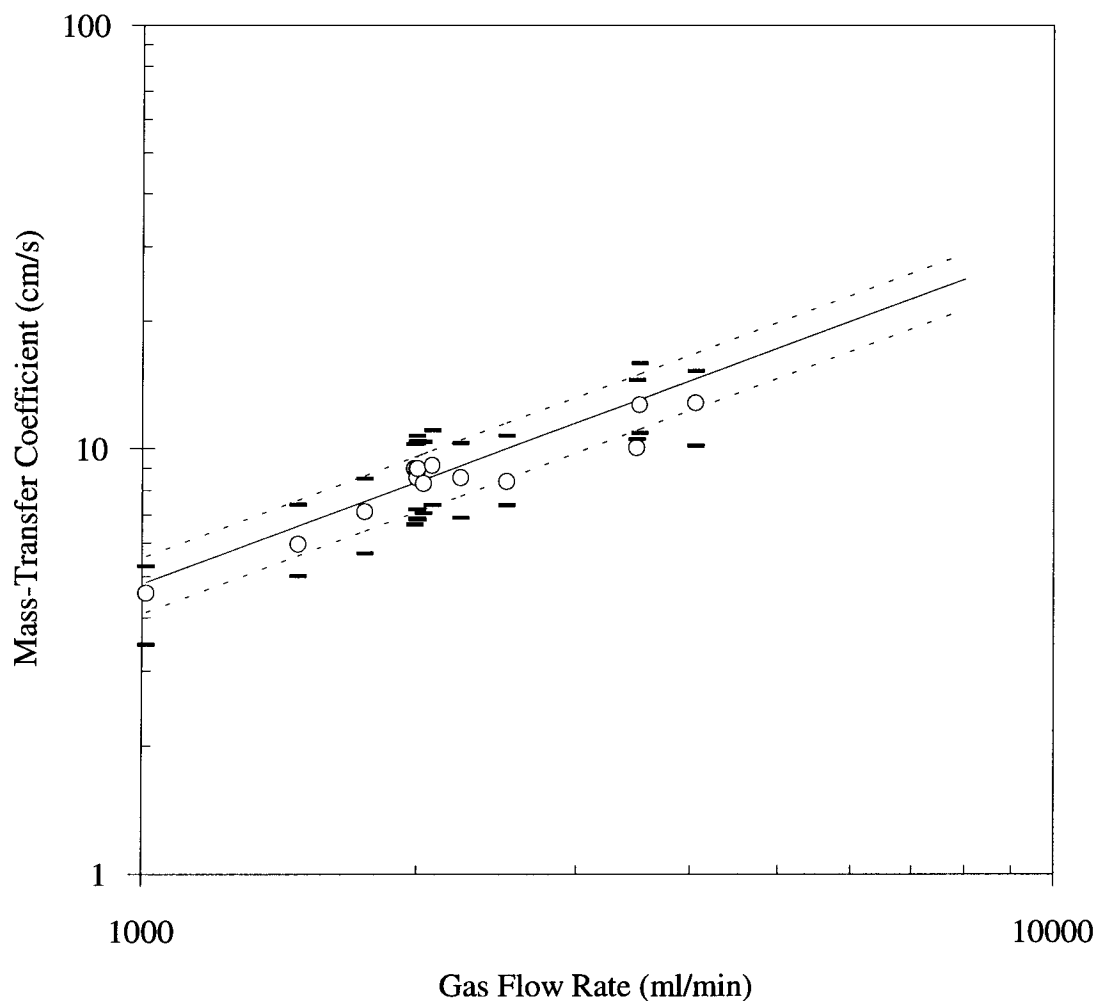


Figure 6.7. The sensitivity of the gas phase mass-transfer coefficient to the reaction interfacial area, for the experimental conditions of 200 grams of  $\text{Cu}_2\text{S}$  at  $1200^\circ\text{C}$ , 3 mm inside diameter lance, 44 mm diameter of the interfacial reaction area and 10 mm distance from the nozzle to the reaction surface;  $\circ$  mean, determined from measurement ( $A = 15.14 \text{ cm}^2$ );  $\blacksquare$  uncertainty bars ( $\delta A = 3.028 \text{ cm}^2$  equivalent to 20 % variation); ——— predicted ( $A = 15.14 \text{ cm}^2$ ); - - - - - predicted uncertainty limits ( $\delta A = 3.028 \text{ cm}^2$  equivalent to 20 % variation).

## 6.5. Sensitivity Analysis of the Effect of Temperature on Gas Phase Mass-Transfer Coefficient

In the calculation of transport coefficients, such as the gas phase mass-transfer coefficient or the heat-transfer coefficient, the temperature at which the thermophysical properties are computed, is often considered to be the mean film temperature. In systems of high gas velocity and a very steep thermal gradient between the reaction region and the gas delivery regions (such as the lance nozzle), it is feasible to consider the temperature of the gas to be at a mean temperature between the hot zone and the gas. However, in the system under investigation, the lance extends over a distance of approximately 400 mm in which the thermal gradient inside the reaction tube<sup>26</sup> is relatively gradual. This allows the gas to reach a temperature close to that of the hot zone. Due to the exothermic heat of reaction, depending on the gas flow rate and oxygen content in the gas, the temperatures of the bath and the gas were observed to increase by up to 60 °C, relative to the start of reaction. Due to the expected small effect of temperature on the reaction rate, and to the short life of the alumina thermocouple sheaths in the vicinity of the reaction, it was not possible to obtain a continuous temperature measurement for some of the runs. However, reasonably sufficient data, on the thermal behaviour of the reaction system, have been gathered<sup>27</sup> to reveal that the temperature rise is proportional to the increase in the oxygen content and gas flow rate of the reaction gas, as given by Equations (6.22)-(6.24) and shown in Figures 6.8 and 6.9.

---

<sup>26</sup>Refer to Section 4.1.1 (Figure 4.1).

<sup>27</sup>Melt and gas temperature measurements are provided in Appendix D.

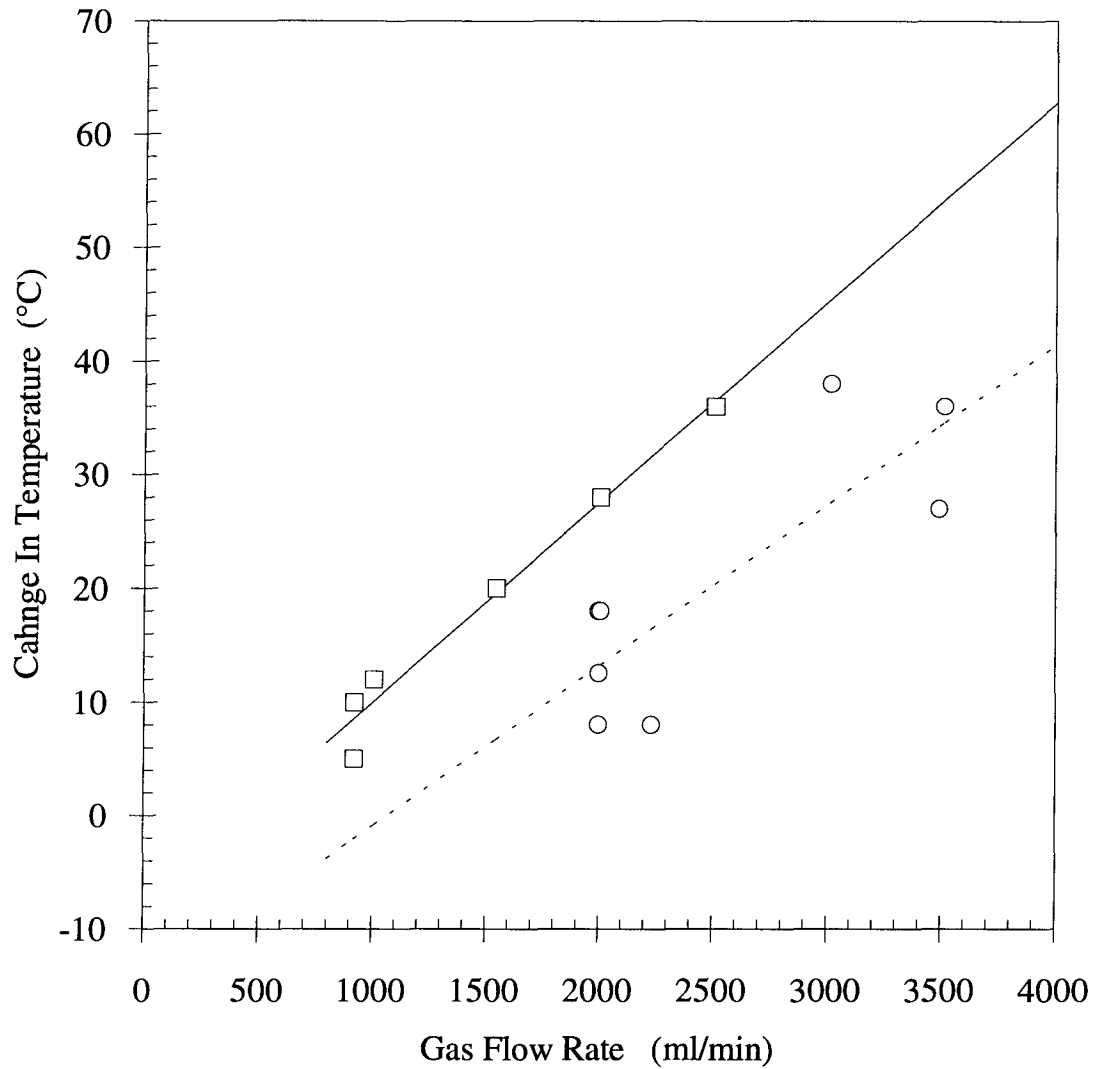


Figure 6.8. The temperature change, due to the heat of reaction, as a function of the reaction gas flow rate;  $\square$  melt temperature change (the tip of the thermocouple sheath was located at the center of the melt); — regression line (Equation (6.22));  $\circ$  gas temperature change (the tip of the thermocouple sheath was located at the same height as that of the lance nozzle<sup>28</sup>); - - - regression line (Equation (6.23)).

<sup>28</sup>Due to the poor heat transfer conditions between the thermocouple and the gas, the gas temperature measurements are expected to be lower than the actual temperature (for more accurate measurements to be conducted, a suction thermocouple should be used).

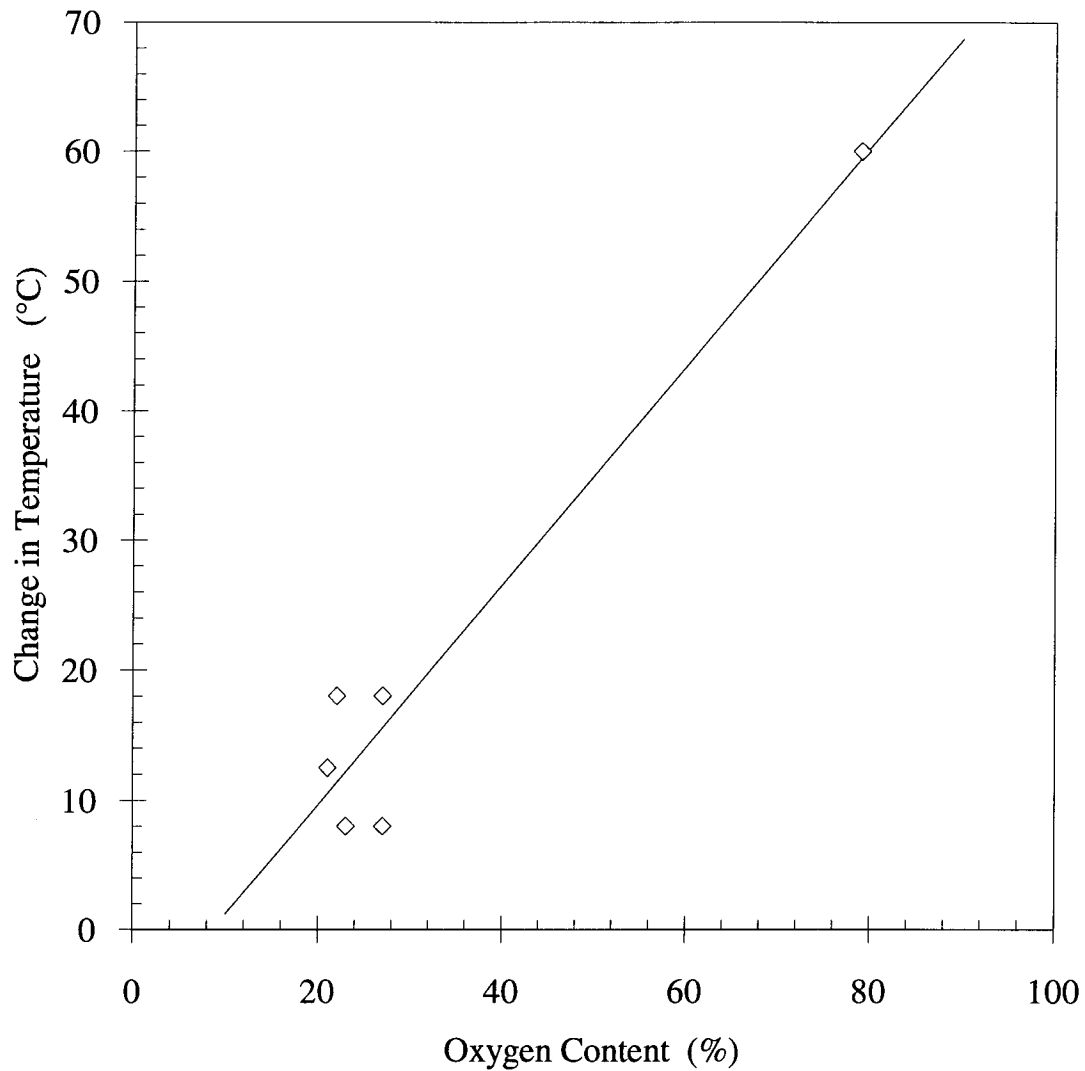


Figure 6.9. The temperature change, due to the heat of reaction, as a function of the reaction gas oxygen content; ◇ gas temperature change (the tip of thermocouple sheath was located at the same height as that of the lance nozzle); — regression line (Equation (6.24)).

$$\Delta T_{melt} = -8 + 0.018Q_r^a \quad (6.22)$$

$$\Delta T_{gas} = -15 + 0.014Q_r^a \quad (6.23)$$

$$\Delta T_{gas} = -7.3 + 0.84(\%O_2) \quad (6.24)$$

Using the estimated correlations for  $\Delta T$ , a temperature sensitivity analysis was carried out to investigate the effect of temperature uncertainty on the calculated values of the gas phase mass-transfer coefficients. The mean temperature of the melt and the gas was calculated from the estimated correlations, and it was used to compute the gas phase mass-transfer coefficients, as shown in Figures 5.11-5.12. The gas phase mass-transfer-temperature sensitivity analysis indicated that a  $\pm 50^\circ\text{C}$  uncertainty in temperature can result in approximately  $\pm 4\%$  uncertainty in the calculation of the gas phase mass-transfer coefficients, which is within the tolerance limit, as shown in Figures 6.10 and 6.11.

According to the gas phase mass-transfer correlation, the gas phase mass-transfer coefficient is expected to be slightly dependent on the gas composition mainly through the Schmidt number. However, at high temperatures, the contribution of  $Sc$  is small compared to  $Re$ . When increasing the oxygen content in the reaction gas, the temperature change and surface-tension driven flows are higher. From the above discussion, it appears that the effect of temperature on the gas phase mass transfer coefficient is negligible. The experimental results suggest that the dependence of the gas phase mass-transfer coefficient on the oxygen content in the gas is slightly higher than predicted by the correlation, as shown in Figure 6.11. It seems that there is only a small dependence, for compositions of approximately 50%  $\text{O}_2$  and higher. Since the temperature effect is insignificant, this dependence is attributed to the effect of surface-tension driven flows and the eruption of gas bubbles. Surface observations indicated that the spontaneous motion is increased with increasing oxygen content of the reaction gas (see Section 5.3).

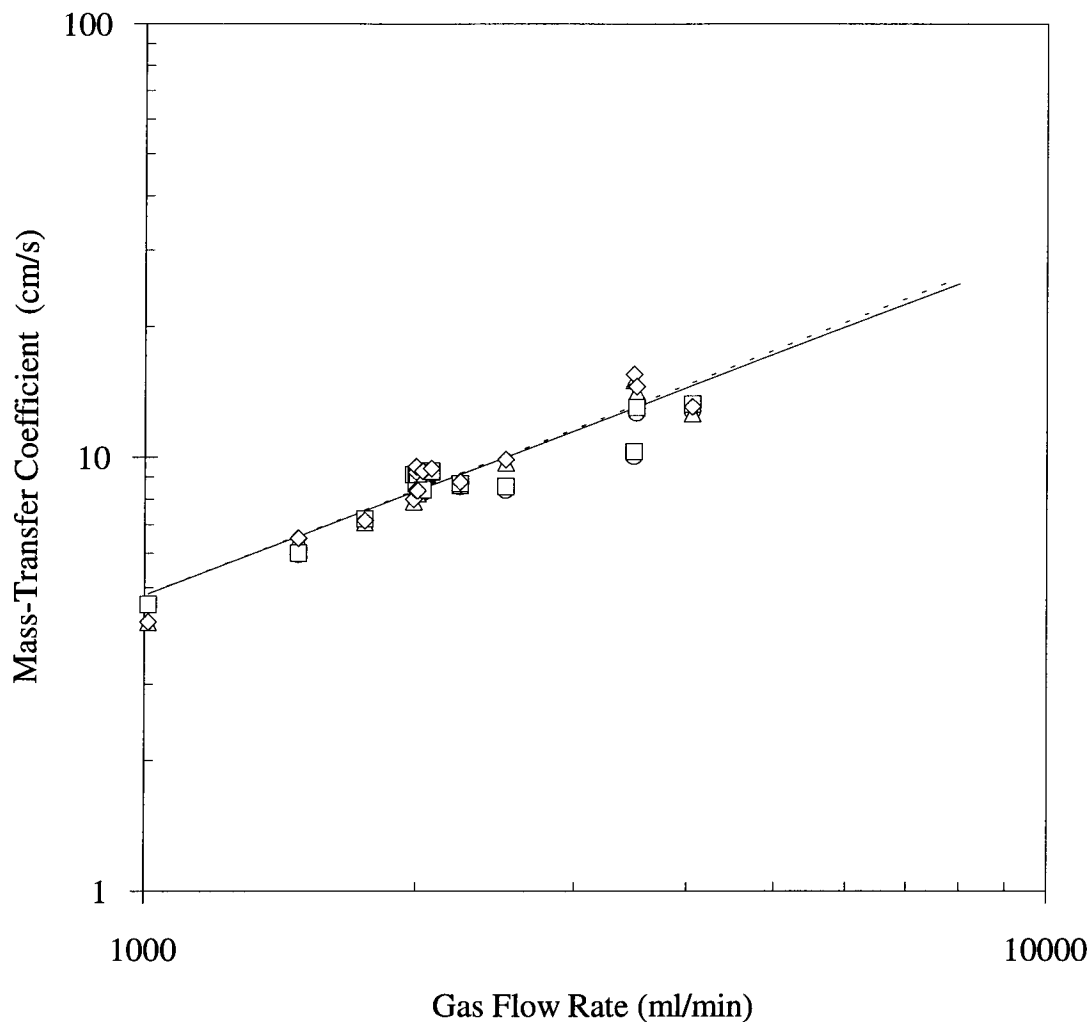


Figure 6.10. The sensitivity of the gas phase mass-transfer coefficient to temperature, for the experimental conditions of 200 grams of  $\text{Cu}_2\text{S}$  at 1200 °C, 20-26%  $\text{O}_2$ , 3 mm inside diameter lance, 44 mm diameter of the interfacial reaction area and 10 mm distance from the nozzle to the reaction surface;  $\circ$  primary measured ( $T = 1200$  °C);  $\square$  secondary measured ( $T = 1200$  °C); ——— predicted ( $T = 1200$  °C);  $\square$  primary measured (mean);  $\diamond$  secondary measured (mean); - - - - - predicted (mean).



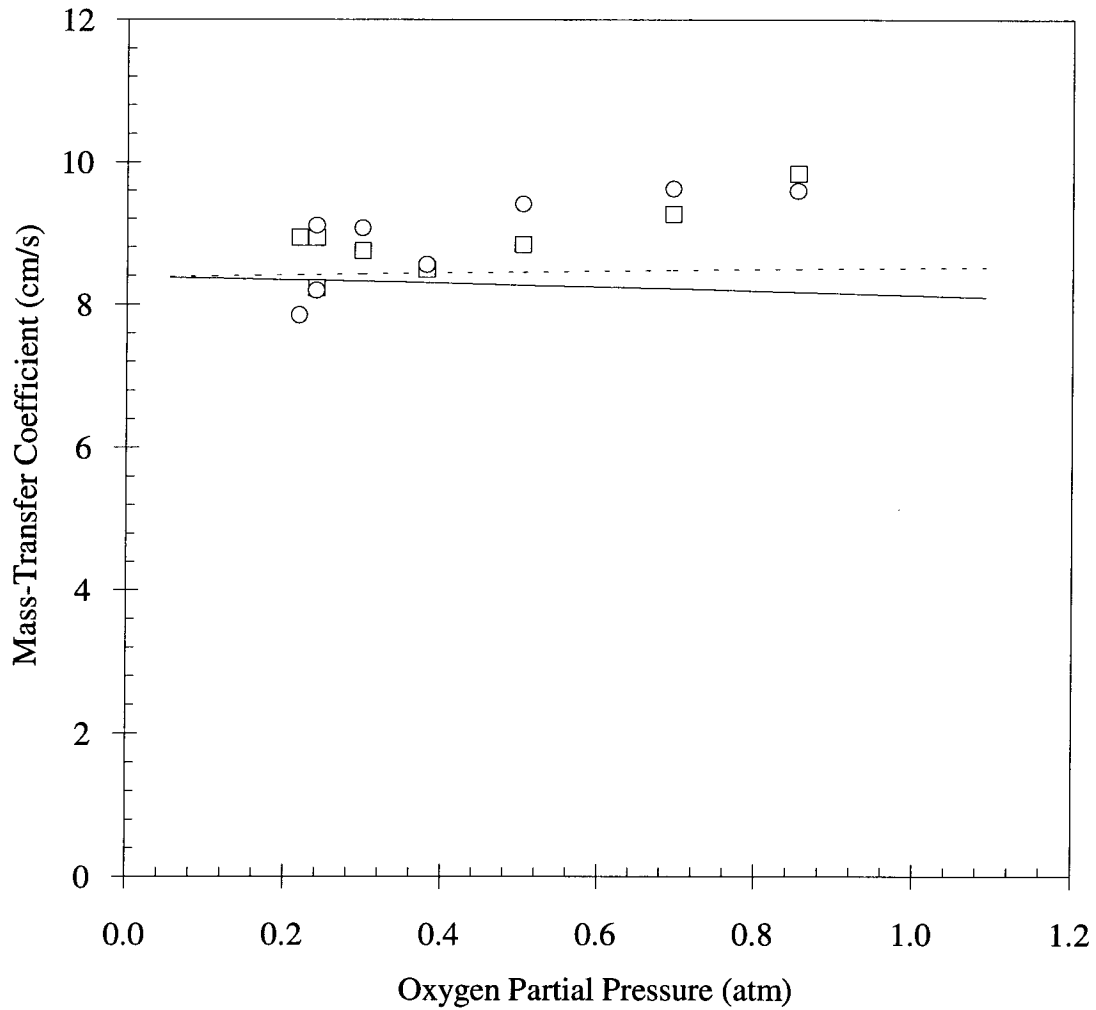


Figure 6.11. The effect of reaction gas composition on the gas phase mass-transfer coefficient, for the experimental conditions of 200 grams of  $\text{Cu}_2\text{S}$ , average system pressure of 1.09 atm, 3 mm inside diameter lance, 44 mm diameter of the interfacial reaction area and 10 mm distance from the nozzle to the reaction surface;  $\square$  primary measured ( $T = 1200\text{ }^\circ\text{C}$ );  $\circ$  secondary measured ( $T = 1200\text{ }^\circ\text{C}$ ); ——— predicted ( $T = 1200\text{ }^\circ\text{C}$ ); - - - - - predicted (mean temperature form Equation (6.26)).

## **7. Mathematical Modeling and Theoretical Predictions**

Having presented and discussed the experimental findings of this work, it is conducive to examine these findings theoretically via mathematical modeling of the oxidation reaction. A theoretical description of the oxidation of molten  $\text{Cu}_2\text{S}$  bath is essential for further understanding of this process and for the support and validation of the experimental measurements. In this chapter, a detailed formulation of the mathematical model is presented. Using the experimental results, validation and sensitivity analyses of this model are also examined. To provide a theoretical description of the oxidation of molten copper sulphide, the oxidation path and the oxidation rates of molten copper sulphide baths are discussed in terms of the model predictions.

### **7.1. Mathematical Model**

#### **7.1.1. Assumptions**

1. The melt is vigorously mixed and consists of a homogeneous solution of  $\text{S}^{2-}$ ,  $\text{O}^{2-}$  and  $\text{Cu}^+$  ions (sulphide phase), during the primary stage. The formation of the copper-rich phase (metal phase) takes place during the secondary stage, as a product of the melt reactions only<sup>29</sup>. The metal phase remains in equilibrium with the sulphide phase until the complete depletion of the sulphide phase at the end of the secondary stage (end of the oxidation reaction).
2. The oxidation reaction is controlled by the gas phase mass transfer of oxygen to the melt surface.

---

<sup>29</sup>Note that Reaction (5.18) is referred to as the surface reaction and Reactions (5.19), (5.21) and (5.22) are referred to as the melt reactions.

3. The melt at the end of the primary stage is assumed to be the equilibrium composition of the sulphide phase saturated with oxygen at the given temperature and pressure.
4. The melt at the end of the secondary stage is assumed to be copper containing equilibrium amounts of oxygen and sulphur.
5. Equilibrium conditions are assumed to prevail at the gas-liquid interface. The surface reaction apparently has a large negative Gibbs free energy with a large equilibrium constant. Thus under gas phase mass transfer control, the interfacial partial pressure of oxygen is very small compared with the bulk partial pressure of oxygen. Due to the absence of thermodynamic data for the activities of  $[S^{2-}]$  and  $[O^{2-}]$  in the melt, it is not possible to calculate the equilibrium partial pressure of oxygen dictated by the surface reaction. The molar flux of oxygen can be described as follow:

$$\dot{n}_{O_2} = \frac{k_{O_2}}{RT} [P_{O_2}^b - P_{O_2}^i] \quad (7.1)$$

6. The transport properties of the gas are assumed to be those of the reaction gas mixture i.e. Ar+O<sub>2</sub>.
7. The transition period from the primary stage to the secondary stage is very small and was assumed to be negligible.
8. Due to the effect of bubbles rising from the melt during the secondary stage, the reaction interfacial area is increased causing the overall rate to increase by a minor amount. This was apparent from the gas phase mass-transfer coefficient determined in the secondary stage which was found to

be slightly higher than that of the primary stage<sup>30</sup>. However, since the measured gas phase mass-transfer coefficient was found to increase only by about 4% in the secondary stage, it is assumed that the gas phase mass-transfer coefficient remains constant throughout the reaction duration.

9. The reaction interfacial area is assumed to be the cross-sectional area of the crucible.

10. Isothermal conditions prevail throughout the duration of the reaction time.

In spite of the fact that the temperature of the system was observed to increase at the beginning of the reaction time and to remain constant throughout the duration of the experiments (as a result of the exothermic reaction), this assumption was adopted because of the small effect that the temperature has on the overall reaction rate.

11. The gas phase is assumed to be at the same temperature as the liquid phase. Due to the low value of the specific heat capacity of gases and to the nature of this reaction system<sup>31</sup>, it is safe to assume that the heat transfer to the reacting gas, in the hot zone, is instantaneous.

### **7.1.2. Reaction Mechanism and Flux Equations**

#### 7.1.2.1. Primary Stage

The formation of copper does not take place until the sulphide phase is saturated with oxygen. This is due to the relatively high oxygen solubility in molten copper sulphide, of approximately 1.47 wt% at 1200°C and 1 atm pressure. During the primary stage, the sulphide melt is partially desulphurized and oxygen saturated until its composition has reached approximately 80.83 wt% Cu, 17.7 wt% S and 1.47 wt% O at 1200 °C and 1 atm

---

<sup>30</sup>For details about the calculation of the measured gas phase mass transfer coefficient, refer to Section 5.1.5.1.

<sup>31</sup>The basis for this assumption has been discussed in detail in Section 5.1.5.2.

[19]. This process is controlled by the gas phase mass transfer of oxygen to the melt surface, where it reacts with sulphide melt, in the absence of any other reactions as shown in Figure (7.1), according to Reaction (5.18).

Due to the Marangoni effect at the bath surface, the sulphur and oxygen concentrations in the melt are assumed to be constant throughout the liquid phase i.e. the liquid phase mass transfer resistance is virtually non-existent. Therefore, as mentioned above, the expression describing the reaction rate is Equation (7.1).

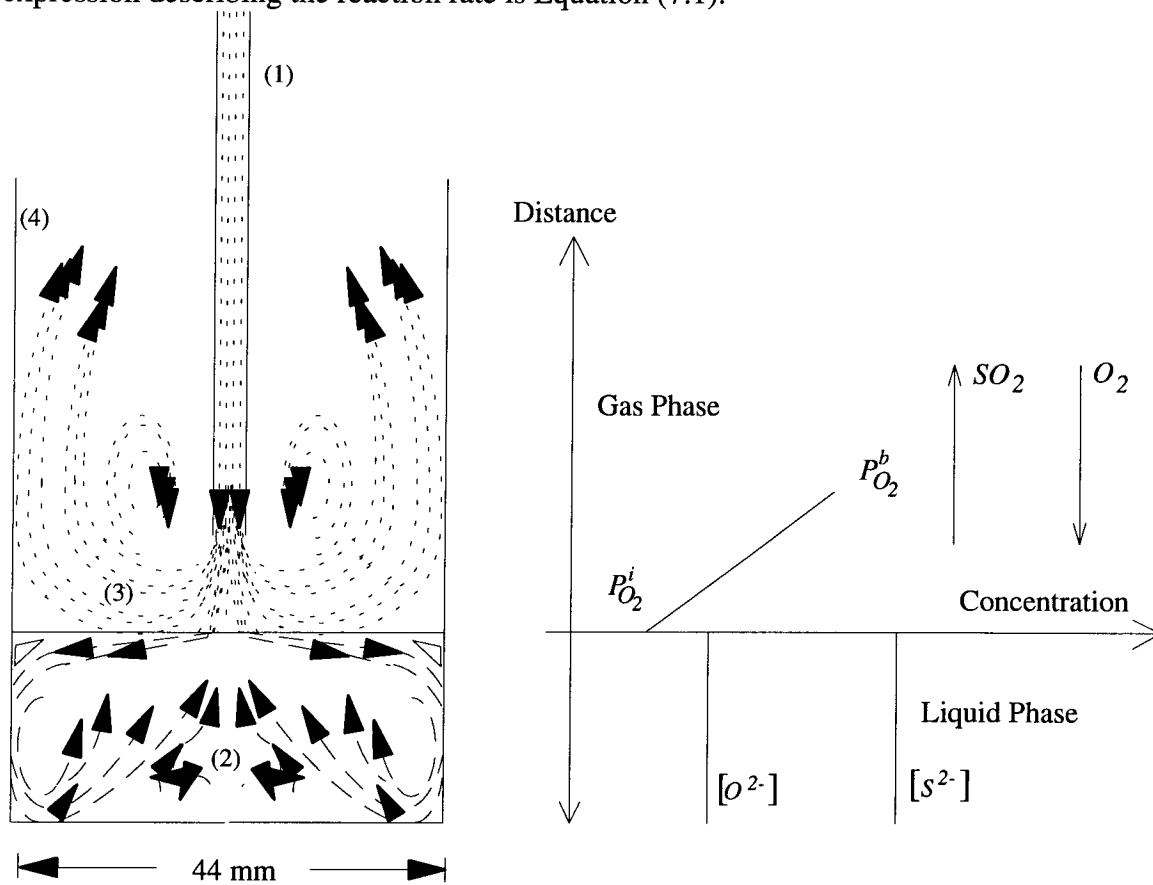


Figure 7.1. Schematic diagram of the primary stage reaction system; (1) alumina lance; (2), vigorously mixed molten sulphide as the result of surface tension driven flows (Marangoni effect); (3) schematic diagram of the reaction gas flow pattern; (4) alumina crucible.

#### 7.1.2.2. Secondary Stage

Immediately upon the melt composition reaching the transition composition of 80.83 wt% Cu, 17.7 wt% S and 1.47 wt% O at 1200 °C and 1 atm, the secondary stage commences.

During the secondary stage, the copper formation reactions (Reactions (5.19), (5.21) and (5.22)) take place beneath the surface throughout the melt. Simultaneously with the formation of copper, oxygen and sulphur dissolve in the metal, according to Reactions (5.21) and (5.22), to yield about 98.89% Cu, 0.95% S and 0.16% O. Reaction (5.19) is triggered when the oxygen concentration at a nucleating site has slightly exceeded the equilibrium concentration of the sulphide phase. Once this reaction initiates, the formation of copper droplets and SO<sub>2</sub> gas bubbles provides more reaction sites to keep the sulphide phase in equilibrium with the metal and gas phases. Because the reactions are electrochemical, ionic mobility and electron transport tremendously retard the liquid phase mass transfer resistance (on the microscopic scale). Growth and coalescence of the gas bubbles are followed by their rise to the melt surface. These phenomena provide an enhancement of the stirring action caused by the surface-tension driven flow. Due to the surface eruptions caused by the rising gas bubbles, the gas-liquid interfacial reaction area increases and enhances the overall reaction rate by up to 6%. The frequency of rising gas bubbles has been observed to increase with increasing flow rate oxygen partial pressure in the reaction gas. Spontaneous mixing of the melt is further enhanced by the coalescence and settlement of the copper droplets. However, because the copper droplets and the gas bubbles exist only during the secondary stage, the melt is believed to be mainly mixed by the effect of surface-tension driven flow phenomena.

The metal phase at the bottom of the bath grows at the expense of the sulphide phase until the secondary stage is ended, at which time all of the sulphide phase is consumed. The secondary stage reaction system is shown schematically in Figures 7.2 and 7.3, from which, it is apparent that the reaction conditions of the secondary stage are slightly different from those of the primary stage. However, the rate limiting step remains the mass transfer of oxygen in the gas phase above the bath.

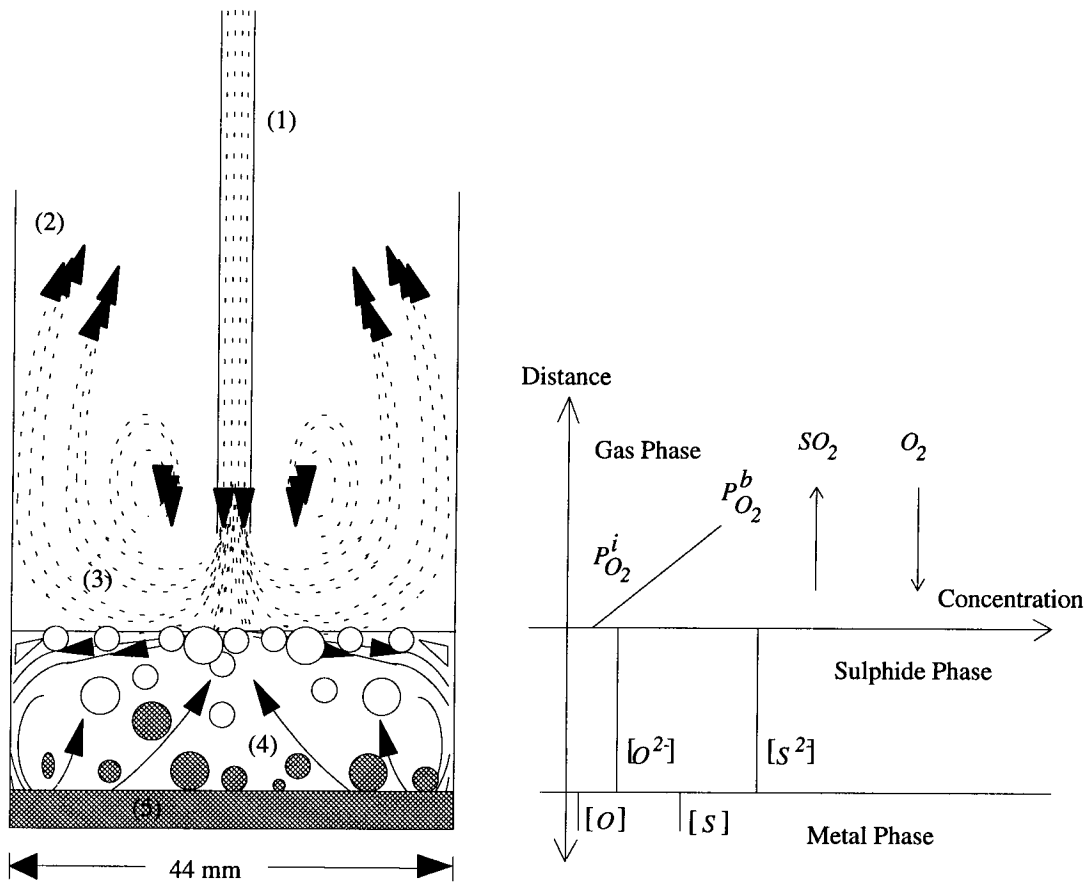


Figure 7.2. Schematic diagram of the secondary stage reaction system; (1) alumina lance; (2) alumina crucible; (3) schematic diagram of the reaction gas flow pattern; (4) sulphide phase; (5) metal phase;  $\circ$  sulphur dioxide gas bubbles;  $\bullet$  copper droplets.

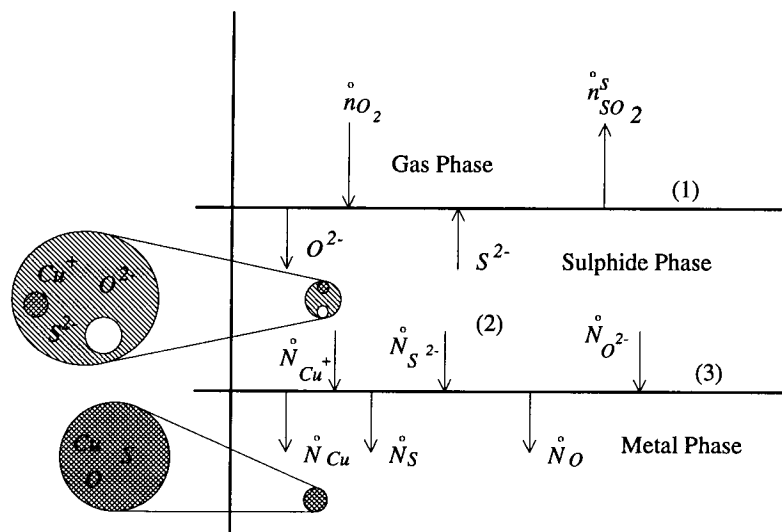


Figure 7.3. Secondary stage; (1) surface reaction interface for Reaction (5.18); (2) reacting sulphide phase (according to Reactions (5.19), (5.21) and (5.22)); (3) sulphide-metal interface (showing the net metal phase formation rates);  $\bullet$  Sulphide phase;  $\circ$  sulphur dioxide gas bubbles;  $\bullet$  copper droplets.

### 7.1.3. Equilibrium at Phase boundaries

It is safe to suggest that equilibrium conditions prevail at the melt surface i.e. at the gas-liquid interface. Therefore the interfacial partial pressure of oxygen is assumed to be the equilibrium partial pressure of oxygen, as dictated by the thermodynamics of Reaction (5.18) and at least one order of magnitude smaller than the bulk partial pressure of oxygen. Then Equation (7.1) is transformed as follows:

$$n_{O_2} \approx \frac{k_{O_2}}{RT} P_{O_2}^b \quad (7.2)$$

Due to the spontaneous mixing of the melt, there is no concentration gradient in either of the liquid phases. The oxygen- and sulphur-saturated metal phase is in equilibrium with both the gas and sulphide phases.

Since the amount of copper formed, due to Reactions (5.19), (5.21) and (5.22), is saturated with oxygen and sulphur, the moles of oxygen and sulphur dissolved in copper can be related to the moles of copper formed via their equilibrium relationships, as follows:

$$N_o = \frac{N_{Cu} M_{Cu} 100}{M_o \left[ \left[ 100 - [\%S]_{Cu} \right] \left[ \frac{100}{[\%O]_{Cu}} - 1 \right] - [\%S]_{Cu} \right]} \quad (7.3)$$

$$N_s = \frac{N_{Cu} M_{Cu} 100}{M_s \left[ \left[ 100 - [\%O]_{Cu} \right] \left[ \frac{100}{[\%S]_{Cu}} - 1 \right] - [\%O]_{Cu} \right]} \quad (7.4)$$



By differentiating Equations (7.3) and (7.4) with respect to time and noting that  $[\%S]_{Cu}$  and  $[\%O]_{Cu}$  are constants, relationships between the rate of copper formation and the rates of oxygen and sulphur dissolution in copper are obtained, as follows:

$$\dot{N}_O = \frac{\dot{N}_{Cu} M_{Cu} 100}{M_O \left[ [100 - [\%S]_{Cu}] \left[ \frac{100}{[\%O]_{Cu}} - 1 \right] - [\%S]_{Cu} \right]} \quad (7.5)$$

$$\text{Let } O_{Cu} = \frac{M_{Cu} 100}{M_O \left[ [100 - [\%S]_{Cu}] \left[ \frac{100}{[\%O]_{Cu}} - 1 \right] - [\%S]_{Cu} \right]} \quad (7.6)$$

$$\therefore \dot{N}_O = O_{Cu} \dot{N}_{Cu} \quad (7.7)$$

$$\dot{N}_S = \frac{\dot{N}_{Cu} M_{Cu} 100}{M_S \left[ [100 - [\%O]_{Cu}] \left[ \frac{100}{[\%S]_{Cu}} - 1 \right] - [\%O]_{Cu} \right]} \quad (7.8)$$

$$\text{let } S_{Cu} = \frac{M_{Cu} 100}{M_S \left[ [100 - [\%O]_{Cu}] \left[ \frac{100}{[\%S]_{Cu}} - 1 \right] - [\%O]_{Cu} \right]} \quad (7.9)$$

$$\therefore \dot{N}_S = S_{Cu} \dot{N}_{Cu} \quad (7.10)$$

The oxygen and sulphur concentrations in the metal phase are calculated from the equilibrium measurements of J. Schmiedl [19], as given by the following equations<sup>32</sup>:

---

<sup>32</sup>Note that  $P_{SO_2}$  (in Equations (7.11)) is in mmHg.

$$[\%O]_{Cu} = 10^{(-1.4 - (1278/T))} \cdot P_{SO_2}^{1/2} \quad (7.11)$$

$$[\%Cu] = 10^{(2 + (24/T))} \quad (7.12)$$

$$[\%S]_{Cu} = 100 - [\%Cu] - [\%O]_{Cu} \quad (7.13)$$

where the SO<sub>2</sub> partial pressure, in the melt, is equal to the system pressure,  $P_s$ , and the average sulphide phase static head on an SO<sub>2</sub> gas bubble located at a mid-distance from the surface,  $P_{st}$ , as follows:

$$P_{SO_2} = P_s + P_{st} \quad (7.14)$$

As seen in Figures 5.18-5.23, the sulphide phase contains the freshly formed copper droplets throughout the secondary stage. Thus, as the metal phase is formed within the sulphide phase, the sulphide melt density is assumed to be the average value for the sulphide phase and metal phase densities, as given by the following equation:

$$P_{st} = \left( \frac{H^i_{Cu_2S}}{2} \right) \left( \frac{\rho_{Cu_2S} + \rho_{Cu}}{2} \right) g \quad (7.15)$$

#### 7.1.4. Stoichiometry

##### 7.1.4.1. Primary Stage

Reaction (5.18) is the surface reaction that takes place when a copper sulphide melt, having a stoichiometric Cu<sub>2</sub>S composition<sup>33</sup>, is brought in contact with oxygen gas. Melt surface observations and micro-examination of quenched bath samples, obtained during the primary stage, indicated very clearly that there is no bubble formation during this period. The stoichiometric relationship between the molar flux of oxygen and the primary molar flux of sulphur dioxide can be obtained from Reaction (5.18) as given by

---

<sup>33</sup>The Cu-S binary, at 1200 °C and 1 atm, indicates that liquid copper sulphide can range in composition from 20 to 22.19 wt % sulphur (refer to Section 2.2).

Equation (7.16). By substituting for  $\dot{n}_{O_2}$  from Equation (7.2) in Equation (7.16), an expression for  $\dot{n}_{SO_2}^{\circ p}$  is obtained as follows:

$$\dot{n}_{SO_2}^{\circ p} = \frac{1}{3/2} \dot{n}_{O_2} \quad (7.16)$$

$$\dot{n}_{SO_2}^{\circ p} = \frac{2}{3} \frac{k_{O_2}}{RT} \cdot P_{O_2}^b \quad (7.17)$$

#### 7.1.4.2. Secondary Stage

During the secondary stage, Reaction (5.18) is no longer the only reaction that is responsible for the sulphur removal from the sulphide phase. Reactions (5.19) and (5.21) take place in the melt, contributing further to sulphur ion removal. By maintaining the sulphide phase composition below the transition composition, the melt reactions sustain the chemical potential for reaction (5.18). Due to the dissolution of oxygen and sulphur in copper, the proportions of Reactions (5.18) and (5.19) are not known. Therefore it is not possible to formulate theoretically a direct stoichiometry between the  $\dot{n}_{O_2}$  and  $\dot{n}_{SO_2}^{\circ s}$ .

The overall reaction for the copper formation can be represented by Reaction (7.18). Therefore the rate of copper ion consumption from the sulphide phase can be directly related to the rate of copper generation, as given by Equation (7.19).



$$\dot{N}_{Cu^+} = \dot{N}_{Cu} \quad (7.19)$$

From the stoichiometry of Reactions (5.21) and (5.22), the relationships between the rates of oxygen and sulphur ions consumption from the sulphide phase are related to the rates of oxygen and sulphur dissolution in the metal phase, as follows:

$$\dot{N}_{O^{2-}} = \dot{N}_O \quad (7.20)$$

$$\dot{N}_{S^{2-}} = \dot{N}_S \quad (7.21)$$

### 7.1.5. Material Balance

For simplicity, this mathematical model will be constructed to describe each of the two stages in a distinct manner. For the primary stage, a material balance on the sulphide phase yields the formulation of a model that predicts the sulphur and oxygen contents of the bath. For the secondary stage, a material balance on the sulphide phase shall be performed to develop expressions for the rates of copper, oxygen and sulphur consumption from the sulphide phase. The description of the metal phase generation can be obtained by performing a material balance on the metal phase. By combining the results of the material balances on the sulphide phase and the metal phase an overall description of the bath, during the secondary stage, can be formulated.

#### 7.1.5.1. Primary Stage

##### 7.1.5.1.1. Sulphur Balance

Assuming that there is no concentration gradient of sulphur in the bath, a molar balance for sulphur in the bath yields the following:

$$\begin{aligned} & [\text{rate of } S^{2-} \text{ input} = 0] - [\text{rate of } S^{2-} \text{ output}] + \\ & [\text{rate of } S^{2-} \text{ generation} = 0] - [\text{rate of } S^{2-} \text{ consumption} = 0] = \\ & \text{rate of } S^{2-} \text{ accumulation} \end{aligned} \quad (7.22)$$

Since the sulphur removed from the bath is in the form of  $SO_2$ , the rate of  $S^{2-}$  output from the bath is directly related to the  $SO_2$  molar flux as follows:

$$\text{rate of } S^{2-} \text{ output} = n_{SO_2}^{\circ P} \cdot A \quad (7.23)$$

Substituting for Equation (7.23) in Equation (7.22);

$$-n_{SO_2}^{\circ P} \cdot A = \frac{dN_{S^{2-}}}{dt} \quad (7.24)$$

### 7.1.5.1.2. Oxygen Balance

Similarly for oxygen;

$$\begin{aligned} & [\text{rate of } O^{2-} \text{ input}] - [\text{rate of } O^{2-} \text{ output}] + \\ & [\text{rate of } O^{2-} \text{ generation} = 0] - [\text{rate of } O^{2-} \text{ consumption} = 0] = \\ & \text{rate of } O^{2-} \text{ accumulation} \end{aligned} \quad (7.25)$$

Oxygen is dissolved in the bath as  $O^{2-}$  and is removed from the bath in the form of  $SO_2$ . Therefore the rate of  $O_2$  input is the product of the molar flux of  $O_2$  and the cross-sectional area of the crucible, as given by Equation (7.26). The rate of  $O_2$  output can be expressed in terms of the molar flux of  $SO_2$ , as given by Equation (7.27).

$$\text{rate of } O^{2-} \text{ input} = 2\dot{n}_{O_2} \cdot A \quad (7.26)$$

$$\text{rate of } O^{2-} \text{ output} = 2\dot{n}_{SO_2}^P \cdot A \quad (7.27)$$

Substituting Equations (7.26) and (7.27) in Equation (7.25), the following expression is obtained:

$$2\dot{n}_{O_2} \cdot A - 2\dot{n}_{SO_2}^P \cdot A = \frac{dN_{O^{2-}}}{dt} \quad (7.28)$$

### 7.1.5.2. Secondary Stage

#### 7.1.5.2.1. Sulphide Phase

##### 7.1.5.2.1.1. Sulphur Ion Balance

As shown in Figure 7.3, some of the sulphur reacts to form  $SO_2$ , according to Reactions (5.18), (5.19), and some dissolves in the metal phase according to Reaction (5.21). A material balance for the sulphur yields the following:

$$\begin{aligned}
& [\text{rate of } S^{2-} \text{ input} = 0] - [\text{rate of } S^{2-} \text{ output}] + \\
& [\text{rate of } S^{2-} \text{ generation} = 0] - [\text{rate of } S^{2-} \text{ consumption}] = \\
& \text{rate of } S^{2-} \text{ accumulation}
\end{aligned} \tag{7.29}$$

The rate of sulphur output is related to the secondary SO<sub>2</sub> molar flux as follows:

$$\text{rate of } S^{2-} \text{ output} = \overset{\circ}{n}_{SO_2} \cdot A \tag{7.30}$$

$$\text{rate of } S^{2-} \text{ consumption} = \overset{\circ}{N}_{S^{2-}} \tag{7.31}$$

Substituting Equations (7.30) and (7.31) in Equation (7.29), we obtain the following expression:

$$-\overset{\circ}{n}_{SO_2} \cdot A - \overset{\circ}{N}_{S^{2-}} = \frac{dN_{S^{2-}}}{dt} \tag{7.32}$$

#### 7.1.5.2.1.2. Oxygen Ion Balance

The oxygen input to the sulphide phase is a known quantity, given by the transport conditions of the reaction system. As outlined in Figure 7.3, some of the oxygen reacts with the sulphur at the melt surface, according to Reaction (5.18); some of it is removed from the bath in the form of SO<sub>2</sub>, according to Reaction (5.19), and some of it dissolves in the metal phase, according to Reaction (5.21). Hence, the oxygen balance yields the following:

$$\begin{aligned}
& [\text{rate of } O^{2-} \text{ input}] - [\text{rate of } O^{2-} \text{ output}] + \\
& [\text{rate of } O^{2-} \text{ generation} = 0] - [\text{rate of } O^{2-} \text{ consumption}] = \\
& \text{rate of } O^{2-} \text{ accumulation}
\end{aligned} \tag{7.33}$$

The rate of oxygen input is related to the O<sub>2</sub> molar flux, as follows:

$$\text{rate of } O^{2-} \text{ input} = 2\overset{\circ}{n}_{O_2} \cdot A \tag{7.34}$$

The rate of oxygen output is related to the secondary SO<sub>2</sub> molar flux, as follows:

$$\text{rate of } O^{2-} \text{ output} = 2\dot{n}_{SO_2} \cdot A \quad (7.35)$$

The rate of oxygen consumption is described as follows:

$$\text{rate of } O^{2-} \text{ consumption} = \dot{N}_{O^{2-}} \quad (7.36)$$

Substituting Equations (7.34), (7.35) and (7.36) into Equation (7.33), an expression for the oxygen balance is obtained, as follows:

$$2\left(\dot{n}_{O_2} - \dot{n}_{SO_2}\right) \cdot A - \dot{N}_{O^{2-}} = \frac{dN_{O^{2-}}}{dt} \quad (7.37)$$

#### 7.1.5.2.1.3. Copper Ion Balance

Similarly for copper;

$$\begin{aligned} & [\text{rate of } Cu^+ \text{ input} = 0] - [\text{rate of } Cu^+ \text{ output} = 0] + \\ & [\text{rate of } Cu^+ \text{ generation} = 0] - [\text{rate of } Cu^+ \text{ consumption}] = \\ & \text{rate of } Cu^+ \text{ accumulation} \end{aligned} \quad (7.38)$$

$$\text{rate of } Cu^+ \text{ consumption} = \dot{N}_{Cu^+} \quad (7.39)$$

$$-\dot{N}_{Cu^+} = \frac{dN_{Cu^+}}{dt} \quad (7.40)$$

#### 7.1.5.2.2. Metal Phase

##### 7.1.5.2.2.1. Sulphur Balance

As shown in Figure 7.3, the sulphur dissolves in the metal phase in the form of neutral sulphur atoms, according to Reaction (5.21). A material balance for the sulphur yields the following:

$$\begin{aligned} & [\text{rate of } S \text{ input} = 0] - [\text{rate of } S \text{ output} = 0] + \\ & [\text{rate of } S \text{ dissolution}] - [\text{rate of } S \text{ consumption} = 0] = \\ & \text{rate of } S \text{ accumulation} \end{aligned} \quad (7.41)$$

$$\text{rate of } S \text{ dissolution} = \dot{N}_S \quad (7.42)$$

$$\dot{N}_S = \frac{dN_S}{dt} \quad (7.43)$$

#### 7.1.5.2.2.2. Oxygen Balance

Similarly for oxygen;

$$\begin{aligned} & [\text{rate of } O \text{ input} = 0] - [\text{rate of } O \text{ output} = 0] + \\ & [\text{rate of } O \text{ dissolution}] - [\text{rate of } O \text{ consumption} = 0] = \\ & \text{rate of } O \text{ accumulation} \end{aligned} \quad (7.44)$$

$$\text{rate of } O \text{ dissolution} = \dot{N}_O \quad (7.45)$$

$$\dot{N}_O = \frac{dN_O}{dt} \quad (7.46)$$

#### 7.1.5.2.2.3. Copper Balance

The copper material balance is described as follows:

$$\begin{aligned} & [\text{rate of } Cu \text{ input} = 0] - [\text{rate of } Cu \text{ output} = 0] + \\ & [\text{rate of } Cu \text{ generation}] - [\text{rate of } Cu \text{ consumption} = 0] = \\ & \text{rate of } Cu \text{ accumulation} \end{aligned} \quad (7.47)$$

$$\text{rate of } Cu \text{ generation} = \dot{N}_{Cu} \quad (7.48)$$

$$\dot{N}_{Cu} = \frac{dN_{Cu}}{dt} \quad (7.49)$$



## 7.1.6. Mathematical Solution

### 7.1.6.1. Primary Stage

For  $0 \leq t \leq t^*$ , where  $t^*$  is the transition time, expressions for the moles of sulphur and oxygen in the bath are developed by integrating Equations (7.24) and (7.28) subject to the following initial condition:

$$\text{at } t = 0, \quad N_{S^{2-}} = N_{S^{2-}}^i \quad \text{and} \quad N_{O^{2-}} = 0$$

$$\int_{N_{S^{2-}}^i}^{N_{S^{2-}}} dN_{S^{2-}} = -\overset{\circ}{n}_{SO_2} \cdot A \int_0^t dt \quad (7.50)$$

Because  $\overset{\circ}{n}_{SO_2} \neq f(N_{S^{2-}})$ , the expression for the moles of sulphur in the bath is given by the following equation:

$$N_{S^{2-}} = N_{S^{2-}}^i - \left( \overset{\circ}{n}_{SO_2} \cdot A \right) \cdot t \quad (7.51)$$

Equation (7.28) is integrated subject to the initial condition, as follows:

$$\int_0^{N_{O^{2-}}} dN_{O^{2-}} = 2 \left( \overset{\circ}{n}_{O_2} - \overset{\circ}{n}_{SO_2} \right) \cdot A \int_0^t dt \quad (7.52)$$

Because  $\overset{\circ}{n}_{SO_2} \neq f(N_{O^{2-}})$  and  $\overset{\circ}{n}_{O_2} \neq f(N_{O^{2-}})$ , the expression for the moles of oxygen in the bath is given by the following equation:

$$N_{O^{2-}} = 2 \left( \overset{\circ}{n}_{O_2} - \overset{\circ}{n}_{SO_2} \right) A \cdot t \quad (7.53)$$

Substituting for  $\overset{\circ}{n}_{SO_2}$  and  $\overset{\circ}{n}_{O_2}$  in Equations (7.51) and (7.53), the final formulations for the sulphur and oxygen in the bath are developed.

$$N_{S^{2-}} = N_{S^{2-}}^i - \left( \frac{2}{3} \frac{k_{O_2}}{RT} A \cdot P_{O_2}^b \right) \cdot t \quad (7.54)$$

$$N_{O_2} = \left( \frac{2}{3} \frac{k_{O_2}}{RT} A \cdot P_{O_2}^b \right) \cdot t \quad (7.55)$$

The primary rates of sulphur removal and oxygen dissolution, as functions of the oxygen partial pressure, are derived as follows:

$$\frac{dN_{S^{2-}}^p}{dt} = - \left( \frac{2}{3} \frac{k_{O_2} A}{RT} \right) P_{O_2}^b \quad (7.56)$$

$$\frac{dN_{O_2}^p}{dt} = \left( \frac{2}{3} \frac{k_{O_2} A}{RT} \right) P_{O_2}^b \quad (7.57)$$

Substituting for the gas phase mass-transfer coefficient expression (Equation (6.18)) in Equations (7.56) and (7.57), the primary rates of sulphur removal and oxygen dissolution can be expressed in terms of the reaction gas flow rate, as follows:

$$\frac{dN_{S^{2-}}^p}{dt} = - \left( \frac{2}{3} \frac{P_{O_2}^b A}{RT} \right) \left[ \frac{0.64 D_{O_2-Ar}}{d} \left( \frac{d}{r_s} \right)^{3/2} \sqrt{\frac{\mu_g}{\rho_g D_{O_2-Ar}}} \left( \frac{\pi d^3 \rho_g}{4 \mu_g} \right)^{0.79} \right] Q^{0.79} \quad (7.58)$$

$$\frac{dN_{O_2}^p}{dt} = \left( \frac{2}{3} \frac{P_{O_2}^b A}{RT} \right) \left[ \frac{0.64 D_{O_2-Ar}}{d} \left( \frac{d}{r_s} \right)^{3/2} \sqrt{\frac{\mu_g}{\rho_g D_{O_2-Ar}}} \left( \frac{\pi d^3 \rho_g}{4 \mu_g} \right)^{0.79} \right] Q^{0.79} \quad (7.59)$$

At the transition time, the sulphide bath composition is dictated by the equilibrium conditions of the system, as given by the following equations:

$$N_{S^{2-}}^* = \frac{N_{Cu^+}^* M_{Cu} 100}{M_S \left[ \left[ 100 - [\%O]_{Cu_2S} \right] \left[ \frac{100}{[\%S]_{Cu_2S}} - 1 \right] - [\%O]_{Cu_2S} \right]} \quad (7.60)$$

$$N_{O^{2-}}^* = \frac{N_{Cu^+}^* M_{Cu} 100}{M_O \left[ \left[ 100 - [\%S]_{Cu_2S} \right] \left[ \frac{100}{[\%O]_{Cu_2S}} - 1 \right] - [\%S]_{Cu_2S} \right]} \quad (7.61)$$

The oxygen and sulphur concentrations in the sulphide phase at the transition time are calculated from the equilibrium measurements of J. Schmiedl [19], as given by the following equations:

$$[\%O]_{Cu_2S} = 10^{(-2+(1013/T))} \cdot P_{SO_2}^{1/2} \quad (7.62)$$

$$[\%Cu]_{Cu_2S} = 79.605 + 0.26 \times 10^{-12} T^4 \quad (7.63)$$

$$[\%S]_{Cu_2S} = 100 - [\%Cu] - [\%O]_{Cu_2S} \quad (7.64)$$

Substituting for the conditions at the transition time in Equation (7.54) or Equation (7.55), an expression for the transition reaction time can be developed as given by the following equation:

$$t^* = \frac{N_{S^{2-}}^i - N_{S^{2-}}^*}{\left( \frac{2}{3} \frac{k_{O_2}}{RT} A \cdot P_{O_2}^b \right)} \quad (7.65)$$

During the primary stage, the moles of copper ions in the bath are constant; therefore the moles of copper ions ( $N_{Cu^+}^*$ ) at transition are the initial moles of copper in the bath.

Using Equations (7.54) and (7.55), an expression for the bath weight as a function of time, during the primary stage, can be expressed as follows:

$$W^p(t) = W(0) + [M_O - M_S] \left[ \frac{2}{3} \frac{k_{O_2}}{RT} A \cdot P_{O_2}^b \right] \cdot t \quad (7.66)$$

An expression for the rate of weight change in the primary stage as a function of the oxygen pressure can be derived by differentiating Equation (7.66) with respect to time, as follows:

$$\dot{W}^p = [M_o - M_s] \frac{2}{3} \frac{k_{O_2} A}{RT} P_{O_2}^b \quad (7.67)$$

The rate of weight change can be expressed in terms of the reaction gas flow rate as follows:

$$\dot{W}^p = \frac{2}{3} [M_o - M_s] \left[ \frac{0.64\pi D_{O_2-Ar} P_{O_2}^b}{RT} \sqrt{\frac{\mu_g dr_s}{\rho_g D_{O_2-Ar}}} \left( \frac{\pi d^3 \rho_g}{4\mu_g} \right)^{0.79} \right] Q^{0.79} \quad (7.68)$$

#### 7.1.6.2. Secondary Stage

Unlike the primary stage, the secondary stage does not offer a direct stoichiometric relationship between the  $\dot{n}_{SO_2}^s$  and  $\dot{n}_{O_2}$ . The following equations are to be solved simultaneously for the unknown reaction rates and the final reaction time<sup>34</sup>.

Sulphide phase sulphur balance:

$$-\dot{n}_{SO_2}^s \cdot A - \dot{N}_{S^{2-}} = \frac{dN_{S^{2-}}}{dt} \quad (7.32)$$

Sulphide phase oxygen balance:

$$2 \left( \dot{n}_{O_2} - \dot{n}_{SO_2}^s \right) \cdot A - \dot{N}_{O^{2-}} = \frac{dN_{O^{2-}}}{dt} \quad (7.37)$$

Sulphide phase copper balance:

$$-\dot{N}_{Cu^+} = \frac{dN_{Cu^+}}{dt} \quad (7.40)$$

---

<sup>34</sup>The unknown reaction rates and the final reaction time are constants in a determined system of equations that can be solved simultaneously.

Sulphur solubility in the metal phase:

$$\dot{N}_{S^{2-}} = S_{Cu} \dot{N}_{Cu^+} \quad (7.69)$$

Oxygen solubility in the metal phase:

$$\dot{N}_{O^{2-}} = O_{Cu} \dot{N}_{Cu^+} \quad (7.70)$$

Experimental results indicated that all reaction rates are constants, i.e. they are neither functions of composition nor functions of time. Integrating Equations (7.32), (7.37) and (7.40) for the following initial conditions:

$$\begin{aligned} \text{at } t = t^*, \quad N_{S^{2-}} &= N_{S^{2-}}^*, \\ N_{O^{2-}} &= N_{O^{2-}}^* \text{ and } N_{Cu^+} = N_{Cu^+}^* \end{aligned}$$

$$\int_{N_{S^{2-}}^*}^{N_{S^{2-}}} dN_{S^{2-}} = - \left( \overset{\circ}{n}_{SO_2} \cdot A + \dot{N}_{S^{2-}} \right) \int_{t^*}^t dt \quad (7.71)$$

$$N_{S^{2-}} = N_{S^{2-}}^* - \left( \overset{\circ}{n}_{SO_2} \cdot A + \dot{N}_{S^{2-}} \right) \cdot [t - t^*] \quad (7.72)$$

$$\int_{N_{O^{2-}}^*}^{N_{O^{2-}}} dN_{O^{2-}} = \left[ 2 \left( \overset{\circ}{n}_{O_2} - \overset{\circ}{n}_{SO_2} \right) \cdot A - \dot{N}_{O^{2-}} \right] \int_{t^*}^t dt \quad (7.73)$$

$$N_{O^{2-}} = N_{O^{2-}}^* + \left[ 2 \left( \overset{\circ}{n}_{O_2} - \overset{\circ}{n}_{SO_2} \right) A - \dot{N}_{O^{2-}} \right] \cdot [t - t^*] \quad (7.74)$$

$$\int_{N_{Cu^+}^*}^{N_{Cu^+}} dN_{Cu^+} = - \dot{N}_{Cu^+} \int_{t^*}^t dt \quad (7.75)$$

$$N_{Cu^+} = N_{Cu^+}^* - \dot{N}_{Cu^+} [t - t^*] \quad (7.76)$$

At the end of the reaction time, the sulphide phase is completely depleted, i.e.

$$\begin{aligned} \text{at } t = t^f, \quad N_{S^{2-}} &= 0, \\ N_{O^{2-}} &= 0 \text{ and } N_{Cu^+} = 0 \end{aligned}$$

Substituting for these final conditions in Equations (7.72), (7.74) and (7.76), permits the solution for the unknown reaction rates<sup>35</sup>, as follows:

$$N_{S^{2-}}^* - \left( \overset{\circ}{n}_{SO_2} \cdot A + \overset{\circ}{N}_{S^{2-}} \right) \cdot [t^f - t^*] = 0 \quad (7.77)$$

$$N_{O^{2-}}^* + \left[ 2 \left( \overset{\circ}{n}_{O_2} - \overset{\circ}{n}_{SO_2} \right) A - \overset{\circ}{N}_{O^{2-}} \right] \cdot [t^f - t^*] = 0 \quad (7.78)$$

$$N_{Cu^+}^* - \overset{\circ}{N}_{Cu^+} [t^f - t^*] = 0 \quad (7.79)$$

Solving for  $[t^f - t^*]$  from Equation (7.79) and substituting in Equations (7.77) and (7.78), the following is obtained:

$$\overset{\circ}{n}_{SO_2} \cdot A + \overset{\circ}{N}_{S^{2-}} = \frac{N_{S^{2-}}^* \cdot \overset{\circ}{N}_{Cu^+}}{N_{Cu^+}^*} \quad (7.80)$$

$$2 \left( \overset{\circ}{n}_{O_2} - \overset{\circ}{n}_{SO_2} \right) A - \overset{\circ}{N}_{O^{2-}} = - \frac{N_{O^{2-}}^* \cdot \overset{\circ}{N}_{Cu^+}}{N_{Cu^+}^*} \quad (7.81)$$

Using Equation (7.69) to solve for  $\overset{\circ}{N}_{Cu^+}$  and substituting in Equations (7.70), (7.80) and (7.81), the following is obtained:

$$\overset{\circ}{N}_{O^{2-}} = \frac{O_{Cu} \cdot \overset{\circ}{N}_{S^{2-}}}{S_{Cu}} \quad (7.82)$$

---

<sup>35</sup>Note that the unknowns are the constants in a system of equations, in which all of the dependent variables are known.

$$\overset{\circ}{n}_{SO_2} \cdot A + \overset{\circ}{N}_{S^{2-}} = \frac{N_{S^{2-}}^* \overset{\circ}{N}_{S^{2-}}}{N_{Cu^+}^* S_{Cu}} \quad (7.83)$$

$$2 \left( \overset{\circ}{n}_{O_2} - \overset{\circ}{n}_{SO_2} \right) A - \overset{\circ}{N}_{O^{2-}} = - \frac{N_{O^{2-}}^* \overset{\circ}{N}_{S^{2-}}}{N_{Cu^+}^* S_{Cu}} \quad (7.84)$$

Substituting for Equation (7.82) in Equation (7.84), and solving for  $\overset{\circ}{N}_{S^{2-}}$ , as follows:

$$\overset{\circ}{N}_{S^{2-}} = \frac{N_{Cu^+}^* S_{Cu} \overset{\circ}{n}_{SO_2} \cdot A}{\left[ N_{S^{2-}}^* - N_{Cu^+}^* S_{Cu} \right]} \quad (7.85)$$

$$\overset{\circ}{N}_{S^{2-}} = \frac{2 N_{Cu^+}^* S_{Cu} \left( \overset{\circ}{n}_{O_2} - \overset{\circ}{n}_{SO_2} \right) A}{\left[ O_{Cu} N_{Cu^+}^* - N_{O^{2-}}^* \right]} \quad (7.86)$$

Equating Equations (7.85) and (7.86), the following expression is obtained:

$$\overset{\circ}{n}_{SO_2} = \frac{1}{\left[ 1 + \frac{\left[ O_{Cu} N_{Cu^+}^* - N_{O^{2-}}^* \right]}{2 \left[ N_{S^{2-}}^* - N_{Cu^+}^* S_{Cu} \right]} \right]} \cdot \overset{\circ}{n}_{O_2} \quad (7.87)$$

Substituting for  $\overset{\circ}{n}_{O_2}$  in Equation (7.87), an expression for the molar flux of SO<sub>2</sub> is obtained as given by the following equation:

$$\overset{\circ}{n}_{SO_2} = \frac{1}{\left[ 1 + \frac{\left[ O_{Cu} N_{Cu^+}^* - N_{O^{2-}}^* \right]}{2 \left[ N_{S^{2-}}^* - N_{Cu^+}^* S_{Cu} \right]} \right]} \frac{k_{O_2} \cdot P_{O_2}^b}{RT} \quad (7.88)$$

Expressions for the consumption rates of sulphur, oxygen and copper ions from the sulphide phase are derived as follows:

$$\dot{N}_{S^{2-}} = \frac{2N_{Cu^+}^* S_{Cu} A}{\left[2\left[N_{S^{2-}}^* - N_{Cu^+}^* S_{Cu}\right] + \left[O_{Cu} N_{Cu^+}^* - N_{O^{2-}}^*\right]\right]} \frac{k_{O_2}}{RT} \cdot P_{O_2}^b \quad (7.89)$$

$$\dot{N}_{O^{2-}} = \frac{2N_{Cu^+}^* O_{Cu} A}{\left[2\left[N_{S^{2-}}^* - N_{Cu^+}^* S_{Cu}\right] + \left[O_{Cu} N_{Cu^+}^* - N_{O^{2-}}^*\right]\right]} \frac{k_{O_2}}{RT} \cdot P_{O_2}^b \quad (7.90)$$

$$\dot{N}_{Cu^+} = \frac{2N_{Cu^+}^* A}{\left[2\left[N_{S^{2-}}^* - N_{Cu^+}^* S_{Cu}\right] + \left[O_{Cu} N_{Cu^+}^* - N_{O^{2-}}^*\right]\right]} \frac{k_{O_2}}{RT} \cdot P_{O_2}^b \quad (7.91)$$

The expression for the final reaction time is derived as follows:

$$t^f = \left[3N_{S^{2-}}^i - N_{S^{2-}}^* - N_{O^{2-}}^* + N_{Cu^+}^* \left[O_{Cu} - 2S_{Cu}\right]\right] \frac{RT}{2Ak_{O_2} \cdot P_{O_2}^b} \quad (7.92)$$

By integrating Equations (7.43), (7.46) and (7.49) for the following initial condition, expressions for the metal phase growth can be derived:

$$\begin{aligned} \text{at } t = 0, \quad N_s &= 0, \\ N_o &= 0 \text{ and } N_{Cu} = 0 \end{aligned}$$

$$\int_0^{N_s} dN_s = \dot{N}_s \int_{t^*}^t dt \quad (7.93)$$

$$N_s = \dot{N}_s \cdot [t - t^*] \quad (7.94)$$

$$\int_0^{N_o} dN_o = \dot{N}_o \int_{t^*}^t dt \quad (7.95)$$

$$N_o = \dot{N}_o \cdot [t - t^*] \quad (7.96)$$

$$\int_0^{N_{Cu}} dN_{Cu} = \dot{N}_{Cu} \int_{t^*}^t dt \quad (7.97)$$



$$N_{Cu} = \dot{N}_{Cu} \cdot [t - t^*] \quad (7.98)$$

By adding the respective equations of the sulphide and metal phases, and utilizing the relationships of Equations (7.19), (7.20) and (7.21), expressions for the secondary moles of copper, sulphur and oxygen in the bath can be derived as follows:

$$N_S^s = N_{S^{2-}}^* - \overset{\circ}{n}_{SO_2} \cdot A \cdot [t - t^*] \quad (7.99)$$

$$N_O^s = N_{O^{2-}}^* + 2 \left( \overset{\circ}{n}_{O_2} - \overset{\circ}{n}_{SO_2} \right) A \cdot [t - t^*] \quad (7.100)$$

$$N_{Cu}^s = N_{Cu^+}^* \quad (7.101)$$

Substituting for  $\overset{\circ}{n}_{O_2}$ ,  $\overset{\circ}{n}_{SO_2}$  and  $t^*$  in Equations (7.99)-(7.101), the expressions for the secondary moles of sulphur and oxygen (total) are given by the following equations:

$$N_S^s = N_{S^{2-}}^* + \left[ \frac{2[N_{S^{2-}}^* - N_{Cu^+}^* S_{Cu}]}{[2N_{S^{2-}}^* - N_{O^{2-}}^* + N_{Cu^+}^* [O_{Cu} - 2S_{Cu}]]} \right] \left[ \frac{3}{2} [N_{S^{2-}}^i - N_{S^{2-}}^*] - \left( \frac{k_{O_2} A P_{O_2}^b}{RT} \right) \cdot t \right] \quad (7.102)$$

$$N_O^s = N_{O^{2-}}^* + \left[ \frac{2[N_{S^{2-}}^* - N_{Cu^+}^* S_{Cu}]}{[2N_{S^{2-}}^* - N_{O^{2-}}^* + N_{Cu^+}^* [O_{Cu} - 2S_{Cu}]]} - 1 \right] \left[ 3[N_{S^{2-}}^i - N_{S^{2-}}^*] - \left( \frac{2k_{O_2} A P_{O_2}^b}{RT} \right) \cdot t \right] \quad (7.103)$$

By differentiating Equations (7.102) and (7.103) with respect to time, expressions for the rate of sulphur and oxygen removal from the bath in the secondary stage as a functions of the oxygen partial pressure are derived as follows:

$$\frac{dN_S^s}{dt} = \left[ \frac{2[N_{S^{2-}}^* - N_{Cu^+}^* S_{Cu}]}{[2N_{S^{2-}}^* - N_{O^{2-}}^* + N_{Cu^+}^* [O_{Cu} - 2S_{Cu}]]} \right] \left( \frac{k_{O_2} A}{RT} \right) P_{O_2}^b \quad (7.104)$$

$$\frac{dN_O^s}{dt} = \left[ \frac{2[N_{S^{2-}}^* - N_{Cu^+}^* S_{Cu}]}{[2N_{S^{2-}}^* - N_{O^{2-}}^* + N_{Cu^+}^* [O_{Cu} - 2S_{Cu}]]} - 1 \right] \left( \frac{2k_{O_2} A}{RT} \right) P_{O_2}^b \quad (7.105)$$

Expressions for the secondary rates of sulphur and oxygen removal in terms of the reaction gas flow rate are derived as follows:

$$\frac{dN_S^s}{dt} = \left[ \frac{2[N_{S^{2-}}^* - N_{Cu^+}^* S_{Cu}]}{[2N_{S^{2-}}^* - N_{O^{2-}}^* + N_{Cu^+}^* [O_{Cu} - 2S_{Cu}]]} \right] \left[ \frac{0.64\pi D_{O_2-Ar} P_{O_2}^b}{RT} \sqrt{\frac{\mu_g dr_s}{\rho_g D_{O_2-Ar}}} \left( \frac{\pi d^3 \rho_g}{4\mu_g} \right)^{0.79} \right] Q^{0.79} \quad (7.106)$$

$$\begin{aligned} \frac{dN_O^s}{dt} &= \left[ \frac{2[N_{S^{2-}}^* - N_{Cu^+}^* S_{Cu}]}{[2N_{S^{2-}}^* - N_{O^{2-}}^* + N_{Cu^+}^* [O_{Cu} - 2S_{Cu}]]} - 1 \right] \\ &\times \left[ \frac{1.28\pi D_{O_2-Ar} P_{O_2}^b}{RT} \sqrt{\frac{\mu_g dr_s}{\rho_g D_{O_2-Ar}}} \left( \frac{\pi d^3 \rho_g}{4\mu_g} \right)^{0.79} \right] Q^{0.79} \end{aligned} \quad (7.107)$$

An expression for the bath weight as a function of time in the secondary stage is derived as follows:

$$\begin{aligned} W^s(t) &= W(t^*) - \left[ 2M_O - [2M_O - M_S] \left[ \frac{2[N_{S^{2-}}^* - N_{Cu^+}^* S_{Cu}]}{[2N_{S^{2-}}^* - N_{O^{2-}}^* + N_{Cu^+}^* [O_{Cu} - 2S_{Cu}]]} \right] \right] \times \\ &\left[ \frac{3}{2} [N_{S^{2-}}^i - N_{S^{2-}}^*] - \left( \frac{k_{O_2} A P_{O_2}^b}{RT} \right) \cdot t \right] \end{aligned} \quad (7.108)$$

The rate of weight change as a function of the oxygen partial pressure in the secondary stage is derived by differentiating Equation (7.108) with respect to time as follows:

$$\dot{W}^s = \left[ 2M_O - [2M_O - M_S] \left[ \frac{2[N_{S^{2-}}^* - N_{Cu^+}^* S_{Cu}]}{[2N_{S^{2-}}^* - N_{O^{2-}}^* + N_{Cu^+}^* [O_{Cu} - 2S_{Cu}]]} \right] \right] \left( \frac{k_{O_2} A}{RT} \right) P_{O_2}^b \quad (7.109)$$

Similarly, the rate of weight change in the secondary stage is expressed in terms of the reaction gas flow rate as follows:

$$\begin{aligned} \dot{W}^s = & \left[ 2M_O - [2M_O - M_S] \left[ \frac{2[N_{S^{2-}}^* - N_{Cu^+}^* S_{Cu}]}{[2N_{S^{2-}}^* - N_{O^{2-}}^* + N_{Cu^+}^* [O_{Cu} - 2S_{Cu}]]} \right] \right] \\ & \times \left[ \frac{0.64\pi D_{O_2-Ar} P_{O_2}^b}{RT} \sqrt{\frac{\mu_g dr_s}{\rho_g D_{O_2-Ar}}} \left( \frac{\pi d^3 \rho_g}{4\mu_g} \right)^{0.79} \right] Q^{0.79} \end{aligned} \quad (7.110)$$

## 7.2. Model Validation

The general criteria for the model validity are comparison of its prediction of the sulphur and oxygen contents for the two stages and their time domains to measurements from the laboratory experiments. From Equations (7.54) and (7.55), the primary sulphur and oxygen molar contents were calculated; the reaction transition time was calculated from Equation (7.65); and the secondary sulphur and oxygen molar contents were calculated from Equations (7.102) and (7.103). These predicted results were plotted along with the corresponding measured values for typical runs, as shown in Figures 7.4-7.5.

The apparent curvature of the measured oxygen content is due to experimental scatter. It is important to note that the accuracy of the sulphur content measurement is higher than that of the oxygen content measurement<sup>36</sup>. The relative disagreement between the predicted and the measured results is attributed to the errors associated with the input parameters to the model (reaction gas flow rate, reaction gas composition and the measured pressure of the system) and the estimation of the gas phase mass transfer coefficient. The model predictions, however, appear to be in very good agreement with the measured results, for the employed range of the reaction gas flow rate, as shown in Figure 7.4.

---

<sup>36</sup>The sulphur content was determined by the acid-base titration method, which is a more conventionally accurate method than the gas flow rate measurement technique, which was used in the determination of the oxygen content. As explained in Section 4.1.5.5, in general, the error in the measurement of the reaction gas flow rate is proportional to the flow rate.

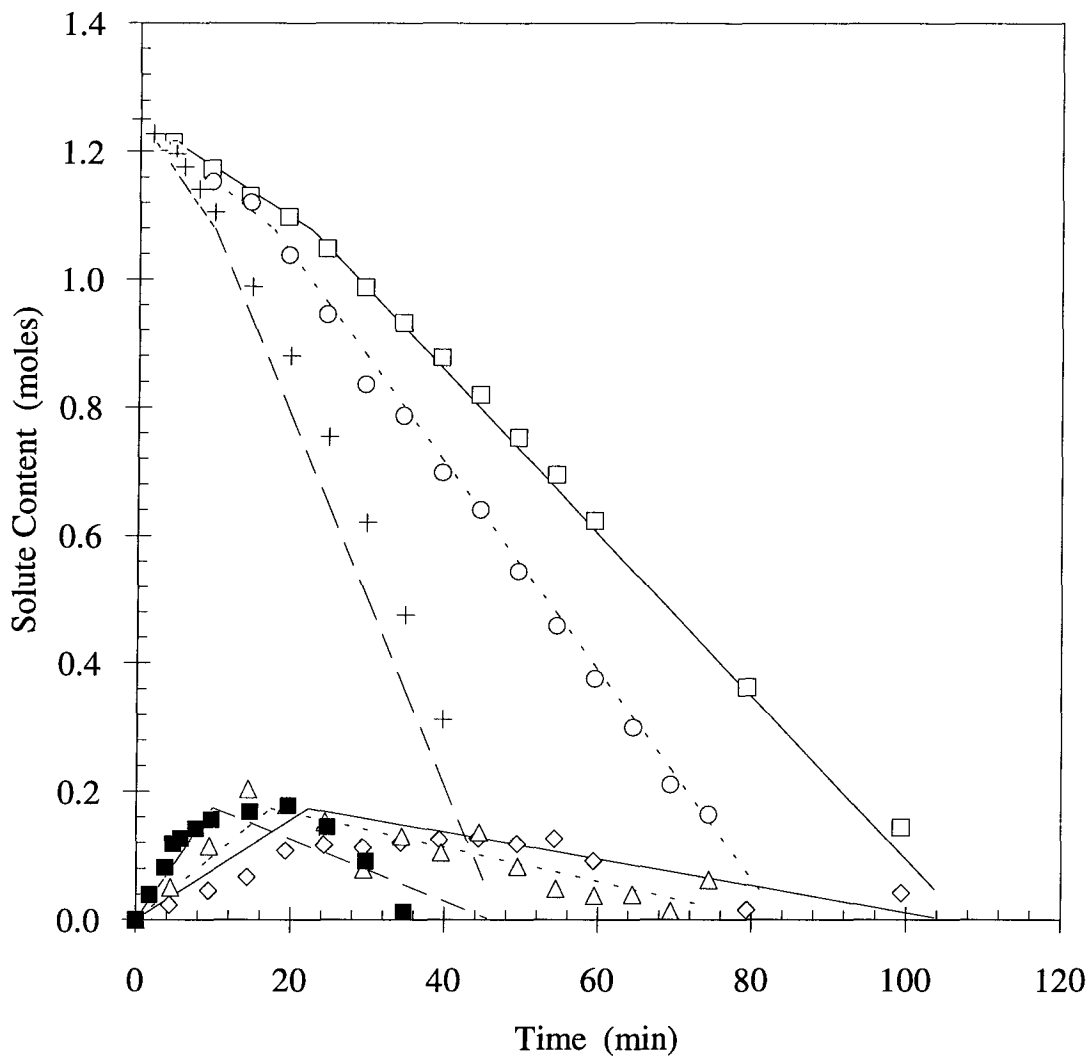


Figure 7.4. Comparison of model predictions to measurements of the sulphur and oxygen contents in the bath as a function of time at a constant reaction gas composition and for the range of reaction gas flow rate of 1480-4055 ml/min; for the experimental conditions of: 200 grams of  $\text{Cu}_2\text{S}$  of: 22%  $\text{O}_2$  and 78% Ar, at 1200 °C; ——— predicted for 1480 ml/min;  $\square$  measured sulphur content for 1480 ml/min;  $\diamond$  measured oxygen content for 1480 ml/min; - - - - predicted for 2006 ml/min;  $\circ$  measured sulphur content for 2006 ml/min;  $\triangle$  measured oxygen content for 2006 ml/min; - · - · predicted for 4055 ml/min; + measured sulphur content for 4055 ml/min;  $\blacksquare$  measured oxygen content for 4055 ml/min.

Similarly for the reaction gas composition range, the predicted and measured results are as shown in Figure 7.5.

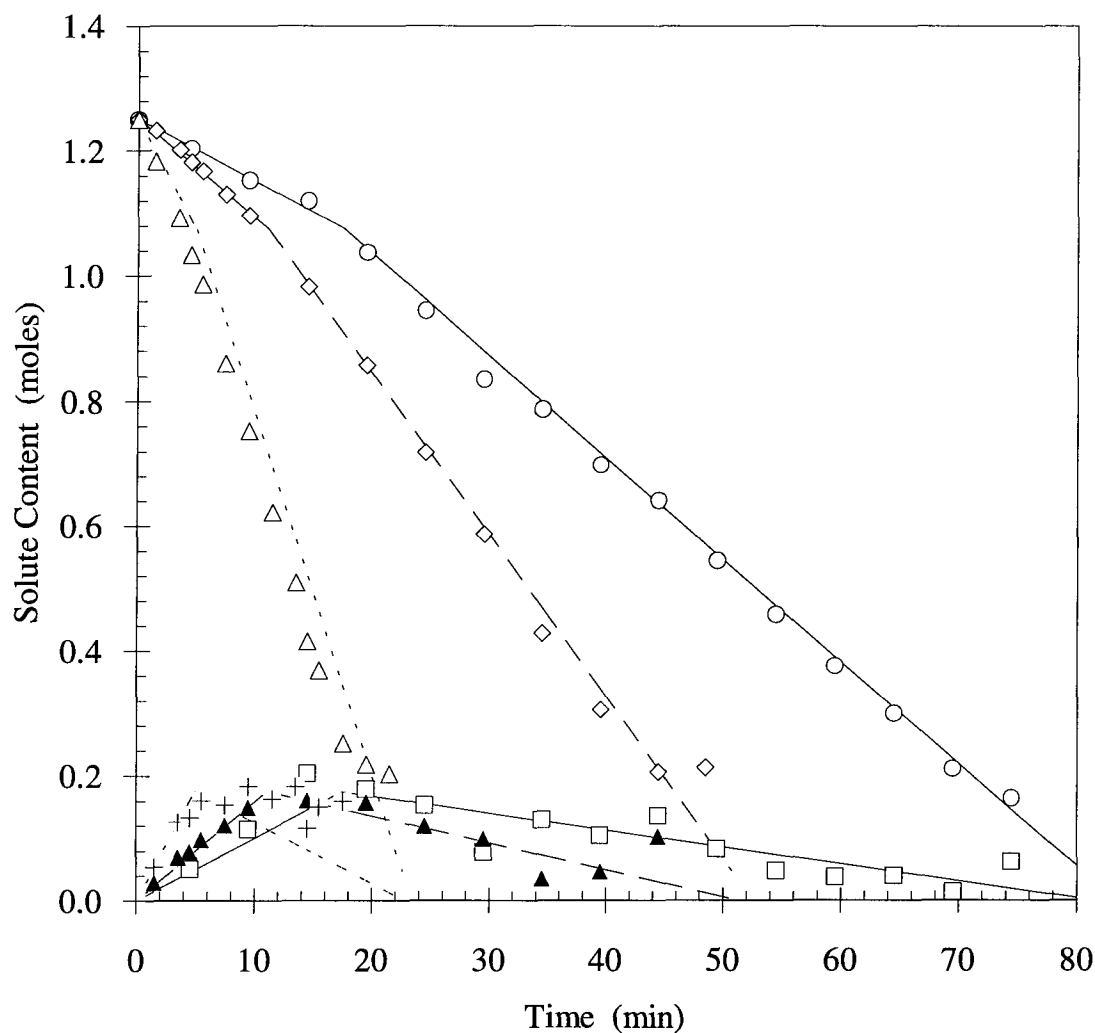


Figure 7.5. Comparison of model predictions to measurements of sulphur and oxygen contents in the bath as a function of time at a constant reaction gas flow rate and for the range of reaction gas composition of 22-78% O<sub>2</sub>; for the experimental conditions of: 200 grams of Cu<sub>2</sub>S of: 2000 ml/min, at 1200 °C; ——— predicted for 22% O<sub>2</sub>; ○ measured sulphur content for 22% O<sub>2</sub>; □ measured oxygen content for 22% O<sub>2</sub>; - - - predicted for 35% O<sub>2</sub>; ◇ measured sulphur content for 35% O<sub>2</sub>; ▲ measured oxygen content for 35% O<sub>2</sub>; ····· predicted for 78% O<sub>2</sub>; △ measured sulphur content for 78% O<sub>2</sub>; + measured oxygen content for 78% O<sub>2</sub>.

The relative deviation from the measured results, at the highest reaction gas composition conditions, is mainly attributed to the effect of surface-tension driven flows<sup>37</sup>. It is evident, however, that the model provides an acceptable predictability for the experimental range of reaction gas composition.

Considering the error involved in the measured results, the model predictions appear to be well within the experimental uncertainty of the measured values. It is therefore reasonable to state that the model predictions are in good agreement with the overall range of the measured results.

### **7.3. Model Sensitivity**

Since all of the reaction parameters are set or read with some degree of uncertainty, it is inevitable that the input variables to the mathematical model carry some degree of error. In order to examine the effect of these uncertainties on the model predictions, and to isolate as much as possible the experimental error from the model deviations, this analysis is carried out using the results of a run that appears to contain the least relative errors.

#### **7.3.1. Temperature**

As shown in Figure 7.6, the uncertainty in the temperature evidently has a very minor effect on the overall model predictions. An error of  $\pm 50$  °C (2.5%) results in less than 1% error in the sample weight prediction and less than 6% error in the prediction of the transition time.

---

<sup>37</sup>The effect of surface-tension driven flows was found to be higher with oxygen content in the reaction gas; as a result, the transport conditions are enhanced beyond the accountability of the model (see Figure 6.2).

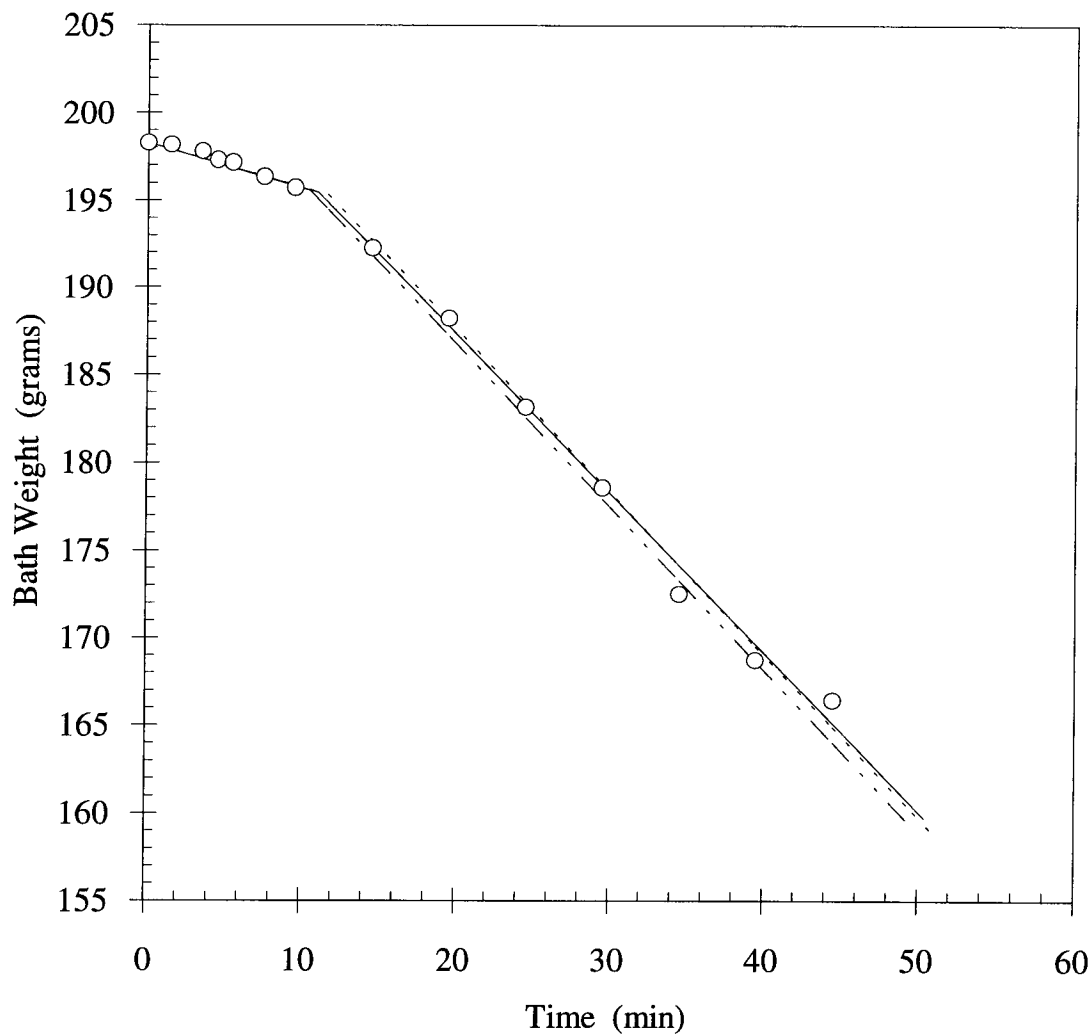


Figure 7.6. Model-predicted sensitivity of transient bath weight to bath temperature<sup>38</sup> for the experimental conditions of; ——— predicted for 1200 °C; ○ measured at 1200 °C; - - - - predicted for 1150 °C; - · - · - predicted for 1250 °C.

### 7.3.2. Pressure

Due to the pressure head created by the SO<sub>2</sub> absorber, the measurements were conducted under pressures of slightly higher than that of the atmospheric pressure viz., 1.05-1.112 atm. For systems such as that under study, however, it is well known that the pressure

<sup>38</sup>The experimental conditions of this run, used in all of the sensitivity analyses, are: 200 grams of Cu<sub>2</sub>S, 2000 ml/min of 35% O<sub>2</sub> and 65% Ar

has a minor effect on most thermodynamic properties [114]. As shown in Figure 7.7, the results of this sensitivity analysis indicated that a 5% uncertainty in the pressure of the system results in less than 3% error in the prediction of the reaction transition time and a less than 2% error in the prediction of the sample weight.

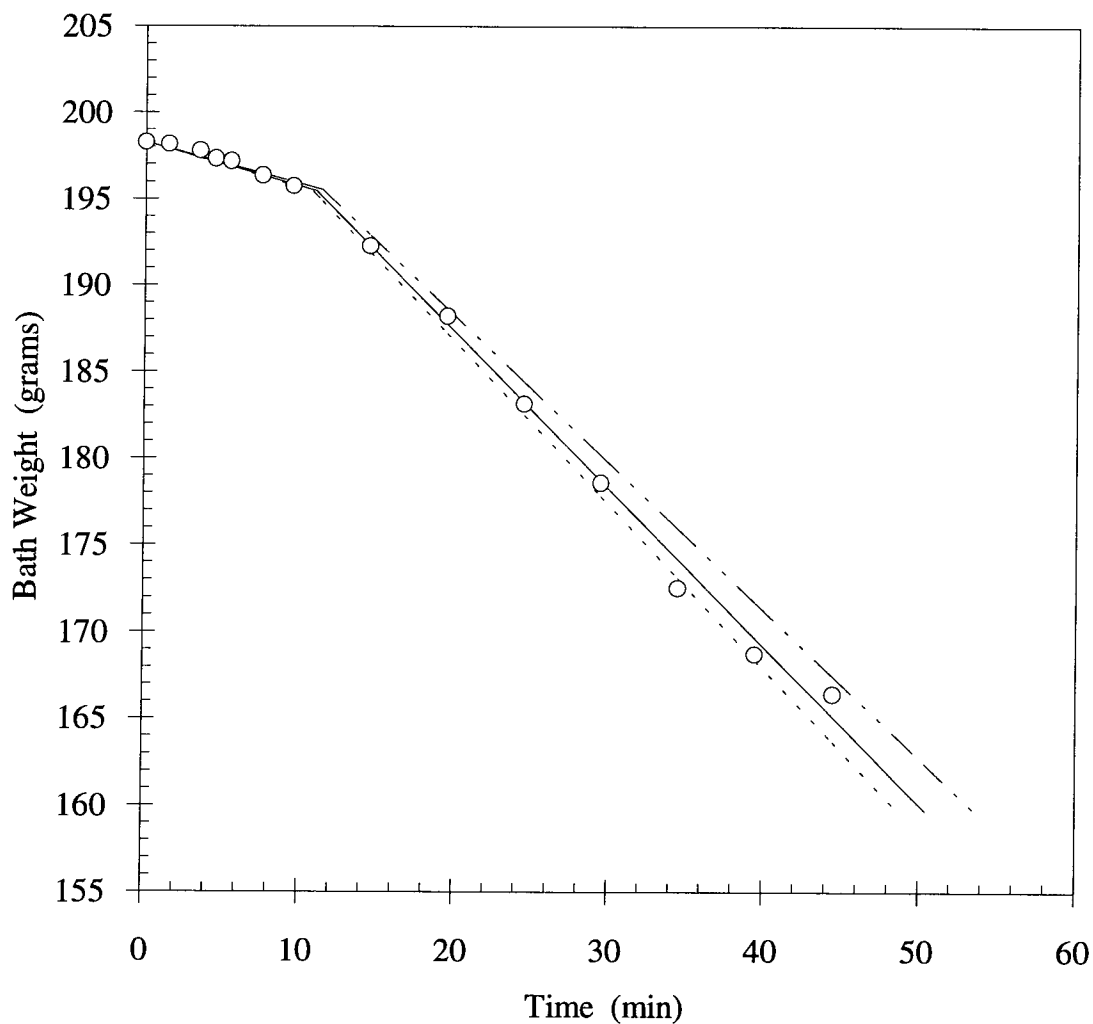


Figure 7.7. Model-predicted sensitivity of transient bath weight to total pressure; ——— predicted for 1.09 atm; ○ measured at 1.09 atm; - - - - predicted for 1 atm; ····· predicted for 1.15 atm.



### 7.3.3. Reaction Gas Flow Rate

As shown in Figure 7.8, the results of the model-reaction gas flow rate sensitivity analysis indicated that a 5% error in the reaction gas flow rate results in less than 4% error in the prediction of the reaction transition time and less than 0.8% error in the prediction of the sample weight.

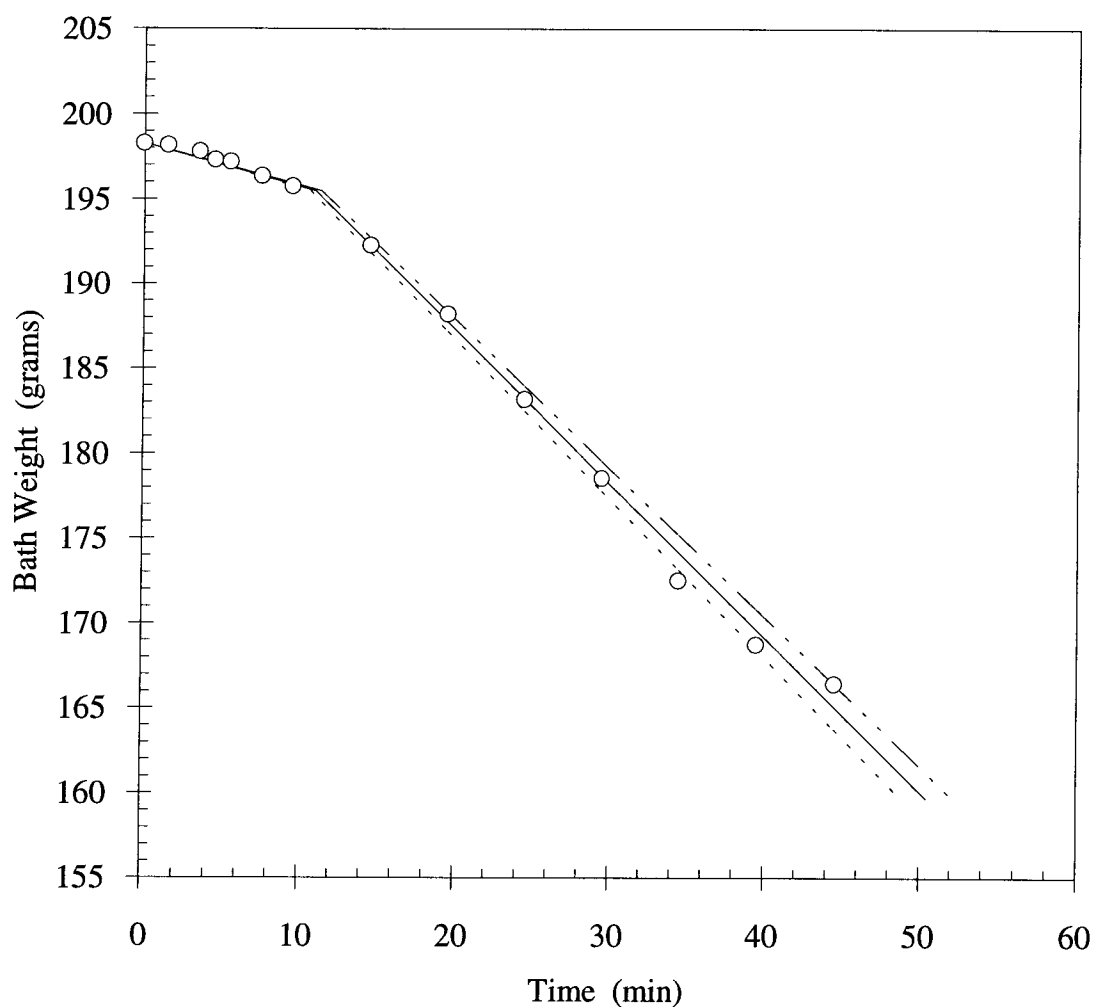


Figure 7.8. Model-predicted sensitivity of transient bath weight to flow rate of admitted gas; ——— predicted for 2000 ml/min; ○ measured for 2000 ml/min; - - - - predicted for 1900 ml/min; - · - · - predicted for 2100 ml/min.

### 7.3.4. Reaction Gas composition

In this analysis, a 5% uncertainty in the reaction gas composition was found to result in less than 6% error in the prediction of the reaction transition time and less than 2% error in the prediction of the sample weight, as shown in Figure 7.9.

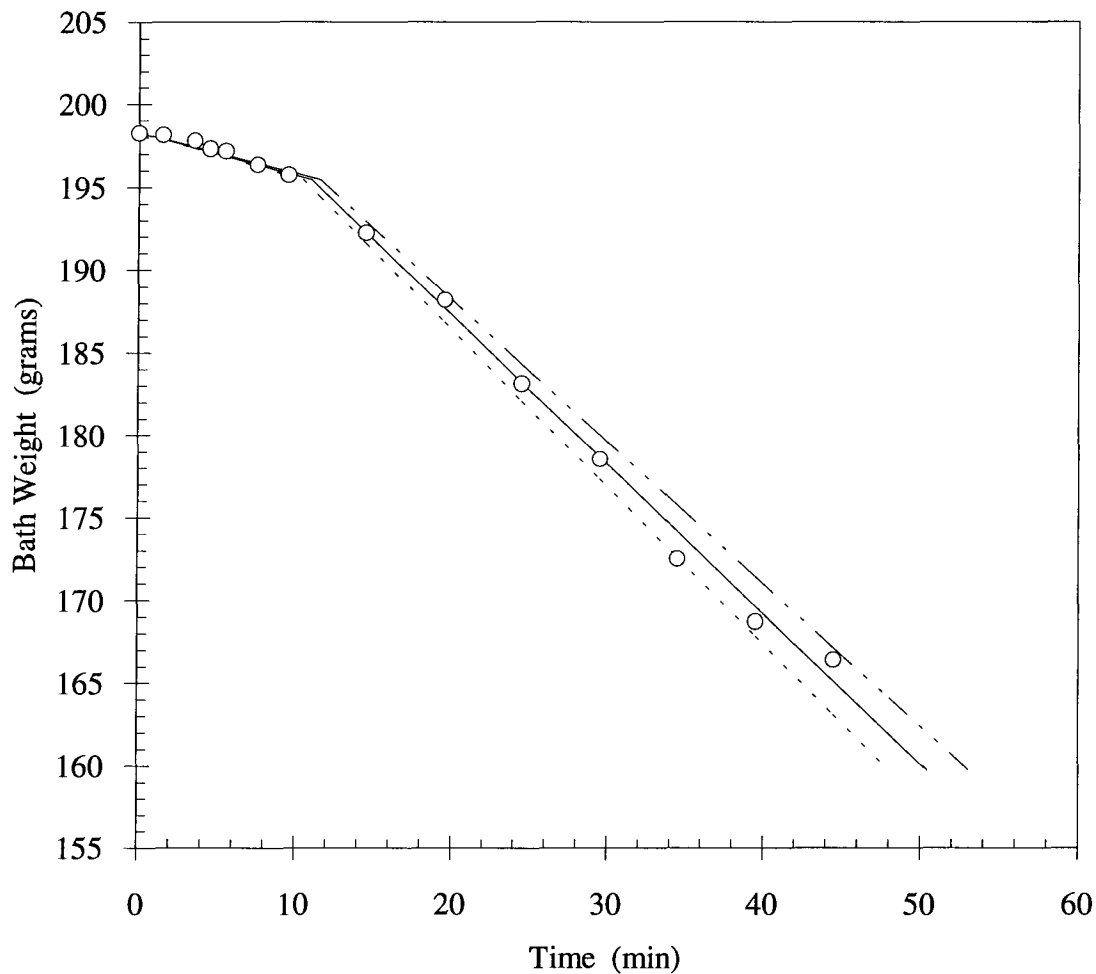


Figure 7.9. Model-predicted sensitivity of transient bath weight to composition of admitted gas; ——— predicted for 35% O<sub>2</sub>; ○ measured for 35% O<sub>2</sub>; - - - - predicted for 33% O<sub>2</sub>; · · · · · predicted for 37% O<sub>2</sub>.

In the experiments, the reaction gas mixture was obtained by metering each gas stream using a separate rotameter. Thus the error in the reaction gas composition is approximately the sum of the errors of the two readings. Since the reaction rate is

directly proportional to the reaction gas composition, its error contribution is expected to be higher than that of the reaction gas flow rate.

### 7.3.5. Reaction Interfacial Area

If the error associated with the reaction interfacial area was 5%, then the corresponding errors were 5% and 1% in the predictions of the reaction transition time and the sample weight respectively, as shown in Figure 7.10.

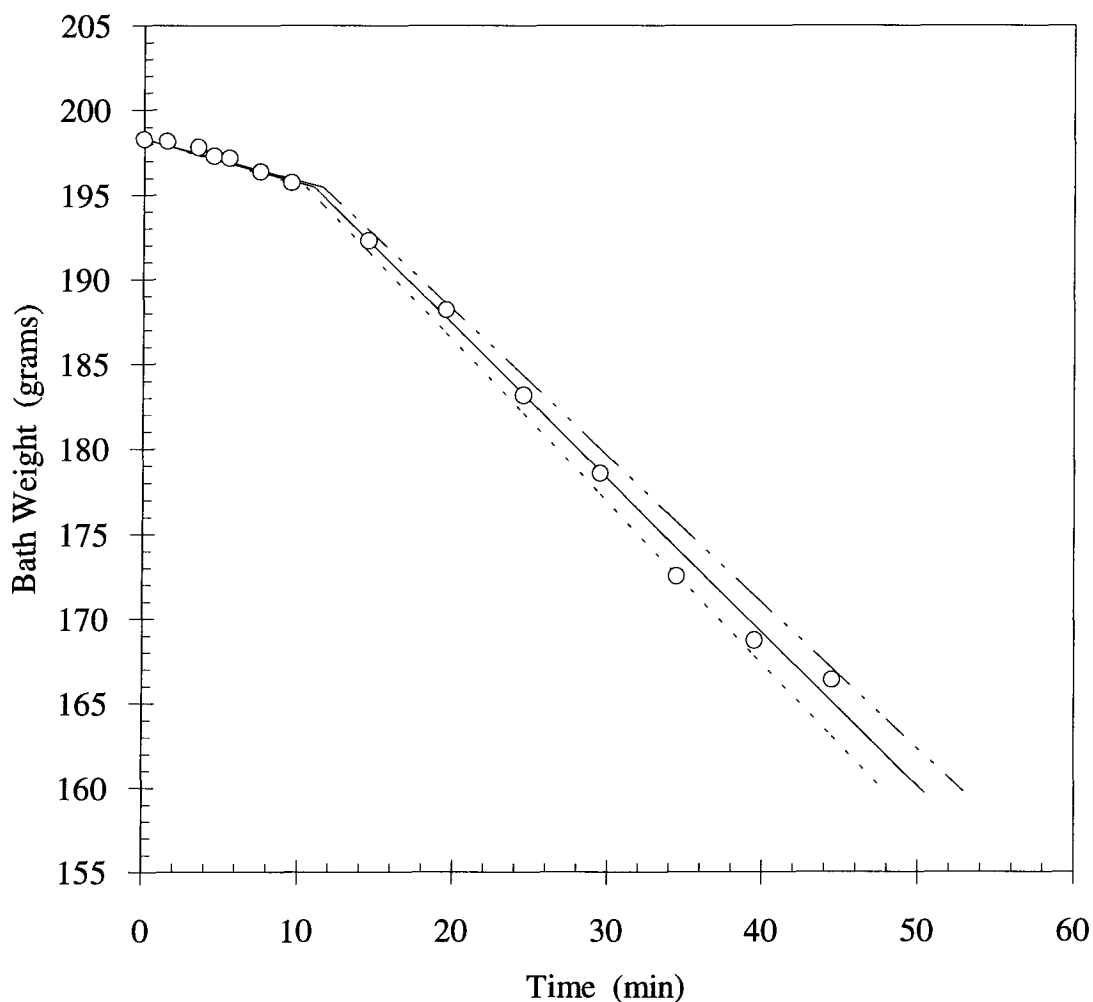


Figure 7.10. Model-predicted sensitivity of transient bath weight to bath surface area; — predicted for 15.14 cm<sup>2</sup>; ○ measured for 15.14 cm<sup>2</sup>; - - - predicted for 14.38 cm<sup>2</sup>; - · - · - predicted for 15.90 cm<sup>2</sup>.

## 7.4. Theoretical Predictions

### 7.4.1. Oxidation Path

As presented and discussed in Chapter 5, gas analysis measurements and gravimetric measurements revealed that the oxidation reaction of molten copper sulphide proceeds according to two distinct stages, during which the rates are constant, as shown in Figures 5.5 and 5.6. The fact that these two independent measurements are in general agreement is evidence of their validity. The melt composition at transition and the molar ratio of reacted oxygen to removed sulphur ( $\alpha$ ) are independent of reaction conditions (see Table 5.1).

By eliminating time from the expressions for the molar sulphur and oxygen contents (Equations (7.51), (7.53), (7.99) and (7.100)), the relationship between the sulphur and oxygen contents are found to be independent of the oxidation kinetics as given by the following equations:

$$N_S^p = N_S^i - N_O^p \quad (7.111)$$

$$N_S^s = N_S^* + \left[ \frac{N_{S^{2-}}^* - S_{Cu} N_{Cu^+}^*}{N_{O^{2-}}^* - O_{Cu} N_{Cu^+}^*} \right] \left[ N_O^s - N_{O^{2-}}^* \right] \quad (7.112)$$

Although the experimental scatter is considerable, experimental measurements are in agreement with the predictions of Equations (7.111) and (7.112) as shown in Figure 7.11. The experimental results indicate very clearly that the oxidation path is controlled primarily by the thermodynamics of the Cu-S-O system. From Figure 7.11, the predicted results indicate that the effect of temperature on the oxidation path is minimal, where a 100 °C increase in temperature causes a slight shift in point b and appears to have no effect on point c.

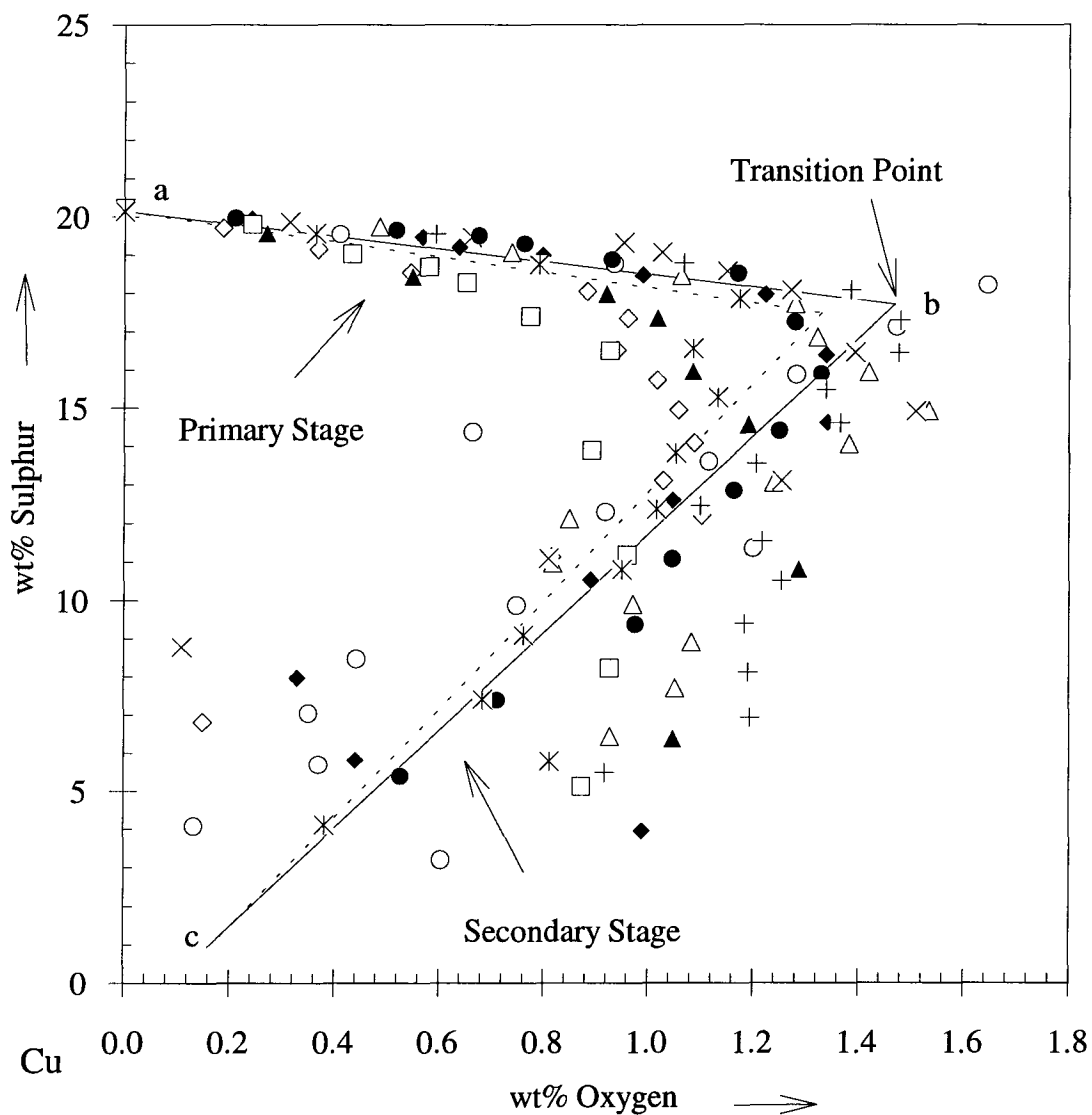


Figure 7.11. The sulphur content as a function of the oxygen content in the bath, showing the oxidation path of molten copper sulphide; ——— predicted at 1200 °C and 1 atm; - - - - - predicted at 1300 °C and 1 atm; measured at 1200 °C and 24 % O<sub>2</sub>, ◇ 1480 ml/min, △ 1755 ml/min, + 1987 ml/min, ○ 2006 ml/min, × 4055 ml/min; \* measured at 1200 °C and 2510 ml/min of 23 % O<sub>2</sub>; measured at 1200 °C and 2000 ml/min, ● 27 % O<sub>2</sub>, ◆ 35 % O<sub>2</sub>, □ 46 % O<sub>2</sub>, ▲ 64 % O<sub>2</sub>.

Based on the findings of the current work and on earlier thermodynamic studies of the ternary system, the oxidation path of Cu<sub>2</sub>S is constructed as shown in Figure 7.12.

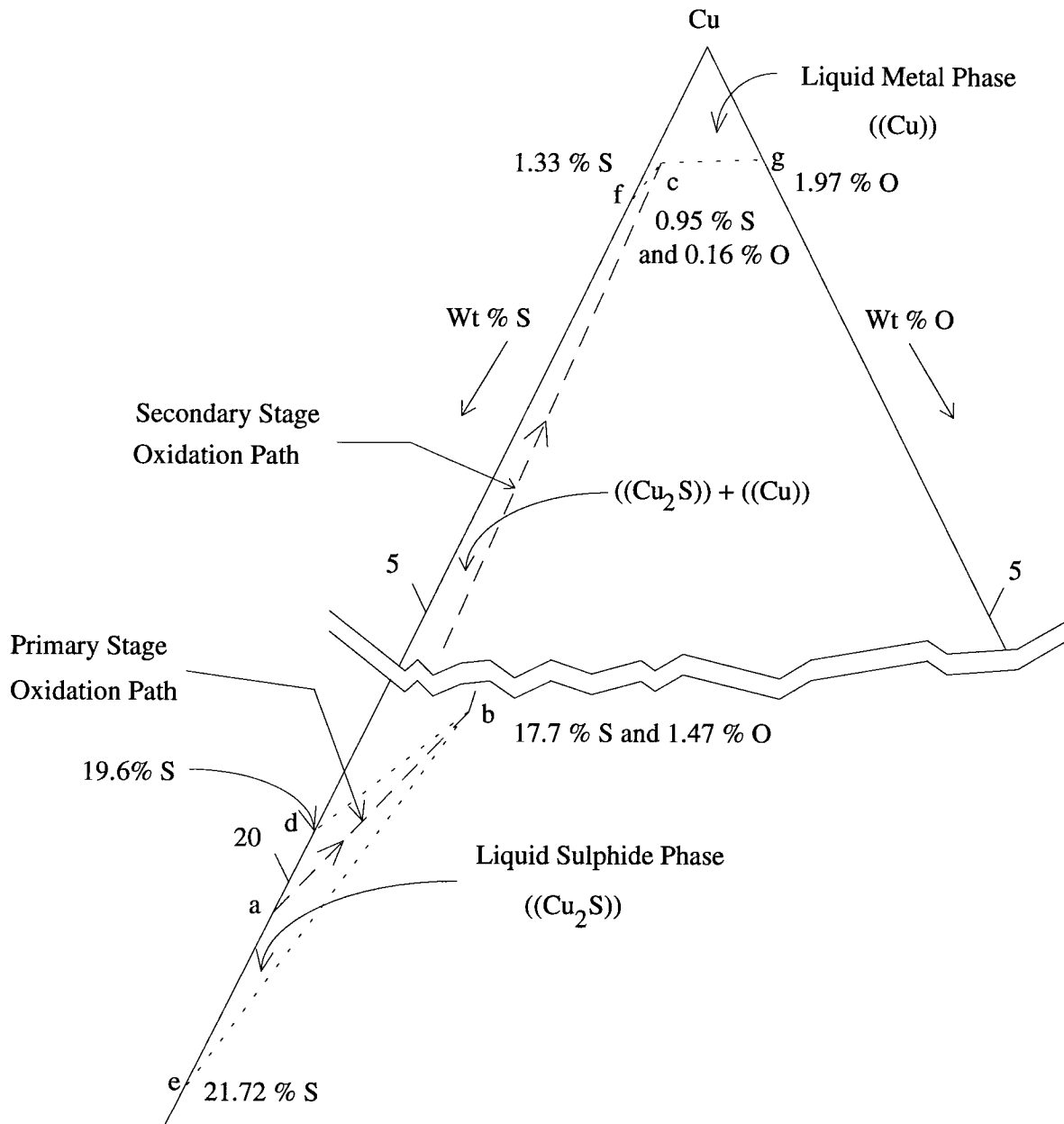


Figure 7.12. Selected portions of the Cu-S-O isothermal section, showing the oxidation path of molten  $\text{Cu}_2\text{S}$  at  $1200\text{ }^\circ\text{C}$  and  $1\text{ atm}$  (points b and c are after Schmiedl [19]; points d, e, f and g are after Elliott [20]). Note that the dashed lines outlining the metal and sulphide phases are assumed.

As stated in Section 5.1.3.2, gas analysis measurements yielded  $16.94 \pm 0.10\%$  and  $1.37 \pm 0.07\%$  for the sulphur and oxygen transition concentrations respectively. Rottmann and Wuth [71] found that the melt oxygen content at the end of the primary stage is  $0.6\%$ . Peretti [10] suggested that, based on the Cu-S binary phase diagram, in the Peirce-Smith

converter, the second step of the copper-making reaction starts when the melt composition is about 19.4% sulphur. Peretti, however, ignored the effect of oxygen by considering the melt to be a binary system. According to the present work, the binary assumption can be misleading in studying the reaction mechanism of the oxidation of copper sulphide. The 1300 °C isothermal section, shown in Figure 2.3, indicates that the sulphur and oxygen concentrations at saturation in  $\text{Cu}_2\text{S}$  are approximately 18.59% and 1.38% respectively. At 1200 °C and 1 atm, the equilibrium measurements of Schmiedl [19] yielded 17.7% and 1.47% for the sulphur and oxygen solubilities in  $\text{Cu}_2\text{S}$  respectively. From comparing the measured transition composition to the equilibrium composition of sulphur and oxygen in the melt, clearly the melt composition at transition is that of the equilibrium composition of oxygen and sulphur. Therefore, during the primary stage, the melt is partially desulphurized and oxygen saturated without any formation of copper according to path a-b in Figure 7.12. Once the melt reaches point b, the chemical potential for the formation of the metal phase is attained. An increased degree of desulphurization accompanies the metal phase formation which takes place according to path b-c, as shown in Figures 7.11 and 7.12.

As discussed in Section 5.1.3.2, the average value for  $\alpha^p = 1.46$  permitted the postulation of Reaction (5.18) as the principal reaction in the primary stage. In the formulation of the mathematical model, this postulate was implemented in deriving the relationships between the reaction rates of the primary stage. As shown in Figures 7.4 and 7.5, the model predictions of the primary stage are in good agreement with the measured results. This can best be seen by concentrating on the prediction of the transition point. It is clear, therefore, that Reaction (5.18) is the only reaction that takes place during the primary stage. It is very important to note that obtaining a large number of relatively accurate measurements permitted the calculation of a statistically valid mean for  $\alpha^p$ , from which it was possible to postulate Reaction (5.18). Although the time duration of the primary

stage is only about 20-25 % of the total time of the oxidation reaction, the understanding of the chemical reactions of the primary stage is very crucial to the comprehension of the secondary stage.

During the secondary stage, the molar ratio of reacted oxygen to removed sulphur was found to be  $\alpha^s = 0.96 \pm 0.052$ . At first glance this might seem to be an indication that the actual ratio is unity. However, this can be a very misleading judgment. As discussed above, because of the reactions are electrochemical in which the dissolution of oxygen and sulphur in copper, according to Reactions 5.21 and 5.22, is accompanied by electron transfer, the degree of desulphurization during the secondary stage is further enhanced. It is important to note that, as explained in Sections 5.1.3.2 and 7.1.2.2, without considering the electrochemical nature of the system it would not have been possible to account for the oxygen and sulphur in the metal phase.

## 7.4.2. Oxidation Rates

### 7.4.2.1. Oxidation Rate as a Function of Gas Flow Rate

From the mathematical model, the oxygen gas phase mass transfer rate is related to the reaction gas volumetric flow rate as follows:

$$\dot{N}_{O_2} = \left[ \frac{0.64\pi D_{O_2-Ar} P_{O_2}^b}{RT} \sqrt{\frac{\mu_g dr_s}{\rho_g D_{O_2-Ar}}} \left( \frac{\pi d^3 \rho_g}{4\mu_g} \right)^{0.79} \right] Q^{0.79} \quad (7.113)$$

For the oxidation reaction to be gas phase mass transfer limited, the oxygen reaction rate must be equal to the oxygen gas phase mass transfer rate, predicted by Equation (7.113). In Figure 7.13, the predicted oxygen reaction rate is compared to the measured oxygen reaction rate, from which the theoretical prediction appears to be in good agreement with measured rates.



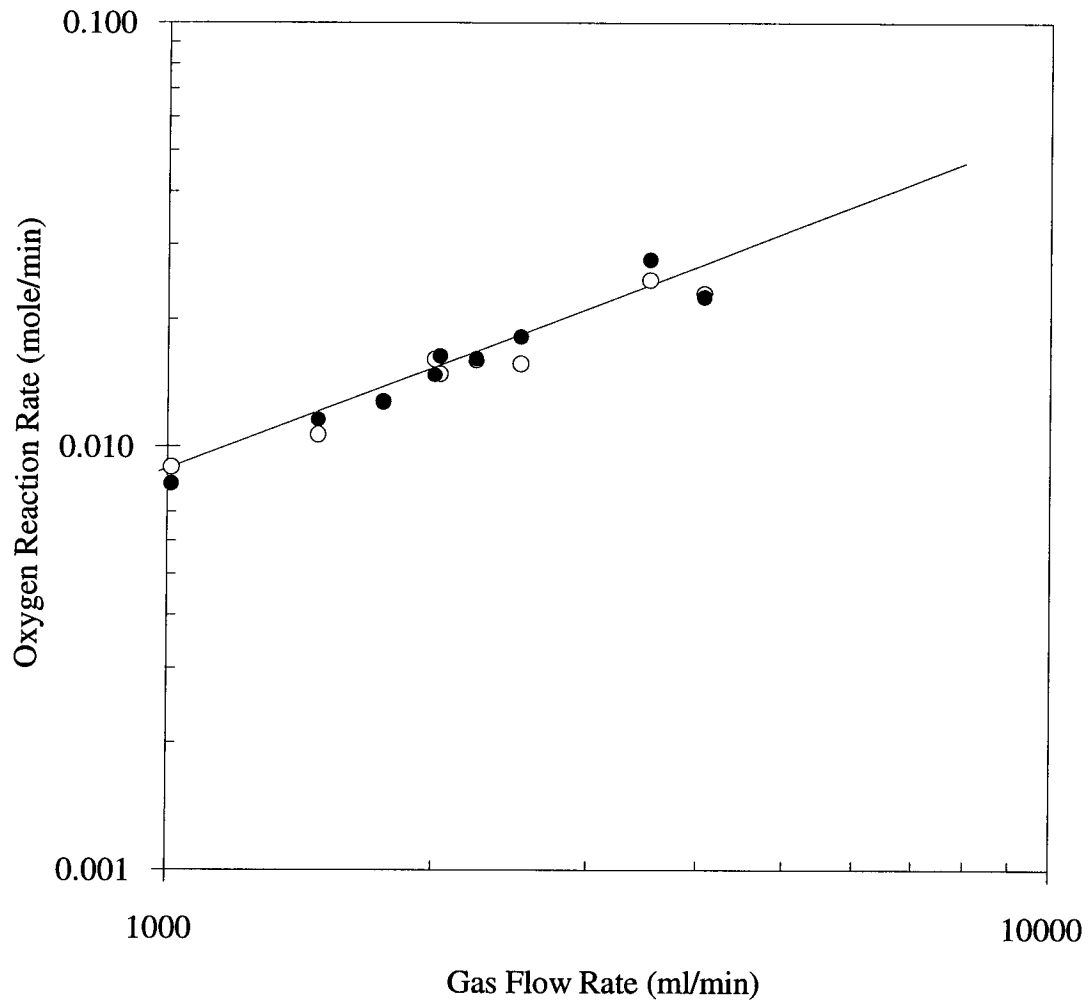


Figure 7.13. Oxygen reaction rate ( $\dot{N}_{O_2}$ ) as a function of reaction gas volumetric flow rate for the experimental conditions of: 200 gram samples, 1200 °C, 23 % O<sub>2</sub> and average pressure of 1.08 atm; ——— predicted ; ○ primary measured; ● secondary measured.

In Figure 7.14, the measured and predicted sulphur removal rates (Equations (7.56) and (7.58)) are plotted against the gas flow rate. As expected, since the sulphur removal rates are limited by gas phase mass transfer, the predicted and measured rates appear to be in good agreement.

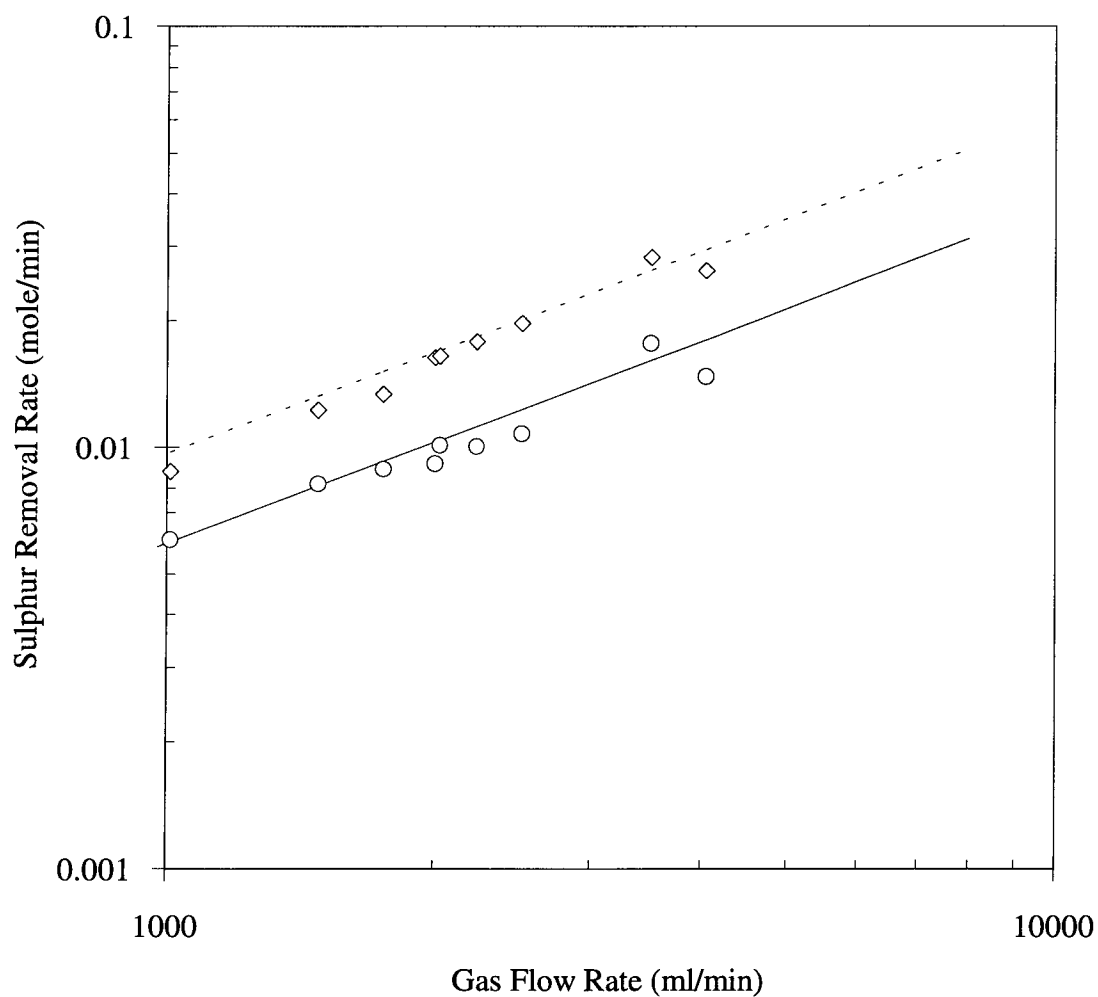


Figure 7.14. Sulphur removal rate ( $\dot{N}_S$ ) as a function of reaction gas volumetric flow rate for the experimental conditions of: 200 gram samples, 1200 °C, 23 % O<sub>2</sub> and average pressure of 1.08 atm; — primary predicted; ○ primary measured; - - - secondary predicted; ◇ secondary measured.

The predictions of Equations (7.68) and (7.110) and the measured rates of weight loss were predicted and plotted against the admitted gas flow rate in Figure 7.15. Considering the experimental scatter, the predicted measured results appear to be in general agreement.

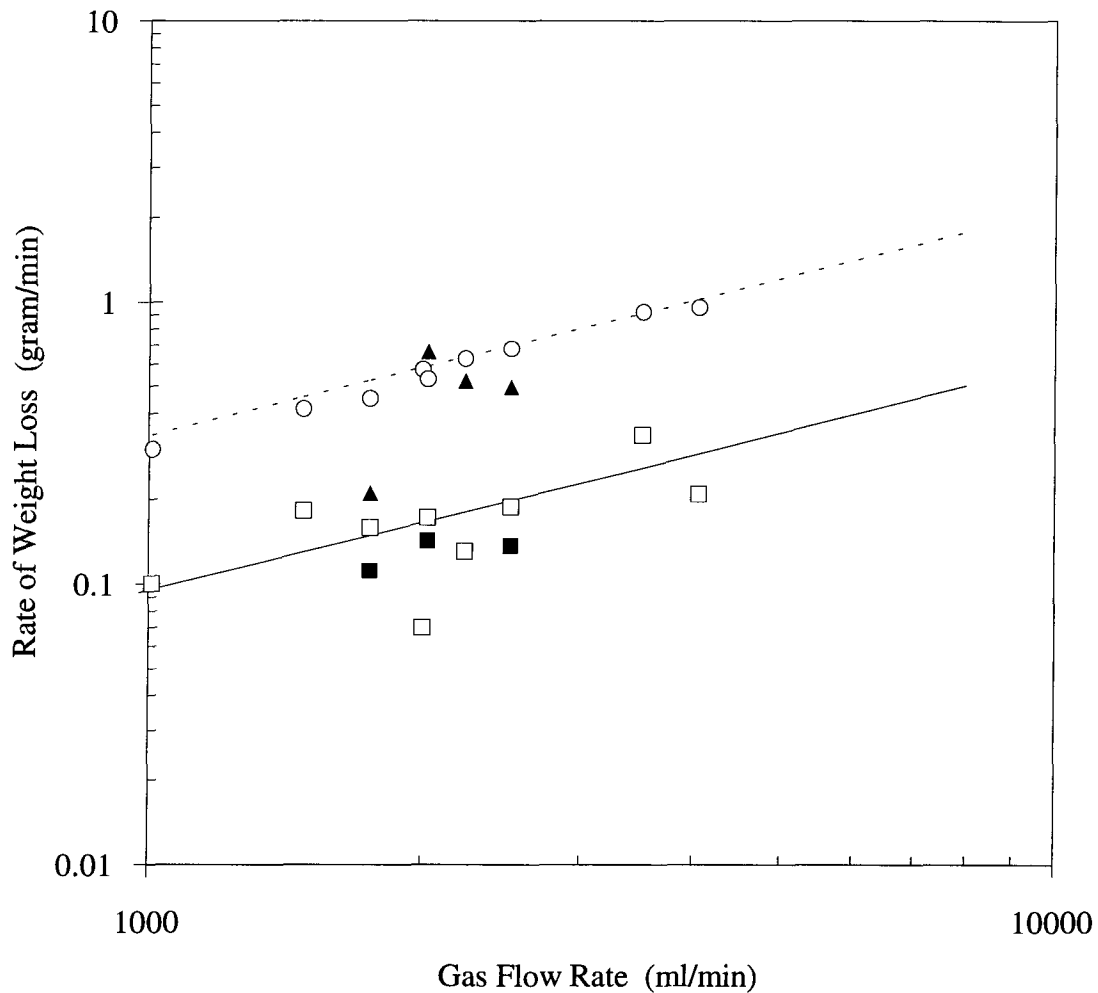


Figure 7.15. Rate of weight loss ( $\dot{W}$ ) as a function of reaction gas volumetric flow rate for the experimental conditions of: 200 gram samples, 1200 °C, 23 % O<sub>2</sub> and average pressure of 1.08 atm; ——— primary predicted; □ primary obtained from gas analysis; ■ primary obtained from gravimetric measurement; - - - - secondary predicted; ○ secondary obtained from gas analysis; ♦ secondary obtained from gravimetric measurement.

#### 7.4.2.2. Oxidation Rate as a Function of Gas Composition

As shown in Figure 7.16, the predicted and experimentally determined oxygen reaction rates are plotted against the partial pressure of oxygen.

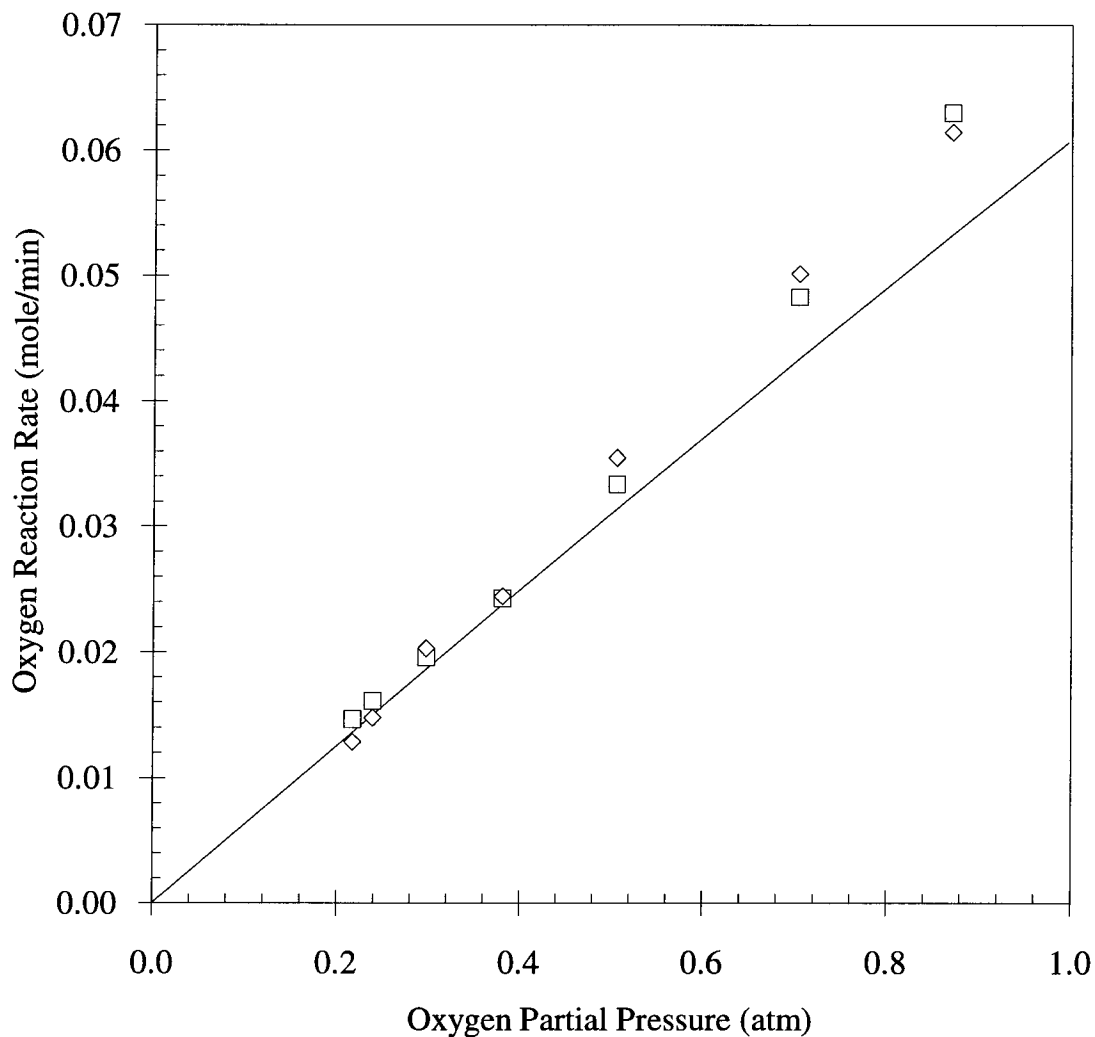


Figure 7.16. Oxygen reaction rate ( $\dot{N}_{O_2}$ ) as a function of oxygen partial pressure for the experimental conditions of: 1200 °C and 2000 ml/min; ——— predicted; □ measured primary; ◇ measured secondary.

In a linear fashion, as shown in Figure 7.17, the measured oxygen reaction rate appears to deviate from the predicted rate of oxygen gas phase mass transfer for oxygen partial pressures of greater than 0.11.

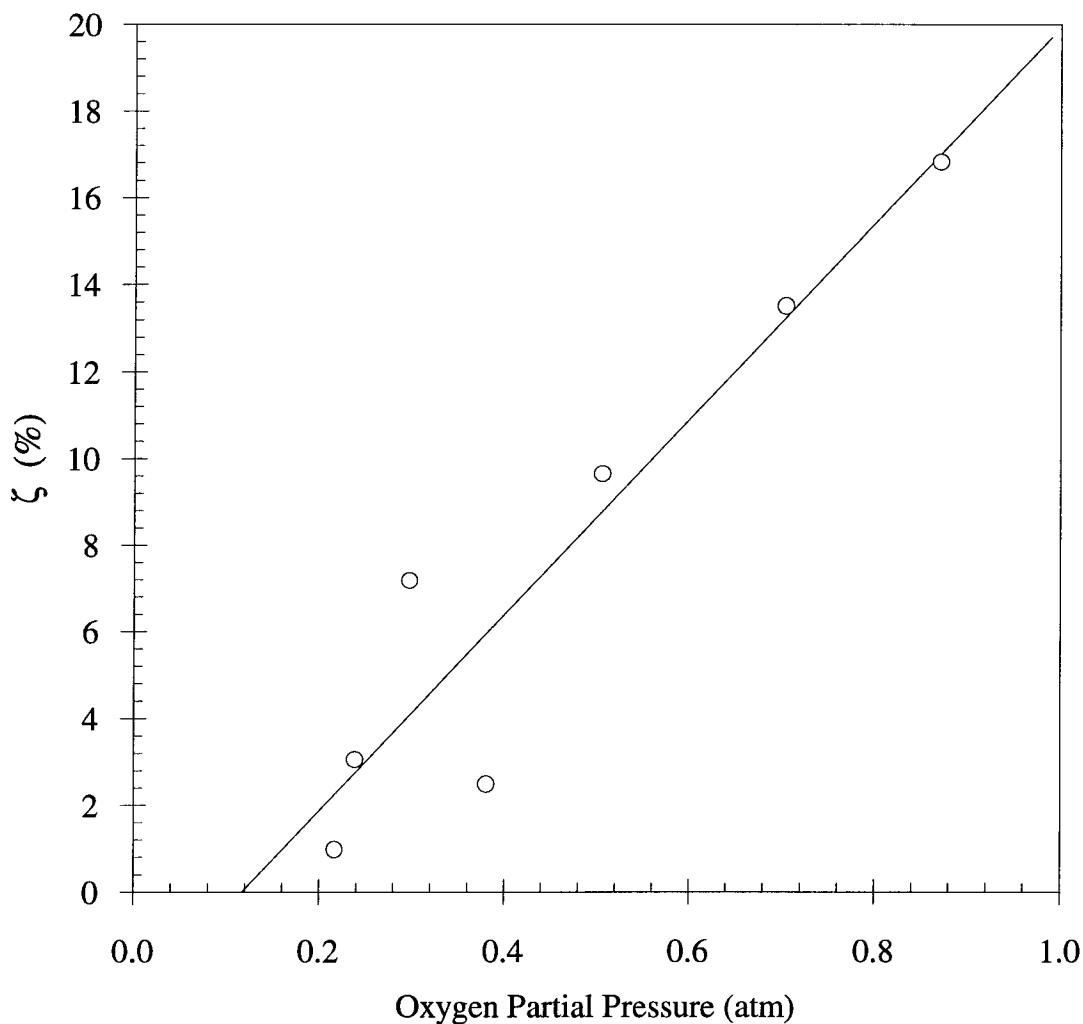


Figure 7.17. Percent increase in gas phase mass transfer as a function of oxygen partial pressure for the experimental conditions of: 1200 °C and 2000 ml/min; — regression line; ○ determined from measurement.

This deviation is attributed to the increase in the gas phase mass-transfer coefficient, due to surface tension-driven flows (the *Marangoni effect*), which were observed to increase with the partial pressure of oxygen. In mathematical terms, the percent increase in gas phase mass transfer,  $\zeta$ , likely due to the Marangoni effect, was found to correlate to the partial pressure of oxygen as follows:

$$\zeta = (22.7 \pm 3.6)P_{O_2}^b - (2.7 \pm 1.9) \quad (7.114)$$

Because, the gas phase mass-transfer coefficient was calculated from a correlation which does not account for the increase in the transport conditions due to surface-tension driven flows, the predicted reaction rates are less than the measured reaction rates.

As discussed in Chapter 5, if the reaction is to be controlled by gas phase mass transfer the sulphur and oxygen molar contents in the bath must be linear with time.

Experimental results presented in Chapter 5 and the mathematical validation in Chapter 7 established that the rate controlling mechanism of the oxidation reaction of molten  $\text{Cu}_2\text{S}$  is gas phase mass transfer (see Figures 5.4, 7.4 and 7.5).

The rates of sulphur removal are directly proportional to the partial pressure of oxygen, as described by Equations (7.56) and (7.104). In Figure 7.18, the measured rates of sulphur removal were plotted against the partial pressure of oxygen along with the theoretical predictions of Equations (7.56) and (7.104). In a similar behaviour to the oxygen reaction rates, the rates of sulphur removal appear to be influenced by the increased degree of gas phase mass transfer. In general, however, there is a reasonable agreement between the predicted and measured rates of sulphur removal, which is an additional evidence that the rates of sulphur removal are limited by the rates of oxygen gas phase mass transfer.

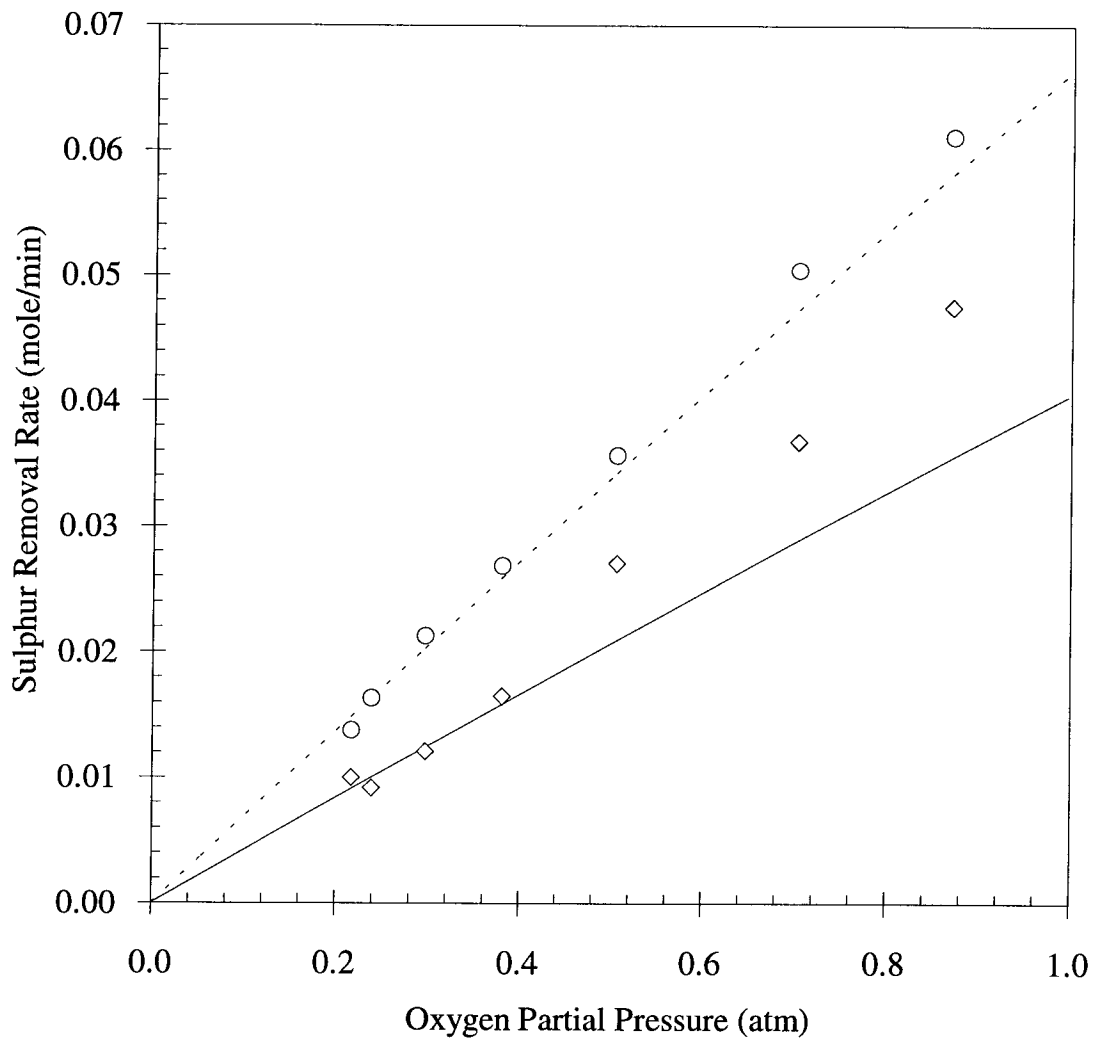


Figure 7.18. Sulphur removal rate ( $dN_S/dt$ ) as a function of oxygen pressure for the experimental conditions of: 1200 °C and 2000 ml/min; — primary predicted;  $\diamond$  primary measured; - - - secondary predicted;  $\circ$  secondary measured.

Increase in the reaction rate with oxygen concentration in the reaction gas, in the oxidation of molten  $\text{Cu}_2\text{S}$ , was also exhibited by the experimental results of Rottmann and Wuth [71], as shown in Figure 7.19.

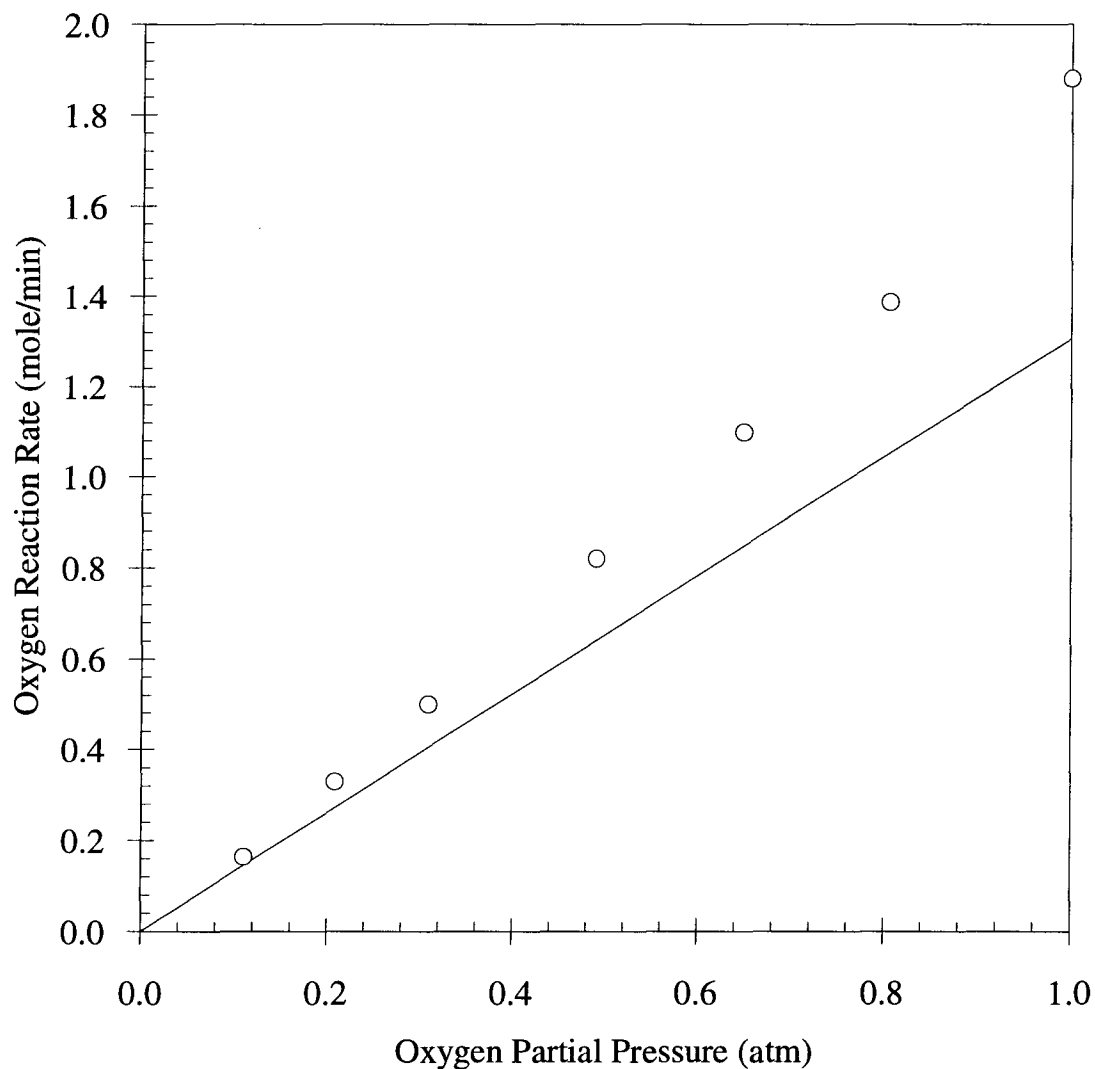


Figure 7.19. Oxygen reaction rate ( $\dot{N}_{\text{O}_2}$ ) as a function of oxygen pressure for the experimental conditions of: 1500 grams of  $\text{Cu}_2\text{S}$  under the top-lancing of high velocity jets of  $\text{O}_2\text{-N}_2$  gas mixtures at  $1250^\circ\text{C}$ , nozzle pressure of  $5.4 \times 10^5 \text{ N/m}^2$ , nozzle diameter of 1 mm, nozzle to bath distance of 65 mm and crucible inner diameter of 100 mm; ——— predicted (after Rottmann and Wuth [71] (based on gas phase mass transfer of oxygen through a viscous sub-layer));  $\circ$  measured (after Rottmann and Wuth).



As discussed in Section 2.4, Rottmann and Wuth measured the reaction rates of the oxidation of molten  $\text{Cu}_2\text{S}$  for different oxygen concentrations in the bulk gas at 1250 °C. In their prediction of the reaction rates, Rottmann and Wuth assumed that the reaction is limited by the oxygen diffusion in a viscous sub-layer of thickness  $\delta_{visc}$ . Using a correlation for the thickness of the boundary layer at a plate exposed parallel to a turbulent stream, they calculated  $\delta_{visc}$  as follows:

$$\delta_{visc} = \frac{29v^{0.9}x^{0.1}}{U_{g,max}^{0.9}} \quad (7.115)$$

from which the rate of oxygen reaction was calculated as follows:

$$n_{O_2} = \frac{D_{O_2-N_2}}{\delta_{visc}} \frac{\Delta P_{O_2}}{RT} \quad (7.116)$$

Because they did not measure the reaction rates for a range of gas flow rates, it is not possible to validate the assumption of diffusion through a viscous layer and in turn determine the validity of Equation (7.116). It is likely, however, that the predicted reaction rates are linear with the oxygen pressure in the gas phase. Assuming that the actual reaction rates are very close to those predicted by Rottmann and Wuth, it is suggested that the deviation exhibited by the measured results is due to increased surface-tension driven flows with oxygen concentration in the admitted gas. The percent increase in the gas phase mass transfer was similarly correlated to the partial pressure of oxygen as follows:

$$\zeta = (29 \pm 4)P_{O_2}^b + (12 \pm 2) \quad (7.117)$$

in which, the slope is slightly higher than that in Equation (7.114). It is therefore, suggested that, due to the Marangoni effect, the gas phase mass transfer conditions are enhanced with increasing oxygen concentration in the reaction gas phase. As discussed in Section 2.5, increases in mass transfer, due to the Marangoni effect, have been observed

to occur in many systems [56,82,84,99,101,121]. In the oxidation of molten  $\text{Cu}_2\text{S}$ , as shown in Section 5.3, there is an overwhelming evidence that surface-tension driven flows play an important role in the overall reaction rate kinetics. By stirring the bath, surface-tension driven flows virtually eliminate any liquid phase mass transfer resistance, as shown in Figure 5.15. As the radial movement of the surface is increased with higher concentrations of oxygen in the gas phase, the mass transfer conditions are likely to increase as the moving liquid causes further drag of the gas, thereby, enhancing the reaction rate beyond the values accounted for by ordinary transport conditions.

#### 7.4.2.3. Oxidation Rate as a Function of Temperature

From Equation (7.2), the rate of oxygen reaction is inversely proportional to temperature. The predicted and measured oxygen reaction rates are plotted against temperature in Figure 7.20. Although the gas phase mass-transfer coefficient is positively dependent on temperature, the predicted oxygen reaction rate appears to have a slight negative dependence on temperature, as shown in Figure 7.20. In general, however, it can be stated that both the measured and predicted oxygen reaction rates are effectively independent of temperature.

In comparing Equations (7.56) and (7.104) theoretically, the temperature dependence of the rate of sulphur removal during the secondary stage is greater than that during the primary stage. In Equation (7.104), the secondary molar ratio of reacted oxygen to removed sulphur,  $\alpha^s$ , is a function of the equilibrium concentrations of the melt, as described by the following equation:

$$\alpha^s = 1 + \left[ \left[ O_{\text{Cu}} N_{\text{Cu}^+}^* - N_{\text{O}^{2-}}^* \right] / 2 \left[ N_{\text{S}^{2-}}^* - S_{\text{Cu}} N_{\text{Cu}^+}^* \right] \right] \quad (7.118)$$

which yields 0.9169 and 0.9250 for  $\alpha^s$  at 1200 and 1300 °C respectively. Conversely, the primary molar ratio of reacted oxygen to removed sulphur dioxide,  $\alpha^p$ , is 1.5 (independent of temperature).

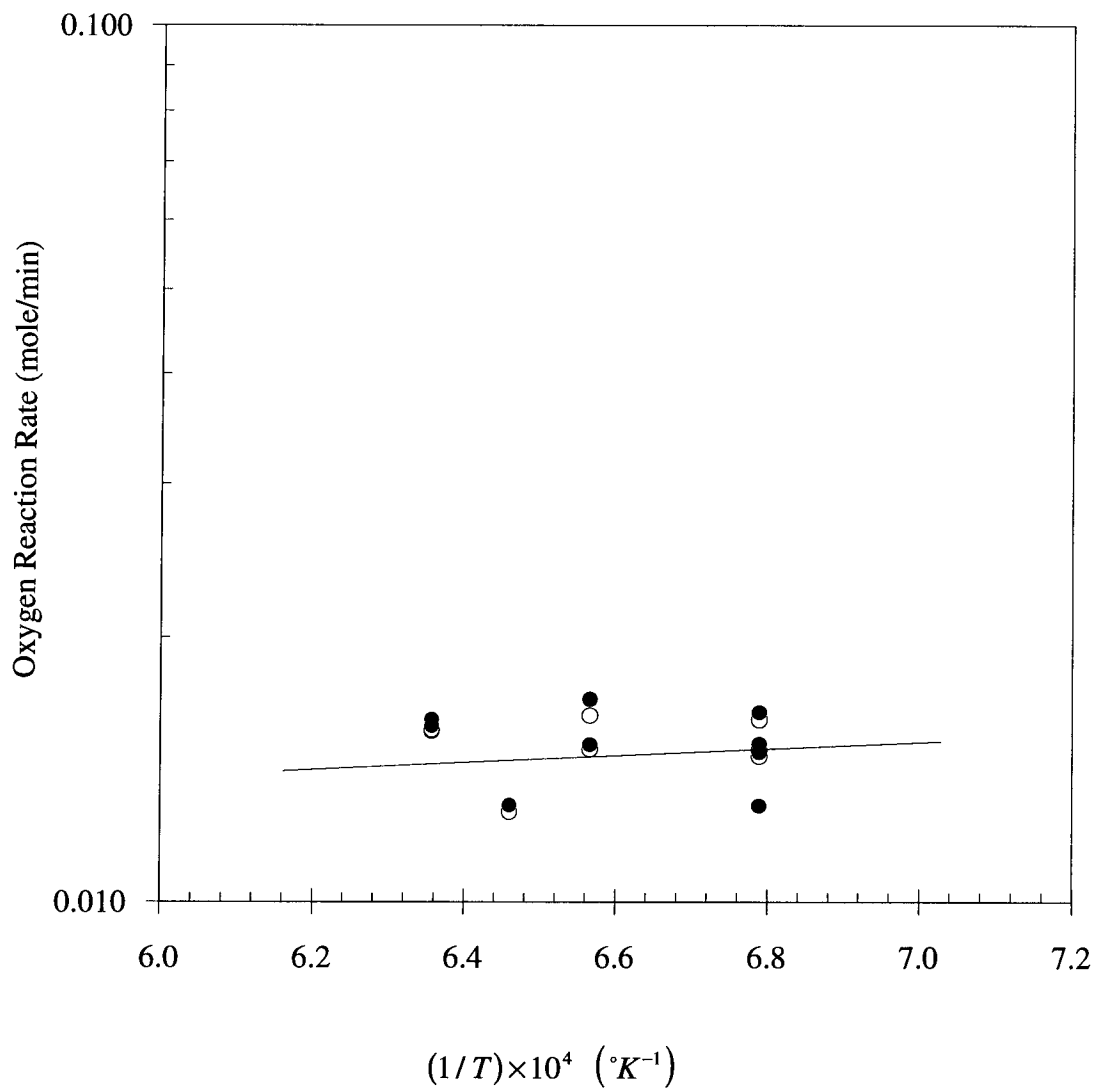


Figure 7.20. Oxygen reaction rate ( $\dot{N}_{O_2}$ ) as a function of temperature for the experimental conditions of: 2000 ml/min of 20-23 %  $O_2$  and average pressure of 1.08 atm; — primary predicted 22 %  $O_2$ ;  $\circ$  primary measured;  $\bullet$  secondary measured.

In Figure 7.21, the predicted and measured rates of sulphur removal are plotted against temperature, from which it appears that measured and predicted results are in agreement. The primary rate of sulphur removal seems to have a similar behaviour to that of the oxygen reaction rate, but the secondary rate of sulphur removal appears to be virtually independent of temperature.

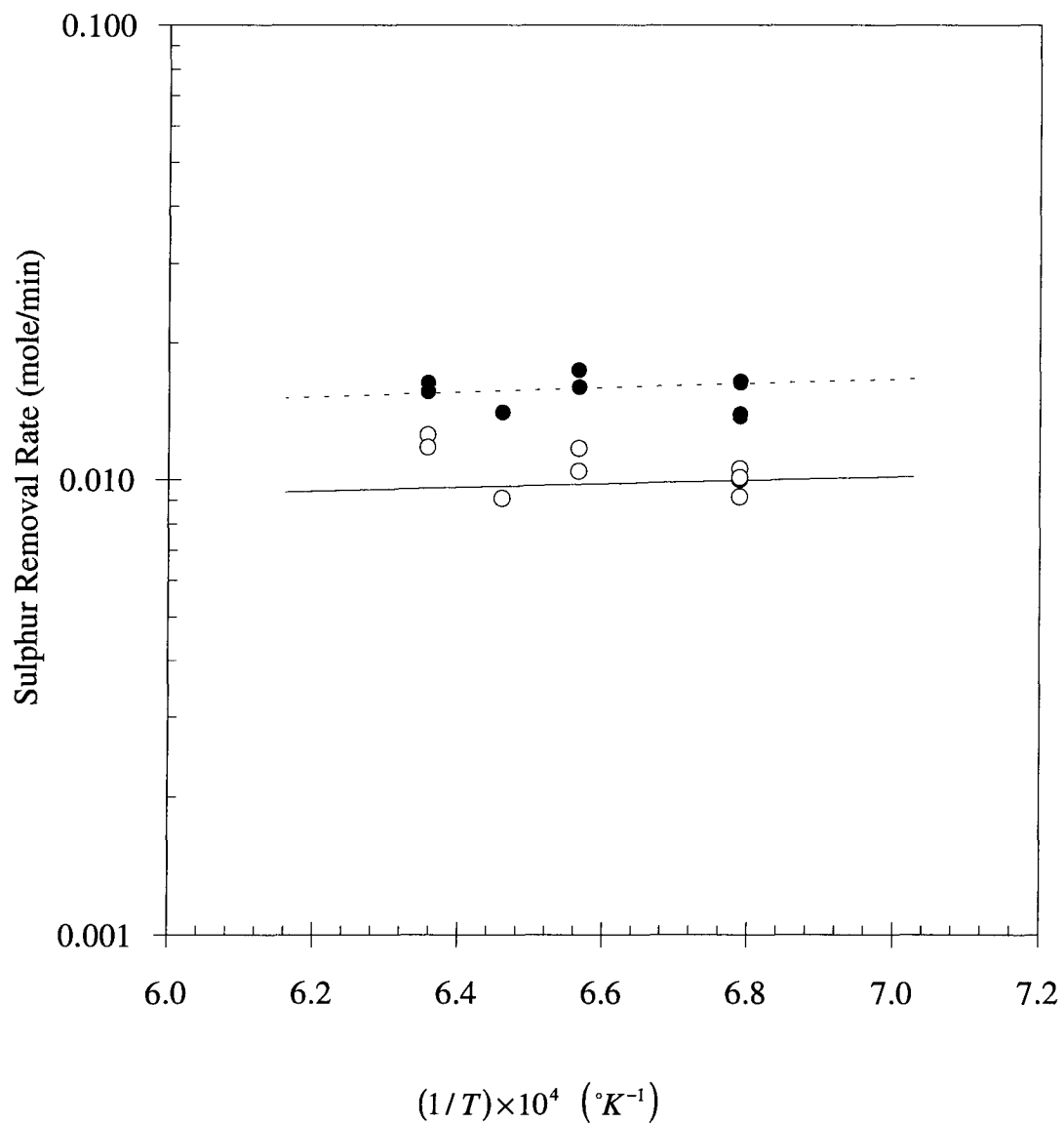


Figure 7.21. Sulphur removal rate ( $dN_S/dt$ ) as a function of temperature for the experimental conditions of: 2000 ml/min of 20-23 %  $O_2$  and average pressure of 1.08 atm; — primary predicted 22 %  $O_2$ ; - - - secondary predicted 22 %  $O_2$ ;  $\circ$  primary measured;  $\bullet$  secondary measured.

### 7.4.3. Oxygen Utilization

The oxygen utilization as a function of gas flow rate is shown in Figure 7.22, from which it appears that very high reaction efficiencies are attained in the oxygen-Cu<sub>2</sub>S system.

This is consistent with the observed oxygen utilization in the Peirce-Smith converter.

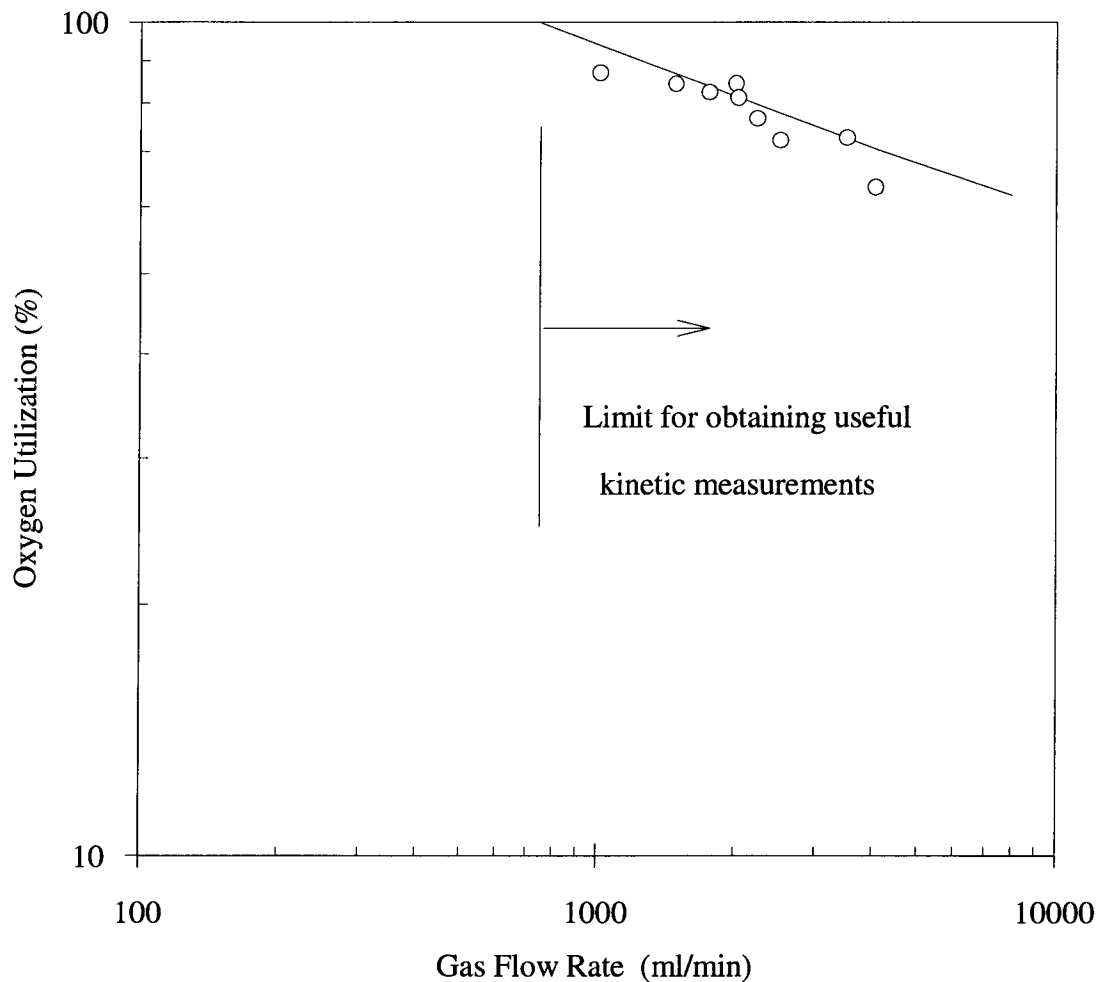


Figure 7.22. Oxygen utilization as a function of reaction gas volumetric flow rate for the top-blown conditions of: 200 grams of Cu<sub>2</sub>S at 1200 °C, 1.08 atm, 23% O<sub>2</sub>, reaction interfacial diameter of 44 mm, lance nozzle diameter of 3 mm and lance nozzle to initial interfacial area of approximately 10 mm; ——— predicted; ○ measured.

To obtain valid kinetic measurements of heterogeneous reaction systems in laboratory tests, reactants must be supplied at rates beyond their rates of consumption by the reaction

at the given experimental conditions. From Figure 7.22, the predicted oxygen curve indicates that the limit for obtaining useful kinetic measurements is 750 ml/min i.e. below this value the oxidation reaction rate is higher than that of the rate of oxygen supply.

Industrial processes in which gas-liquid reactions are involved, the utilization of the reaction gas is of high economic importance. It is important that the reaction gas efficiency be as high as possible. Since however, the high efficiency is accompanied by lower reaction rates, the optimization of a given process may dictate that the gas utilization be much lower than can be attained.

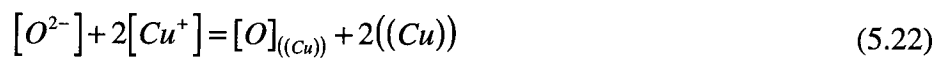
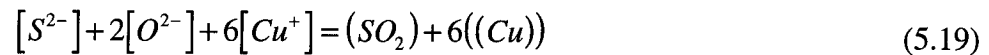
## 8. Summary and Conclusions

The primary objective of this work was to investigate the oxidation kinetics of molten copper sulphide under top-blown conditions. The major findings of this work can be summarized as follows:

1. The oxidation reaction of molten copper sulphide takes place according to two distinct stages.
2. During the primary stage, the melt is a single phase, being partially desulphurized and becoming oxygen saturated, according to the surface reaction as follows:



3. Upon saturation of the melt with oxygen, the secondary stage commences, during which the following reactions in the sulphide phase produce metallic copper:



while the surface reaction involving gaseous oxygen continues to take place until the end of the secondary stage.

4. The rate of sulphur removal and oxygen dissolution during the primary stage were found to be independent of sulphur and oxygen contents in the melt. Similarly, the rates of sulphur and oxygen removal during the secondary stage are independent of sulphur and oxygen contents in the melt.
5. The rate controlling mechanism in the oxidation of molten  $Cu_2S$  is gas phase mass transfer of oxygen to the melt surface; the oxidation rate was found to be directly

proportional to the partial pressure of oxygen in the reaction gas. From the experimental data obtained in this work, the gas phase-mass transfer coefficient was correlated to experimental variables via the Sherwood number,  $Sh$ , the Schmidt number,  $Sc$  ( $0.56 \leq Sc \leq 0.63$ ), the Reynolds number,  $Re$  ( $33 \leq Re \leq 300$ ), the radius of the crucible,  $r_s$ , and the diameter of the lance nozzle,  $d$  ( $7 \leq r_s/d \leq 11$ ), as follows:

$$Sh = (0.64 \pm 0.07)(r_s/d)^{-1.5} Sc^{0.5} Re^{(0.79 \pm 0.06)} \quad (6.18)$$

6. Surface-tension driven flows (Marangoni effect) were observed to take place during the oxidation reaction. As a result transport conditions at the gas-liquid interface were slightly enhanced. The degree of surface-turbulence was observed to be a relatively strong function of the oxygen content in the reaction gas, while the gas flow rate was observed to cause only a slight increase. The effect of temperature on surface-tension driven flows was undetectable.
7. In a continuous fashion, the eruption of small numbers of gas bubbles from the melt surface was observed to take place during the secondary stage, while at random time intervals, occasional intense boiling was observed to occur as well. The intensity and frequency of boiling were observed to increase with increasing gas flow rate and oxygen partial pressure.
8. The liquid phase mass transfer resistance was found to be negligible, likely due to the ionic nature of the sulphide melt and the Marangoni effect. Because of the electrochemical nature of the sulphide melt, the local transport of electrons is very rapid (the specific conductance of  $\text{Cu}_2\text{S}$  is  $150 \Omega^{-1}\text{cm}^{-1}$  at  $1500 \text{ }^\circ\text{C}$  [115]), and owing to surface-tension driven flows, the bath is vigorously mixed. During the secondary stage, the degree of mixing in the bath is enhanced by rising  $\text{SO}_2$  bubbles and settling copper droplets. Due to the eruption of gas bubbles at the melt surface, the



dependence of the reaction rate on the gas flow rate was found to be slightly higher as a result of increasing gas-liquid interfacial area.

8. The effect of temperature on the overall reaction rate was found to be negligible.
9. Based on the experimental results and the likely electrochemical reactions, a mathematical model was formulated and was found to provide a reliable description of the oxidation reaction.

The practical implications of these findings are as follows:

1. The high oxygen utilization in the Peirce-Smith converter is due to the ionic nature of the sulphide melt and the effect of surface-tension driven flows which give rise to gas phase mass transfer control.
2. In systems similar to copper sulphide (negligible liquid phase mass transfer resistance and very fast chemical reaction), high reaction gas utilization can be attained under top-lancing conditions. Thus by adopting top-lancing as in the Mitsubishi Process, high oxygen efficiencies are achievable while the problems of refractory wear in tuyere region are eliminated.

### References

1. T. M. Morris, "History of Copper Converting", Journal of Metals, July 1968, pp 73-75.
2. A. K. Biswas and W. G. Davenport, "**Extractive Metallurgy of Copper**", 2nd Edition, Pergamon Press, Beccles and London, 1980.
3. C. L. Milliken and F. F. Hofinger, "An Analysis of Copper Converter Size and Capacity", Journal of Metals, April 1968, pp 39-45.
4. R. E. Johnson, N. J. Themelis and G. A. Eltringham, "A Survey of Worldwide Copper Converter Practices", Copper and Nickel Converters, Conference Proceedings, The Metallurgical Society of AIME, 1979, pp 1-32.
5. F. E. Lathe and L. Hodentt, "Data on Copper Converter Practice in Various Countries", Transactions of The Metallurgical Society of AIME, October 1958, pp 603-615.
6. A. A. Bustos, J. K. Brimacombe and G. G. Richards, "Heat Flow in Copper Converters", Metallurgical Transactions, Volume 17B, No 4, Process Metallurgy, December 1986, pp 677-685.
7. D. W. Ashman, J. W. McKelliget and J. K. Brimacombe, "Mathematical Model of Bubble Formation at the Tuyeres of a Copper Converter", Canadian Metallurgical Quarterly, Volume 20, No 4, 1981, pp 387-395.
8. A. A. Bustos, J. K. Brimacombe and G. G. Richards, "Accretion Growth at the Tuyeres of a Peirce-Smith Copper Converter", Canadian Metallurgical Quarterly, Volume 27, No 1, pp 7-21, 1988.
9. King, A. D. Mah and L. B. Pankratz, "Thermodynamic Properties of Copper and its Inorganic Compounds", INCRA Monograph II, The Metallurgy of Copper, International Copper Research Association, Inc., New York, 1973.
10. E. A. Peretti, "An Analysis of the Converting of Copper Matte", Discuss. Faraday Society 4, 1948, pp 179-184.
11. T. Rosenquist, "**Principles of Extractive Metallurgy**", 2nd Edition, McGraw-Hill, New York, 1983.
12. F. Habashi, "**Principles of Extractive Metallurgy, Volume 3, Pyrometallurgy**", Gordon and Breach, New York, 1986.
13. W. Oelsen in Clausthal, "Die Desoxydation von Kupferschmelzen mit Eisen, mit Phosphor und mit Schwefel", Giesserei Techn.-Wissensch. Beihefte, Heft 6/8, März, 1952, pp 383-387.
14. U. Kuxmann and T. Benecke, "Untersuchungen zur Löslichkeit von Sauerstoff in Kupfersulfid-Schmelzen", Erzmetall, Mai 1966, pp 215-274.
15. H. H. Kellogg, "Thermochemical Properties of the System Cu-S at Elevated Temperature", Canadian Metallurgical Quarterly, Volume 8, No 1, 1969, pp 3-23.

16. A. Yazawa and T. Azakami, "Thermodynamics of Removing Impurities During Copper Smelting", Canadian Metallurgical Quarterly, volume 8, No 3, 1969, pp 257-261.
17. J. Schmiedl, M. Štofko and V. Repcák, "Gleichgewichtsuntersuchungen im System Cu-Fe-O", Neue Hütte, 16 jg, Heft 7, Juli 1971, pp 390-395.
18. F. Y. Bor and P. Tarassoff, "Solubility of Oxygen in Copper Mattes", Canadian Metallurgical Quarterly, Volume 10, No 4, 1971, pp 267-271.
19. J. Schmiedl, "Physical Chemistry of Continuous Copper Smelting", Physical Chemistry of Process Metallurgy: The Richardson Conference, The Institution of Mining and Metallurgy, 1974, pp 127-134.
20. J. F. Elliott, "Phase Relationships in the Pyrometallurgy of Copper", Metallurgical Transactions, Volume 7B, March 1976, pp 17-33.
21. R. C. Sharma and Y. A. Chang, "A Thermodynamic Analysis of Copper-Sulphur System", Metallurgical Transactions, Volume 11B, December 1980, pp 575-583.
22. R. Schmid, "A Thermodynamic Analysis of the Cu-O System with an Associated Solution Model", Metallurgical Transactions, Volume 14B, September 1983, pp 473-481.
23. S. Otsuka and Y. A. Chang, "Activity Coefficient of Oxygen in Copper-Sulphur Melts", Metallurgical Transactions, Volume 15B, June 1984, pp 337-343.
24. J. Lumsden, "Thermodynamics of Iron-Copper-Sulphur-Oxygen Melts", Metal-Slag-Gas Reactions and Processes, The Electrochemical Society, Inc., Princeton, New Jersey, 1975, pp 155-168.
25. T. Rosenquist. "Thermodynamics of Copper Smelting", Advances in Sulphide Smelting, Volume 1, TMS-AIME, 1983, pp 239-255.
26. C. B. Alcock, "**Principles of Pyrometallurgy**", Academic Press, 1976, pp 170-175.
27. F. Ajersch and J. M. Toguri, "Oxidation Rates of Liquid Copper and Liquid Copper Sulphide", Metallurgical Transactions, Volume 3, August 1972, pp 2187-2193.
28. Z. Asaki, F. Ajersch, and J. M. Toguri, "Oxidation of Molten Ferrous Sulphide", Metallurgical Transactions, Volume 5, August 1974, pp 1753-1759.
29. Y. Fukunaka and J. M. Toguri, "The Oxidation of Liquid Ni<sub>3</sub>S<sub>2</sub>", Metallurgical Transactions, Volume 10B, June 1979, pp 191-201.
30. Z. Asaki, S. Ando, and Y. Kondo, "Oxidation of Molten Copper Matte", Metallurgical Transactions, Volume 19B, February 1988, pp 47-52.
31. F. Ajersch and M. Benlyamani, "Thermogravimetric Identification and Analysis of Reaction Products During Oxidation of Solid or Liquid Sulphides", Thermochemica Acta, 143, 1989, pp 221-237.
32. T. Tanabe, K. Kanzaki, M. Kobayashi and Z. Asaki, "Kinetics of Desulphurization and Oxidation of Molten Nickel-Cobalt Sulphide in the Temperature Range between

- 1473 and 1673 °K", Materials Transactions, JIM, Volume 31, No. 3, 1990, pp 207-212.
33. Y. Fukunaka, K. Tamura, N. Taguchi and Z. Asaki, "Deoxidation Rate of Copper Droplet Levitated in Ar-H<sub>2</sub> Gas Stream", Metallurgical Transactions, Volume 22B, October 1991, pp 631-637.
  34. K. Li, D. A. Dukelow, and G.C. Smith, "Decarburization in Iron-Carbon System by Oxygen Top Blowing", Transactions of The Metallurgical Society of AIME, Volume 230, February 1964, 71-76.
  35. R. B. Banks and D. V. Chandrasekhara, "Experimental Investigation of the Penetration of a High-Velocity Gas Jet Through a Liquid Surface", Journal of Fluid Mechanics, Volume 15, Part 1, June 1962, pp 13-34.
  36. Gasstrahlen auf Flüssigkeitsoberflächen, "Zum Wärme- und Stoffaustausch beim Senkrechten Aufblasen", Chemie-Ing-Techn 38, Heft 3, Jahrg 1966, pp 309-314.
  37. G. C. Smith, "Multiple Jet Oxygen Lances-Theoretical Analysis and Correlation with Practice", Journal of Metals, July 1966, pp 846-851.
  38. W. G. Davenport, D. H. Wakelin and A. V. Bradshaw, "Interaction of Both Bubbles and Gas Jets With Liquids", Heat and Mass Transfer in Process Metallurgy, Proceedings of a Symposium held by the John Percy Research Group in Process Metallurgy, Imperial College, London, 19 and 20 April, 1966, Edited by A. W. D. Hills, The Institution of Mining and Metallurgy, 1967, pp 207-237.
  39. N. J. Themelis and P. R. Schmidt, "Deoxidation of Liquid Copper by a Submerged Gas Jet", Transactions of The Metallurgical Society of AIME, Volume 239, September 1967, pp 1313-1318.
  40. N. J. Themelis, P. Tarassoff and J. Szekely, "Gas-Liquid Momentum Transfer in a Copper Converter", Transactions of The Metallurgical Society of AIME, Volume 245, 1969, pp 2425-2433.
  41. N. A. Molloy, "Impinging Jet Flow in a Two-Phase System: The Basic Flow Pattern", Journal of Iron and Steel Institute, October 1970, pp 943-950.
  42. A. Chatterjee and A. V. Bradshaw, "Break-Up of a Liquid Surface by an Impinging Gas Jet", Journal of The Iron and Steel Institute, March 1972, pp 179-187.
  43. J. Szekely and S. Asai, "Turbulent Fluid Flow Phenomena in Metals Processing Operations: Mathematical Description of the Fluid Flow Field in a Bath Caused by an Impinging Gas Jet", Metallurgical Transactions, Volume 5, February 1974, pp 463-467.
  44. J. K. Brimacombe, E. S. Stratigakos and P. Tarassoff, "Mass Transfer Between a Horizontal, Submerged Gas Jet and a Liquid", Metallurgical Transactions, Volume 5, March 1974, pp 763-771.
  45. S. Taniguchi, A. Kikuchi and S. Maeda, "Model Experiments on Mass Transfer in Gas Phase Between an Impinging Jet of Gas and Liquid Iron", Tetsu-to-Hagane, 1976, 62(2), pp 191-200.

46. S. Taniguchi, A. Kikuchi and S. Maeda, "Kinetics of the Oxidation of Graphite by the Impinging Jet of Gas", Tetsu-to-Hagane, 1977, 63(7), pp 1071-1080.
47. S. Taniguchi, A. Kikuchi, T. Tadaki and S. Maeda, "Numerical Analysis on the Gas-Phase Mass Transfer Between an Impinging Jet of Gas and Liquid Iron", Tetsu-to-Hagane, 1979, 65(13), pp 1830-1873.
48. A. Kikuchi, S. Taniguchi, T. Tadaki and S. Maeda, "Fluid Flow and Mass Transfer in the Gas-Liquid Iron System with a Laboratory-Scale Induction Furnace", Metallurgical Applications of Magnetohydrodynamics, Proceedings of a Symposium of the International Union of Theoretical and Applied Mechanics held at Trinity College, Cambridge, UK, 6-10 September 1982, Edited by H. K. Moffatt and M. R. E. Proctor, The Metals Society Institute.
49. J. Zong, H. Park and J. Yoon, "The Cold Model Study on the Decarburization Rate in Oxygen Steelmaking Processes by CO<sub>2</sub>/KOH System", ISIJ International, Volume 30, No 9, 1990, pp 748-755.
50. S. Chung, J. Zong, H. Park and J. Yoon, "The Effect of the Gas Jet on the Gas/Liquid Reactivity in the Metallurgical Vessel", ISIJ International, Volume 31, No 1, 1991, pp 69-75.
51. A. Chatterjee, D. H. Wkelin and A. V. Bradshaw, "Mass Transfer from an Oxygen Jet to Liquid Silver", Metallurgical Transactions, Volume 3, December 1972, pp 3167-3172.
52. J. Szekely and N. J. Themelis, "**Rate Phenomena In Process Metallurgy**", John Wiley & Sons, Inc., 1971.
53. A. Chatterjee and A. V. Bradshaw, "The Influence of Gas Phase Resistance on Mass Transfer to a Liquid Metal", Metallurgical Transactions, Volume 4, May 1973, pp 1359-1364.
54. S. Taniguchi, A. Kikuchi, H. Matsuzaki and N. Bessho, "Dispersion of Bubbles and Gas-Liquid Mass Transfer in a Gas-Stirred System", Transactions ISIJ, Volume 28, 1988, pp 262-270.
55. J. K. Brimacombe and F. Weinberg, "Observations of Surface Movements of Liquid Copper and Tin", Metallurgical Transactions, Volume 3, August 1972, pp 2298-2299.
56. R. G. Barton and J. K. Brimacombe, "Influence of Surface Tension-Driven Flow on the Kinetics of Oxygen Absorption in Molten Copper", Metallurgical Transactions, Volume 8B, September 1977, pp 417-427.
57. H. Jalkanen, "Phenomenology of the Oxidation Kinetics of Molten Cuprous Sulphide and Copper", Scandinavian Journal of Metallurgy 10, 1981, pp 257-262.
58. J. K. Brimacombe, A. A. Bustos, D. Jorgenson and G. G. Richards, "Toward a Basic Understanding of Injection Phenomena in the Copper Converter", Physical Chemistry of Extractive Metallurgy, Edited by V. Kudryk and Y. K. Rao, Warrendale, PA: The Metallurgical Society, 1985, pp 327-351.

59. G.G. Richards, K. J. Legeard, A. A. Bustos, J. K. Brimacombe and D. Jorgenson, "Bath Slopping and Splashing in the Copper Converter", The Reinhardt Schuhmann International Symposium., Warrendale, PA: The Metallurgical Society, 1987, pp 385-402.
60. J. Liow and N. B. Gray, "Slopping Resulting from Gas Injection in a Peirce-Smith Converter, Metallurgical Transactions, Volume 21B, 1990, pp 657-664 and 987-996.
61. H. H. Kellogg and C. Díaz, "Bath Smelting Processes in Non-Ferrous Pyrometallurgy: An Overview", Proceedings of the Savard/Lee International Symposium on Bath Smelting, Edited by J. K. Brimacombe, P. J Mackey, G. J. W. Kor, C. Bickert and M. G. Ranade, The Minerals, Metals & Materials Society, 1992, pp 39-65.
62. Y. Kishimoto, T. Sakuraya and T. Fujii, "Recent Advances in Top and Bottom Blowing Converters Based on a Mathematical model", Proceedings of the Savard/Lee International Symposium on Bath Smelting, Edited by J. K. Brimacombe, P. J Mackey, G. J. W. Kor, C. Bickert and M. G. Ranade, The Minerals, Metals & Materials Society, 1992, pp 293-323.
63. M. Sano and k. Mori, "Fundamentals of Gas Injection in Refining Processes", Proceedings of the Savard/Lee International Symposium on Bath Smelting, Edited by J. K. Brimacombe, P. J Mackey, G. J. W. Kor, C. Bickert and M. G. Ranade, The Minerals, Metals & Materials Society, 1992, pp 465-492.
64. N. B. Gray and M. Nilmani, "Injection in Matte Converting and Metal Refining", Proceedings of the Savard/Lee International Symposium on Bath Smelting, Edited by J. K. Brimacombe, P. J Mackey, G. J. W. Kor, C. Bickert and M. G. Ranade, The Minerals, Metals & Materials Society, 1992, pp 523-551.
65. G. G. Richards, "Submerged Injection in Non-Ferrous Processes", Proceedings of the Savard/Lee International Symposium on Bath Smelting, Edited by J. K. Brimacombe, P. J Mackey, G. J. W. Kor, C. Bickert and M. G. Ranade, The Minerals, Metals & Materials Society, 1992, PP 553-563.
66. G. J. Hadie, I. F. Taylor, J. M. Ganser, J. K. Wright, M. P. Davis and C. W. Boon, " Adoption of Injection Technology for the HIsMelt™ Process", Proceedings of the Savard/Lee International Symposium on Bath Smelting, Edited by J. K. Brimacombe, P. J Mackey, G. J. W. Kor, C. Bickert and M. G. Ranade, The Minerals, Metals & Materials Society, 1992, pp 623-644.
67. G. Savard and R. G. H. Lee, "Submerged Oxygen Injection for Pyrometallurgy", Proceedings of the Savard/Lee International Symposium on Bath Smelting, Edited by J. K. Brimacombe, P. J Mackey, G. J. W. Kor, C. Bickert and M. G. Ranade, The Minerals, Metals & Materials Society, 1992, pp 645-660.
68. T. Emi, W. Boorstein and R. D. Pehlke, "Absorption of Gaseous Oxygen by Liquid Iron", Metallurgical Transactions, Volume 5, September 1974, pp 1959-1966.
69. J. J. Byerley, G. L. Rempel and N. Takebe, "Interaction of Copper Sulphide with Copper Oxides in the Molten State", Metallurgical Transactions, Volume 5, December 1974, pp 2501-2506.

70. H. H. Kellogg vs. J. Byerley, G. L. Rempel and N. Takebe, "Discussion of Interaction of Copper Sulphide with Copper Oxides in the Molten State", Metallurgical Transactions, Volume 6B, January 13 1975, pp 350-351.
71. G. Rottmann and W. Wuth, "Conversion of Copper Matte by Use of the Top-Blowing Technique", Copper Metallurgy: Practice and theory, Edited by M. J. Jones, The Institution of Mining and Metallurgy, 1975, pp 49-52.
72. C. F. Acton and G. R. Belton, "On the Kinetics of Oxidation of Liquid Copper and Copper-Sulphur Alloys by Carbon Dioxide", Metallurgical Transactions, Volume 7B, December 1976, pp 693-697.
73. V. A. Bryukvin, O. I. Tsybin, L. I. Blokhina and G. N. Zviadadze, "An Investigation of the Oxidation Kinetics of a Copper Sulphide Melt with Oxygen", UDC 669:546.221, (Moscow), 1976, pp 24-27.
74. V. A. Bryukvin, O. I. Tsybin, L. I. Blokhina and G. N. Zviadadze, "Phase Composition of Oxidation Products of Molten Copper Sulphide", UDC 669.332, (Moscow), 1977, pp 51-53.
75. R. H. Radzilowski and R. D. Pehlke, "Absorption of Gaseous Oxygen by Liquid Cobalt, Copper, Iron and Nickel", Metallurgical Transactions, Volume 9B, March 1978, pp 129-137.
76. Y. Fukunaka, K. Nishikawa, H. S. Sohn and Z. Asaki, "Desulphurization Kinetics of Molten Copper by Gas Bubbling", Metallurgical Transactions, Volume 22B, February 1991, pp 5-11.
77. Z. Asaki, Y. Chiba, T. Oishi and Y. Kondo, "Kinetic Study on the Reaction of Solid Silica with Molten Matte", Metallurgical Transactions, Volume 21B, February 1990, pp 19-25.
78. R. Ohno, "Desulphurization and Deoxidation of Cu-S-O Alloy in Induction Melting and Solidification under Argon and their Rates of Elimination in Vacuum Induction Melting", Metallurgical Transactions, Volume 22B, August 1991, pp 405-416.
79. R. B. Bird, W. E. Stewart and E. N. Lightfoot, "**Transport Phenomena**", John Wiley & Sons, Inc. New York, 1960, pp 570.
80. J. T. Davies and E. K. Rideal, "**Interfacial Phenomena**", Academic Press, New York, 1961.
81. J. K. Brimacombe, A. D. Graves and D. Inman, "Origins of Spontaneous Movements at Interfaces Between Amalgams and Aqueous Electrolyte", Chemical Engineering Science, 25, 1970, pp 1917-2008.
82. J. K. Brimacombe and F. D. Richardson, "Mass Transfer and Interfacial Phenomena in Bubble-Agitated Systems", Transactions of The Institution of Mining and Metallurgy, Section C: Mineral Process and Extractive Metallurgy, 80, 1971, pp 140-151.

83. J. K. Brimacombe, "Interfacial Turbulence in Liquid-Metal Systems", Physical Chemistry of Process Metallurgy: The Richardson Conference, The Institution of Mining and Metallurgy, 1974, pp 175-185.
84. F. D. Richardson, "Interfacial Phenomena in Metallurgical Reactions", Special Lecture, Transactions ISIJ, Volume 14, 1974, pp 1-8.
85. R. G. Barton and J. K. Brimacombe, "Interfacial Turbulence during Dissolution of Solid  $\text{Cu}_2\text{S}$  in Molten Copper", Metallurgical Transactions, Volume 7B, March 1976, pp 144-145.
86. P. L. T. Brian, "Effect of Gibbs Adsorption on Marangoni Instability", AICHE Journal, Volume 17, No. 4, July 1971, pp 765-672.
87. K. Monma and H. Suto, "Effect of Dissolved Sulphur, Oxygen, Selenium and Tellurium on the Surface Tension of Liquid Copper", Transactions of JIM, Volume 2, 1961, pp 148-153.
88. J. C. Berg and A. Acrivos, "The Effect of Surface Active Agents on Convection Cells Induced Surface Tension", Chemical Engineering Science, Volume 20, 1965, pp 737-745.
89. R. E. Davis and A. Acrivos, "The Influence of Surfactants on the Creeping Motion of Bubbles", Chemical Engineering Science, Volume 21, 1966, pp 681-685.
90. J. C. Berg and C. R. Morig, "Density Effects in Interfacial Convection", Chemical Engineering Science, Volume 24, 1969, pp 937-946.
91. O. Smigelschi, D. G. Suciuc and E. Ruckenstein, "Absorption under the Action of Artificially Provoked Marangoni Effect", Chemical Engineering Science, Volume 24, 1969, pp 1227-1234.
92. P. P. Pugachevich and V. B. Lazarev, "Surface Phenomena in Ternary Metal Solutions", The Role of Surface Phenomena in Metallurgy, Edited by V. N. Eremenko, Consultants Bureau New York, 1963, pp 24-30.
93. Y. V. Naidich, V. N. Eremenko, V. V. Fesenko, M. I. Vasiliu and L. F. Kirichenko, "Variation of the Surface Tension of Pure Copper with Temperature", The role of Surface Phenomena in Metallurgy, Edited by V. N. Eremenko, Consultants Bureau New York, 1963, pp 41-45.
94. P. P. Pugachevich and V. I. Yashkichev, "Measurement of Surface Tension of Liquid Metals at High Temperatures", The Role of Surface Phenomena in Metallurgy, Edited by V. N. Eremenko, Consultants Bureau New York, 1963, pp 46-53.
95. V. N. Eremenko, Y. V. Naidich, "Surface Activity of Oxygen in the Silver-Oxygen System", The Role of Surface Phenomena in Metallurgy, Edited by V. N. Eremenko, Consultants Bureau New York, 1963, pp 65-67.
96. V. V. Fesenko, "Determination of the Surface Tension by the Method of the Maximum Pressure in a Bubble for Nonwetting Systems", The Role of Surface Phenomena in Metallurgy, Edited by V. N. Eremenko, Consultants Bureau New York, 1963, pp 80-84.



97. Bernard and C. H. P. Lupis, "The Surface Tension of Liquid Silver Alloys: Part II. Ag-O Alloys", Metallurgical Transactions, Volume 2, November 1971, pp 2991-2998.
98. Rubin and C. J. Radke, "Dynamic Interfacial Tension Minima in Finite Systems", Chemical Engineering Science, Volume 35, 1980, pp 1129-1138.
99. F. D. Richardson, "Interfacial Phenomena and Metallurgical Processes", Canadian Metallurgical Quarterly, Volume 21, No. 2, 1982, pp 111-119.
100. J. C. Berg, "Interfacial Hydrodynamics: An Overview", Canadian Metallurgical Quarterly, Volume 21, No. 2, 1982, pp 121-136.
101. G. R. Belton, "The Interplay Between Strong Adsorption of Solutes and Interfacial Kinetics at the Liquid Metal Surface", Canadian Metallurgical Quarterly, Volume 21, No. 2, 1982, pp 137-143.
102. K. W. Lange and M. Wilken, "Marangoni Type Interfacial Phenomena In High and Low temperature Systems", Canadian Metallurgical Quarterly, Volume 22, No. 3, 1983, pp 321-326
103. J. C. Slattery, "**Interfacial Transport Phenomena**", Springer-Verlag, New York, 1990.
104. C. Choo, K. Mukai and J. M. Toguri, "Marangoni Interaction of a Liquid Droplet Falling onto a Liquid Pool", Welding Research Supplement, April 1992, pp 139-146.
105. J. B. Kennedy and A. M. Neville, "**Basic Statistical Methods For Engineers and Scientists**", 2nd Edition, New York, 1976, pp 255-276.
106. D. A. Skoog and D. M. West, "**Fundamentals of Analytical Chemistry**", Fourth Edition, CBS College Publishing, 1982, pp 740-743.
107. D. A. Skoog and D. M. West, "**Fundamentals of Analytical Chemistry**", Fourth Edition, CBS College Publishing, 1982, pp 195-216.
108. D. A. Skoog and D. M. West, "**Fundamentals of Analytical Chemistry**", Fourth Edition, CBS College Publishing, 1982, pp 696.
109. J. O. Hirschelder, C. F. Curtiss, R. B. Bird, "**Molecular Theory of Gases and Liquids**", John Wiley & Sons, Inc., New York, 1954, pp (528, 604-605).
110. J. O. Hirschelder, C. F. Curtiss, R. B. Bird, "**Molecular Theory of Gases and Liquids**", John Wiley & Sons, Inc., New York, 1954, pp (530).
111. N. H. Chen and D. F. Othmer, "New Generalized Equation for Gas Diffusion Coefficient", Journal of Chemical Engineering Data, Volume 7, No. 1, January 1962, pp (37-41).
112. R. B. Bird, W. E. Stewart and E. N. Lightfoot, "**Transport Phenomena**", John Wiley & Sons, Inc. New York, 1960, pp 744.
113. J. J. Byerley and N. Takebe, "Densities of Molten Nickel Mattes", Metallurgical Transactions, Volume 2, April 1971, pp 1107-1111.

- 114.D. R. Gaskell, "**Introduction To Metallurgical Thermodynamics**", Second Edition, McGraw-Hill Book Company, New York, 1981, pp 164-167.
- 115.F. D. Richardson, "**Physical Chemistry of Melts in Metallurgy**", Volume 1, Academic Press Inc., New York, 1974, pp 61-62.
- 116.F. D. Richardson, "**Physical Chemistry of Melts in Metallurgy**", Volume 2, Academic Press Inc., New York, 1974, pp 318-325.
- 117.L. Coudurier, D. W. Hopkins, I. Wilkomirsky, "**Fundamentals of Metallurgical Processes**", 2nd Edition, Pergamon Press, 1985, pp 225-227.
- 118.T. Rosenquist, "**Principles of Extractive Metallurgy**", 2nd Edition, McGraw-Hill, New York, 1983, pp 105-106.
- 119.J. B. Kennedy and A. M. Neville, "**Basic Statistical Methods For Engineers and Scientists**", 2nd Edition, New York, 1976, pp 232,460-461.
- 120.R. B. Bird, W. E. Stewart and E. N. Lightfoot, "**Transport Phenomena**", John Wiley & Sons, Inc. New York, 1960, pp 601-619.
- 121.G. H. Geiger and D. R. Poirier, "**Transport Phenomena In Metallurgy**", Addison-Wesley, 1973, pp 527.

## Appendix A Experimental

### 1. Reactor Insulating Materials

Insulating alumina refractories (Alundum L) were supplied by NORTON

REFRATORIES. The supplied properties of this insulating material are as follows:

Table A.1. Physical properties of the insulating alumina brick.

Bulk Density	1.36 (g/cm <sup>3</sup> )
Total Porosity	65-70%
Maximum Operating Temperature	1850 °C
Compressive Deformation at 1500 °C	0 % to 10 p.s.i.
Thermal Conductivity at 860 °C	0.89 (watt/m.°K)
Thermal Expansion from 21-1510 °C	1.02×10 <sup>-5</sup> (°C <sup>-1</sup> )

Table A.2. Chemical analysis (approximate).

Alumina (Al <sub>2</sub> O <sub>3</sub> )	99.01%
Silica (SiO <sub>2</sub> )	0.58%
Other	0.41%

Porcelain wool (refractory fibrous material) was supplied by THE CARBORUNDUM COMPANY. REFRACTORY DIVISION. The manufacturer supplied properties of this insulating material are as follows:

Table A.3. Thermal conductivity as a function of mean temperature (0.08 g/cm<sup>3</sup>).

Temperature (°C)	200	427	760	980
Thermal Conductivity (watt/m.°K)	0.66	1.12	2.08	3.11

Table A.4. Approximate chemical analysis (wt % - binder removed).

Silica (SiO <sub>2</sub> )	46.8
Alumina (Al <sub>2</sub> O <sub>3</sub> )	50.9
B <sub>2</sub> O <sub>3</sub>	1.2
Na <sub>2</sub> O	0.8
Trace Inorganic	0.3-0.5

## 2. Reactor Power Supply

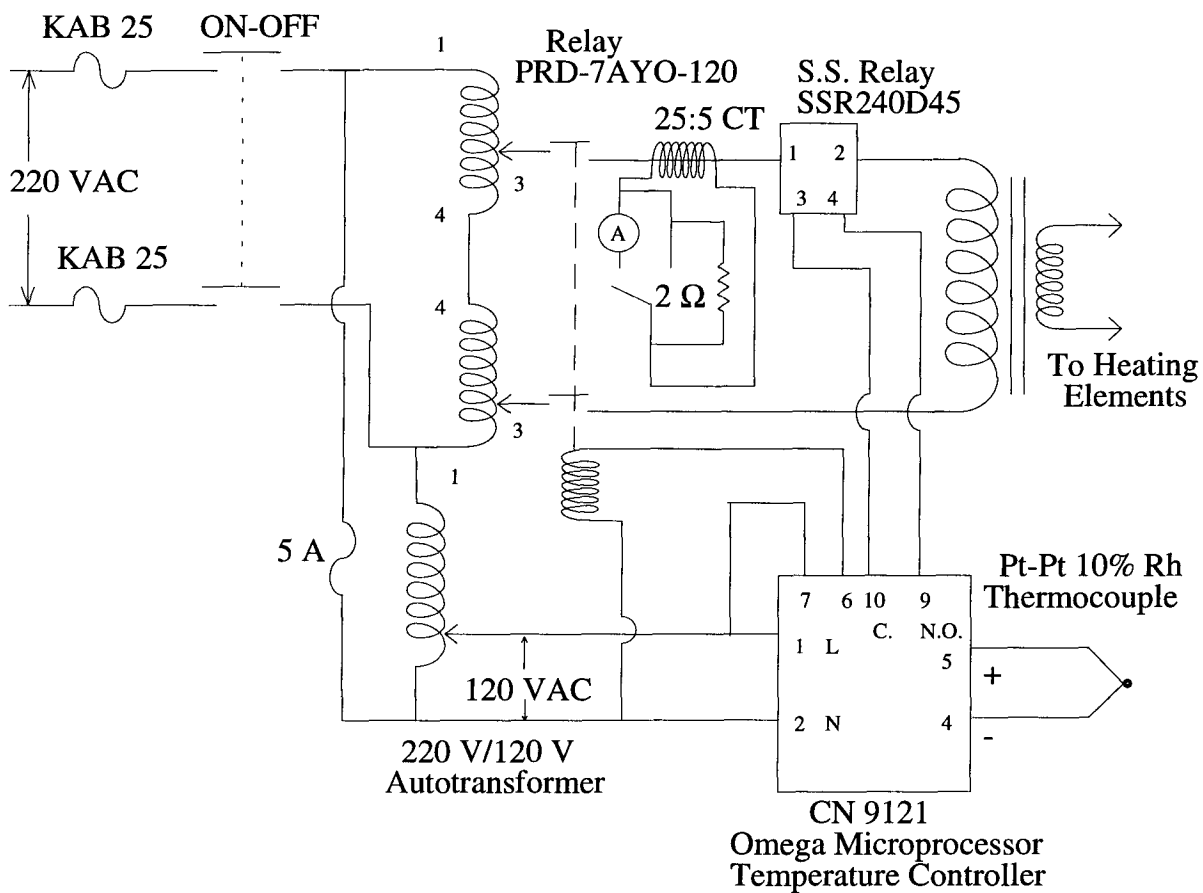


Figure A.1. Electrical circuit for the furnace power supply.

### 3. Load Cell Components

Table A.5. Strain gauges manufacturer (HBM ELEKRISCHES MESSEN MECHANISCHER GRÖSSEN) specifications.

Gauge factor	$2.05 \pm 1 \%$
Temperature coefficient of gauge factor	$95 \text{ ppm}/^\circ\text{K}$
Resistance	$120 \Omega \pm 0.02 \%$

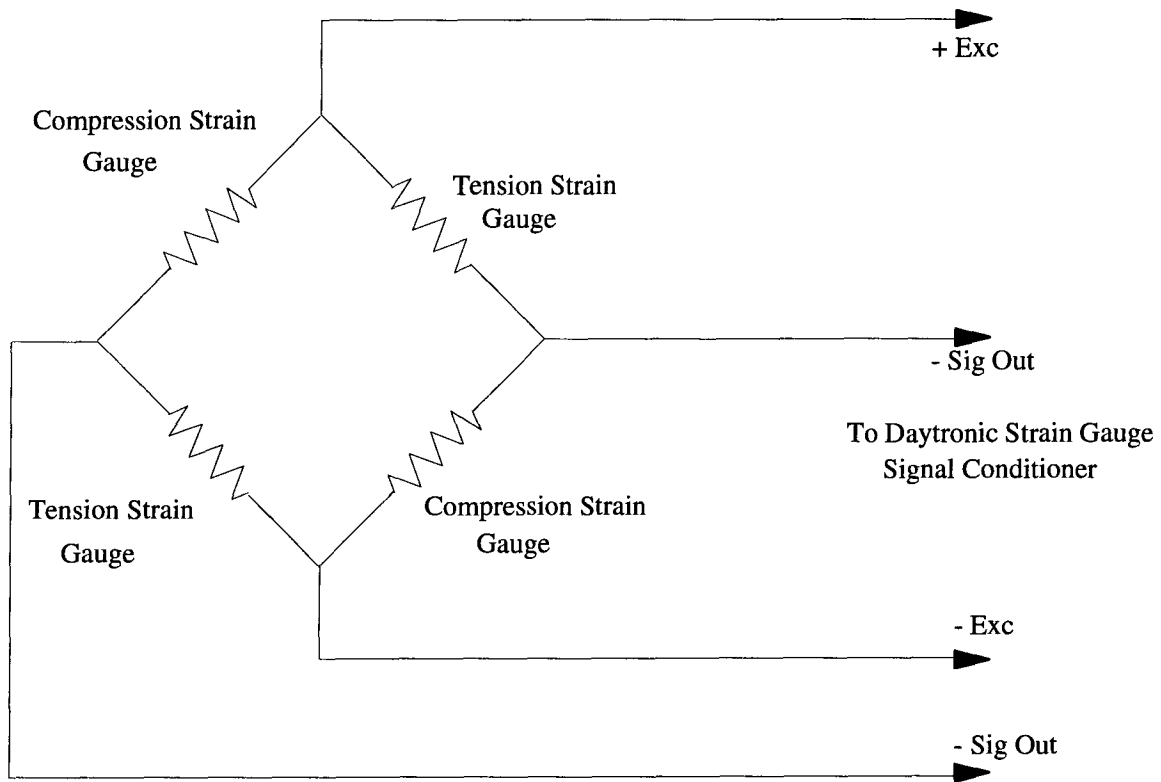


Figure A.2. Circuit design of the load cell.

### Appendix B Gas Analysis Raw Data

Table B.1. Run No. 4, the data for the experimental conditions of: 922 ml/min of 26% O<sub>2</sub> and 74% Ar, at 1200 °C, 1.05 atm pressure, ambient temperature of 23 °C, average final gas temperature of 23 °C #.

Time	$N_{SO_2}(t)$	$Q_{off}^f(t)$	$\delta Q_{off}^f(t)$
(min)	(mole)	(ml/min)	(ml/min)
0	0.000		
5	0.000		
10	0.032		
15	0.075		
20	0.084		
30	0.108		
40	0.163		
50	0.224		
60	0.284		
70	0.367		
80	0.451		
90	0.526		
100	0.605		
110	0.694		
120	0.769		

Table B.2. Run No. 5, the data for the experimental conditions of: 922 ml/min of 26% O<sub>2</sub> and 74% Ar, at 1200 °C, 1.05 atm pressure, ambient temperature of 23 °C, average final gas temperature of 23 °C #.

Time	$N_{SO_2}(t)$	$Q_{off}^f(t)$	$\delta Q_{off}^f(t)$
(min)	(mole)	(ml/min)	(ml/min)
0	0.000		
5	0.038		
10	0.067		
15	0.086		
20	0.117		
30	0.163		
40	0.197		
50	0.266		
60	0.352		
70	0.426		
80	0.497		
90	0.584		
100	0.669		
110	0.751		
120	0.835		

# This run was carried out using prepared Cu<sub>2</sub>S (20.30% sulphur and 79.05% copper).

Table B.3. Run No. 6, the data for the experimental conditions of: 922 ml/min of 26% O<sub>2</sub> and 74% Ar, at 1200 °C, 1.05 atm pressure, ambient temperature of 23 °C, average final gas temperature of 25 °C.

Time	$N_{SO_2}(t)$	$Q_{off}^f(t)$	$\delta Q_{off}^f(t)$
(min)	(mole)	(ml/min)	(ml/min)
0	0.000		
5	0.019		
10	0.049		
15	0.078		
20	0.108		
30	0.131		
40	0.171		
50	0.203		
60	0.255		
70	0.340		
80	0.439		
90	0.528		
100	0.611		
110	0.716		
120	0.804		

Table B.4. Run No. 7, the data for the experimental conditions of: 922 ml/min of 26% O<sub>2</sub> and 74% Ar, at 1200 °C, 1.05 atm pressure, ambient temperature of 23 °C, average final gas temperature of 25 °C.

Time	$N_{SO_2}(t)$	$Q_{off}^f(t)$	$\delta Q_{off}^f(t)$
(min)	(mole)	(ml/min)	(ml/min)
0	0.000	0	0
5	0.019	756	9
10	0.044	749	8
15	0.072		
20	0.104		
25	0.131	744	7
30	0.166	747	14
35	0.203	748	18
40	0.246	760	14
45	0.286	745	4
50	0.329	746	11
55	0.374	744	1
60	0.416	751	10
80	0.603	754	11
100	0.778	746	8
120	0.963	758	10
140	1.142	744	1
160	1.137		



Table B.5. Run No. 8, the data for the experimental conditions of: 1010 ml/min of 24% O<sub>2</sub> and 76% Ar, at 1200 °C, 1.05 atm pressure, ambient temperature of 23 °C, average final gas temperature of 24 °C.

Time	$N_{SO_2}(t)$	$Q_{off}^f(t)$	$\delta Q_{off}^f(t)$
(min)	(mole)	(ml/min)	(ml/min)
0	0.000	0	0
5	0.031	798	7
10	0.061	783	12
15	0.089	789	16
20	0.117	776	10
25	0.145	789	12
30	0.174	803	14
35	0.213	799	19
40	0.251	788	17
45	0.295	797	21
50	0.333	796	9
55	0.372	801	8
60	0.415	792	9
80	0.588	814	3
100	0.757	823	15
120	0.971	816	19
140	1.120	817	20
160	1.156	814	7
180	1.165	822	15

Table B.6. Run No. 9, the data for the experimental conditions of: 1480 ml/min of 22% O<sub>2</sub> and 79% Ar, at 1200 °C, 1.07 atm pressure, ambient temperature of 23 °C, average final gas temperature of 23 °C.

Time	$N_{SO_2}(t)$	$Q_{off}^f(t)$	$\delta Q_{off}^f(t)$
(min)	(mole)	(ml/min)	(ml/min)
0	0.000	0	0
5	0.037	1213	14
10	0.077	1235	11
15	0.120	1222	2
20	0.153	1220	8
25	0.203	1221	4
30	0.263	1198	4
35	0.319	1194	21
40	0.373	1213	10
45	0.432	1192	12
50	0.498	1179	23
55	0.556	1178	15
60	0.627	1218	28
80	0.889	1209	13
100	1.107	1195	10
120	1.123	1243	17
140	1.118	1287	16
160	1.150	1326	11

Table B.7. Run No. 10, the data for the experimental conditions of: 2078 ml/min of 20% O<sub>2</sub> and 80% Ar, at 1200 °C, 1.07 atm pressure, ambient temperature of 23 °C, average final gas temperature of 24 °C.

Time	$N_{SO_2}(t)$	$Q_{off}^f(t)$	$\delta Q_{off}^f(t)$
(min)	(mole)	(ml/min)	(ml/min)
0	0.000	0	0
5	0.050	1620	10
10	0.105	1665	19
15	0.152	1677	41
20	0.207	1688	12
25	0.271	1712	17
30	0.345	1663	16
35	0.416	1665	19
40	0.483	1639	15
45	0.555	1677	41
50	0.627	1639	15
55	0.697	1665	19
60	0.750	1677	41
65	0.826	1665	19
70	0.896		
75	0.976	1639	15
80	1.055	1677	41
85	1.106	1665	19

Table B.8. Run No. 11, the data for the experimental conditions of: 1987 ml/min of 20% O<sub>2</sub> and 80% Ar, at 1200 °C, 1.05 atm pressure, ambient temperature of 23 °C, average final gas temperature of 25 °C.

Time	$N_{SO_2}(t)$	$Q_{off}^f(t)$	$\delta Q_{off}^f(t)$
(min)	(mole)	(ml/min)	(ml/min)
0	0.000	0	0
5	0.036	1607	6
10	0.088	1604	5
15	0.136	1673	11
20	0.194	1691	14
25	0.256	1703	12
30	0.326		
35	0.387	1695	4
40	0.461	1690	11
45	0.534	1680	12
50	0.592	1690	10
55	0.657	1685	14
60	0.726	1689	4
65	0.802	1640	7
70	0.872	1670	22
75	0.956	1676	6
80	1.014	1675	14
85	1.016	1972	11
90	1.018	1578	3

Table B.9. Run No 12, the data for the experimental conditions of: 1580 ml/min of 22% O<sub>2</sub> and 78% Ar, at 1200 °C, 1.06 atm pressure, ambient temperature of 25 °C, average final gas temperature of 25 °C.

Time	$N_{SO_2}(t)$	$Q_{off}^f(t)$	$\delta Q_{off}^f(t)$
(min)	(mole)	(ml/min)	(ml/min)
0	0.000		
1	0.005		
2	0.012		
3	0.011		
4	0.023		
10	0.079		
15	0.120		
20	0.169		
25	0.231		
30	0.295		
35	0.367		
40	0.435		
45	0.512		
50	0.588		
55	0.665		

Table B.10. Run No. 13, the data for the experimental conditions of: 1521 ml/min of 20% O<sub>2</sub> and 80% Ar, at 1200 °C, 1.08 atm pressure, ambient temperature of 27 °C, average final gas temperature of 26 °C<sup>‡</sup>.

Time	$N_{SO_2}(t)$	$Q_{off}^f(t)$	$\delta Q_{off}^f(t)$
(min)	(mole)	(ml/min)	(ml/min)
0	0.000	0	0
1	0.002	1234	2
2	0.006		
3	0.013		
4	0.017		
5	0.025		
10	0.060	1238	6
15	0.100	1236	6
20	0.140	1233	7
25	0.191	1231	17
30	0.250	1218	0
35	0.312	1224	4
40	0.366	1218	6
50	0.484	1253	4
60	0.611	1259	12
70	0.734	1244	13
80	0.869	1217	12
90	0.987	1232	13
99	1.076	1240	23

‡. Approximately 2 mm inside diameter alumina lance was used in this run.

Table B.11. Run No. 14, the data for the experimental conditions of: 1530 ml/min of 21% O<sub>2</sub> and 79% Ar, at 1200 °C, 1.07 atm pressure, ambient temperature of 22 °C, average final gas temperature of 22 °C<sup>‡‡</sup>.

Time	$N_{SO_2}(t)$	$Q_{off}^f(t)$	$\delta Q_{off}^f(t)$
(min)	(mole)	(ml/min)	(ml/min)
0	0.000	0	0
5	0.027	1236	7
10	0.063	1250	14
15	0.104	1247	10
20	0.130	1247	9
25	0.180	1250	6
30	0.215	1262	8
40	0.317	1267	8
50	0.433	1260	8
60	0.555	1252	18
70	0.652	1245	14
80	0.810	1220	46
90	0.947	1245	14
95	1.010	1236	9

Table B.12. Run No. 15, the data for the experimental conditions of: 2006 ml/min of 22% O<sub>2</sub> and 78% Ar, at 1200 °C, 1.07 atm pressure, ambient temperature of 26 °C, average final gas temperature of 27 °C.

Time	$N_{SO_2}(t)$	$Q_{off}^f(t)$	$\delta Q_{off}^f(t)$
(min)	(mole)	(ml/min)	(ml/min)
0	0.000	0	0
5	0.047	1614	15
10	0.099	1598	16
15	0.131	1635	14
20	0.213	1664	13
25	0.306	1617	8
30	0.416	1653	13
35	0.464	1645	12
40	0.553	1636	12
45	0.611	1647	7
50	0.707	1668	31
55	0.793	1672	22
60	0.876	1631	16
65	0.952	1635	5
70	1.040	1639	8
75	1.087	1668	13

<sup>‡‡</sup>. Approximately 2 mm inside diameter alumina lance was used in this run. Prepared Cu<sub>2</sub>S, of approximately 19% sulphur and 77.05% copper, was used in this run.

Table B.13. Run No. 16, the data for the experimental conditions of: 2510 ml/min of 23% O<sub>2</sub> and 77% Ar, at 1200 °C, 1.08 atm pressure, ambient temperature of 25 °C, average final gas temperature of 25 °C.

Time	$N_{SO_2}(t)$	$Q_{off}^f(t)$	$\delta Q_{off}^f(t)$
(min)	(mole)	(ml/min)	(ml/min)
0	0.000	0	0
5	0.039	2196	13
10	0.095	2124	6
15	0.156	2111	35
20	0.253	2089	43
25	0.342	2077	40
30	0.444	2059	62
35	0.542	2066	85
40	0.641	2067	104
45	0.747	2064	93
50	0.847	2058	70
55	0.939	2045	30
60	1.031	2194	211
65	1.072	2270	241

Table B.14. Run No. 17, the data for the experimental conditions of: 1755 ml/min of 22% O<sub>2</sub> and 78% Ar, at 1200 °C, 1.07 atm pressure, ambient temperature of 22 °C, average final gas temperature of 24 °C.

Time	$N_{SO_2}(t)$	$Q_{off}^f(t)$	$\delta Q_{off}^f(t)$
(min)	(mole)	(ml/min)	(ml/min)
0	0.000	0	0
5	0.030	1425	13
10	0.078	1445	7
15	0.120	1455	14
20	0.171	1442	64
25	0.234	1439	92
30	0.300	1410	21
35	0.370	1384	57
40	0.430	1508	59
45	0.500	1467	26
50	0.564	1557	17
55	0.637	1414	18
60	0.703	1399	7
65	0.763	1440	18
70	0.835	1422	10
75	0.908	1436	7

Table B.15. Run No. 18, the data for the experimental conditions of: 2230 ml/min of 23% O<sub>2</sub> and 77% Ar, at 1200 °C, 1.08 atm pressure, ambient temperature of 23 °C, average final gas temperature of 23 °C.

Time	$N_{SO_2}(t)$	$Q_{off}^f(t)$	$\delta Q_{off}^f(t)$
(min)	(mole)	(ml/min)	(ml/min)
0	0.000	0	0
5	0.033	1863	29
10	0.086	1894	6
15	0.145	1881	17
20	0.239	1839	96
25	0.327	1865	64
30	0.420	1831	48
35	0.516	1868	63
40	0.606	1860	46
45	0.698	1962	45
50	0.782	1956	120
55	0.876	1812	17
60	0.959	1849	3
65	1.043	1862	22
69	1.071	1899	7

Table B.16. Run No. 19, the data for the experimental conditions of: 3015 ml/min of 22% O<sub>2</sub> and 78% Ar, at 1200 °C, 1.07 atm pressure, ambient temperature of 26 °C, average final gas temperature of 27 °C<sup>##</sup>.

Time	$N_{SO_2}(t)$	$Q_{off}^f(t)$	$\delta Q_{off}^f(t)$
(min)	(mole)	(ml/min)	(ml/min)
0	0.000	0	0
2	0.020	2435	5
4	0.066		
5	0.089		
6	0.110		
8	0.173		
10	0.214	2377	24
15			
20	0.492	2375	47
25	0.637	2454	17
30	0.762	2526	10
35	0.877	2476	29
40	0.979	2470	27
44	1.051	2556	19

<sup>##</sup> The lance nozzle was located at the melt surface in this run. In all of the other runs the initial lance to melt surface was fixed at approximately 1 cm.

Table B.17. Run No. 21, the data for the experimental conditions of: 4055 ml/min of 22% O<sub>2</sub> and 78% Ar, at 1200 °C, 1.13 atm pressure, ambient temperature of 26 °C, average final gas temperature of 26 °C.

Time	$N_{SO_2}(t)$	$Q_{off}^f(t)$	$\delta Q_{off}^f(t)$
(min)	(mole)	(ml/min)	(ml/min)
0	0.000	0	0
2	0.023	3448	63
4	0.049		
5	0.055		
6	0.074		
8	0.109	3514	33
10	0.145	3507	27
15	0.262	3429	32
20	0.371	3480	19
25	0.497	3507	36
30	0.630	3518	176
35	0.775	3526	65
40	0.938	3429	25

Table B.18. Run No. 22, the data for the experimental conditions of: 2006 ml/min of 27% O<sub>2</sub> and 73% Ar, at 1200 °C, 1.10 atm pressure, ambient temperature of 26 °C, average final gas temperature of 26 °C.

Time	$N_{SO_2}(t)$	$Q_{off}^f(t)$	$\delta Q_{off}^f(t)$
(min)	(mole)	(ml/min)	(ml/min)
0	0.000	0	0
2	0.016	1528	34
4	0.037		
5	0.047		
6	0.061		
8	0.091		
10	0.114		
15	0.207	1525	10
20	0.304	1523	17
25	0.408	1526	13
30	0.515	1516	10
35	0.629	1487	24
40	0.735	1513	3
45	0.855	1499	9
50	0.968	1502	7
55	1.044	1534	27

Table B.19. Run No. 23, the data for the experimental conditions of: 2009 ml/min of 35% O<sub>2</sub> and 65% Ar, at 1200 °C, 1.10 atm pressure, ambient temperature of 21 °C, average final gas temperature of 21 °C.

Time	$N_{SO_2}(t)$	$Q_{off}^f(t)$	$\delta Q_{off}^f(t)$
(min)	(mole)	(ml/min)	(ml/min)
0	0.000	0	0
2	0.018	1503	22
4	0.050	1415	5
5	0.069	1457	8
6	0.083	1463	12
8	0.120	1452	24
10	0.154	1457	20
15	0.268	1459	23
20	0.393	1441	21
25	0.532	1459	8
30	0.664	1446	46
35	0.822	1432	12
40	0.945	1416	17
45	1.045	1419	66
49	1.038	1377	35

Table B.20. Run No. 24, the data for the experimental conditions of: 1997 ml/min of 46% O<sub>2</sub> and 54% Ar, at 1200 °C, 1.10 atm pressure, ambient temperature of 24 °C, average final gas temperature of 24 °C.

Time	$N_{SO_2}(t)$	$Q_{off}^f(t)$	$\delta Q_{off}^f(t)$
(min)	(mole)	(ml/min)	(ml/min)
0	0.000	0	0
2	0.029	1339	90
4	0.086	1208	24
5	0.108	1270	54
6	0.140	1185	25
8	0.202	1196	75
10	0.265	1177	17
15	0.447	1176	8
20	0.623	1176	9
25	0.804	1180	14
30	0.982	1202	12
35	1.071	1204	54
39	1.081	1179	6



Table B.21. Run No. 25, the data for the experimental conditions of: 1997 ml/min of 64% O<sub>2</sub> and 36% Ar, at 1200 °C, 1.10 atm pressure, ambient temperature of 22 °C, average final gas temperature of 22 °C.

Time	$N_{SO_2}(t)$	$Q_{off}^f(t)$	$\delta Q_{off}^f(t)$
(min)	(mole)	(ml/min)	(ml/min)
0	0.000	0	0
2	0.046	1005	252
4	0.128	809	22
5	0.156	777	2
6	0.202		
8	0.302	765	14
10	0.398		
15	0.644	810	15
20	0.911	796	6
25	1.066	789	46
29	1.066	807	10

Table B.22. Run No. 27, the data for the experimental conditions of: 1998 ml/min of 23% O<sub>2</sub> and 77% Ar, at 1250 °C, 1.13 atm pressure, ambient temperature of 23 °C, average final gas temperature of 23 °C.

Time	$N_{SO_2}(t)$	$Q_{off}^f(t)$	$\delta Q_{off}^f(t)$
(min)	(mole)	(ml/min)	(ml/min)
0	0.000	0	0
2	0.014	1570	13
4	0.028	1684	9
5	0.045	1624	12
6	0.051	1648	36
8	0.068	1619	6
10	0.094	1709	42
15	0.151	1657	9
20	0.220	1670	17
25	0.301	1650	10
29	0.372	1639	18
35	0.447	1624	12
40	0.538	1639	18
45	0.617	1679	28
50	0.708	1677	27
55	0.804	1672	32
60	0.848		

Table B.23. Run No. 28, the data for the experimental conditions of: 1999 ml/min of 23% O<sub>2</sub> and 77% Ar, at 1300 °C, 1.08 atm pressure, ambient temperature of 22 °C, average final gas temperature of 22 °C.

Time	$N_{SO_2}(t)$	$Q_{off}^f(t)$	$\delta Q_{off}^f(t)$
(min)	(mole)	(ml/min)	(ml/min)
0	0.000	0	0
2	0.013	1675	57
4	0.024	1660	41
5	0.027		
6	0.070		
8	0.076		
10	0.096	1617	3
15	0.156	1627	13
20	0.228		
25	0.315	1632	15
29	0.372	1652	30
35	0.463	1627	19
40	0.543	1631	16
45	0.619	1623	12
50	0.719	1589	22
55	0.797	1601	19
60	0.873	1648	31
65	0.931	1687	63
70	0.992	1673	8

Table B.24. Run No. 29, the data for the experimental conditions of: 1994 ml/min of 21% O<sub>2</sub> and 79% Ar, at 1275 °C, 1.08 atm pressure, ambient temperature of 24 °C, average final gas temperature of 24 °C.

Time	$N_{SO_2}(t)$	$Q_{off}^f(t)$	$\delta Q_{off}^f(t)$
(min)	(mole)	(ml/min)	(ml/min)
0	0.000	0	0
2	0.014	1674	65
4	0.029		
6	0.037		
8	0.069		
10	0.083	1687	41
15	0.125	1686	33
20	0.178		
25	0.245		
30	0.301		
35	0.370		
40	0.432		
45	0.498		
50	0.573		
55	0.630		
60	0.729	1662	16
65	0.805	1680	19
70	0.888	1665	14

Table B.25. Run No. 30, the data for the experimental conditions of: 2006 ml/min of 22% O<sub>2</sub> and 78% Ar, at 1325 °C, 1.08 atm pressure, ambient temperature of 25 °C, average final gas temperature of 24 °C.

Time	$N_{SO_2}(t)$	$Q_{off}^f(t)$	$\delta Q_{off}^f(t)$
(min)	(mole)	(ml/min)	(ml/min)
0	0.000	0	0
2	0.009	1632	13
4	0.029	1629	13
5	0.043	1625	5
6	0.057	1634	1
8	0.083	1637	5
10	0.103	1635	4
15	0.166	1633	9
20	0.243	1634	15
25	0.327	1637	12
30	0.403	1632	10
35	0.481	1633	10
40	0.570	1617	5
45	0.654	1600	13
50	0.738	1605	28
55	0.828	1602	16
60	0.907	1640	25
65	0.975	1654	6
70	1.043	1684	9
74	1.045	1652	8

Table B.26. Run No. 31, the data for the experimental conditions of: 2006 ml/min of 22% O<sub>2</sub> and 78% Ar, at 1275 °C, 1.08 atm pressure, ambient temperature of 23 °C, average final gas temperature of 21 °C.

Time	$N_{SO_2}(t)$	$Q_{off}^f(t)$	$\delta Q_{off}^f(t)$
(min)	(mole)	(ml/min)	(ml/min)
0	0.000	0	0
2	0.008	1626	1
4	0.029	1597	4
5	0.044	1611	3
6	0.057	1626	13
8	0.071	1626	13
10	0.105	1627	13
15	0.166	1625	7
20	0.245	1614	5
25	0.331	1609	10
30	0.418	1597	23
35	0.538	1596	13
40	0.606	1595	3
45	0.687	1596	19
50	0.784	1603	11
55	0.881	1599	13
60	0.975	1605	8
65	1.028	1607	17
68	1.053	1624	31

Table B.27. Run No. 33, the data for the experimental conditions of: 3490 ml/min of 27% O<sub>2</sub> and 73% Ar, at 1200 °C, 1.11 atm pressure, ambient temperature of 24 °C, average final gas temperature of 22 °C.

Time	$N_{SO_2}(t)$	$Q_{off}^f(t)$	$\delta Q_{off}^f(t)$
(min)	(mole)	(ml/min)	(ml/min)
0	0.000	0	0
2	0.012	3039	21
4	0.051	3119	18
5	0.062	3073	0
6	0.086	3196	32
8	0.110	3145	41
10	0.163	3289	28
15	0.295	3271	37
20	0.438	2883	64
25	0.581	2827	39
30	0.765	2787	50
35	0.924	2806	24
38	1.042	2798	37

Table B.28. Run No. 34, the data for the experimental conditions of: 1996 ml/min of 78% O<sub>2</sub> and 22% Ar, at 1200 °C, 1.11 atm pressure, ambient temperature of 23 °C, average final gas temperature of 22 °C.

Time	$N_{SO_2}(t)$	$Q_{off}^f(t)$	$\delta Q_{off}^f(t)$
(min)	(mole)	(ml/min)	(ml/min)
0	0.000	0	0
2	0.066	447	20
4	0.157	426	13
5	0.217	436	3
6	0.264	471	8
8	0.390	476	11
10	0.498	479	17
12	0.629	489	17
14	0.741		
15	0.836	486	2
16	0.882	428	2
18	0.999	481	36
20	1.033	384	18
22	1.049	406	18

Table B.29. Run No. 36, the data for the experimental conditions of: 2032 ml/min of 22% O<sub>2</sub> and 78% Ar, at 1200 °C, 1.08 atm pressure, ambient temperature of 23 °C, average final gas temperature of 22 °C\*\*.

Time	$N_{SO_2}(t)$	$Q_{off}^f(t)$	$\delta Q_{off}^f(t)$
(min)	(mole)	(ml/min)	(ml/min)
0	0.000	0	0
2	0.012	1735	6
4	0.027	1768	29
5	0.032	1757	12
6	0.041	1724	23
8	0.065	1713	11
10	0.082	1724	32
15	0.148	1717	19
20	0.219	1708	10
25	0.302	1691	21
30	0.391	1711	10
35	0.462	1691	15
40	0.544	1691	7
45	0.629	1696	6
50	0.711	1677	9
55	0.795	1692	7
60	0.882	1688	18
65	0.969	1693	12

Table B.30. Run No. 37, the data for the experimental conditions of: 2000 ml/min of 21% O<sub>2</sub> and 79% N<sub>2</sub>, at 1200 °C, 1.08 atm pressure, ambient temperature of 21 °C, average final gas temperature of 22 °C.

Time	$N_{SO_2}(t)$	$Q_{off}^f(t)$	$\delta Q_{off}^f(t)$
(min)	(mole)	(ml/min)	(ml/min)
0	0.000	0	0
2	0.012	1590	32
4	0.024	1616	16
5	0.042	1603	9
6	0.048	1645	0
8	0.060	1639	7
10	0.077	1651	8
15	0.117	1631	23
20	0.198	1635	7
25	0.271	1598	16
30	0.361	1584	23
35	0.451	1608	47
40	0.540	1599	12
45	0.636	1587	12
50	0.713	1582	6
55	0.801	1594	13
60	0.896	1583	17
65	0.990	1597	12
70	1.018	1559	4

\*\* Approximately 77 ml/min argon was used for invoking bath mixing. in this run.

Table B.31. Run No. 41, the data for the experimental conditions of: 3516 ml/min of 24% O<sub>2</sub> and 76% Ar, at 1200 °C, 1.10 atm pressure, ambient temperature of 24 °C, average final gas temperature of 24 °C.

Time	$N_{SO_2}(t)$	$Q_{off}^f(t)$	$\delta Q_{off}^f(t)$
(min)	(mole)	(ml/min)	(ml/min)
0	0.000	0	0
2	0.024	3029	64
4	0.049	3053	13
5	0.067	2971	82
6	0.103	3017	40
8	0.130	2830	10
10	0.167	2933	53
15	0.261	2889	50
20	0.388	2902	110
25	0.545	2938	27
30	0.690	2888	36
35	0.827	2883	43
40	1.001	2839	17

Table B.32. The effect of volumetric flow rate of reaction gas on the reaction rates; sample weight of 200 grams of  $\text{Cu}_2\text{S}$ ; at 1200 °C and 1.08 atm; 22%  $\text{O}_2$  and 78% Ar; lance inside diameter of 3 mm.

Run	$Q_r^a$	$\overset{\circ}{N}_{SO_2}^P$	$\overset{\circ}{N}_{SO_2}^S$	$\overset{\circ}{N}_{O_2}^P$	$\overset{\circ}{N}_{O_2}^S$	$t^*$	$\overset{\circ}{W}_{ga}^P$	$\overset{\circ}{W}_{ga}^S$	$\overset{\circ}{W}_w^P$	$\overset{\circ}{W}_w^S$
	(ml/min)	(mol/min)	(mol/min)	(mol/min)	(mol/min)	(min)	(g/min)	(g/min)	(g/min)	(g/min)
9	1480	0.008	0.012	0.011	0.012	25	-0.18	-0.42		
12	1579	0.009	0.015			24				
17	1755	0.009	0.013	0.013	0.013	19	-0.16	-0.45	-0.11	-0.21
15	2006	0.009	0.016	0.016	0.015	14	-0.07	-0.57		
36	2032	0.010	0.016	0.015	0.016	14	-0.17	-0.53	-0.14	-0.66
21	4055	0.015	0.026	0.023	0.002	11	-0.21	-0.95		

Table B.33. The effect of volumetric flow rate of reaction gas on the reaction rates; sample weight of 200 grams of  $\text{Cu}_2\text{S}$ ; at 1200 °C and 1.08 atm; 24%  $\text{O}_2$  and 76% Ar; lance inside diameter of 3 mm.

Run	$Q_r^a$	$\overset{\circ}{N}_{SO_2}^P$	$\overset{\circ}{N}_{SO_2}^S$	$\overset{\circ}{N}_{O_2}^P$	$\overset{\circ}{N}_{O_2}^S$	$t^*$	$\overset{\circ}{W}_{ga}^P$	$\overset{\circ}{W}_{ga}^S$	$\overset{\circ}{W}_w^P$	$\overset{\circ}{W}_w^S$
	(ml/min)	(mol/min)	(mol/min)	(mol/min)	(mol/min)	(min)	(g/min)	(g/min)	(g/min)	(g/min)
8	1010	0.006	0.009	0.009	0.008	36	-0.10	-0.30		
41	3516	0.018	0.028	0.025	0.028	13	-0.34	-0.92		

Table B.34. The effect of reaction gas composition on the reaction rates; sample weight of 200 grams of  $\text{Cu}_2\text{S}$ ; at 1200 °C and 1.10 atm, 2000 ml/min, lance inside diameter of 3 mm.

Run	%O <sub>2</sub>	$\overset{\circ}{N}_{SO_2}^P$ (mol/min)	$\overset{\circ}{N}_{SO_2}^S$ (mol/min)	$\overset{\circ}{N}_{O_2}^P$ (mol/min)	$\overset{\circ}{N}_{O_2}^S$ (mol/min)	$t^*$ (min)	$\overset{\circ}{W}_{ga}^P$ (g/min)	$\overset{\circ}{W}_{ga}^S$ (g/min)	$\overset{\circ}{W}_w^P$ (g/min)	$\overset{\circ}{W}_w^S$ (g/min)
15	22	0.009	0.016	0.016	0.015	14	-0.07	-0.57		
22	27	0.012	0.021	0.020	0.020	11	-0.15	-0.71	-0.14	
23	35	0.017	0.027	0.024	0.024	11	-0.28	-0.94		
24	46	0.027	0.036	0.033	0.036	7	-0.67	-1.15		-1.42
25	64	0.037	0.050	0.048	0.050	5	-0.81	-1.63		
34	78	0.048	0.061	0.063	0.061	5	-1.03	-1.95	-0.85	-2.18

Table B.35. The effect of temperature on the reaction rates; sample weight of 200 grams of  $\text{Cu}_2\text{S}$ ; at 1.09 atm, 2000 ml/min of 22% O<sub>2</sub> and 78% Ar, lance inside diameter of 3 mm.

Run	T (°C)	$\overset{\circ}{N}_{SO_2}^P$ (mol/min)	$\overset{\circ}{N}_{SO_2}^S$ (mol/min)	$\overset{\circ}{N}_{O_2}^P$ (mol/min)	$\overset{\circ}{N}_{O_2}^S$ (mol/min)	$t^*$ (min)	$\overset{\circ}{W}_{ga}^P$ (g/min)	$\overset{\circ}{W}_{ga}^S$ (g/min)	$\overset{\circ}{W}_w^P$ (g/min)	$\overset{\circ}{W}_w^S$ (g/min)
15	1200	0.009	0.016	0.016	0.015	14	-0.07	-0.57		
31	1250	0.012	0.017	0.016	0.017	13	-0.23	-0.57	-0.16	-0.98
30	1300	0.013	0.016	0.016	0.016	17	-0.30	-0.53	-0.29	-0.87



Table B.36. The effect of temperature on the reaction rates; sample weight of 200 grams of  $\text{Cu}_2\text{S}$ ; at 1.09 atm, 2000 ml/min of 23%  $\text{O}_2$  and 77% Ar, lance inside diameter of 3 mm.

Run	T	$\overset{\circ}{N}_{SO_2}^P$	$\overset{\circ}{N}_{SO_2}^S$	$\overset{\circ}{N}_{O_2}^P$	$\overset{\circ}{N}_{O_2}^S$	$t^*$	$\overset{\circ}{W}_{ga}^P$	$\overset{\circ}{W}_{ga}^S$	$\overset{\circ}{W}_w^P$	$\overset{\circ}{W}_w^S$
	(°C)	(mol/min)	(mol/min)	(mol/min)	(mol/min)	(min)	(g/min)	(g/min)	(g/min)	(g/min)
27	1250	0.010	0.016	0.015	0.015	15	-0.19	-0.54		-0.31
28	1300	0.012	0.016	0.016	0.016	16	-0.25	-0.49	-0.16	-0.34

Table B.37. The effect of bath mixing on the reaction rates; sample weight of 200 grams of  $\text{Cu}_2\text{S}$ ; at 1200 °C and 1.09 atm, 2000 ml/min of 22%  $\text{O}_2$  and 78% Ar, lance inside diameter of 3 mm (‡ approximately 77 ml/min Ar was used to invoke artificial mixing).

Run	$Q_r^a$	$\overset{\circ}{N}_{SO_2}^P$	$\overset{\circ}{N}_{SO_2}^S$	$\overset{\circ}{N}_{O_2}^P$	$\overset{\circ}{N}_{O_2}^S$	$t^*$	$\overset{\circ}{W}_{ga}^P$	$\overset{\circ}{W}_{ga}^S$	$\overset{\circ}{W}_w^P$	$\overset{\circ}{W}_w^S$
	(ml/min)	(mol/min)	(mol/min)	(mol/min)	(mol/min)	(min)	(g/min)	(g/min)	(g/min)	(g/min)
15	2006	0.009	0.016	0.016	0.015	14	-0.07	-0.57		
36‡	2032	0.010	0.016	0.015	0.016	14	-0.17	-0.53	-0.14	-0.66

Table B.38. The effect of carrier gas type on the reaction rates; sample weight of 200 grams of  $\text{Cu}_2\text{S}$ ; at 1200 °C and 1.09 atm, 2000 ml/min of 21%  $\text{O}_2$  and 79% Ar, lance inside diameter of 3 mm.

Run	Gas	$\overset{\circ}{N}_{SO_2}^P$	$\overset{\circ}{N}_{SO_2}^S$	$\overset{\circ}{N}_{O_2}^P$	$\overset{\circ}{N}_{O_2}^S$	$t^*$	$\overset{\circ}{W}_{ga}^P$	$\overset{\circ}{W}_{ga}^S$	$\overset{\circ}{W}_w^P$	$\overset{\circ}{W}_w^S$
	Type	(mol/min)	(mol/min)	(mol/min)	(mol/min)	(min)	(g/min)	(g/min)	(g/min)	(g/min)
37	Nitrogen	0.008	0.018	0.015	0.016	16	-0.05	-0.61	-0.04	-0.45
29	Argon	0.009	0.014	0.013	0.023	22	-0.18	-0.49	-0.08	-0.51

## Appendix C Reaction Gas Transport Properties

### 1. Viscosity

The  $k^{\text{th}}$  approximation of the coefficient of viscosity is given by Equation (C.1), where the function of  $f_{\mu}^{(k)}$  is a very slowly varying function of  $T^*$  and differs only slightly from unity [109].

$$\mu_k = 266.93 \times 10^{-7} \frac{\sqrt{MT}}{\sigma^2 \Omega^{(2,2)*}(T^*)} f_{\mu}^{(k)} \quad (\text{C.1})$$

Example C.1. This example is to illustrate the procedure for the calculation of the viscosity of a pure gas. The viscosity of pure argon gas at 1200 °C is calculated as follows: The molecular weight of argon is  $M_{Ar} = 39.948$  g/g.mole. The force constants for argon are  $\epsilon/K = 124^\circ K$  and  $\sigma = 3.418 \text{ \AA}$ . The reduced temperature is then  $T^* = KT/\epsilon = 11.935$ . The data for the integral  $\Omega^{(2,2)*}$ , for the Lennard-Jones potential (taken from Hirschfelder et al. [109]) was fitted to a function of the reduced temperature, as given by Equation (B.2). The value for argon is 0.819. The higher approximation coefficient, for the viscosity, is  $f_{\mu}^{(k)} = 1.0073$ . Substituting for these values in Equation (C.1), yields  $\mu_{Ar} = 6.83 \times 10^{-4}$  g/cm.sec.

$$\Omega^{(2,2)*} = 1.208474/T^{*0.15703} \quad (\text{C.2})$$

The viscosity of binary gas mixtures was calculated as follows [110]:

$$\mu_{mix} = \left[ 1 / \left[ \frac{x_A}{\sqrt{\mu_A}} + \frac{x_B}{\sqrt{\mu_B}} \right] \right]^2 \quad (\text{C.3})$$

Example C.2. The viscosity of a gas mixture of 20% O<sub>2</sub> and 80% Ar, at 1200 °C, is calculated, Using Equation (C.3), as given by Equation (B.4). The parameters for O<sub>2</sub> gas are the molecular weight of oxygen is  $M_{O_2} = 31.9988$  g/g.mole. The force constants for

oxygen are  $\epsilon/K = 113^\circ K$  and  $\sigma = 3.433 \text{ \AA}$ . The reduced temperature is then  $T^* = KT/\epsilon = 13.035$ . The higher approximation coefficient is  $f_\mu^{(k)} = 1.008$ . Substituting for these values in Equation (C.1), the viscosity of pure  $O_2$ , at  $1200^\circ C$ , is calculated to be  $6.16 \times 10^{-4} \text{ g/cm.sec}$ .

$$\mu_{Ar-O_2} = \left[ \frac{1}{\sqrt{\frac{0.8}{6.84 \times 10^{-4}} + \frac{0.2}{6.16 \times 10^{-4}}}} \right]^2 = 6.67 \times 10^{-4} (\text{g/cm.sec}) \quad (\text{C.4})$$

The viscosity of Ar- $O_2$  gas mixtures for the temperature range of  $1000\text{-}1500^\circ C$  and at 1 atm is presented below.

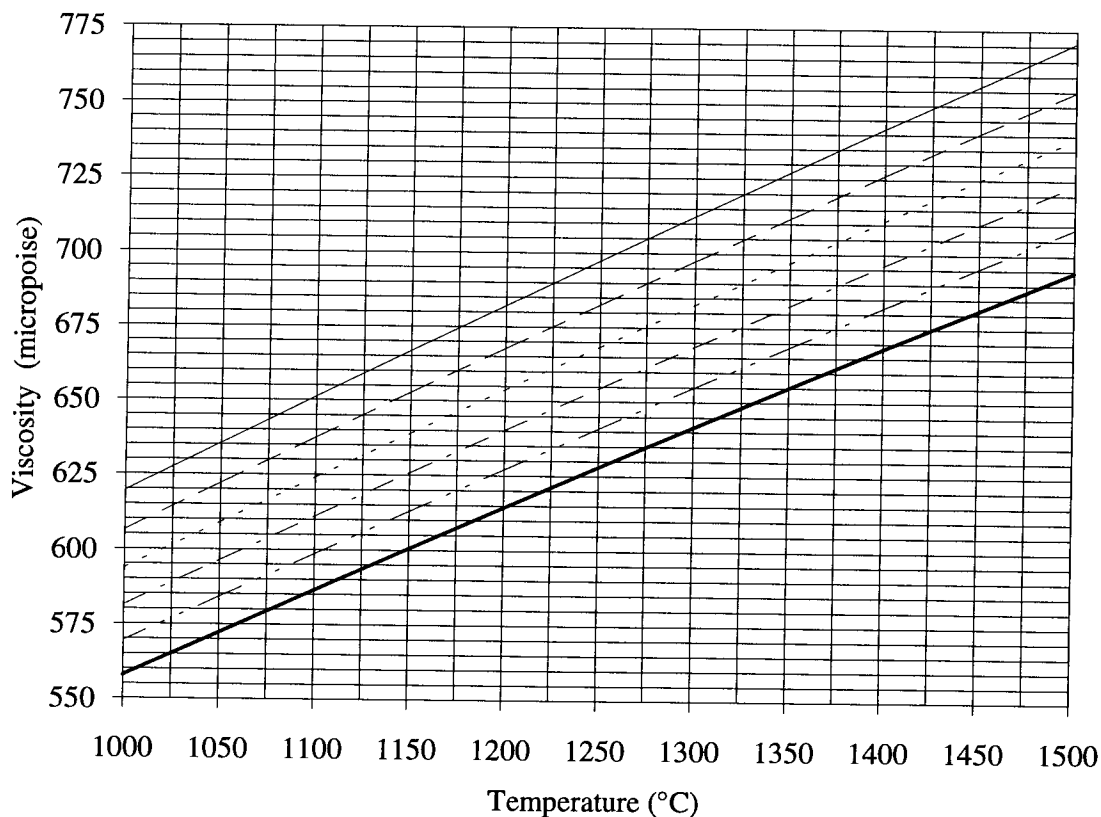


Figure C.1. The viscosity of Ar- $O_2$  gas mixtures as a function of temperature, at 1 atm; — pure Ar; - - - 20%  $O_2$ ; ····· 40%  $O_2$ ; - · - · 60%  $O_2$ ; - - - 80%  $O_2$ ; — pure  $O_2$ .

## 2. Diffusion Coefficient

The diffusion coefficients of some selected binary gas mixtures are calculated using Equation (C.5), as given by equations (C.6-C.10) [111]. The critical properties for these gases are provided in Table B.1. The results of these calculations were found to compare very favorably with the measured and calculated results of Hirschfelder et al [109], as shown in Figure C.2.

$$D_{A-B} = \frac{0.43 \left( \frac{T}{100} \right)^{1.81} \left( \frac{1}{M_A} + \frac{1}{M_B} \right)^{0.5}}{P \left( \frac{T_{c_A} T_{c_B}}{10,000} \right)^{0.1405} \left[ \left( \frac{V_{c_A}}{100} \right)^{0.4} + \left( \frac{V_{c_B}}{100} \right)^{0.4} \right]^2} \quad (C.5)$$

Table C.1. The critical properties of some selected gases (taken from Bird et al. [112]).

Gas	$T_c$ (°K)	$P_c$ (atm)	$V_c$ (cm <sup>3</sup> /mole)
Argon	151	48.0	75.2
Nitrogen	126.2	33.5	90.1
Oxygen	154.4	49.7	74.4
Sulphur Dioxide	430.7	77.8	122.0

$$D_{O_2-Ar} = \frac{0.028565}{P} \left[ \frac{T}{100} \right]^{1.81} \quad (C.6)$$

$$D_{O_2-N_2} = \frac{0.0272107}{P} \left[ \frac{T}{100} \right]^{1.81} \quad (C.7)$$

$$D_{SO_2-O_2} = \frac{0.020118}{P} \left[ \frac{T}{100} \right]^{1.81} \quad (C.8)$$

$$D_{SO_2-Ar} = \frac{0.020103}{P} \left[ \frac{T}{100} \right]^{1.81} \quad (C.9)$$

$$D_{SO_2-N_2} = \frac{0.019287}{P} \left[ \frac{T}{100} \right]^{1.81} \quad (C.10)$$

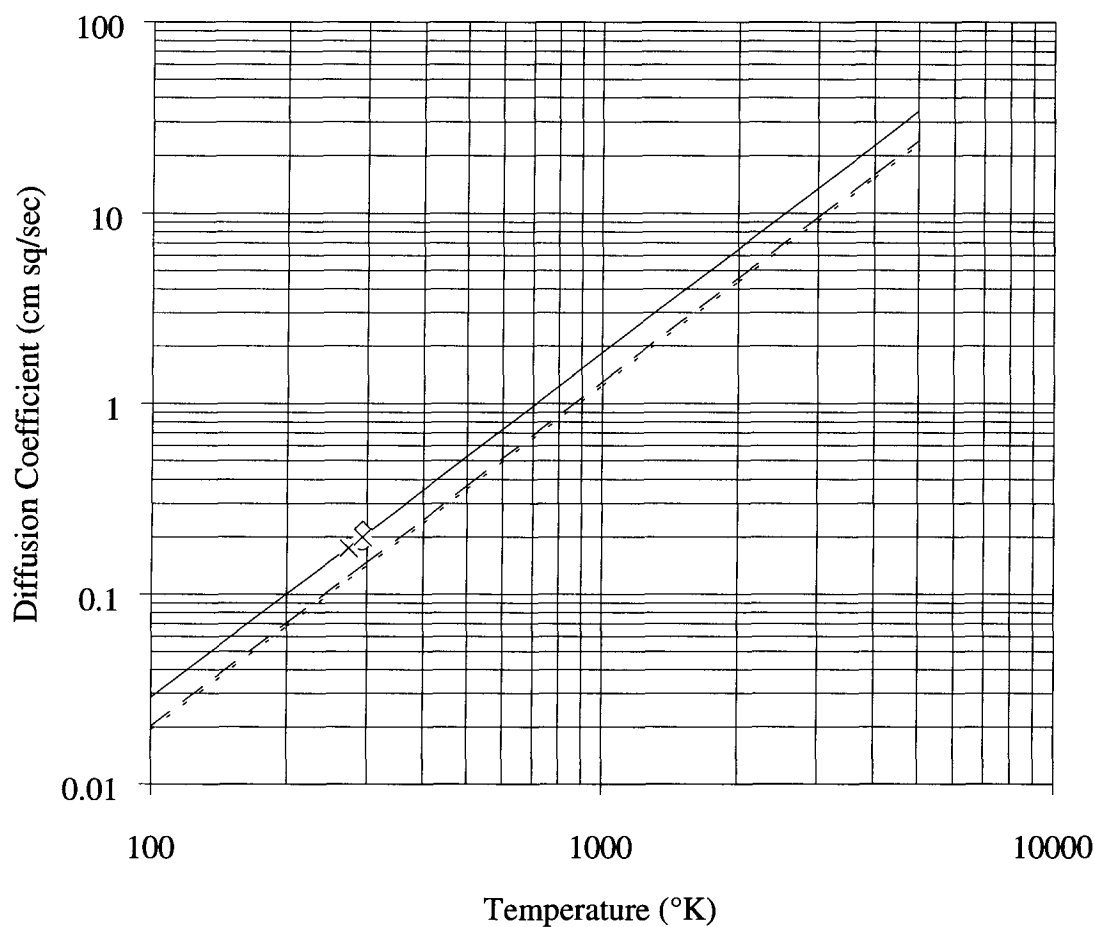


Figure C.2. The diffusion coefficients of some selected binary gas mixtures as a function of temperature, at 1 atm; ——— O<sub>2</sub>-Ar; ○ O<sub>2</sub>-Ar (after Hirschfelder, calculated); □ O<sub>2</sub>-Ar (after Hirschfelder, measured); × O<sub>2</sub>-N<sub>2</sub> (after Hirschfelder, calculated); ◇ O<sub>2</sub>-N<sub>2</sub> (after Hirschfelder, measured); - - - O<sub>2</sub>-SO<sub>2</sub>; - · - · - N<sub>2</sub>-SO<sub>2</sub>.

### 3. Density

Assuming that the gases involved and their mixtures are ideal, the calculation of the gas density of a pure gas was done via the following equation:

$$\rho_A = \frac{PM_A}{RT} \quad (\text{C.11})$$

The density of a gas mixture was calculated from Equation (C.12), where the molecular weight of the gas mixture was calculated using Equation (C.13). The results of these calculations are shown in Figure C.3.

$$\rho_{mix} = \frac{PM_{mix}}{RT} \quad (\text{C.12})$$

$$M_{mix} = x_A M_A + x_B M_B + \dots + x_Z M_Z \quad (\text{C.13})$$

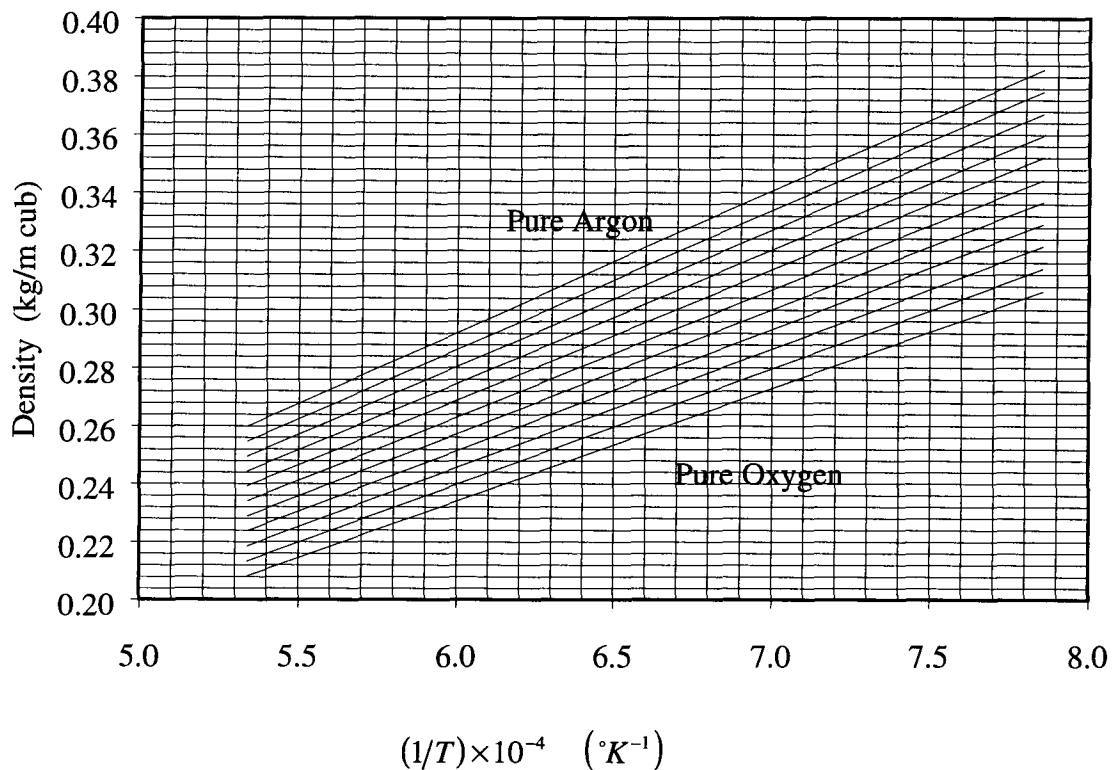


Figure C.3. The density of Ar-O<sub>2</sub> gas mixtures as a function of temperature; for each 10% increments.

### Appendix D Temperature Measurements

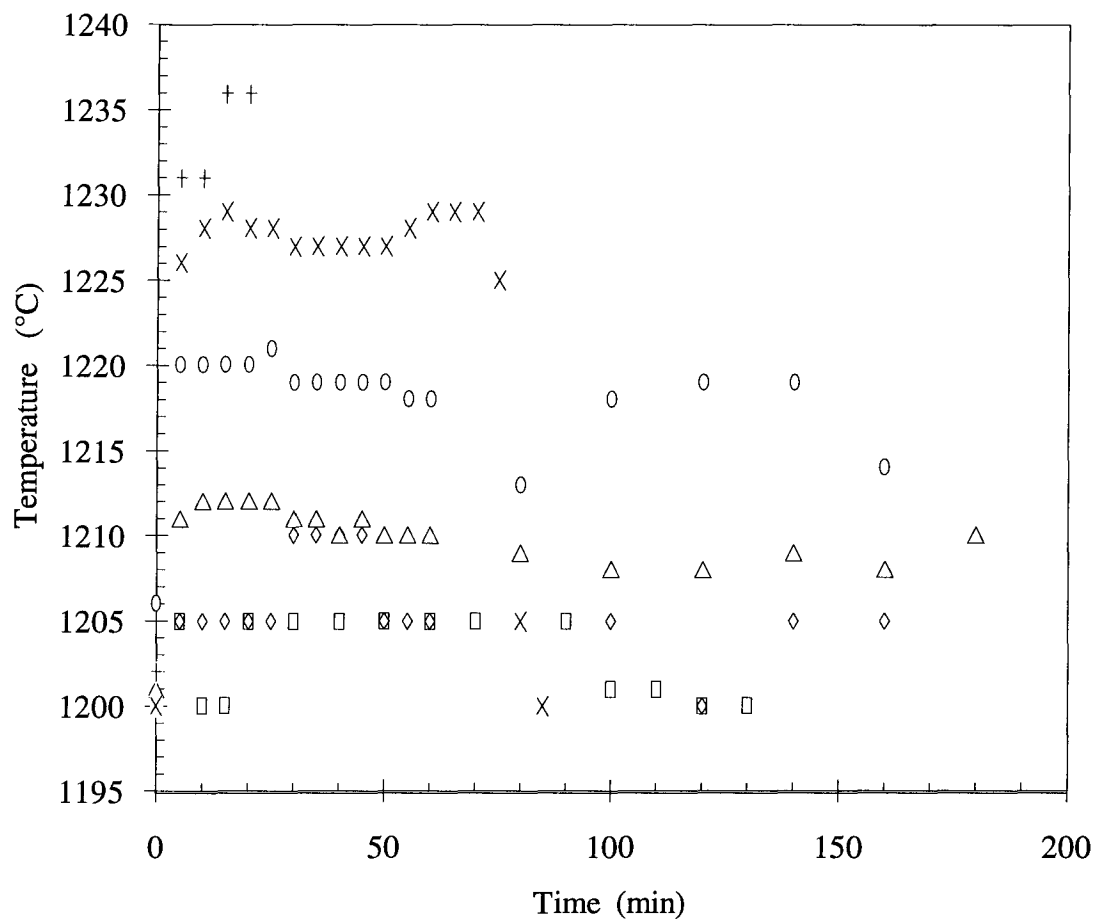


Figure D.1. The manual temperature measurement of the center of the melt; 200 grams  $\text{Cu}_2\text{S}$ , at 1200 °C,  $\square$  Run No. 5. (922 ml/min of 26% $\text{O}_2$  and 74% Ar);  $\diamond$  Run No.7 (922 ml/min of 26% $\text{O}_2$  and 74% Ar);  $\triangle$  Run No. 8 (1010 ml/min of 24% $\text{O}_2$  and 76% Ar);  $\circ$  Run No. 9. (1546 of 24% $\text{O}_2$  and 76% Ar);  $\times$  Run No. 15. (2006 ml/min of 22% $\text{O}_2$  and 78% Ar);  $+$  Run No. 16. (2510 ml/min of 23% $\text{O}_2$  and 77% Ar).

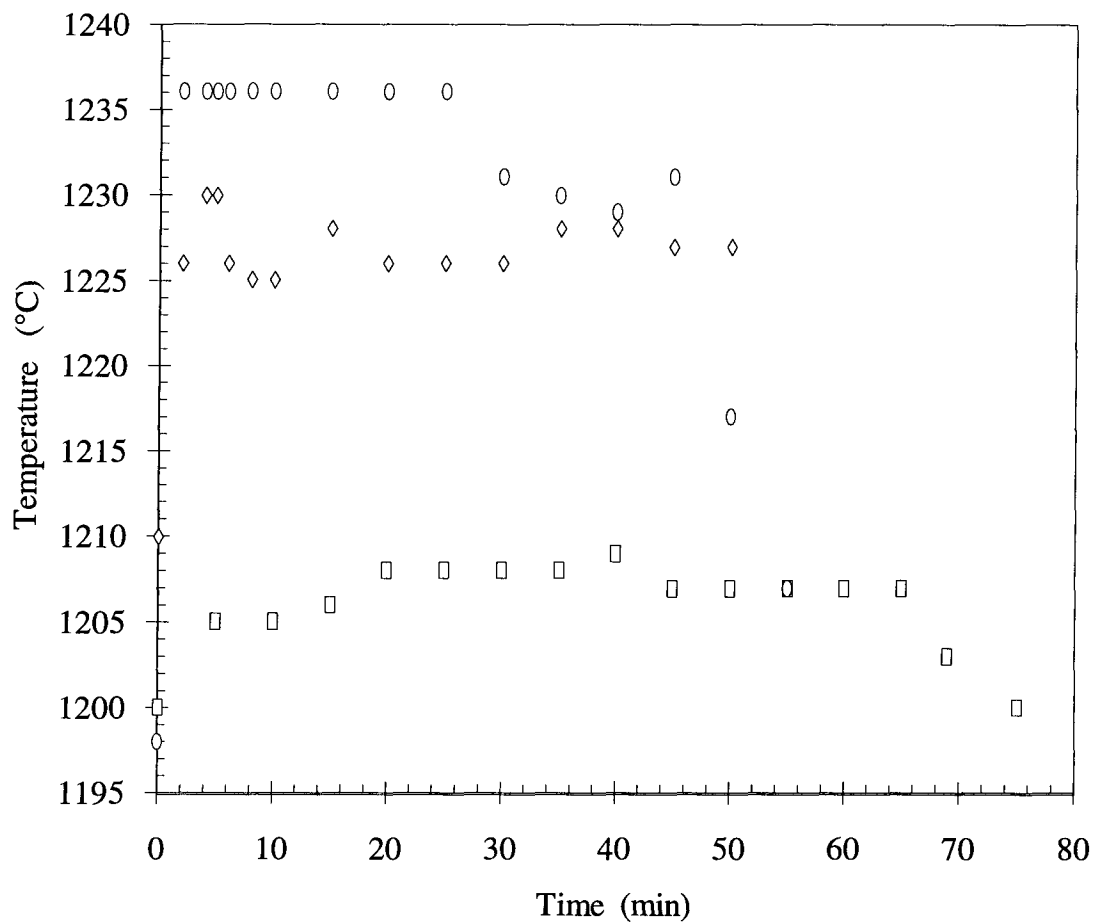


Figure D.2. The manual temperature measurement of the gas at the same height of the lance nozzle; 200 grams  $\text{Cu}_2\text{S}$ , at 1200 °C,  $\square$  Run No. 18. (2234 ml/min of 23% $\text{O}_2$  and 77% Ar);  $\diamond$  Run No. 22. (1998 ml/min of 27% $\text{O}_2$  and 73% Ar);  $\circ$  Run No. 19. (3015 of 23% $\text{O}_2$  and 77% Ar).



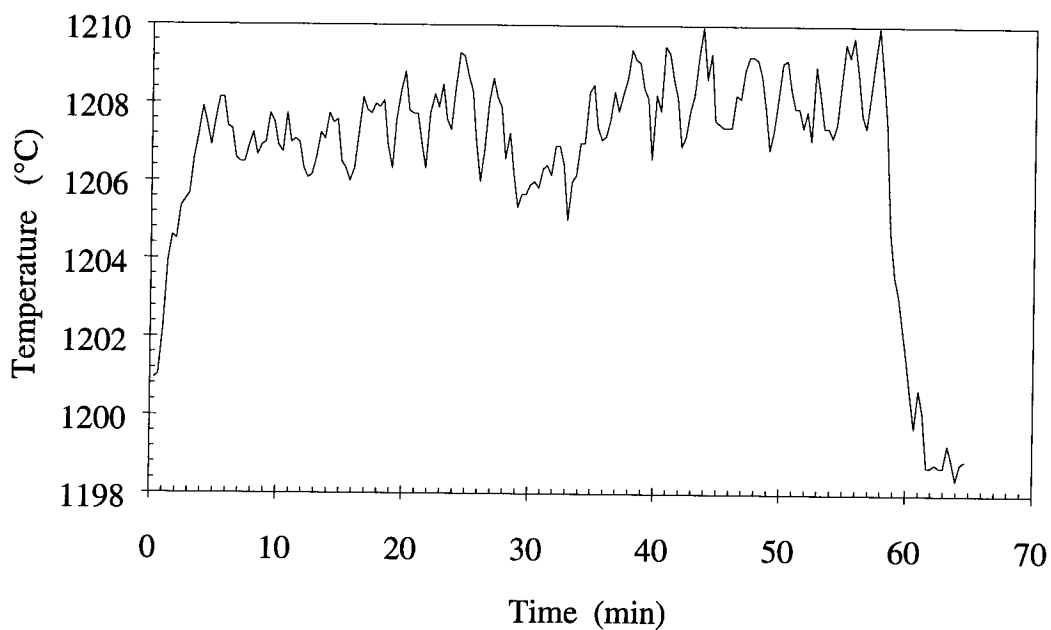


Figure D.3. The gas temperature measurement at the same height of the lance nozzle for Run No. 27, the experimental conditions of 200 grams  $\text{Cu}_2\text{S}$ , at 1200 °C, 1998 ml/min of 27%  $\text{O}_2$  and 73% Ar.

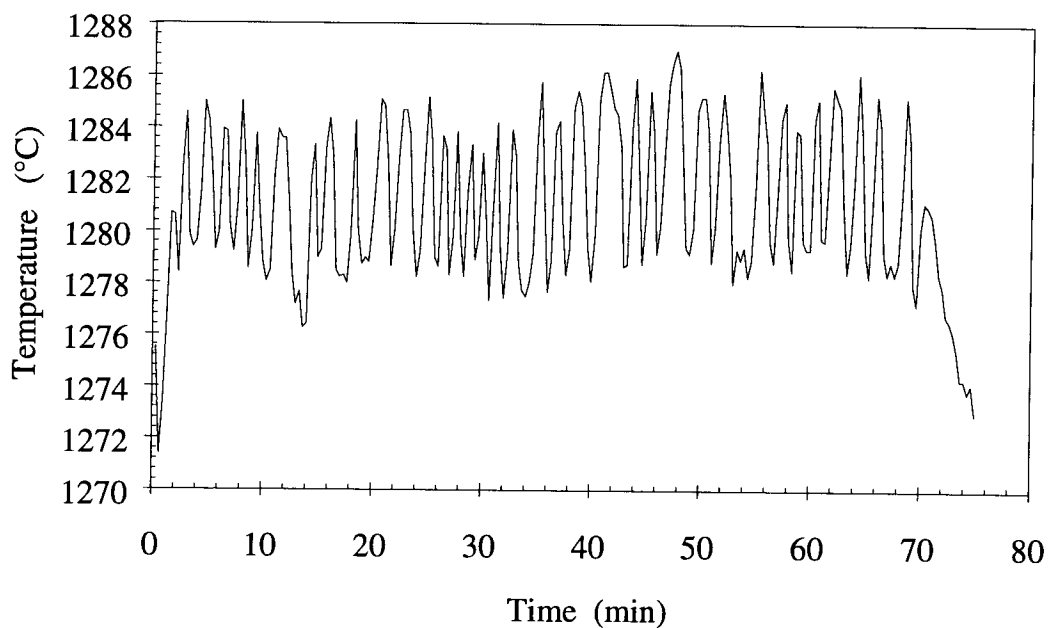


Figure D.4. The temperature measurement at the center of the melt for Run No. 29, the experimental conditions of 200 grams  $\text{Cu}_2\text{S}$ , at 1275 °C, 1994 ml/min of 23%  $\text{O}_2$  and 77% Ar.

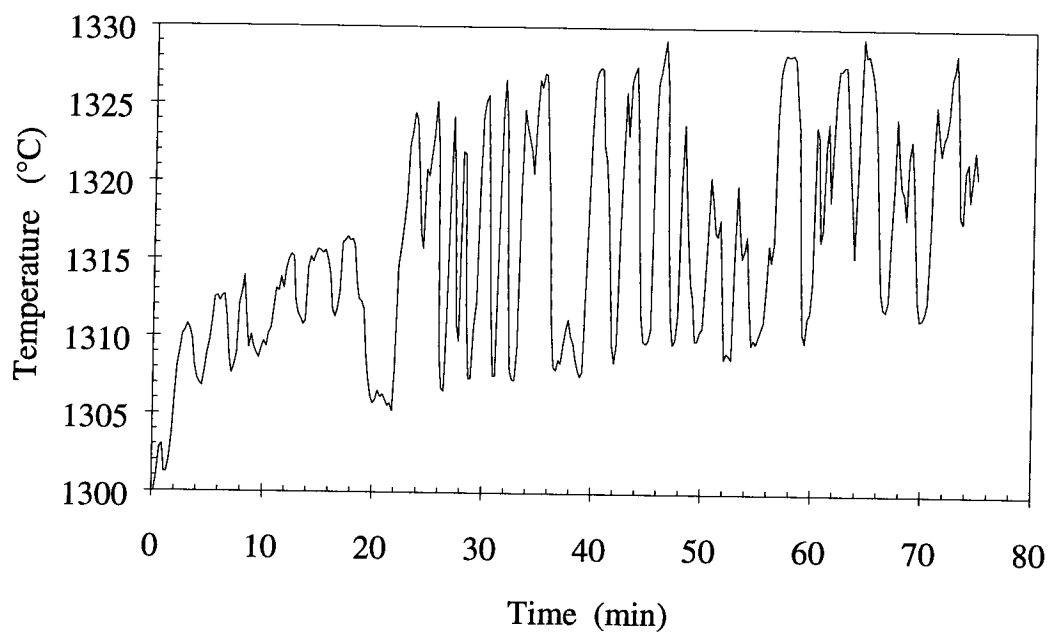


Figure D.5. The gas temperature measurement at the same height of the lance nozzle for Run No. 30, the experimental conditions of 200 grams  $\text{Cu}_2\text{S}$ , at 1300 °C, 2000 ml/min of 22%  $\text{O}_2$  and 78% Ar.

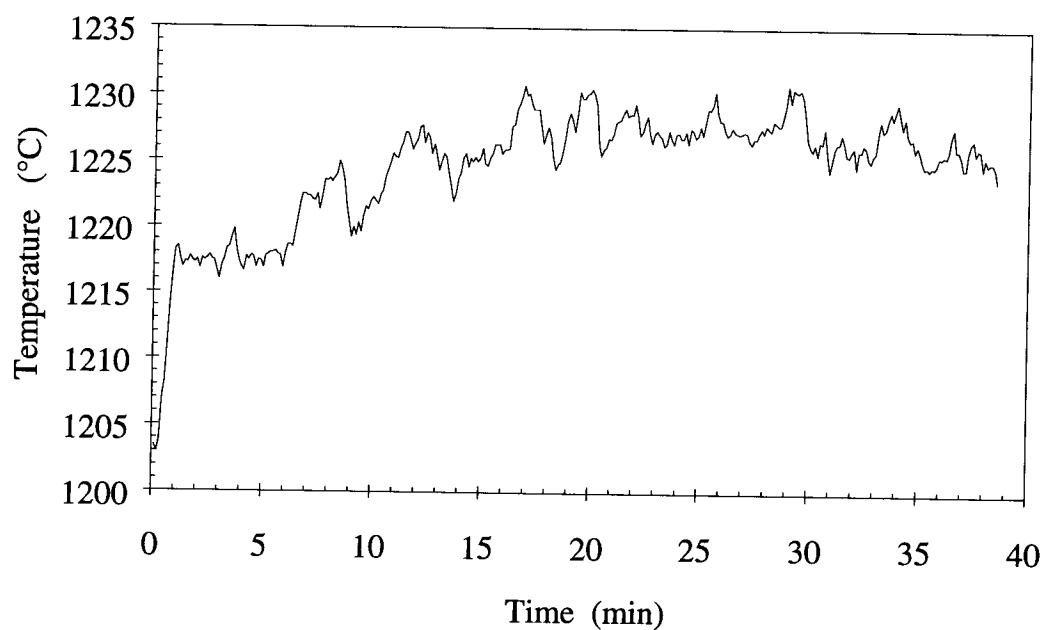


Figure D.6. The gas temperature measurement at the same height of the lance nozzle for Run No. 33, the experimental conditions of 200 grams  $\text{Cu}_2\text{S}$ , at 1200 °C, 3500 ml/min of 29%  $\text{O}_2$  and 71% Ar.

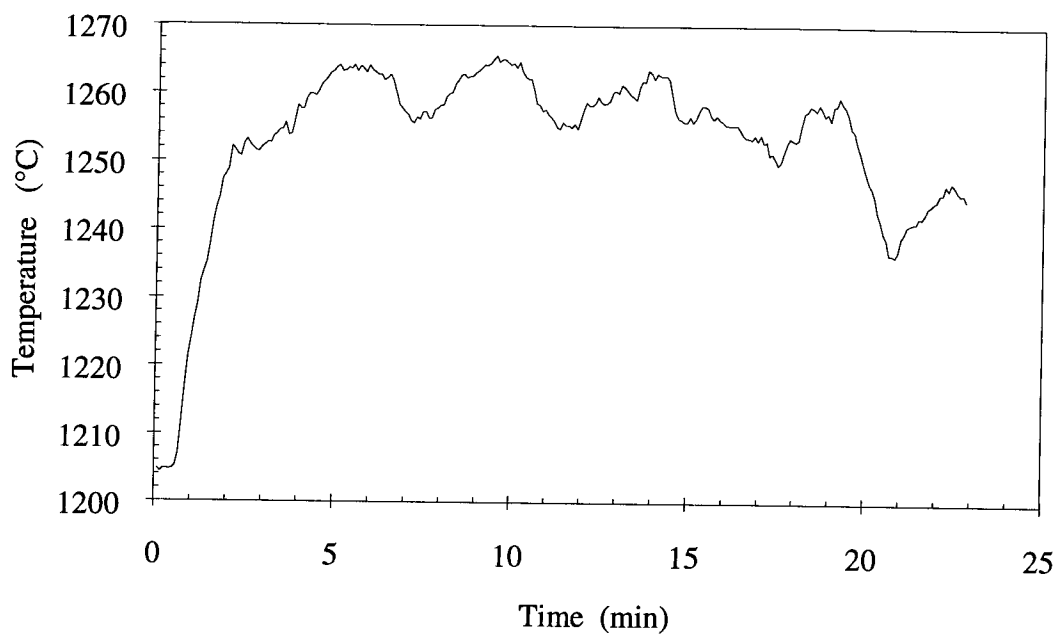


Figure D.7. The gas temperature measurement at the same height of the lance nozzle for Run No. 34, the experimental conditions of 200 grams  $\text{Cu}_2\text{S}$ , at 1200 °C, 2000 ml/min of 79%  $\text{O}_2$  and 21% Ar.

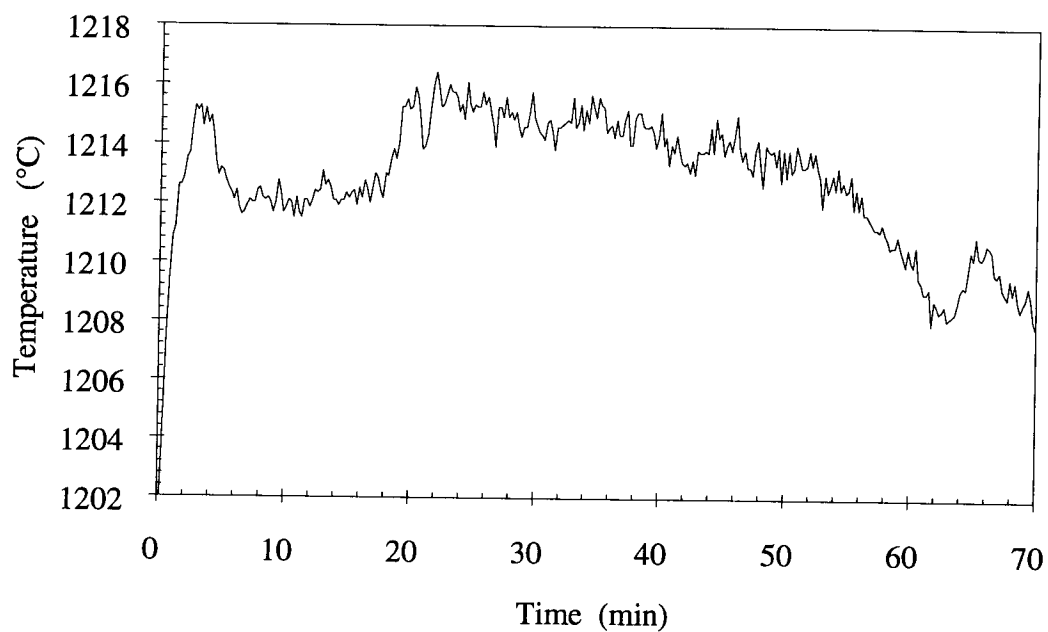


Figure D.8. The gas temperature measurement at the same height of the lance nozzle for Run No. 37, for the experimental conditions of 200 grams of  $\text{Cu}_2\text{S}$  at 1200 °C, 2000 ml/min of 21%  $\text{O}_2$  and 79%  $\text{N}_2$ .

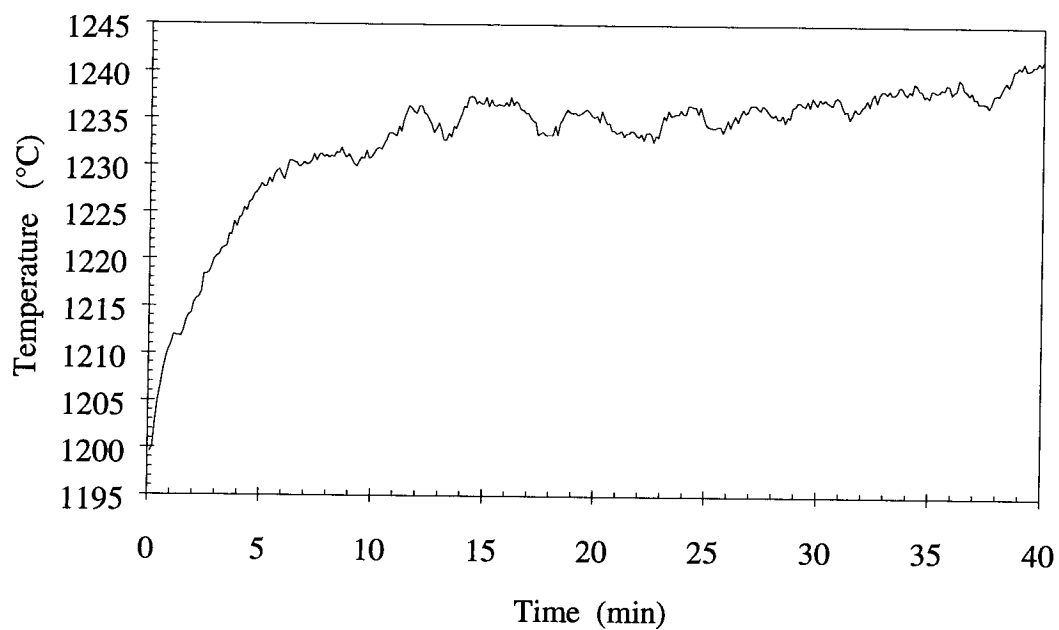


Figure D.9. The gas temperature measurement at the same height of the lance nozzle for Run No. 41, for the experimental conditions of 200 grams of  $\text{Cu}_2\text{S}$  at 1200 °C, 3500 ml/min of 24%  $\text{O}_2$  and 76% Ar.